Genetic control of tissue tension in plants

Robert Bellow

Thesis submitted for the Degree of Doctor of Philosophy

University of East Anglia
John Innes Centre

Submitted March 2022

Abstract

Plant organs are made from a complex arrangement of cells. Development of organs involves cellular coordination. Organs have a layered arrangement and interactions between cell layers are key for organ development. Genes could act non-autonomously between layers through biochemical signalling, mechanosensing or via mechanics. However, distinguishing between these mechanisms has been difficult. Here, I use genetic and hormonal application methods, in systems to visualise altered mechanical interactions. One such system is *Utricularia gibba*, which has internally patterned air spaces. A *U. gibba* dwarf mutant exhibits reduced organ and cell anisotropy. Cell size and length in epidermis of the stolon is reduced, and vasculature is wiggly. The stolon phenotype is most readily explained by reduced epidermal specified growth causing elevated tissue tension in epidermis and compression of internal tissue. Growth analyses suggest that early arrest of epidermal specified growth leads to tissue compression of vasculature that continues to grow. The dwarf mutation is in a gene required for synthesis of the plant growth hormone, brassinosteroid. Treating the mutant with brassinosteroid increases cell size and length in epidermis and rescues the vasculature wiggly phenotype. The proposed effects of brassinosteroid on tissue tension-compression are further supported by analysis of the *Arabidopsis* cell adhesion mutant *quasimodo2-1*. Treatment with brassinosteroid inhibitor leads to increased epidermal cell separation, consistent with brassinosteroid inhibition causing elevated tissue tension in epidermis and compression of internal tissue. Treating with brassinosteroid rescues the cell separation phenotype, consistent with reduced tissue tension-compression. Data from both systems suggests that promotion of epidermal growth by brassinosteroid can act non-autonomously to reduce compression on internal tissue, promoting vascular growth via mechanics. These results are not replicated when altering action of the growth hormone gibberellin, suggesting they are brassinosteroid-specific. Thus, genes controlling brassinosteroid synthesis can act non-autonomously between cell layers to coordinate growth via tissue mechanics.

Contents

List of Figures

List of Tables

Abbreviation list

.BAM – Binary Alignment Map

.SAM – Sequence Alignment Map

.vcf – Virtual Card Format

°C – degree centigrade

µl – micro litres

µm – micrometers

µM – micro molars

6-BA - 6-Benzylaminopurine

A - Adenine

BLAST - Basic Local Alignment Search Tool

bp – base pair

BR - brassinosteroid

BRZ - brassinazole

C - Cytosine

CAS – Chinese Academy of Science

CDS – coding sequence

cM - centimorgans

cm - centimetres

DAS – days after stratification

DNA - deoxyribonucleic acid

dw1 – dwarf1

E. coli - Escherichia coli

EMS - ethyl methanesulfonate

eod – enhancer of dwarf

epiBL - epibrassinolde

EtOH - ethanol

FRET - Förster resonance energy transfer

G - Guanine

g - grams

GA – gibberellic acid

GATK – Genome Analysis Tool Kit

Gb - gigabytes

GC content – Guanine-Cytosine content

GC/MS - Gas chromatography–mass spectrometry

GFP – green fluorescent protein

Hz - Hertz

JIC – John Innes Centre

KASPAR - KBiosciences Competitive AlleleSpecific PCR

kbp – kilobase-pair

L - length

LB - lysogeny broth

LC/MS - liquid chromatography–mass spectrometry

Mbp - megabase-pair

MeOH - methanol

MES - 2-ethanesulfonic acid

ml - millilitres

mm - millimetres

mM - millimolar

MS - Murashige and Skoog

N_2 - Nitrogen

NAA - 1-Naphthaleneacetic acid

NaCl – sodium chloride

ng - nanograms

nM - nanomolar

nm - nanometer

OD_{600} - optical density of a sample measured at a wavelength of 600 nm

OEW – outer epidermal cell wall

OPT – optical projection tomography

PAC - paclobutrazol

PCR – polymerase chain reaction

pH – per hydrogen

qua2-1 – quasimodo 2-1

r - radius

RFU – relative fluorescence units

rpm – revolutions per minute

SAM – shoot apical meristem

SD – standard deviation

SDS - sodium dodecyl sulfate

SEM – standard error of the mean

SLURM - Simple Linux Utility for Resource Management

SNP – single nucleotide polymorphism

spp. - species

T - Thymine

TEM – transmission electron microscopy

v/v – volume by volume

w/v – weight by volume

WGS – whole genome sequencing

wt – wild type

$\bar{x}$ - average

π - pi

Acknowledgements

I would firstly like to thank Enrico Coen for his incredible supervision, support, patience and belief in me over the past years. At the start of this endeavour, he told me that a PhD is one of the most wonderfully formative things you can do, and with his input it certainly has been. I am very grateful for the time and effort you have put in to guiding me and my work. A particular thanks to Chris Whitewoods, the only other whose patience surpassed Rico's. Your support, kind words and friendship has helped me massively over the past few years. This project would not be what it is without you. Same for Karen Lee, whose infectious kindness and help has been the warmest of comforts in the lab.

Thanks to all members of the Coen lab who I have been lucky enough to share my time with. In particular, Des Bradley for cakes, biscuits, discussions and troubleshooting, Jordi Chan for having a good whinge with, Annabel Whibley for provide incredible support and being a buoyancy aid whilst I was thrown in at the deep end, and to Beatriz Gonçalves as a guide for best practice. Thanks to Claire Bushell, Jamie Spooner and Man Yu, who amongst others helped set up the mutagenesis, this could not have been done without you. Thank you to Lucy Copsey, Matty Couchman, Dan Richardson, Becky Horn, Sam Fox, Abbi Taylor, Yohei Koide, Tingting Li, Haoge Li and John Fozard for all the memories.

Thanks to the Smith Lab for all our discussions, to Richard Smith, Brendan Lane, Mateusz Majda, Nicola Trozzi, Clinton Durney and Marco D'Ario. Thanks to the Bioimaging team, especially Grant Calder, Eva Wegel and Sergio Lopez for light microscopy help, and to Kim Findlay and particularly Elaine Barclay for electron microscopy. Thanks to the Metabolomics team, Paul Brett and Baldeep Kumar for your time and perseverance in developing detection methods. A huge thanks to Horticultural Services, to Catherine Taylor, Lesley Phillips, Tim Wells and Damian Alger for your friendliness and approachability when needing help or wanting to do something challenging. Thanks to the lab support team, Tim Hicks, Vanessa Miles and Roy Dunford, and a big thanks to Dawn Nash for fuelling all the work I needed to do.

Thank you to all our collaborators and friends in China who made my visit unforgettable. To Minlong, Chulan, Chen, Lu, Momo and Yu in Zhejiang, thank you for your all the time you dedicated to making me feel welcome. To Ting, Huang, Feifei and of course Yong in Beijing, thank you for your kindness and hospitality.

Thanks to all the other students I have met on the way, in particular Tom Bridge and Lucía Campos-Domínguez who helped bring me down a peg or two. Thanks to the JIC Bikers – Cell Angels: Cat Gardener, Thorsten Langer, Clem Marchal, Julia Mundy and Josh Joyce for all of the evening trips we took, it was an amazing way to wind down after a long day.

Thanks to my family, for both supporting me and bringing me back down to earth. A huge thank to my Dad who instilled in me a fascination about plants. And finally, to Niamh, who together with we created our own little source of tissue tension, who has also turned into the most wonderfully formative thing we could do.

1 General Introduction

1.1 Layered organisation of tissues

Multicellular organisms have a complex three-dimensional organisation. Many plants and animals originate from a zygote, a single cell that undergoes stages of cleavage and mitosis to become multicellular (Gilbert, 2000). Cellular arrangements are found at these early stages of development, where vertebrate embryos are arranged into three germ layers: the endoderm, mesoderm, and ectoderm (Hall, 1998). In plants, cell files in the root and internal patterning of the leaf have a distinct layered arrangement that has been linked to function of the mature organ (Sinha & Hake, 1990; Petrášek & Friml, 2009). How the three-dimensional patterning of these organs arises through cellular growth is a key question in biology. Some cells may grow faster, some may grow slower depending on the intrinsic factors defining growth rate (Coen & Rebocho, 2016), but all cells are coordinated to form final organ shape, and amazingly this coordination occurs throughout the depth of the organ. One way of thinking about how organs form is by looking at how epidermal and inner tissues are patterned. In plants, organs arise from meristems which have been found to have a layered structure (Steeves & Sussex, 1989).

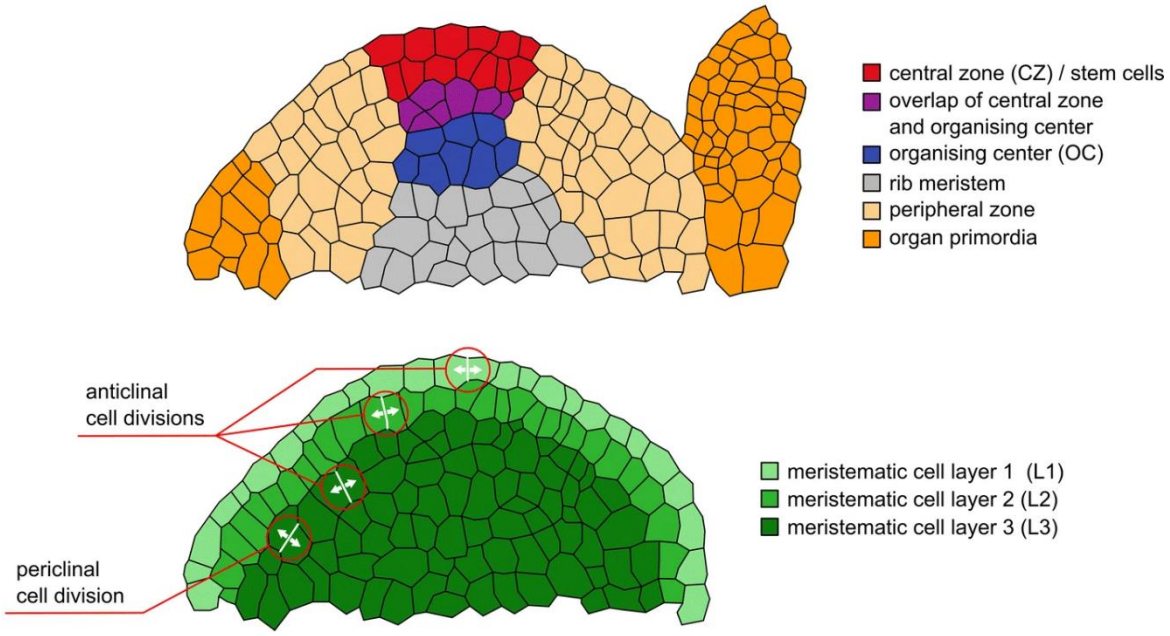

Figure 1.1 Schematic of a typical shoot apical meristem of higher plants

Taken from (Fuchs & Lohmann, 2020) Open Access

The layered organisation has been described in histological terms in mature tissues, where cells in different layers have differentiated and exhibit distinct gene expression patterns (Poethig, 1989). In this sense, the function of the cell depends on its position within the tissue. Recent studies into the role of tissue layers during growth have used layer-specific gene expression or layer-specific promotors to determine the role of tissue layers during growth (Sessions *et al.*, 1999). To determine the origins of the mature tissue layers, we have to look at where they arise.

The shoot apical meristem (SAM) of higher plants consists of a region pluripotent stem cells from which all vegetative parts arise (Steeves & Sussex, 1989; Barton, 1998; Lenhard & Laux, 1999; Traas & Vernoux, 2002). The SAM can be subdivided into regions of activity, a central zone where stem cells are produced and maintained through anticlinal divisions, a peripheral zone where lateral organs such as leaves are initiated and a rib zone where stem or stolon tissue is formed (figure 1.1). These zones are fixed in the developing meristem where growing and dividing cells transition from one region to

another. The SAM can also be subdivided by layers (von Hanstein, 1868; Satina *et al.*, 1940). Cells in each layer of the SAM undergo rounds of division to form clonally distinct layers. The L1 is a single layer of cells that forms the epidermis (Thoma *et al.*, 1994; Lu *et al.*, 1996). Cells in the L2 and L3 layers give rise to internal tissue (Jackson *et al.*, 1994; Kelly & Meeks-Wagner, 1995; Bradley *et al.*, 1996). Understanding how these layers interact is a fundamental problem in plant development.

1.2 How do layers interact to control organ growth

Historically, the plant has been thought to be an expanding core, enveloped and resisted by a more rigid epidermis (Hales, 1727; Hofmeister, 1859). These ideas developed into the hypothesis that the epidermal layer is in control of growth (Peters *et al.*, 1992; Rayle & Cleland, 1992; Brown *et al.*, 1995). More recently, studies using dwarf mutants in the plant growth hormone brassinosteroid showed that the mutant could be rescued by expressing the gene just in the epidermis using an epidermal-specific promotor (Savaldi-Goldstein *et al.*, 2007). The study comprehensively analysed brassinosteroid biosynthesis and signalling genes in both the epidermis and inner tissues, but phenotype rescue was only achieved by expressing the respective gene in the epidermis. Thus, brassinosteroid production in the epidermis led to non-autonomous growth promotion of internal tissue. This work supported the hypothesis that the epidermis controls growth in the plant and proposed non-autonomy of brassinosteroid action operated either through a biochemical signal or mechanical stimulus originating from the epidermis to growth of the inner tissues. This paper seems to have been somewhat contradicted by Graeff *et al.* (2020) who restored brassinosteroid perception to the phloem of a dwarf brassinosteroid signalling mutant to rescue the phenotype. This study only looked at brassinosteroid reception, not action.

Biochemical signals between layers may be hormones or molecules that travel either apoplastically (outside of the plasma membrane, typically through the cell wall) or symplastically (inside of the

plasma membrane, typically through the cytoplasm). One example is the movement of auxin in the root, where movement is basipetal (towards the root tip) in the inner layers, but acropetal (away from the root tip) in outer layers (Leyser, 1999). Another example in *Antirrhinum* showed that expression of *floricaula,* a meristem identity gene, in one cell layer promotes transcription of genes in all cell layers (Hantke *et al.*, 1995). A mechanical stimuli could involve mechanical changes in one layer being signalled to another. One potential mechanosensing mechanism could be through cellular ion channels, where stretching of a membrane causes opening or closing of ions channels, resulting in a signalling cascade (Hamant & Haswell, 2017). Mechanosensing in plants has been proposed to explain the touch-induced electrical signals in venus flytrap (Volkov *et al.*, 2007). In these systems, a mechanical stimulus in the epidermis leads to response at the whole organ scale.

In addition to biochemical signalling and mechansosensing, a third potential mechanism for layer interaction is via mechanics, such as tissue tension. The term tissue tension dates back to the 19th century, with the work of pioneering plant physiologists such as Sachs (1865), Hofmeister (1859) and Kraus (1867). This work was based on the idea that the continuous coat of the epidermis that envelops the plant body experiences mechanical stresses due to the higher rates of growth of the inner tissues. Support for this idea came from taking successive longitudinal strips of an internode, where the more lateral strips contained more epidermal tissue and the more medial strips contained more inner tissues. The strips were examined by comparing the length of the strips to the original length of the internode. It was found that the inner tissues expanded while the epidermal tissues contracted. The explanation for this was that the inner tissues expanded as they were released from compression and the epidermis contracted as it was released from tension. Therefore, the term 'tissue tension' can be misleading as it refers to both tissue tension (in this case in the epidermis) and compression (in this case in the internal tissues). The terminology is more accurately described in German in the original texts where 'tension' (*Spannung*) is used a generic term to describe both the tensile and compressive forces (*Zugspannung* and *Druckspannung* respectively). The term *Gewebespannung* coined by Sachs (1875) accurately describes the mutual tissue forces, whereas this meaning is unfortunately lost when

translated into English ‘tissue tension’. I will be referring to the mutual tissue forces as tissue tension-compression in this thesis.

As tissue tension-compression is the state of balanced forces acting on a tissue, it is typically invisible until an intervention, such as cutting or ablation is performed to visualise is effects. These experiments could interfere with a particular signalling pathway and it has therefore been suggested that they may not provide unequivocal evidence for mechanical interactions (Peters & Tomos, 1996). However the speed of signalling would need to be very fast as bending is observable immediately after cutting (Kutschera & Niklas, 2007). In most plants, visualisation of such a mechanical layer interaction has been challenging as the cells are packed tightly together. Looking at genetic mutants with reduced intercellular adhesion has provided one way of visualising the effects of tissue tension in the epidermis through formation of cracks (Verger *et al.*, 2018).

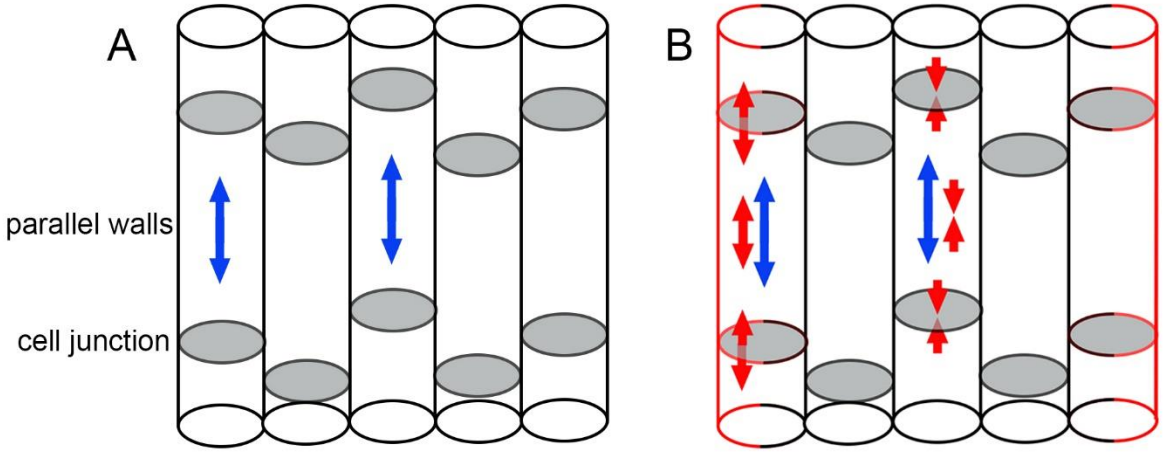

Figure 1.2 The mechanics of tissue tension-compression

A section through a plant stem is represented as cylinders. Blue arrows represent internal cell tension due to turgor, red arrows represent tissue tension or compression A) Internal turgor causes tension on the anticlinal cell wall junctions. B) If outer cell walls have different mechanical property (i.e. are thicker) than the inner walls, then the outermost cells will be under tissue tension and the inner cells under tissue compression.

Tissue tension-compression can be explained as follows. Consider an array of plant cells across the diameter of a stem as idealised pressurised cylinders (figure 1.2A) which have the same properties – same turgor, same wall composition and same wall thickness. Turgor will cause longitudinal tension in the parallel longitudinal walls (shown for two cells with blue arrows, figure 1.2A). Suppose this homogenous array is changed such that the inner cells have a higher specified growth rate than the outer cells (e.g, and the outer cell walls are more resistant to longitudinal stretching (red in figure 1.2B)). The lower specified growth rate in the outer layer will constrain growth of the inner tissues through tissue connectivity, so that the inner walls experience a compressive tissue force (convergent red arrows), and the outer walls experience a tensile tissue force (divergent red arrows). This results in the epidermis growing faster than its specified growth rate (due to the tensile tissue force), and the internal tissue growing slower than its specified growth rate (due to the compressive tissue force). Thus, there is an equalisation of resultant growth rates and coordination between tissue layers.

The overall result on cell walls (sum of blue and red arrows) is that the outer walls have additional tension to turgor tension, while the inner walls experience reduced tension. The tissue stresses also put the epidermal cell junctions under tension (cells are being pulled apart) while the inner cell junctions are under compression (cells are being pushed together). Therefore, a differential in axial specified growth rates between layers leads to tissue tension-compression. To understand the cellular basis of tissue tension-compression in a growing tissue, we need to know the mechanics of cell growth.

1.3 Cellular composition of tissues

Plant tissues are made of immobile cells, characterised by a thick cell wall. It is these walls which are the load-bearing structures of the cell which resist turgor. All living plant cells are under internal turgor from the vacuole. Cell walls may yield irreversibly to this turgor which allows for growth. Plant cell walls grow through a process known as creep, which is the irreversible extension in which the

materials in the wall matrix slowly slide past each other, increasing the surface area of the wall (Cosgrove, 2005). Cell wall-loosening compounds act to relax the wall and allow for water influx into the cell and subsequent expansion. Wall stress relaxation results from the action of wall-loosening enzymes, such as expansins (McQueen-Mason *et al.*, 1992), which rearrange the load-bearing polymers in the wall which reduces turgor pressure and creates a gradient for further water uptake (Lockhart, 1965; Ray *et al.*, 1972; Hamant & Traas, 2010). The rate of wall stress relaxation can be controlled by the cell to determine its extensibility, or its non-elastic deformation of growth (Cosgrove, 1993). Therefore, in the cell, stress-relaxation in the wall allows for turgor pressure to drive cell growth.

The cell wall material is comprised of a range of polymers. These include cellulose (Arioli *et al.*, 1998), hemi-cellulose (Scheller & Ulvskov, 2010), pectin (Atmodjo *et al.*, 2013) and lignin (Vanholme *et al.*, 2019). These products are synthesised inside the cell and deposited in the wall. Cellulose is arranged as long, stiff microfibrils which wrap around the cell. The orientation of how the cell is wrapped by spatially overlapping layers allows for anisotropic expansion of the cell (Somerville, 2006). As cells expand, cellulose is deposited into the sidewalls which undergo diffuse growth (Lloyd, 2007). Cellulose synthesising complexes (CSCs), which are embedded in the plasma membrane, extrude the cellulose microfibril onto the cell wall and are guided by cortical microtubules (Purushotham *et al.*, 2016). Therefore, the microtubule array determines the direction of cell expansion. In a random array, all faces of the cell are equally strengthened so the cell grows isotropically. In a transverse microtubule array, walls of the cell are strengthened to resist transverse but not longitudinal expansion, leading to cell expansion perpendicular to the microtubule array (Lloyd & Chan, 2008).

The processes of cell wall thinning through wall-stress relaxation and cell wall thickening through synthesis must work in harmony to maintain cell wall thickness during growth (Derbyshire *et al.*, 2007). If expansion occurred without synthesis, walls would thin until they could not withstand the turgor pressure and rupture. If synthesis fed new wall material into the wall without expansion, walls would

thicken, and the cell would resist changes in internal pressure and not grow. This happens in secondary thickening of mature cells (Zhong & Ye, 2015). As cell walls are the load-bearing structures of the plant, the thickness of the wall will determine the load or stress that the cell can support. Outer epidermal walls are typically thicker than inner cell walls, reducing wall stress for the same load (Kutschera, 2008).

As illustrated in figure 1.2, tissue tension-compression is a result of differential specified growth between tissue layers. The stiffer the outer wall, the less it will yield to turgor and greater tension will be transferred to it from the inner tissues. Key to tissue tension-compression is cellular connectivity which allows transmission of forces between layers. Therefore, in the work mentioned above of Savaldi-Goldstein *et al.* (2007), whilst it is reasonable to assume that the epidermis controls growth through transmission of a signal, it is also plausible that the epidermis could act a 'signal-less' manner, by reducing tissue compression on the inner tissues to promote turgor-driven creep of the cell walls of internal cells.

1.4 Genetic approach to analyse growth

One way to elucidate the how tissue layers is to look at mutants. If a 'signal-less' form of mechanical tissue layer interaction is under genetic control, then a mutant might reveal a change in tissue tension-compression. To date, no one has identified a gene that modulates tissue tension-compression. If growth is reduced in the epidermis alone, then tissue tension-compression would be increased, and the plant might be smaller overall. Alternatively, a mutant where growth is reduced in the inner tissues alone would have reduced tissue tension-compression, again causing overall reduction in plant height. Mutants such as these may have already been obtained in plants such as *Arabidopsis* but changes in tissue tension-compression not identified because tight cellular packing prevented their effects from

being visible. By contrast, a system such as *U. gibba* which has large intercellular spaces may allow the effects of tissue tension-compression to be readily seen.

In this thesis I present the isolation of a dwarf mutant from a forward screen in *U. gibba*. I show how I mapped the associated gene and explored the development of the mutant and timing of gene activity in wild type. I take what I learnt in *U. gibba* to investigate *Arabidopsis*, finding unifying links, and defining how genes influence tissue layer interactions by modifying tissue tension-compression.

2 Analysis of a mutant affecting *U. gibba* trap, stolon and leaf morphology

2.1 Introduction

To identify a mutant with altered tissue layer interaction, *U. gibba* is a tractable system as the tissue layer arrangement is different to *Arabidopsis,* such that internal air spaces form in the leaves and stolon. A mutation that affects tissue layer interaction may affect all parts of the plant (Wang *et al.*, 2001), one organ specifically (Kempin *et al.*, 1993) or have a greater affect in some areas more than others. It may even be a mutation that exclusively affects one tissue layer (Marks & Feldmann, 1989). Or it may be a mutation that affects cells in different ways, for example, it may have a greater effect on larger or more anisotropic cells (Zhao *et al.*, 2020). To understand how a mutation may affect the tissue patterning of *U. gibba*, we need to know the morphology of the plant.

2.1.1 Introducing *U. gibba*

The genus *Utricularia,* commonly known as bladderworts, belong to the family Lentibulariaceae and the order Lamiales. There are up 200 species of *Utricularia* worldwide, making it the most species-rich genus of carnivorous plant on the planet (Lloyd, 1942). Bladderworts can have either a terrestrial or aquatic habit and obtain nutrients through prey capture in leaf traps (Vincent *et al.*, 2011).

Utricularia gibba L., known as the humped bladderwort, is an aquatic species of *Utricularia* that is found on all continents except Antarctica. It forms a mat-like structure through overlapping stolon

growth. Growth is initiated in the circinate apex, a tissue that has a number of overlapping leaves surrounding the meristem (figure 2.1i). Vegetative tissues comprising of the determinate dichotomously branching leaves (figure 2.1iv), internodes (figure 2.1iii) and traps (figure 2.1v) subsequently grow and mature. Axial side shoots often form (figure 2.1ii) which give the plant an indeterminate structure and assist in the mat-like growth habit.

The traps on *U. gibba* are a form of highly modified cup-shaped (epiascidiate) leaves. Epiascidiate leaves have evolved four times independently: in the families Nepenthaceae, Sarraceniaceae, Cephalotaceae, and Lentibulariaceae (Lloyd, 1942; Ellison & Gotelli, 2009) In all these cases, the epiascidiate form is associated with carnivory – animals are trapped within the cup-shaped vessel and digested to release nutrients for the plant to uptake. The trap in *U. gibba* can be viewed in three planes (figure 2.2a), sagittal, frontal and transverse and consists of a curved sheet, two cell layers thick, with a lid that functions as a trap door (figure 2.2B). Therefore, instead of being a volumetric organ, it can be thought of as a continuous layer where the epidermis provides both the inner and outer cell layers. The trapping mechanism works via suction and has two phases: in the first phase, glands actively pump water out of the trap lumen, leading to a lower internal hydrostatic pressure. At this point the bladder has concave walls and the trap door (with its trigger hairs) is closed to keep the entrance watertight. When prey, typically *Daphnia* spp., brushes past the trigger hairs, the lid is triggered to open, leading to the second phase: the bladder wall rapidly relaxes leading to water and prey being sucked in, followed by the closing of the trap door and the digestion of prey with the aid of digestive enzymes secreted by internal glands (Vincent *et al.*, 2011; Poppinga *et al.*, 2015).

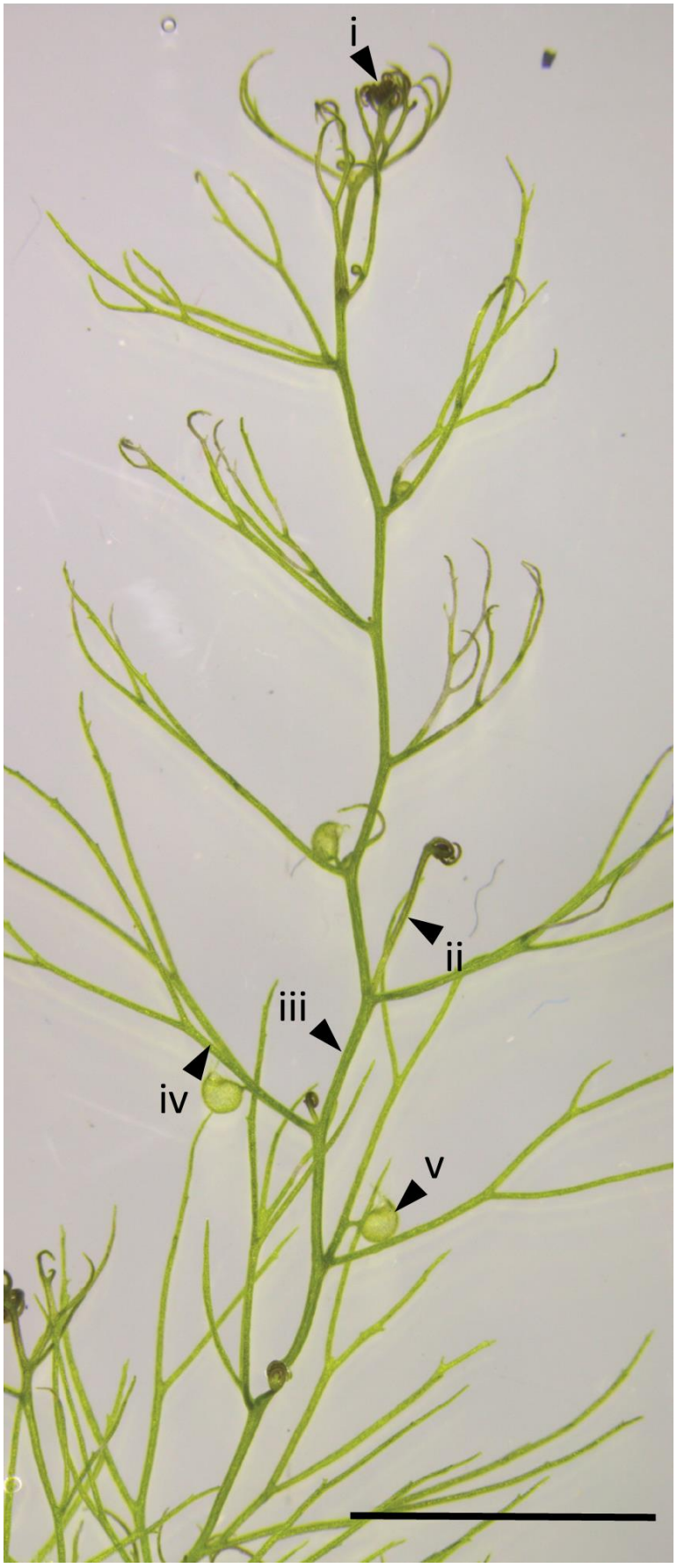

Figure 2.1 *U. gibba* growth habit

Body plan of *U. gibba*, i) circinate apex, ii) axial side shoot, iii) internode, iv) leaf and v) trap

Scale bar is 5cm

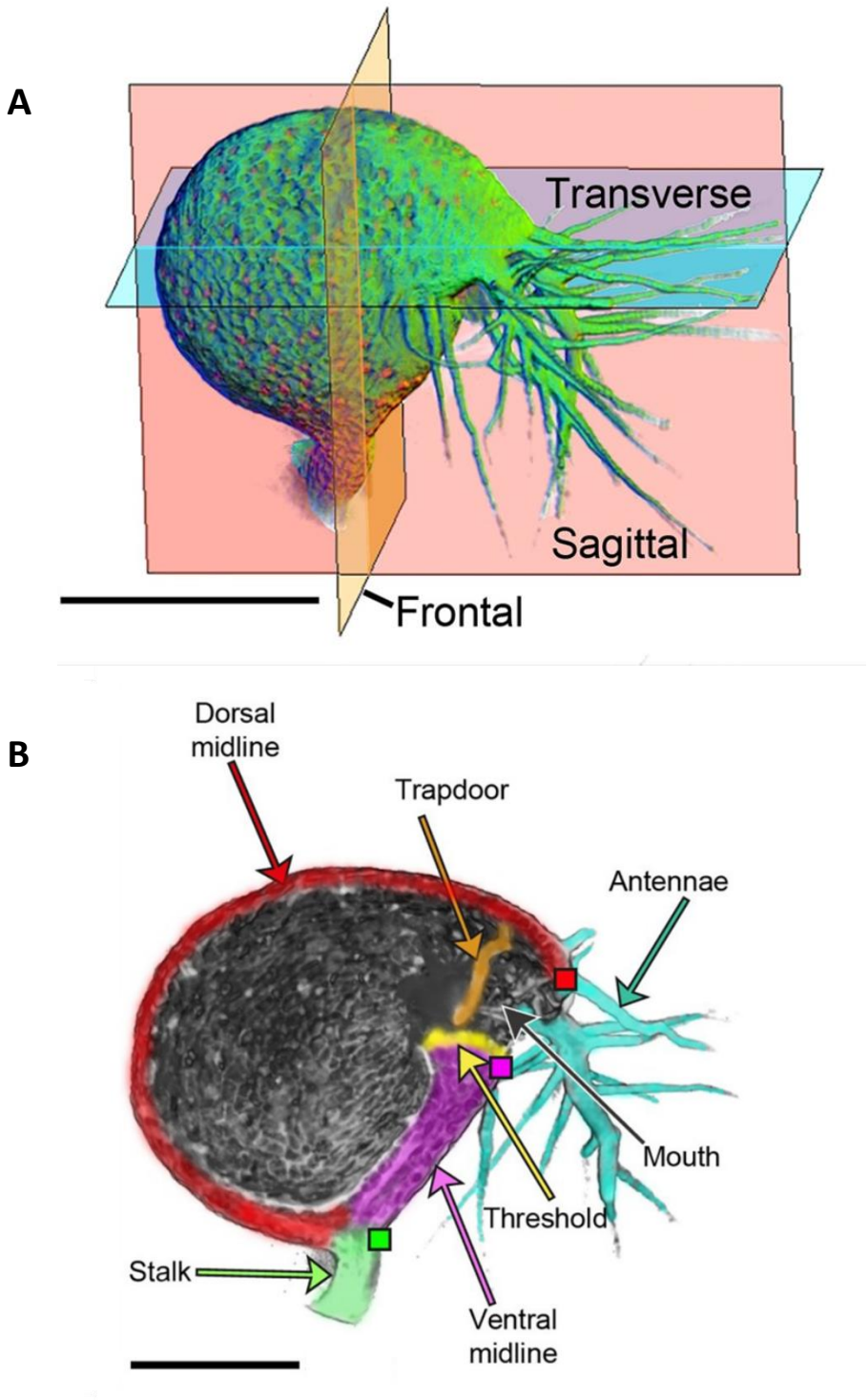

Figure 2.2 Mature *U. gibba* trap orientations

A) Volume view of mature U. gibba trap with three differential planes of orientation. Scale bar is 500 µm.
B) Volume view of mature U. gibba clipped in the sagittal plane. Coloured squares indicate landmarks: dorsal lip (red), ventral lip (magenta), and stalk indentation (green). Scale bar is 350 µm.

Taken from (Lee *et al.*, 2019) Open access

The internal tissues of *U. gibba* leaves and stolons have internally patterned air spaces (figure 2.3B, yellow) to assist with the plants' floating habit. The cylindrical tissues are comprised of an epidermal layer (figure 2.3Ai & Ci). The sub-epidermal cells are arranged in a sheet-like structure along the stolon, forming a connective tissue between epidermis and inner tissues (figure 2.3Aii & Cii). The inner tissues are comprised of vasculature companion cells (figure 2.3Aiii & Ciii) and the vasculature bundle (figure 2.3Aiv & Civ) form in a straight line through the tissue. In terms of meristem identity, it is unclear where each layer originates from (Theresa & Jennifer, 2012; Reut & Płachno, 2020). It could be that the epidermal layer is the L1, the subepidermal connective tissue is the L2 and the vasculature companion cells and bundle are the L3. For the purpose of this work, I will refer to the epidermis as the outermost cell layer, and the inner tissue as all other cell layers held within. In between these cellular regions are internally patterned air spaces. These spaces do not form due to targeted cell death, but through growth (Whitewoods, 2021). These negative spaces between tissue layers will be exploited to visualise changes in tissue layer interactions.

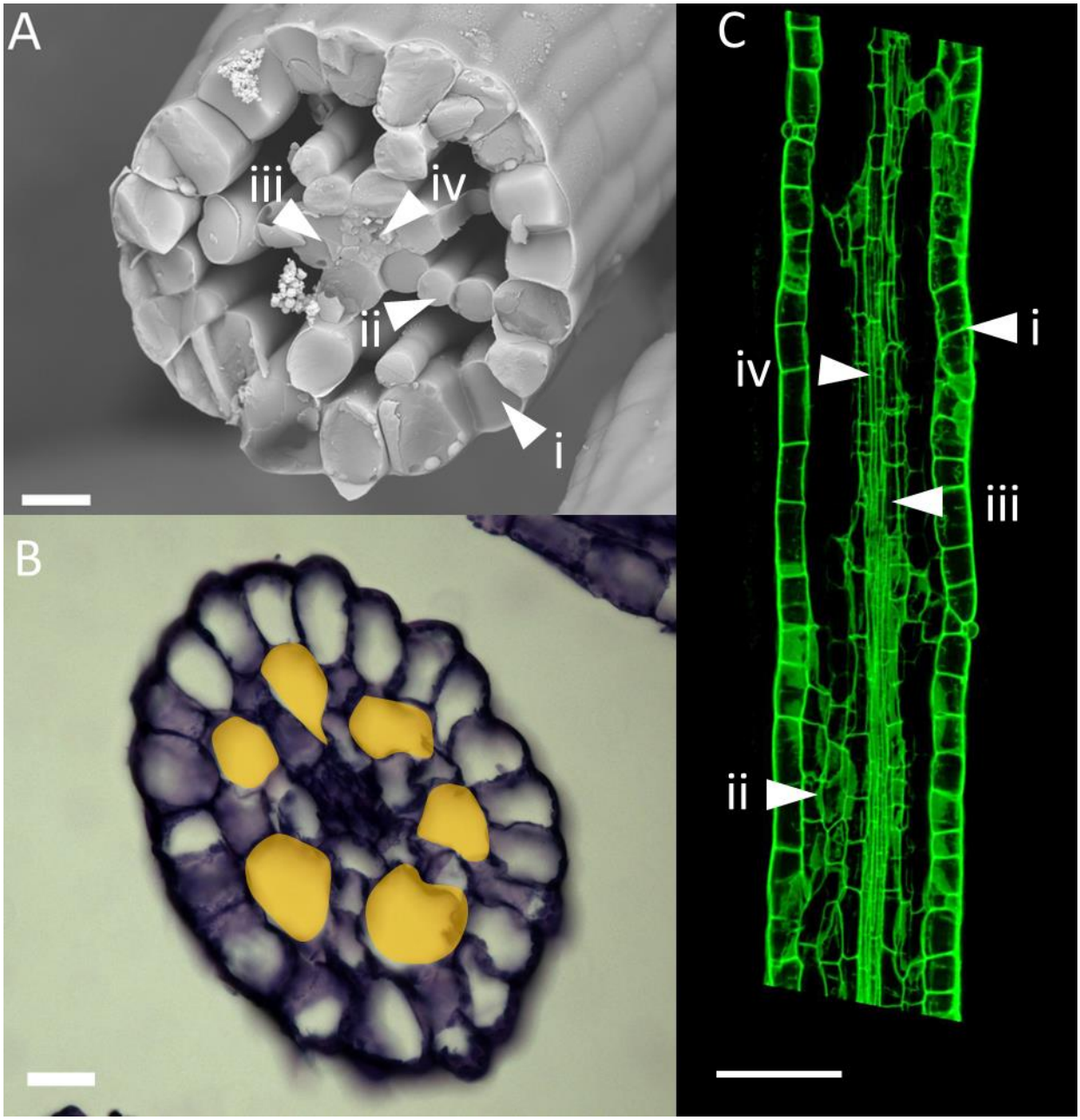

Figure 2.3 Tissue layer and air space arrangement of U. gibba

A) Freeze fracture SEM showing i) epidermal layer is a continuous cylindrical layer of cells, ii) sub-epidermal cells comprising of connective tissue between epidermis and inner tissues, iii) vasculature companion cells surrounding the iv) vasculature bundle. Image taken from (Whitewoods, 2021) Open access

B) Toluidine blue stain wax slice showing same cellular arrangement as in A. Air spaces are highlighted in yellow. Image taken by Chris Whitewoods

C) Z-slice from a confocal scan of internode section in longitudinal view showing i) epidermis is comprised of a single cell layer ii) subepidermal connective tissue, iii) vasculature companion cells and iv) vasculature bundle. Scale bar is 20 µm in A and B, 100 µm in C.

2.1.2 EMS screen in *U. gibba*

A forward genetic screen is a powerful tool to generate novel phenotypes and identify their genetic basis (Schneeberger, 2014). By creating random mutations across the genome, mutant offspring can be screened for phenotypes of interest without the bias of knowing which gene is mutated (Blumenstiel *et al.*, 2009). Of the chemical agents available, ethyl methanesulfonate (EMS) is commonly used (Kim, Schumaker*, et al.*, 2006). *U. gibba* is diploid (2n = 28), flowers and self-fertilises readily in glasshouse and CER conditions and has had it small (~100 Mbp) genome sequenced and annotated (Ibarra-Laclette *et al.*, 2013; Lan *et al.*, 2017). Identifying genes related to a phenotype of interest in *U. gibba* could uncover novel genes or attribute novel functions to known genes. As this is the first time a mutant screen was performed in a carnivorous plant, we were interested in any phenotypes that arose, especially in the traps. At the time of setting up the mutagenesis, how these traps developed was unclear. Therefore, there was an initial interest in screening for trap phenotypes to identify genes associated with them.

Aims of this chapter:

- To recover a growth mutant from EMS mutagenesis
- To generate a segregating mutant family to provide a population of individuals for mapping by WGS
- To analyse differences between tissue layers to undercover cellular evidence for tissue tension-compression

2.2 Results

2.2.1 Generating mutants in a carnivorous plant for the first time

To generate mutants in *U. gibba*, sections of stolon and seeds from a single progenitor (U59) were mutagenised with ethyl methanesulfonate (EMS) (figure 2.4). To our knowledge, this is the first time a mutagenesis has been performed on a carnivorous plant. For ease of identifying novel mutations, we had a reference genome sequenced from the progenitor using Chromium 10x technology at TGAC (now the Earlham Institute, UK). 11 mutagenising treatments were performed at EMS concentrations ranging from 0.01 % to 0.25 % on both tissue and seed. I will focus on tissue mutagenesis here as it provided the most viable material. For tissue EMS, a mutation that is induced in one chromosome may be passed on to daughter cells after cell division. Therefore, a mutation in a meristematic cell will result in a chimeric tissue. Some of these cells will later contribute to the L2 layer of floral meristems (Jankowicz-Cieslak & Till, 2016) and gametes passed onto the next generation. As each individual piece of tissue received a random set of mutations, the resulting chimeric plants were considered to be the M1 generation (M1, figure 2.4). 2000 EMS-treated explants were grown to maturity, of which 441 flowered and gave viable seed. Progeny (M2) were screened for individuals with morphological phenotypes. Where possible, M3 generations were grown from mutants and their siblings for whole-genome sequencing and to establish segregation ratios.

Segregating M2 mutant families comprising of 30 different phenotypes were recovered. The phenotypes included altered traps, absent traps, reduced leaf and stolon growth, long flower spurs, spiky leaves, multiple traps on leaves, and fasciation. One M2 family (D90-2) segregated for individuals with small oval-shaped traps, short internodes and leaves, which we named a dwarf phenotype. This dwarf mutant family arose from an explant treated with 0.15 % EMS on 27/1/14 (table 2.1). Wild-type siblings of the dwarf mutants readily flowered and produced seed of segregating mutant offspring (progeny of D90-2, M3), showing that the mutagenesis successfully produced a heritable mutation.

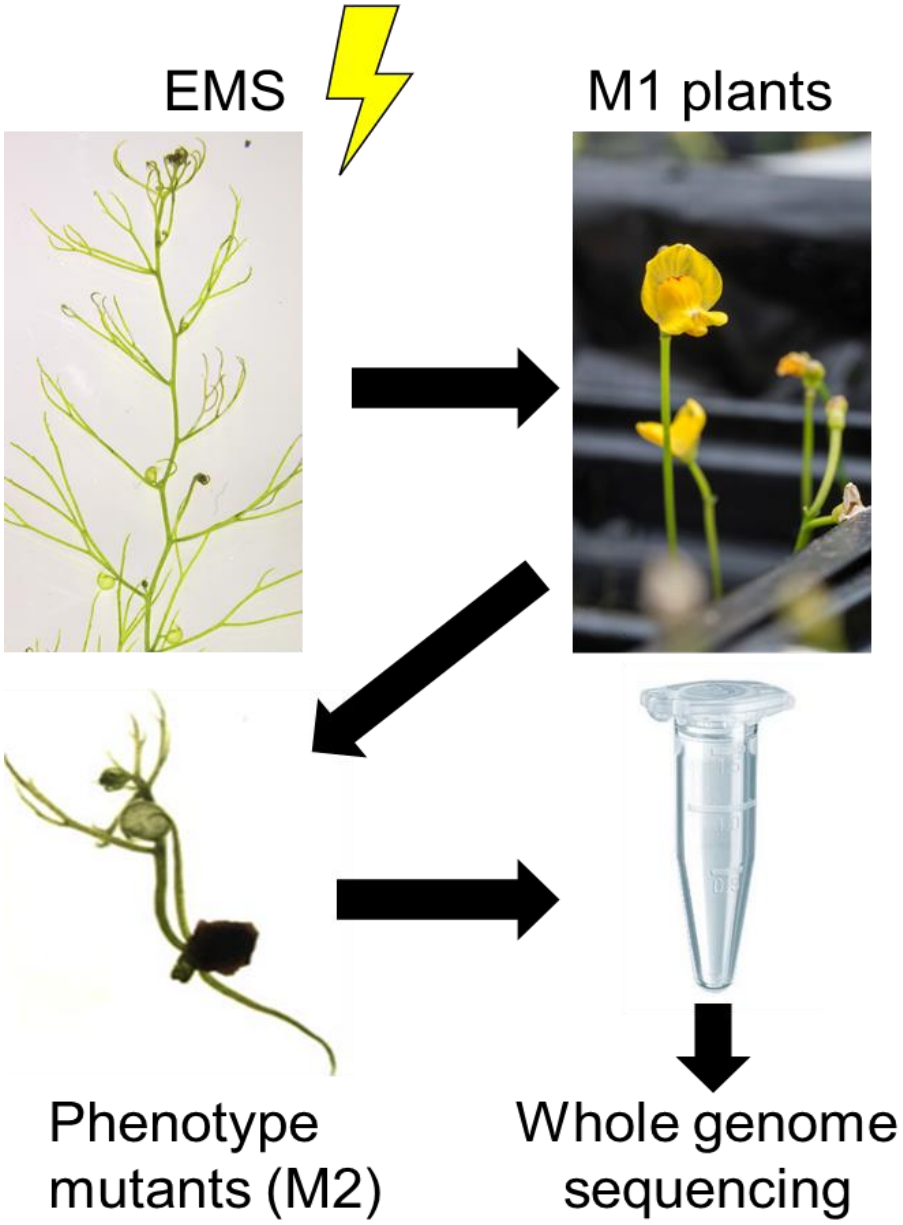

Figure 2.4 Generating mutants through mutagenizing tissue with EMS

2000 stolons were isolated from a single progenitor, treated with EMS and grown on to flower (M1), the progeny of which (M2) were screened for phenotypes of interest. M2 mutant siblings were used to create larger segregating M3 populations so that individuals could be sent for whole genome sequencing.

Table 2.1 Pedigree of dwarf mutant

Individual tissue explants were given a unique name prior to EMS treatment, as were subsequently M1 chimeras and their offspring, so that a mutant of interest could be traced back to a single seed pod. Highlighted are the M2 and M3 lines that produced the dwarf mutant of interest and other mutant lines are examples that are not related.

OS46	24/4/12 Obtained *U. gibba* 'Bergh Apton (BA) ' plant from Pauline Steward, The Fly Trap Plants. http://tftplants.co.uk/ Plants had been grown in the same aquarium tank for about 20 years. This was named OS46 (see 'Accessions' Excel file)	
U59	U59 is the sowing number of seed pod number 7 from OS46 box 3. Seed was sown 27/6/12	M1
U59-12-H	U59-12-H is tissue from seed pot number 12 division H	M1
C3	**EMS 6 tissue treatment 27/1/14 0.15% EMS** C3 is U59-12-H tissue treated with EMS and divided into 333 boxes containing 6 compartments e.g. Seed harvested C3-20-1-a was from mutagenesis C3, box 20, compartment 1, seed envelope 'a'	M1
D114	D114 sown 14/1/14 was ex C3-99-2-a	M2
D208	D208 was ex C3-6-5-a	M2
D90	D90 sown 14/1/14 was ex C3-89-1-a	M2
D685	Ex D114-8	M3
D682	Ex D208-1	M3
D675	Ex D90-2	M3

I grew an M3 family of 49 plants from wild-type plant of D90-2 (G1), which gave 37 wild types and 12 dwarf mutants. This segregation is consistent with a single gene recessive mutation in this family (x^2 = 0.007, dF = 1, *p* = 0.672). The dwarf mutants fell into two classes, one class had small oval traps and extremely short internodes and leaves, and the other had small oval traps with internode and leaf lengths intermediate between the extreme and wild type (figure 2.5). No other phenotypes segregated in the population. These results suggested the family was segregating for two mutations: recessive *dwarf1*, which causes a dwarfing phenotype, and a modifier of *dwarf1*. If the modifier was a recessive enhancer, *dwarf1* would cause the intermediate phenotype, and modifier homozygotes would cause the extreme phenotype when present with *dwarf1*. In this situation, only 1 in 4 mutants would have the extreme phenotype. If the modifier was a recessive suppressor, *dwarf1* would cause the extreme phenotype, and modifier homozygotes or heterozygotes would cause the intermediate phenotype when present with *dwarf1*. In this situation, only 1 in 4 mutants would have the intermediate phenotype. Of the 12 mutant plants in this M3 family, 9 had the intermediate phenotype and 3 had the extreme phenotype. This suggests that the modifier is a recessive enhancer and will be referred to as *enhancer of dwarf1* (*eod*). This segregation is consistent with two gene recessive mutations in this family (x^2 = 0.007, dF = 2, *p* = 0.914). The segregation of phenotypes in this M3 family suggests that *eod d*oes not have a phenotypic effect on its own. Whilst it is challenging to distinguish what the role of the potential modifier is, it provides a working hypothesis to apply when searching for candidate SNPs.

Figure 2.5 Dwarf mutant phenotypes

Phenotypes of progeny from D90-2, A) wild type, B) *dw1 EOD* and C) *dw1 eod*.

Scale bar is 10 mm.

2.2.2 Mutant traps are smaller and with a different shape than wild type

To characterise mutant trap size, I took light microscope images of mature traps in the sagittal plane. Measuring size of an irregular 3D shape is challenging, but previous work had used trap length to stage the development of wild type traps as it was found to be a good proxy for overall trap size. Trap length is measured from the centre of the upper mouth region to the point on the dorsal midline furthest from the mouth. Using this method, I could find an initial comparison between wild type and mutant traps (figure 2.6A). Trap length of both *dw1 EOD* ($\bar{x}$ = 0.821 mm, *SEM* = 0.201) and the *dw1 eod* ($\bar{x}$ = 0.749 mm, *SEM* = 0.286) is around 70 % of the size of wild type ($\bar{x}$ = 1.076 mm, *SEM* = 0.012) (figure 2.6B). Whilst there is a difference in average trap length between *dw1 EOD* and *dw1 eod*, the difference is not statistically significant ($p < 0.05$). Therefore, traps of both mutants are smaller than wild type.

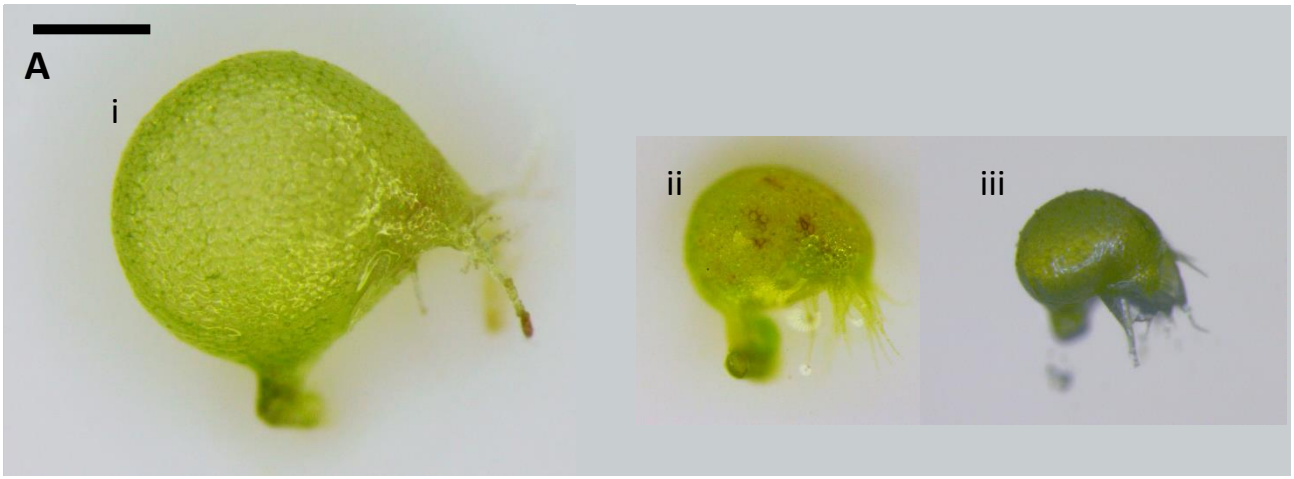

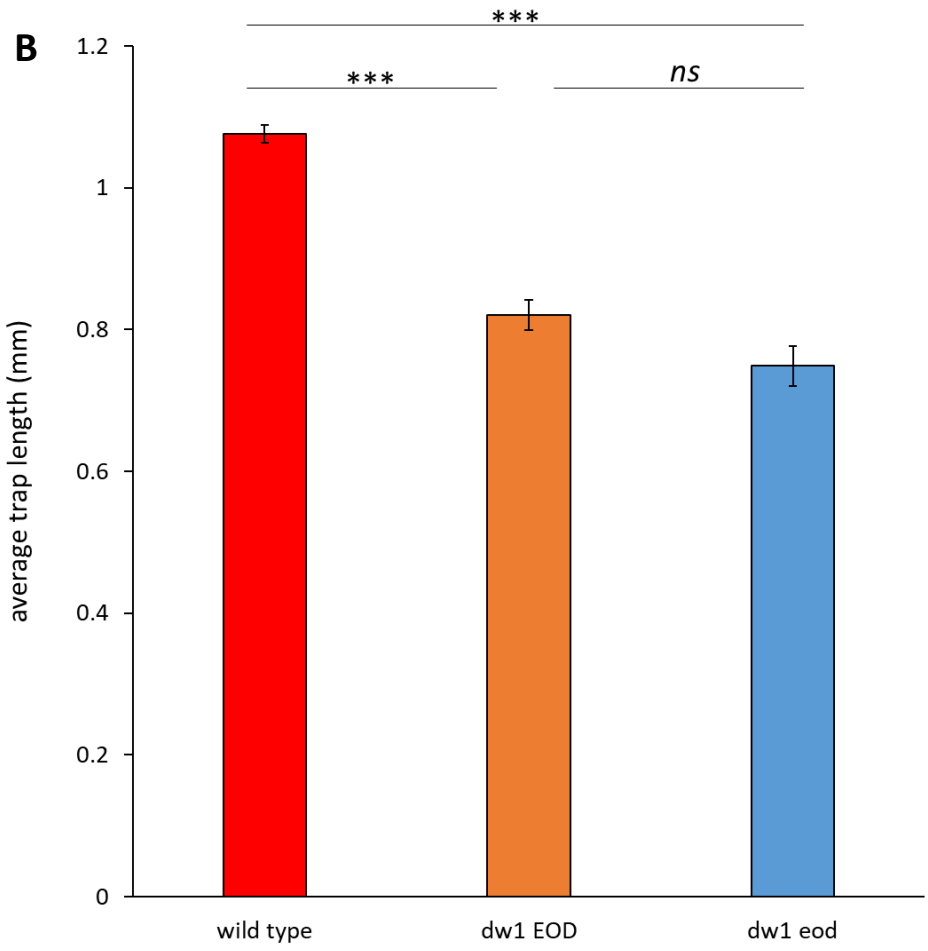

Figure 2.6 Mutant traps are smaller than wild type

A) Light microscope images of individually dissected matures traps from i) wild type, ii) *dw1 EOD* and iii) *dw1 eod*. Scale bar is 50 µm for all traps.

B) Both *dw1 EOD* and *dw1 eod* mutant traps are significantly smaller than wild type. Trap length is measured from the mouth to the furthest most point on the dorsal midline. Error bars show SEM. Wild type n = 6, *dw1 EOD* n = 12, *dw1 eod* n = 7. *t* tests: wild type to *dw1 EOD p* = 1.54534E-08 (***), wild type to *dw1 eod p* = 5.5853E-06 (***) and *dw1 EOD* to *dw1 eod p* = 0.06549472 (*ns*)

To further characterise the mutant traps Optical Projection Tomography (OPT) was performed in collaboration with Karen Lee. These observations are subjective and unquantified. Comparing the mutant traps to wild type in the sagittal plane (figure 2.7Ai and Bi) possibly shows a shorter ventral midline, altered angle of mouth regions, more oval shape and smaller antae. In the frontal plane (figure 2.7Aii and Bii), *dw1 EOD* trap appears rounder with more compact antae. In the transverse plane (figure 2.7Aiii and Biii), the trap appears rounder in the dorsal region, but narrows towards a smaller mouth.

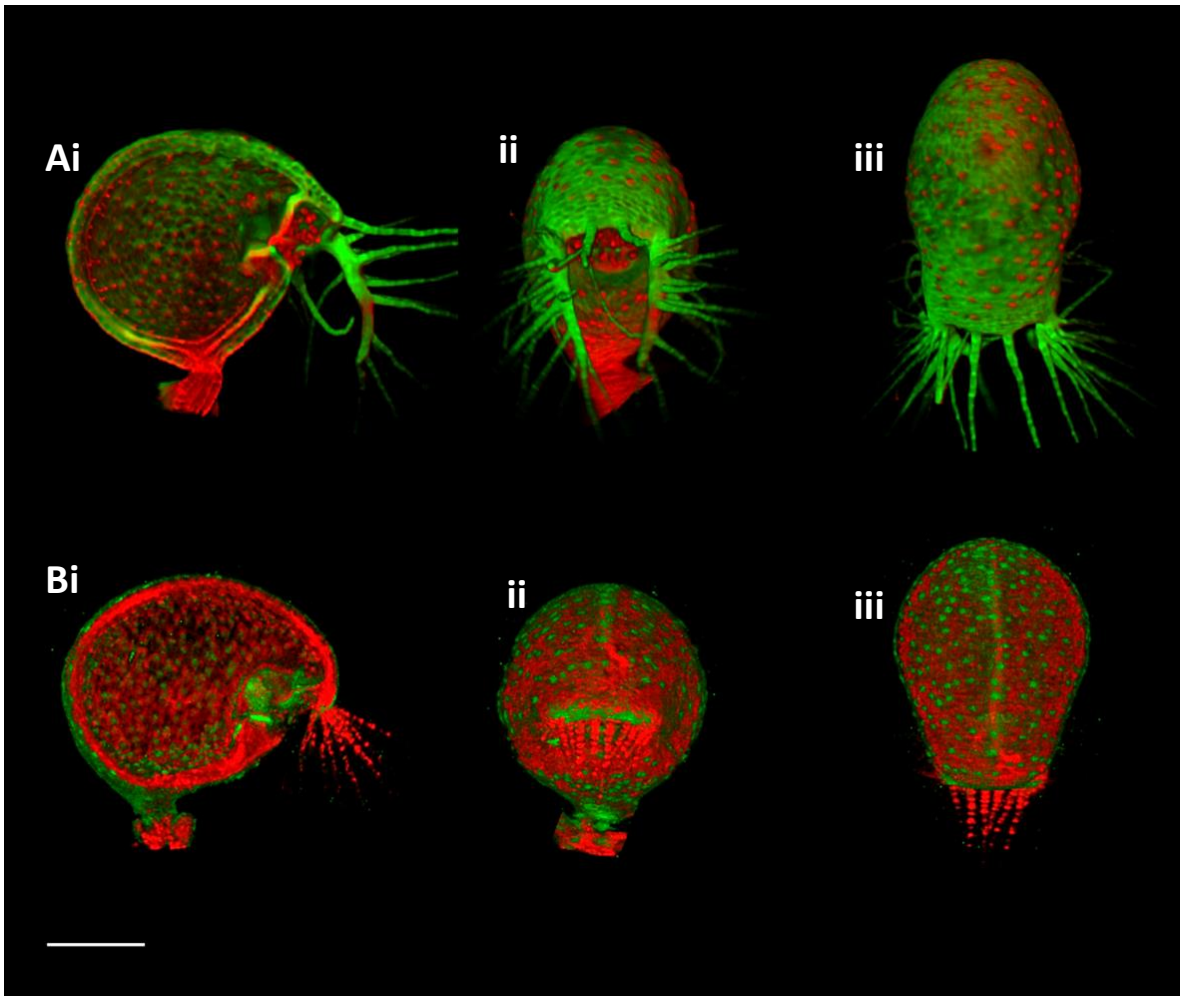

Figure 2.7 3D scanning using Optical Projection Tomography reveals a subtle shape differen*ce* in *dw1 EOD*

OPT scans of mature wild type traps in the Ai) sagittal plane clipped to the midline of the trap ii) frontal plane and iii) transverse plane. Mature *dw1 EOD* traps in the Bi) sagittal plane clipped to the midline of the trap ii) frontal plane and iii) transverse plane.

Scale bar is 300 µm

To capture some of the differences in trap shape between wild type and *dw1 EOD*, I made outline drawings of traps in the sagittal plane (figure 2.8Ai and ii). These outlines suggest that the *dw1 EOD* trap is rounder and more oval in shape, with the landmark points in slightly different places (red and green squares). It also seems that the ventral midline (magenta line) is shorter and thicker, and the stalk is wider in *dw1 EOD*. I then artificially enlarged *dw1 EOD* trap, so it was the same size as wild type (figure 2.8Bi and ii). Again, subtle differences in shape were observed, indicating that the *dw1 EOD* trap was not a fully developed wild type trap that is reduced in size. Overlaying these two images (figure 2.8Biii) showed that the landmark points did not line up with each other. To determine if the *dw1 EOD* trap phenotype is due to an early arrest in development, I identified the wild type trap earlier in development that was the same length (~800 μm) as the mature *dw1 EOD* trap (figure 2.8Ci and ii) (Lee *et al.*, 2019). The immature wild-type trap has a reduced ventral midline and/or the dorsal midline has grown as such that it seems to overlap the dorsal lip (figure 2.8 Ci, red and magenta squares). In fact, the mouth has not opened, and no antennae have formed in the immature wild type. Overlaying these two images also shows that the landmark points do not line up. These differences in trap shape indicate that the *dw1 EOD* trap shape is not due to an early arrest in growth but is fully matured with a subtle change in sculpting of its shape.

To identify if the ventral midline is indeed shorter in *dw1 EOD* as observed in figure 2.8Aii, I took measurements of both the dorsal and ventral midline in the sagittal plane to obtain circumference lengths. Both *dw1 EOD* and *dw1 eod* mutants had trap length and circumference about 70 % of that of wild type (figure 2.9). Previous computational modelling indicated that highly anisotropic growth in the ventral midline region was essential for wild-type trap shape development (Lee *et al.*, 2019). Therefore, an alteration in the ratio between dorsal and ventral midline lengths should change trap shape as well as size. The ratio of ventral midline to dorsal midline was similar across genotypes (wild type = 0.227, *dw1 EOD* = 0.237 and *dw1 eod* = 0.260). Therefore, whilst the ventral midline is indeed shorter in the mutants, the dorsal midline is reduced by roughly the same amount as well.

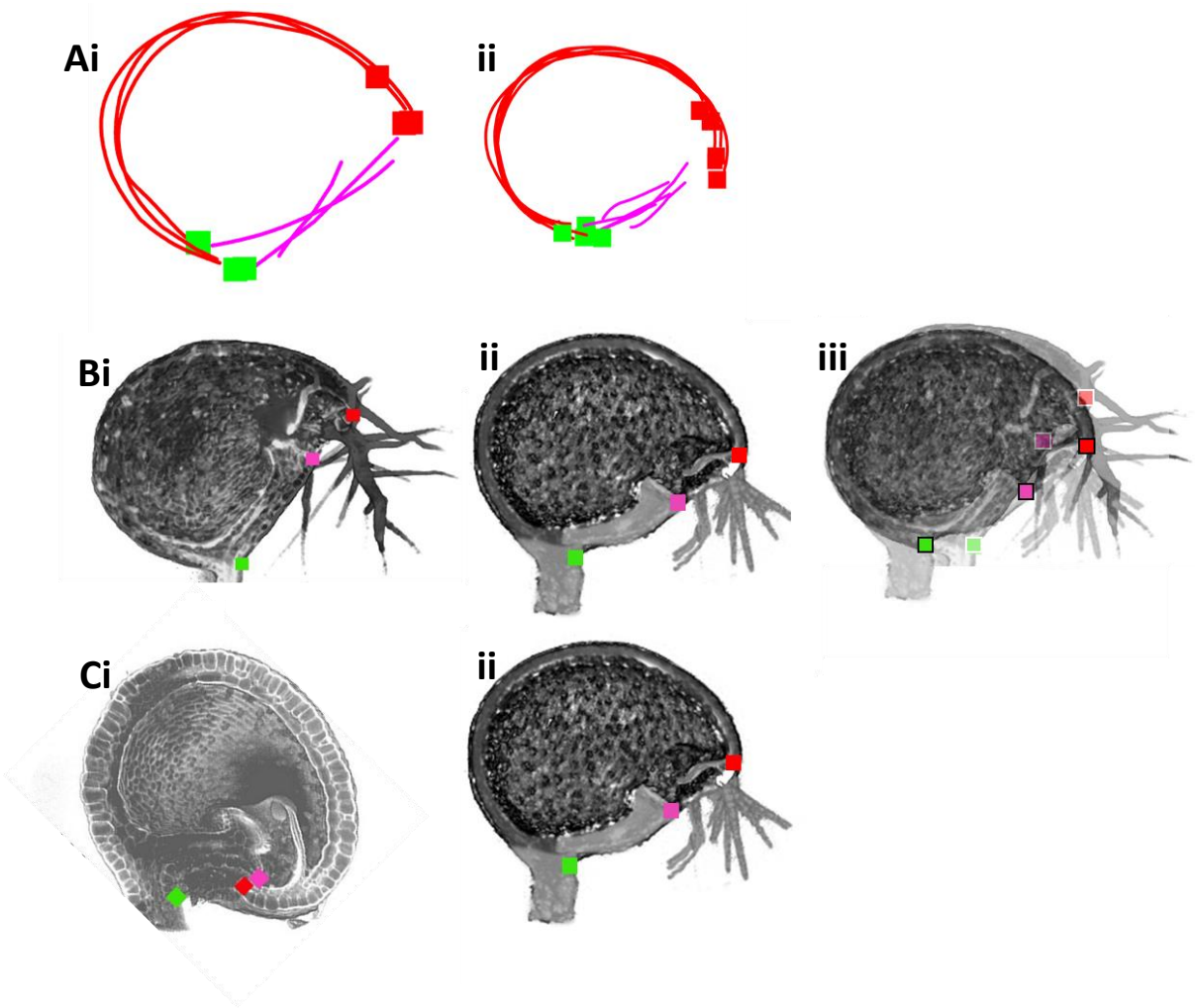

Figure 2.8 Resizing *dw1 EOD* trap to compare with wild type suggests *dw1 EOD* trap shape is not due to an early arrest in growth

A) Outlined drawings of mature i) wild type and ii) *dw1 EOD* traps in the sagittal plane. Outlines are comprised of dorsal midline (red), ventral midline (magenta), dorsal lip (red square) and stalk indentation (green square)

B) Shape comparison of *dw1 EOD* trap at mature wild type size. i) mature wild type trap (length 1000 µm), ii) *dw1 EOD* trap enlarged to 1000 µm in length, iii) i and ii overlayed where landmark points with white outlines are wild type and black outlines are *dw1 EOD*.

Ci) Wild type traps at an earlier developmental stage where trap length is the same as mature *dw1 EOD* traps (~800 µm), ii) mature *dw1 EOD* trap

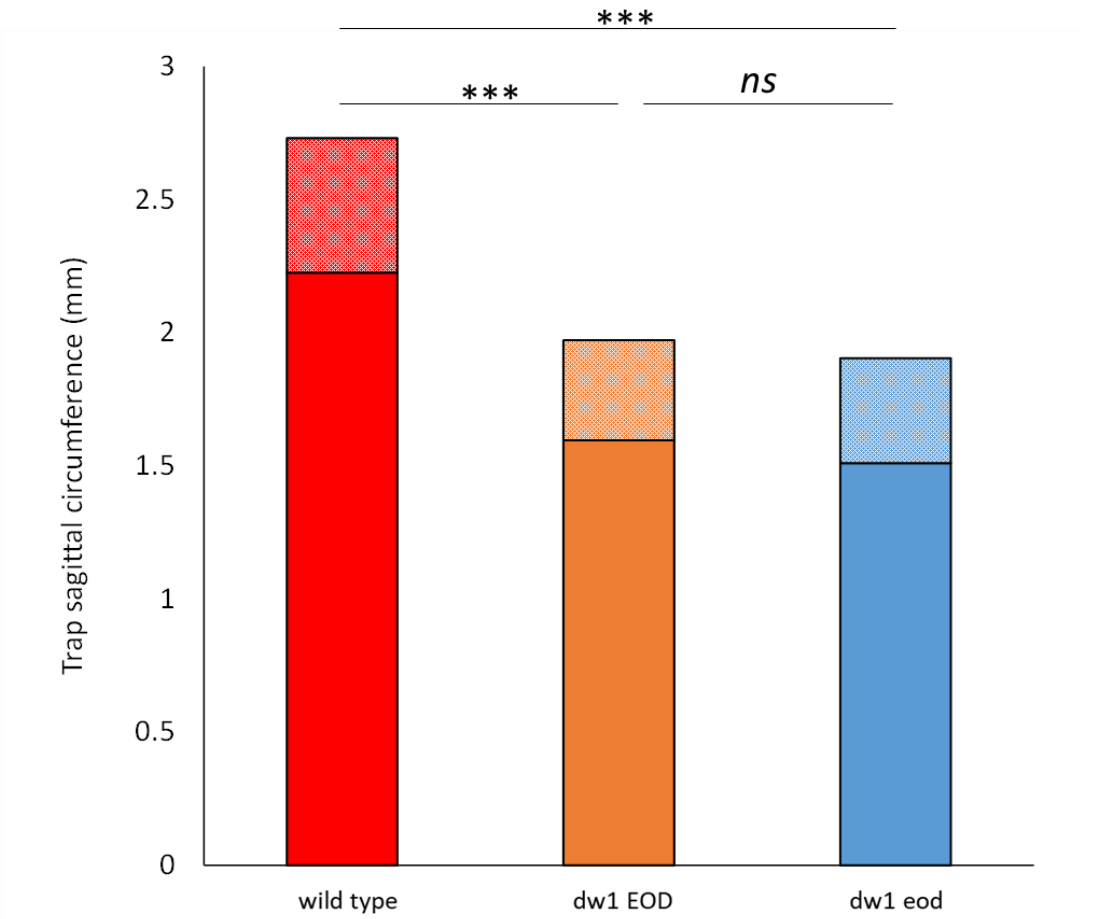

Figure 2.9 Ratio of ventral to dorsal lengths are comparable across genotypes even though circumferences differ

A) Sagittal view of mature wild type trap. Landmark points (squares) make for consistent locations on traps to measure distances between. Stalk (green) and mouth (red). Ventral midline (magenta) and dorsal midline (red).

B) Total average circumference of mutant traps is smaller than that of wild type. The sagittal circumference is made up of the length of the ventral midline plus (hatched area) the dorsal midline (solid area). Wild type n= 6; *dw1 EOD* n = 5; *dw1 eod* n = 7. *t* tests based on circumference: wild type to *dw1 EOD p* = 5.24966E-05 (***), wild type to *dw1 eod p* = 3.01445E-06 (***) and *dw1 EOD* to *dw1 eod p* = 0.55825857 (*ns*)

To obtain a cellular characterisation of mutant traps, I took confocal microscopy scans of mature wild type and *dw1 EOD* traps in the sagittal plane and of the ventral midline in the frontal plane. These scans were processed for cellular segmentation in MorphoGraphX in collaboration with Karen Lee (figure 2.10A and 2.11A). We found that average cell area is reduced in *dw1 EOD* traps compared to wild type by 55 % in the sagittal plane and 60 % in the ventral midline region (wild type sagittal cell area: $\bar{x}$ = 994 μm^2 , *SEM* = 14, *dw1 EOD* sagittal cell area: $\bar{x}$ = 549 μm^2, *SEM* = 6, wild type ventral cell area: $\bar{x}$ = 833 μm^2, *SEM* = 31, *dw1 EOD* ventral cell area: $\bar{x}$ = 503 μm^2, *SEM* = 15 (figure 2.10B)). This reduction in cell size suggests that *dw1* affects all parts of the trap. We also calculated cell anisotropy as cell MAX length/ (cellMAX length + cellMIN length). An area of greater cellular anisotropy can be seen in heat maps of the ventral midline region in wild type (figure 2.11Ai and ii). In *dw1 EOD* and area of anisotropic cells is present near the mouth in the sagittal plane (figure 2.11Aiii), but cells are more isotropic in the centre of the ventral midline in the frontal plane (figure 2.11Aiv). This is a key region for cellular anisotropy in forming the wild type (Lee *et al.*, 2019), therefore the isotropic cells in this region may explain the subtle mutant shape. The anisotropic cells in this region of *dw1 EOD* could be a result of resolving the tissue curvature around the mouth region. The presence of these cells could explain why there is no statically significant difference in ventral midline cell anisotropy between wild type and *dw1 EOD* (figure 2.11B). Therefore, the subtle difference in shape observed in *dw1 EOD* can be explained through smaller more isotropic cells.

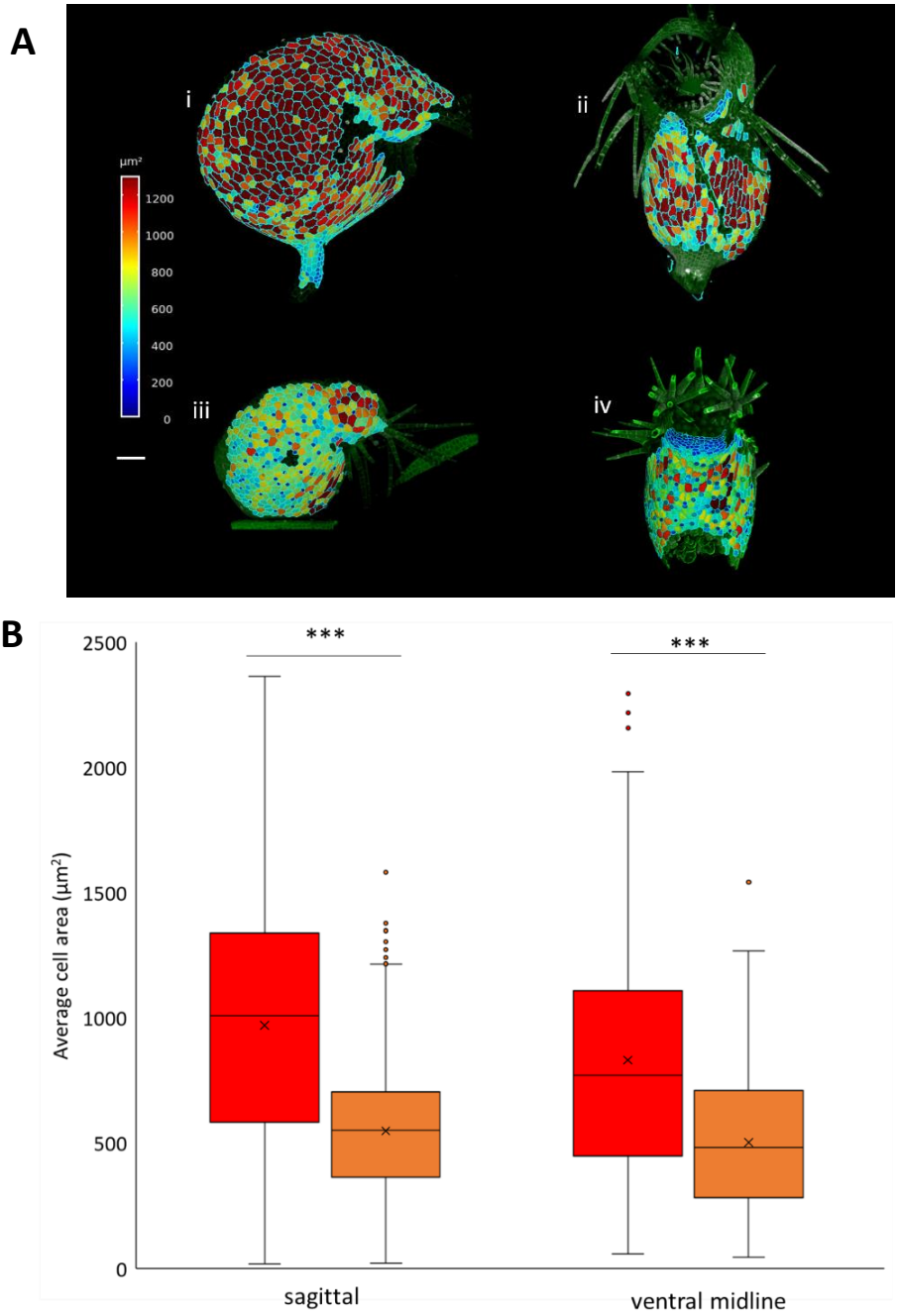

Figure 2.10 *dw1 EOD* cells are smaller in both the sagittal plane and the ventral region

A) Heat maps of cell area for i) wild type in sagittal plane, ii) wild type ventral region, iii) *dw1 EOD* in sagittal plane and iv *dw1 EOD* ventral region. Scale bar is 100 µm.

B) Cell area of traps in sagittal plane and in chin (ventral midline) from mature wild type traps (red) and mature *dw1 EOD* traps (orange). Horizontal line shows median, cross shows mean, box shows Q1 – Q3, whiskers show maximum and minimum, and outliers are plotted as single points. *t* tests: wild type *dw1 EOD* in sagittal plane *p* = 1.5432E-155 (***), wild type to *dw1 EOD* chin *p* = 2.5388E-19 (***), Wild type in sagittal plane: traps n = 2, cells n = 1354. *dw1 EOD* in sagittal plane: traps n = 3, cells n = 1554. Wild type ventral region: traps n = 1, cells n = 262. *dw1 EOD* ventral region: traps n = 1, cells n = 359.

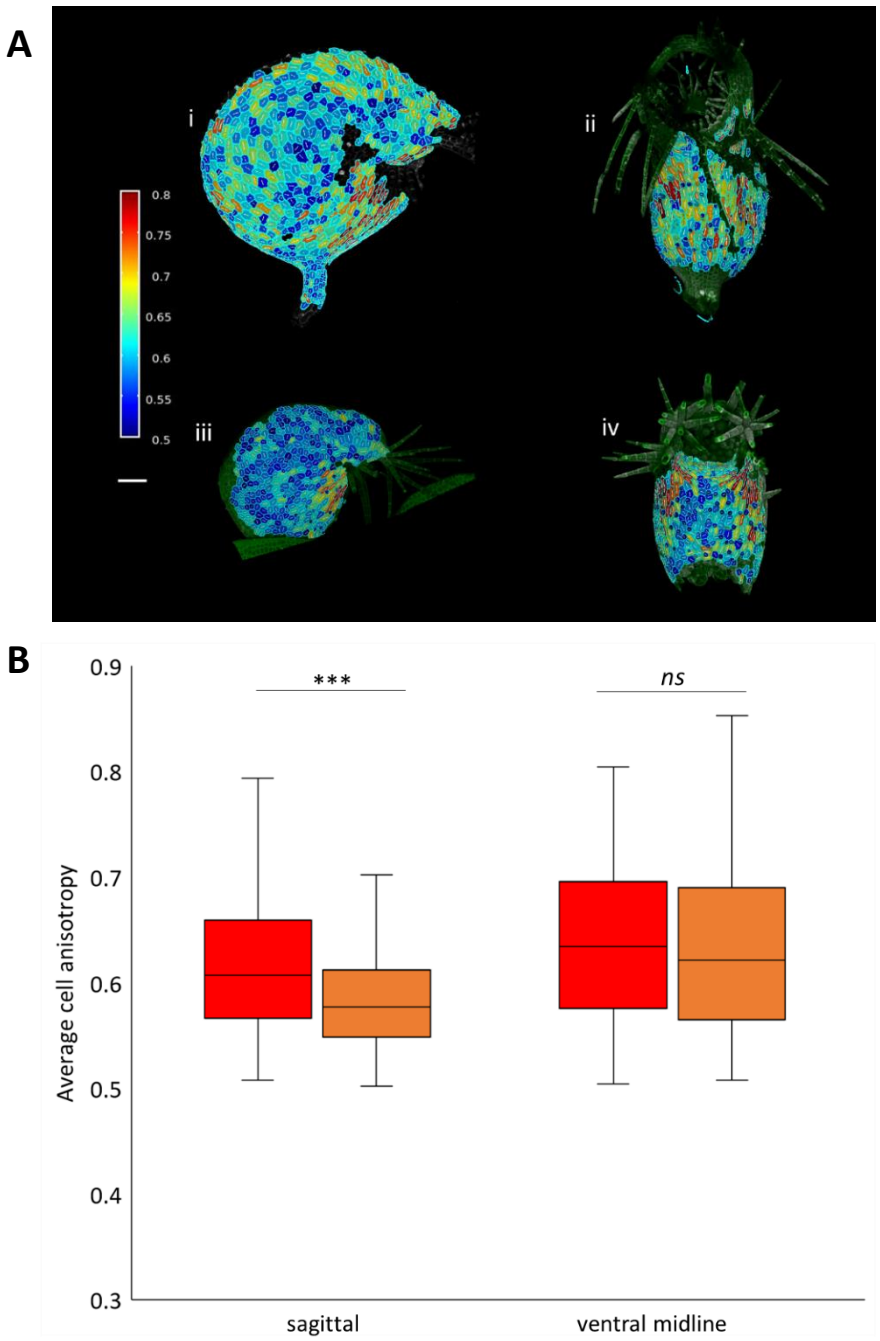

Figure 2.11 *dw1 EOD* cells are more isotropic in sagittal plane, but less affected in ventral region

A) Heat maps of cell anisotropy for i) wild type in sagittal plane, ii) wild type chin region, iii) *dw1 EOD* in sagittal plane and iv) *dw1 EOD* chin region. Anisotropy is calculated as cell MAX length/ (cellMAX length + cellMIN length). Scale bar is 100 µm.

B) Cell anisotropy of traps in sagittal plane and ventral midline from mature wild type traps (red) and mature *dw1 EOD* traps (orange). Horizontal line shows median, cross shows mean, box shows Q1 – Q3, whiskers show maximum and minimum, and outliers are plotted as single points. *t* tests: wild type to *dw1 EOD* in sagittal plane p = 1.36725E-61 (***), wild type to *dw1 EOD* ventral midline p = 0.388466747 (*ns*). Wild type in sagittal plane: traps n = 2, cells n = 1354. *dw1 EOD* sagittal plane: traps n = 3, cells n = 1554. Wild type ventral midline: traps n = 1, cells n = 262. *dw1 EOD* ventral midline: traps n = 1, cells n = 359.

Wild type traps can catch prey for nutrient acquisition. To understand if the reduced size in the mutants affect trap function, I analysed prey capture in wild type and mutant lines. I took four genotypes from the family of D90-2 as well as the parent and two genotypes of *dw1 EOD* and two genotypes of *dw1 eod* and grew them in containers with *Daphnia* in. After two weeks I looked at the traps to identify the presence of any captured prey (figure 2.12). Across all genotypes with the wild type phenotype, prey was identified in multiple traps. However, for genotypes in both classes of mutant there were no traps with prey inside. Therefore, the mutation adversely affects trap function and prevents prey capture.

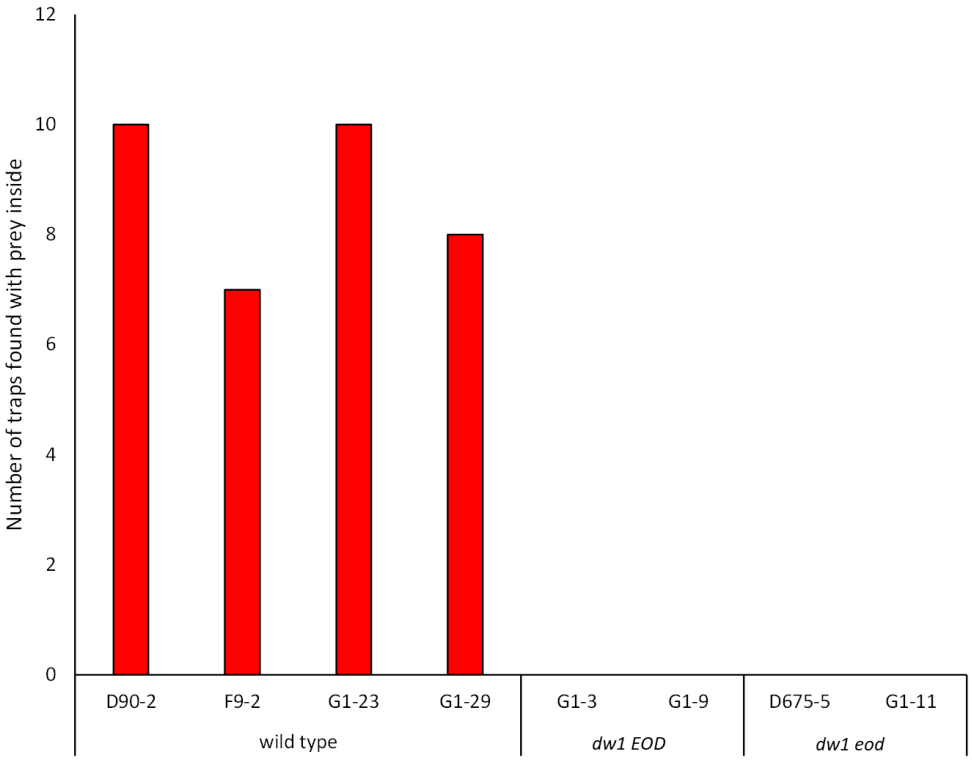

Figure 2.12 Traps from both class of mutant are not able to capture prey

Number of traps identified across a range of genotypes that contained *Daphnia* or other prey in. Total number of traps imaged: D90-2 n = 10, F9-2 n = 17, G1-23 n = 27, G1-29 n = 35, G1-3 n = 47, G1-9 n = 85, D675-5 n = 7, G1-11 n = 55

2.2.3 Mutants have reduced leaf and internode lengths

To understand how the mutations had affected other organs of the plant, I measured mature leaf and internode lengths from images of dissected stolons taken by light microscope (figure 2.13A). In *dw1 EOD*, mature leaf length ($\bar{x}$ = 1.99 mm, *SD* = 0.38, *SEM* = 0.06) was about 25% of that in wild type ($\bar{x}$ = 7.96 mm, *SD* = 1.96, *SEM* = 0.20), and mature internode length ($\bar{x}$ = 0.91 mm *SD* = 0.28, *SEM* = 0.04) was about 40% of that in wild type ($\bar{x}$ = 2.59 mm, *SD* = 0.71, *SEM* = 0.56). In *dw1 eod*, mature leaf length ($\bar{x}$ = 0.54 mm, *SD* = 0.14, *SEM* = 0.03) was about 7% of wild type, and internode length ($\bar{x}$ = 0.42 mm, *SD* = 0.12, *SEM* = 0.04) about 15 % of wild type. Along with the traps, this data shows clear dwarfism in the mutants compared to wild type, with some parts of the plant exhibiting stronger dwarfism than others.

I also measured mature internode and leaf widths (figure 2.13B). Compared to wild type ($\bar{x}$ = 0.165 mm, *SD* = 0.026, *SEM* = 0.006), the measured diameter of *dw1 EOD* leaf was 20 % wider in the leaf ($\bar{x}$ = 0.194, *SD* = 0.032, *SEM* = 0.008), whereas *dw1 eod* was similar to wild type ($\bar{x}$ = 0.168 mm *SD* = 0.074, *SEM* = 0.009). For internodes, *dw1 EOD* ($\bar{x}$ = 0.178 mm *SD* = 0.041, *SEM* = 0.004) was around 15 % wider than wild type and *dw1 eod* ($\bar{x}$ = 0.199 mm, *SD* = 0.045, *SEM* = 0.018) was around 25 % wider in than wild type ($\bar{x}$ = 0.157 mm, *SD* = 0.034, *SEM* = 0.005).

To understand the relationship between organ length and width, I plotted the ratio of length/width from figure 2.13A and B (figure 2.12C). The length/width for leaves of *dw1 EOD* ($\bar{x}$ = 10.30, *SEM* = 0.45) was around 20 % of wild type ($\bar{x}$ = 48.37, *SEM* = 5.64) and *dw1 eod* ($\bar{x}$ = 3.21, *SEM* = 0.30) was around 7 % of wild type. The length/width of internodes of *dw1 EOD* ($\bar{x}$ = 5.14, *SEM* = 0.30) was around 30 % of wild type ($\bar{x}$ = 16.49, *SEM* = 1.22) and *dw1 eod* ($\bar{x}$ = 2.11, *SEM* = 0.19) was around 13 %.

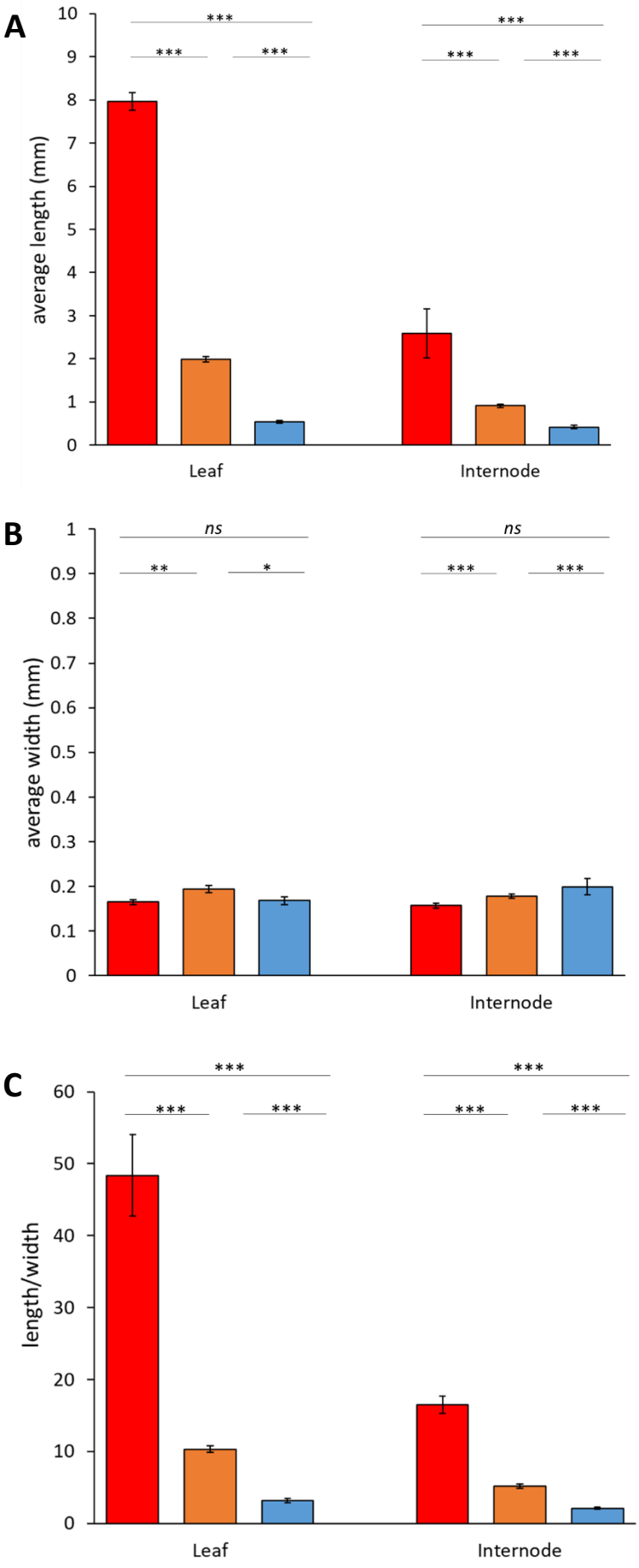

Figure 2.13 Mutant leaves and internodes are reduced in length but not width

A) Average leaf and internode length measurements of wild type (red), *dw1 EOD* (orange) and *dw1 eod* (blue). Internode length *t* tests: wt to *dw1 EOD p* = 2.84866E-06 (***), wt to *dw1 eod p* = 3.12303E-07 (***) and *dw1 EOD* to *dw1 eod p* = 3.31286E-09 (***). Leaf length *t* tests: wt to *dw1 EOD p* = 1.72018E-07 (***), wt to *dw1 eod p* = 3.03494E-07 (***) and *dw1 EOD* to *dw1 eod p* = 3.85684E-22 (***). B) Average leaf and internode width measurements. Internode width *t* tests: wt to *dw1 EOD p* = 7.41161E-06 (***), wt to *dw1 eod p* = 0.416283545 (*ns*) and *dw1 EOD* to *dw1 eod p* = 1.64225E-06 (***). Leaf width *t* tests: wt to *dw1 EOD p* = 0.006209193 (**), wt to *dw1 eod p* = 0.715054883 (*ns*) and *dw1 EOD* to *dw1 eod p* = 0.039694499 (*). C) Ratios of average leaf length to width and average internode length to width. Internode ratio *t* tests: wt to *dw1 EOD p* = 3.66424E-07 (***), wt to *dw1 eod p* = 2.71643E-06 (***) and *dw1 EOD* to *dw1 eod p* = 2.12441E-11 (***). Leaf width ratio *t* tests: wt to *dw1 EOD p* = 2.15594E-17 (***), wt to *dw1 eod p* = 1.15526E-07 (***) and *dw1 EOD* to *dw1 eod p* = 1.04434E-07 (***).

Error bars show SEM. wild type: 3 individuals, stolons n= 12, *dw1 EOD*: 10 individuals, stolons n = 40, *dw1 eod*: 4 individuals, stolons n = 16

2.2.4 Mutant stolons have a greater circumference than wild type

Measuring internode width from light microscopy images may not give accurate comparative data for how the mutation is affecting mature organ shape in directions other than axial. Therefore, I measured the circumference of mature stolons. This was done in collaboration with Karen Lee who performed the image analysis and data acquisition. We used mounted PI-stained tissue and took confocal images with a fine z-step to project the volume in z (figure 2.14). We found that average circumference length (figure 2.14A) is increased in *dw1 eod* ($\bar{x}$ = 557 µm, *SEM* = 21) is around 30 % longer than wild type ($\bar{x}$ = 423 µm, *SEM* = 11) and *dw1 EOD* ($\bar{x}$ = 651 µm, *SEM* = 50) is around 50 % longer than wild type.

To determine if circumferential cell number had changed in the mutants, we counted the number of epidermal cells which made up the circumference (figure 2.15B). *dw1 eod* ($\bar{x}$ = 32, *SEM* = 0.7) had around 45 % more cells than wild type ($\bar{x}$ = 23, *SEM* = 0.8) and *dw1 EOD* had nearly 80 % more cells ($\bar{x}$ = 39, *SEM* = 3.9). Therefore, both classes of mutant have a greater number of cells in the epidermis than wild type.

The process of preparing tissue samples for PI staining and mounting involves a number of dehydration and clearing steps (see Methods). In a system such as *U. gibba* where the stolons have internal air spaces, these preparation steps may affect the structure of the tissue. We therefore measured stolon height, from the top of the z-stack to the bottom, and stolon width, orthogonal to height measurement, to determine if the stolon had flattened (figure 2.15C). We found that for wild type (height $\bar{x}$ = 104.2 µm, *SEM* = 5.6; width $\bar{x}$ = 160.6, *SEM* = 5.7), *dw1 EOD* (height $\bar{x}$ = 165.8 µm, *SEM* = 12.7; width $\bar{x}$ = 240.0, *SEM* = 18.1) and *dw1 eod* (height $\bar{x}$ = 124.8 µm, *SEM* = 13.7; width $\bar{x}$ = 214.8, *SEM* = 4.0) had height measurements that were around 50 % smaller than width measurements, suggesting that flattening may had occurred.

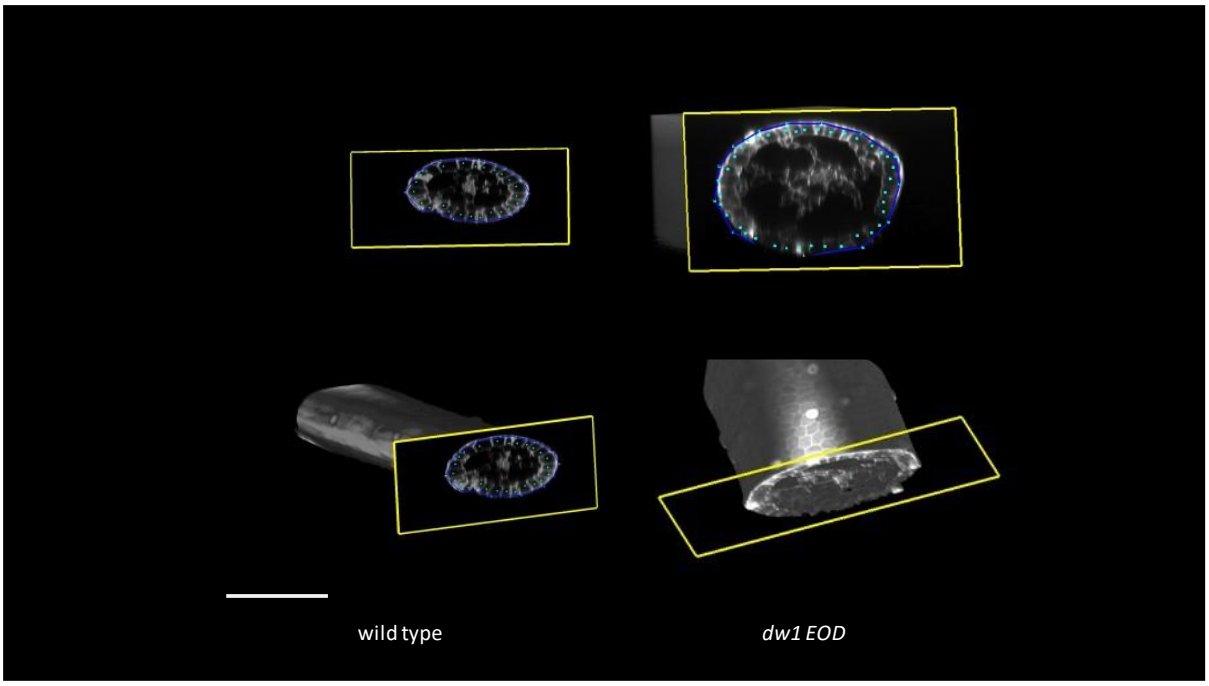

Figure 2.14 Volume views of internode circumference

Projections of confocal scans of wild type and *dw1 EOD* stolons. Circumference measurements are marked in blue. Scale bar is 150 µm

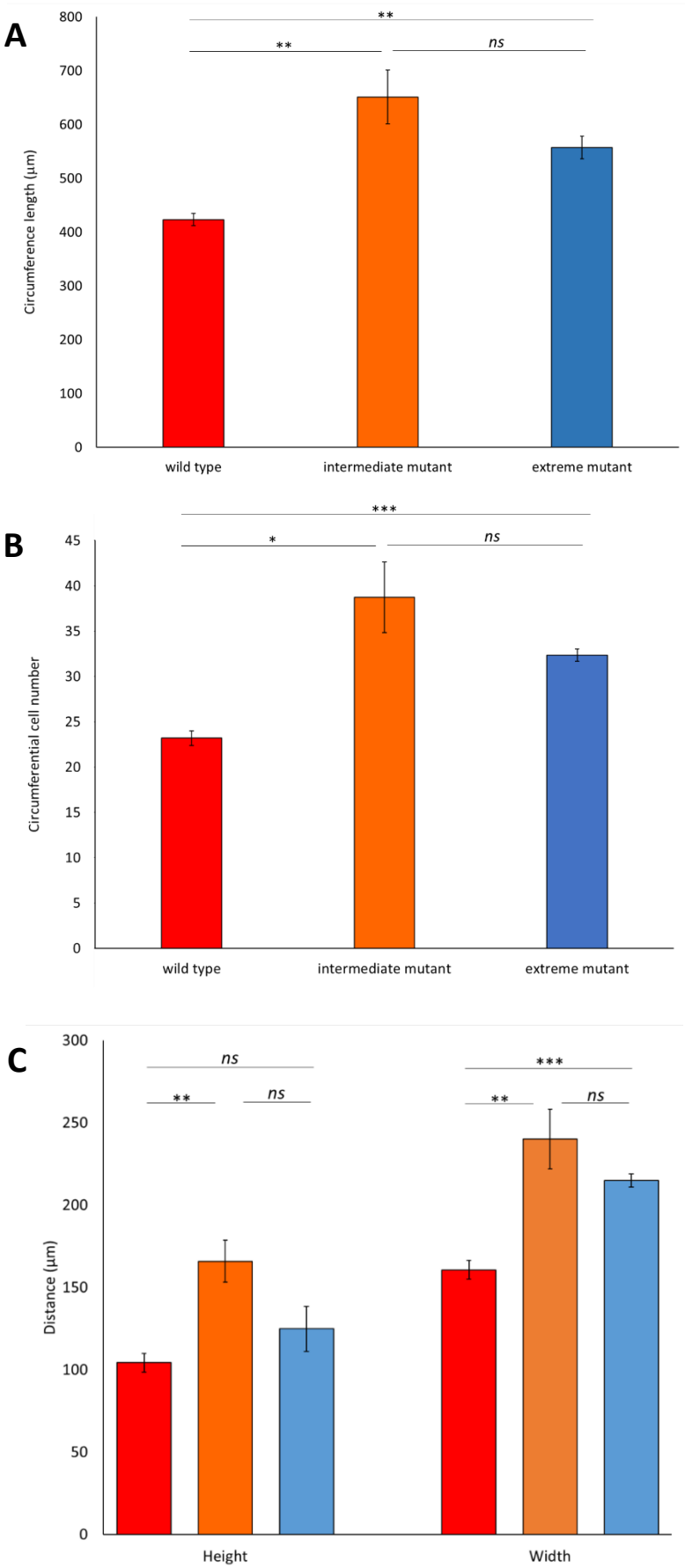

Figure 2.15 Circumference measurements of mature internodes

A) Average circumference length of wild type (red), *dw1 EOD* (orange) and *dw1 eod* (blue) mutants. *t* tests: wild type to *dw1 EOD p* = 0.009122321 (**), wt to *dw1 eod p* = 0.003024475 (**), *dw1 EOD* to *dw1 eod p* = 0.140739087 (ns). Wild type n = 5, *dw1 EOD* n = 5, *dw1 eod*= 4

B) Average cell number in circumference. *t* tests: wt to *dw1 EOD p* = 0.025755431 (*), wild type to *dw1 eod p* = 0.000140411 (***), *dw1 EOD* to *dw1 eod p* = 0.198541568 (ns). Wild type n = 5, *dw1 EOD* n = 4, *dw1 eod*= 3

C) Average stolon height and width. Stolon height *t* tests: wild type to *dw1 EOD p* = 0.005449521 (**), wt to *dw1 eod p* = 0.23683098 (ns), *dw1 EOD* to *dw1 eod p* = 0.065803269 (ns), stolon width *t* tests: wt to *dw1 EOD p* = 0.009586294 (**), wt to *dw1 eod p* = 0.000132542 (***), *dw1 EOD* to *dw1 eod p* = 0.240010787 (ns). Wild type n = 5, *dw1 EOD* n = 5, *dw1 eod* = 4

Error bars show SEM

2.2.5 Epidermal cells in mutants are smaller and more isotropic than wild type

To determine how cell shape and size had changed in the epidermis of the mutants, surface segmentation using MorphoGraphX was performed on mature internodes of the three genotypes (figure 2.16). Cells in both *dw1 EOD* and *dw1 eod* where less than 50 % the area (*dw1 EOD* $\bar{x}$ = 292.86 μm^2, *SEM* = 4.78, *dw1 eod* $\bar{x}$ = 416.37μm^2, *SEM* = 9.46) of wild type ($\bar{x}$ = 845.74 μm^2, *SEM* = 24.07) (figure 2.17A).

Cell length parallel to the stolon was about four times longer in wild type ($\bar{x}$ = 41.69 µm, *SEM* = 0.98) than in either mutant area (*dw1 EOD* $\bar{x}$ = 13.17 µm, *SEM* = 0.15, *dw1 eod* $\bar{x}$ = 16.11 µm, *SEM* = 0.30) (figure 2.17B). The absolute average cell lengths perpendicular to the stolon appear to be comparable for all three genotypes (wild type $\bar{x}$ = 18.66 µm, *SEM* = 0.33, *dw1 EOD* $\bar{x}$ = 17.08 µm, *SEM* = 0.23, *dw1 eod* $\bar{x}$ = 16.84 µm, *SEM* = 0.34) (figure 2.17C). However, a statistically significant difference ($p < 0.001$) was found between each genotype. This could be due to the large sample size for each genotype (n cells > 1000), indicating that whilst the difference is small, the mutation does have an effect on cell length parallel to the stolon. Nevertheless, the mutation caused preferential reduction in epidermal cell elongation in the long axis of the stolon.

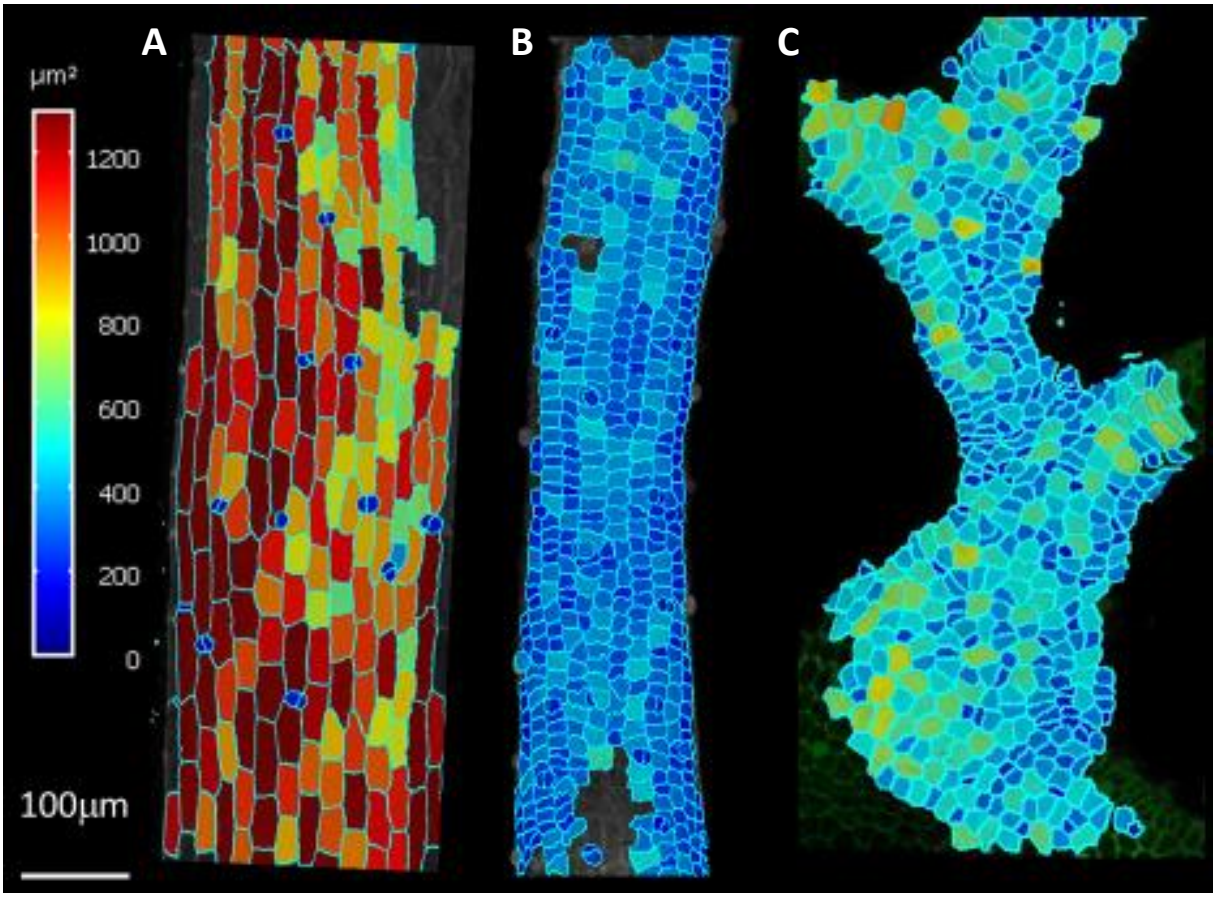

Figure 2.16 Epidermal cells are smaller in both mutants compared to wild type

2.5D surface segmentations of epidermal cells in mature stolon sections of A) wild type, B) *dw1 EOD* and C) *dw1 eod*. Scans are of representative stolons to provide an indication of a typical cell area heat map per phenotype. Segmentation was performed with MorphoGraphX. Scale bar is 100 µm.

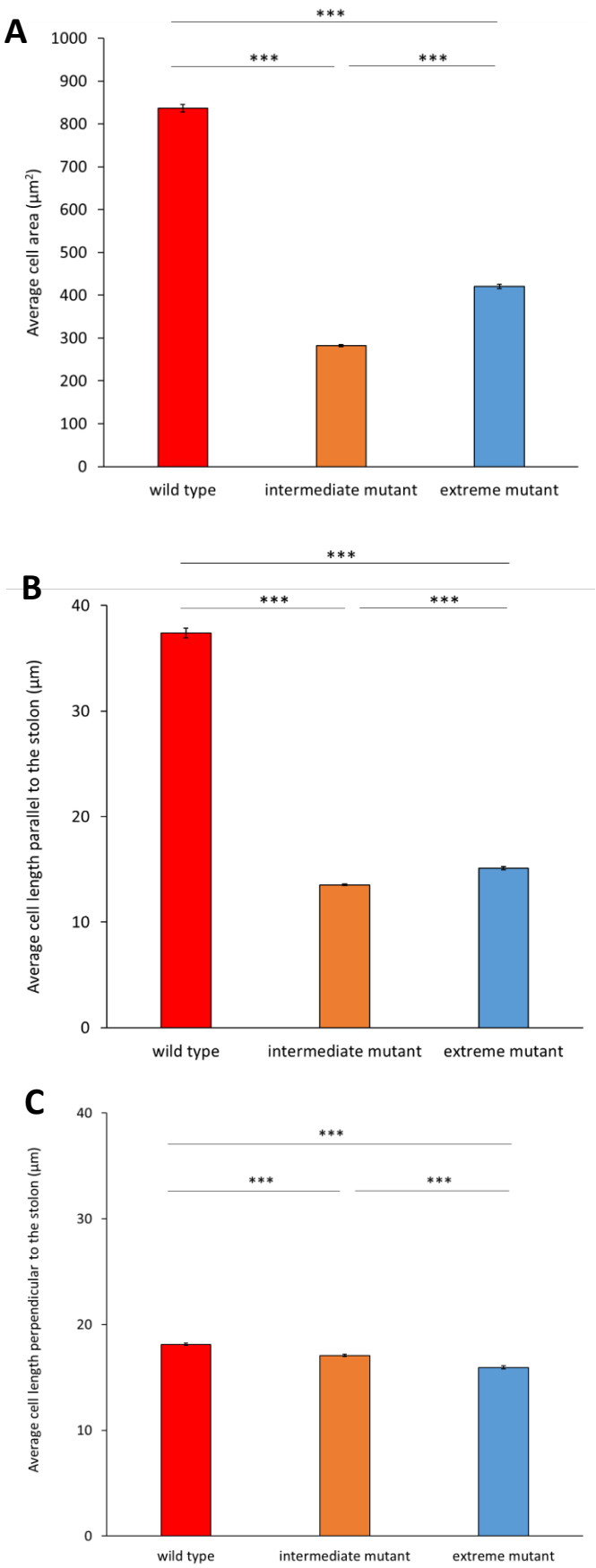

Figure 2.17 2.5D segmentation reveals smaller cells in mutants are due to a reduction in length parallel to the stolon but not perpendicular

A) Average cell area of epidermal cells from mature internodes. *t* tests: wild type to *dw1 EOD* mutant $p = 0$ (***), wild type to extreme mutant $p = 0$ (***) and *dw1 EOD* to *dw1 eod* - $p = 1.0649E-137$ (***)

B) Average cell length parallel to the stolon. Orientation is determined by a manually placed Bezier line. *t* tests: wild type to *dw1 EOD* - $p = 0$ (***), wild type to *dw1 eod* - $p = 0$ (***) and *dw1 EOD* to *dw1 eod* - $p = 2.60257E-20$ (***)

C) Average cell length perpendicular to the stolon. Orientation is determined by a manually placed Bezier line. *t* tests: wild type to *dw1 EOD* - $p = 3.9677E-11$ (***), wild type to *dw1 eod* - $p = 4.74024E-27$ (***) and *dw1 EOD* to *dw1 eod* - $p = 3.23761E-09$ (***)

Wild type stolons n = 8, cells n = 1817. *dw1 EOD* stolons n = 5, cells n = 2289. *dw1 eod* stolons n = 4, cells n = 1494

2.2.6 Mutants have altered internal tissue

To find if the mutation had affected the internal tissue in the same way as the epidermis, I imaged and characterised the internal tissue of mature stolons using confocal microscopy (figure 2.18A). In wild type, vasculature was straight (figure 2.18A). *dw1 EOD* vasculature was not straight, but often wiggly, where the vasculature bundle had appeared to bend into the air spaces (figure 2.18A). The vasculature in the *dw1 eod* was not wiggly, but air spaces were small or absent.

To quantify the length of the vasculature compared to the epidermis, length measurements were taken of the two tissue layers in collaboration with Karen Lee (figure 2.18B). The ratio between length of the epidermis and length of the vasculature for wild type (0.981, *SEM* = 0.012) and the *dw1 eod* (1.020, *SEM* = 0.014) was about 1, showing that the two tissue layers are similar in length. The ratio for *dw1 EOD* was higher (1.127, *SEM* = 0.045), indicating that the vasculature was about 10 % longer than the epidermis on average.

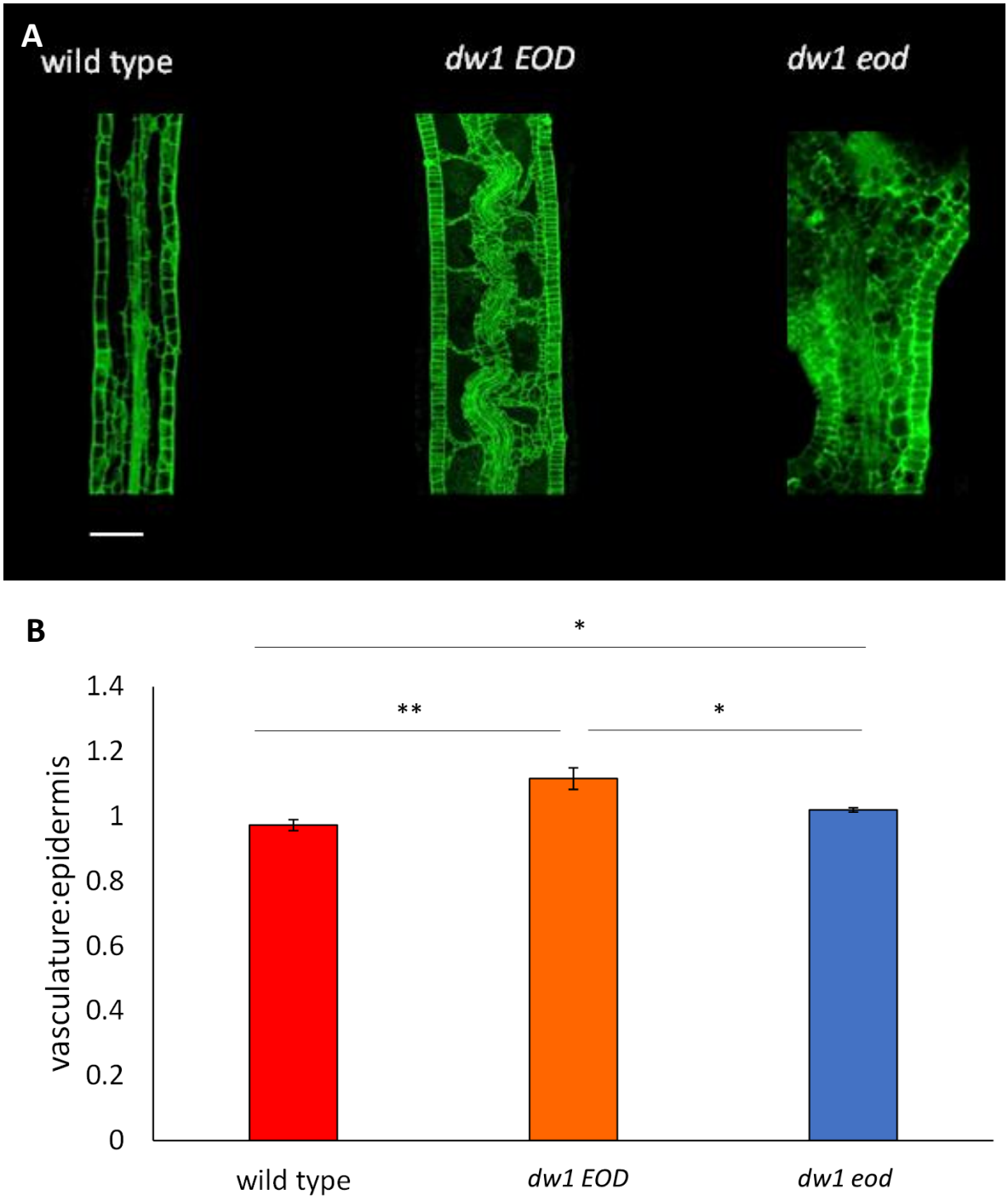

Figure 2.18 *dw1 EOD* vasculature is wiggly

A) Confocal microscopy scans of mature stolons. Images are of z-sections. In wild type, vasculature grows straight, parallel to the stolon. In *dw1 EOD*, the vasculature is wiggly. In *dw1 eod,* the vasculature is not as wiggly as in the *dw1 EOD*. Scale bar is 100 µm

B) In the wild type and *dw1 eod*, the length of the vasculature is the same as the epidermis because the ratio of lengths between is around 1. In *dw1 EOD*, the vasculature is longer than the epidermis as the ratio is 1.1. Error bars show SEM. Wild type n = 4, *dw1 EOD* n = 4, *dw1 eod* n = 4. *t* tests: wild type to *dw1 EOD* - *p* = 0.008341192 (**), wild type to *dw1 eod*- *p* = 0.040051391 (*) and *dw1 EOD* to *dw1 eod*- *p* = 0.029120118 (*)

To further characterise the cells of the inner tissue compared to the epidermis, 3D cell segmentation was performed on confocal scans with a fine z-step. I performed sample preparation and image acquisition and Karen Lee undertook image processing and segmentation. We analysed mature wild type and *dw1 EOD* internodes and produced a heat map of cell length for epidermal cells and outer vasculature bundle cells (vein cells) (figure 2.19A). Cells within the vasculature itself were too small for segmentation. We find that cells in both layers are generally shorter in the mutant compared to the wild type, showing that the mutation not only affects the epidermis but also influences vein cell length. We produced a cloud of the orientations of the maximal lengths in each cell (figure 2.19B) showing the direction in which each individual cell is most elongated. In wild type, cells of both the vein and epidermis are elongated parallel to the direction of growth of the stolon. In *dw1 EOD*, cells in the vein are elongated in the direction of the wiggly vein. In the epidermis however, the orientation of the maximal length of the cell is not parallel to the stolon, but perpendicular. This change in major axis orientation of the mature cell implies a change in the major direction of growth of epidermal cells from parallel to the direction of stolon growth in wild type to perpendicular in *dw1 EOD.* From visual observations, this implies that either the epidermal cells in the mutant are reduced in length parallel to the stolon and/or cell length is increased perpendicular to the stolon.

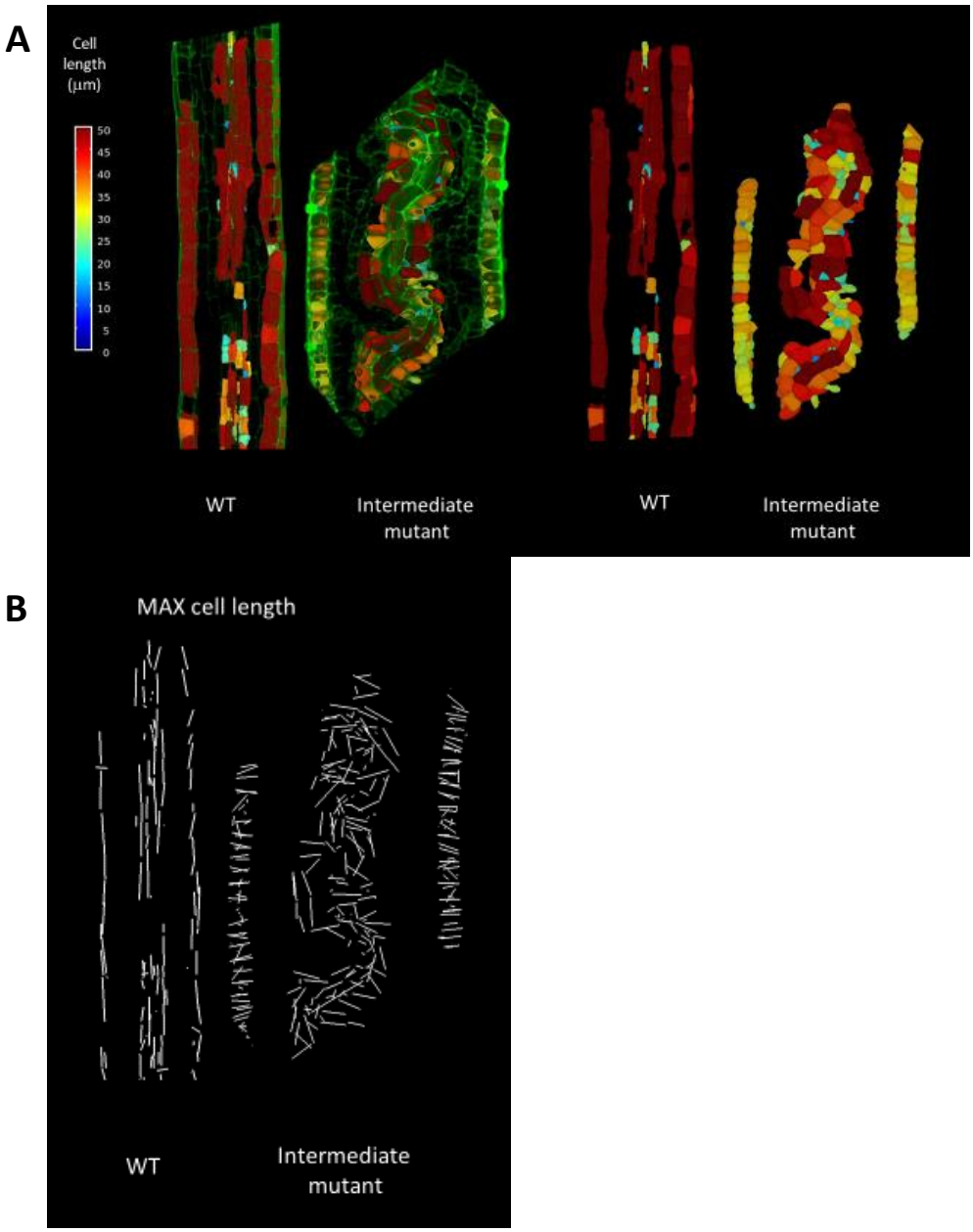

Figure 2.19 3D cell segmentation reveals reduced cell size and change in orientation of major axis in *dw1 EOD*

A) Heat maps showing maximal cell length of epidermal cells and vasculature of wild type and *dw1 EOD*. The set of images on the right show the segmentation overlayed with the confocal scan. The images on the right are just of the segmented cells

B) Map of orientations of maximal cell length of the scans shown in A.

2.3 Discussion

2.3.1 *dwarf1* affects traps differently from leaves and stolon

I have analysed morphological mutants in a family derived from a forward screen in *U. gibba*. Segregation analysis indicates that two genes are likely involved: *DWARF1* (*DW1*) and *ENHANCER OF DWARF1* (*EOD*). *dw1 EOD* mutants have an intermediate dwarf phenotype and *dw1 eod* mutants have an extreme dwarf phenotype. Phenotypic analysis shows that in both cases, all plant parts are affected: traps, leaves and the stolon are reduced in length compared to wild type. This finding suggests that these genes do not act in an organ-specific manner but have general effects on growth, as found with other mutations (Kohorn *et al.*, 2021). They therefore resemble dwarf mutants such which affect both leaf and stem length, such as *bri1* in *Arabidopsis* (Wang et al., 2001), in contrast to mutant such as *Le-1* in pea (Martin David *et al.*, 1997), *Rht1* in wheat (Peng *et al.*, 1999) or *Slr1* in rice (Monna *et al.*, 2002) which mainly affect stem length.

Although all plant parts are affected by *dwarf1* and *eod,* they are not affected equally. Leaf length is most affected: *dw1 EOD* and *dw1 eod* have leaf lengths that are 25 % and 7 % of wild type respectively. Stolon length is less affected: *dw1 EOD* and *dwf1 eod* have stolon internode lengths 40 % and 15 % of wild type respectively. Both *dw1 EOD* and *dw1 eod*, increase stolon width slightly (percent values), and *dw1 eod* also increases leaf width slightly (percent). Thus, whereas wild type leaves and stolon internodes have an anisotropic overall shape, with length:width ratios of 48.36 and 16.48 respectively, leaves and stolons of *dw1 EOD* are more isotropic, with length:width ratios of 10.30 and 5.13, and *dw1 eod* have still lower ratios of 3.21 and 2.11

Trap length for both *dw1 EOD* and *dw1 eod* is about 70% of that in wild type. As the traps are near spherical, trap length has been used as a proxy for overall trap size. This assumption is based on the

trap being completely isotropic, which it is not (figure 2.7). To be able to compare mutant trap shape directly with wild type, trap width and trap length:width data will need to be acquired. Thus, severity of the organ length phenotype correlates with the anisotropy of the organ in wild type: leaf > stolon > trap. Correspondingly, in *Arabidopsis* dwarfing mutants, inflorescence internodes are typically more affected than leaves or petals (Bichet *et al.*, 2001). Therefore, *dw1* and *eod* act in a similar manner to dwarf mutants in other species, which have a greater effect on more anisotropic structures.

Although *dw1* has a relatively small effect on length of traps, it alters trap function: Wild type traps catch prey by pumping water out of their lumen and creating a vacuum which is sealed by the trap door (Poppinga *et al.*, 2015). Mutant traps do not catch prey, therefore *dw1* could affect the ability of traps to pump water out, or the change in mouth or trap door shape may prevent formation of a water-tight seal.

2.3.2 *dwarf1* affects epidermal cell size and anisotropy

The *dw1* and *eod* mutations could affect cell number, cell size and/or cell shape. Epidermal cells of wild-type stolons are anisotropic, with a length:width ratio of 2.23 and the longest cell axis oriented parallel to the stolon axis. By contrast, epidermal cells in stolons of *dw1 EOD* are more isotropic, with a length:width ratio of 0.77 and the longest cell axis oriented mediolaterally to the stolon axis. In *dw1 eod,* epidermal cells are also more isotropic than wild type, with a length:width ratio of 0.96.

Circumferential length and cell number is greater in both mutants, where *dw1 EOD* is on average over 200 µm longer in circumference and has on average 15 more cells than wild type, and *dw1 eod* is on average 100 µm longer in circumference and 10 more cells than wild type. Whilst data for both cell area in z and comparative data for cell length in the major or minor axis has been acquired, the combination of an increase in total circumferential length and circumferential cell number suggest

that both *dw1* and *eod* have an effect on cell division. It appears that the PI staining and mounting method caused the stolons to flatten (figure 2.14 and 2.15). Future work will use OPT gather accurate width and circumference measurements and to see if *U. gibba* might naturally be flattened.

Stolon epidermal cells are less anisotropic than those of wild type, and the orientation of anisotropy is changed from parallel to the stolon axis to a medio-lateral orientation. This change reflects a preferential reduction in cell length parallel to the stolon axis, reduced in *dw1 EOD* by around 70 % and in *dw1 eod* by around 60 %. This effect is seen throughout the mature stolon but is restricted to the ventral midline of traps. Cells in the ventral midline are highly anisotropic wild-type traps, much like the stolon. Thus changes in organ length of *dw1* and *eod* may be attributed to a preferentially reduction in length of highly anisotropic cells and an effect in increasing circumferential cell division

2.3.3 *dw1* affects inner tissues differently from epidermis

In contrast to the epidermis, which remains straight, vasculature is wiggly in *dw1 EOD* mutants. Thus, *dw1 eod* causes a smaller reduction in vasculature length than epidermal length. The internode length of wild type is 2-5 times greater than that of *dw1 EOD*. Thus, if *dw1* had no effect on vasculature length, vasculature would be 2.5 times longer than the epidermis. However, even in wiggly regions of the stolon, vasculature in *dw1* is only 1.1 times longer on average than the epidermis (figure 2.18B). Thus, vasculature length is also reduced in *dw1*, but to a lesser extent than epidermal length. This suggests that *dw1* affects all tissue layers but has a greater effect on the epidermis.

The wiggly vasculature phenotype has not been reported for dwarf mutants of other species. Perhaps the presence of internal air spaces in *Utricularia* allows the wiggly vasculature to form. If specified growth is reduced by *dw1* more in the epidermis than the vasculature, growth differential between

tissue layers would lead to increased epidermal tissue tension and correspondingly increased internal tissue compression. If internal compressive tissue forces go past a critical point, and there is sufficient surrounding air space available, buckling would occur, which could explain the wiggly vasculature phenotype. Vasculature of *dw1 eod* is straighter than *dw1 EOD*. This could be explained by the lack of air spaces in *dw1 eod*, preventing vasculature deformation. An alternative to the tissue tension-compression hypothesis is that the wiggly vasculature in *dw1 EOD* is caused by changes in growth orientation which are corrected in *dw1 eod*. If *dw1* is in a known gene, comparing its phenotype to that in other species may allow these hypotheses to be tested.

2.3.4 Conclusions

DW1 promotes cell shape anisotropy *U. gibba*, with effects on organ shape that correlates with the extent of cell shape anisotropy in wild type. The *dw1* mutation causes a striking vasculature phenotype that may be explained through increased tissue tension in the epidermis and correspondingly increased compression of the vasculature leading to buckling when sufficient surrounding air space is available. If *dw1* is in a known gene, the phenotype of corresponding mutants in other species could give insights into the general role of *dw1*.

3 *DW1* is a Brassinosteroid biosynthesis gene

3.1 Introduction

In chapter 1, I identified a mutant family from a forward screen segregating for two classes of dwarfism: intermediate and extreme, hypothesised to correspond to *dw1 EOD* and *dw1 eod* respectively. Dwarfism is due to reduced cell elongation leading to organs which are shorter than wild type by amounts that vary according to the degree of organ anisotropy. For both classes of mutant, epidermal cells are reduced in length preferentially in the directional of growth and, in *dw1 EOD*, a striking wiggly vasculature phenotype is observed. One explanation for the wiggly vasculature is that elevated tissue tension in the epidermis and associated tissue compression in the vasculature causes vascular buckling. Therefore, *DW1* increases organ size, promotes epidermal cell length in a preferential direction and may reduce tissue compression so that the vasculature does not buckle. This chapter aims to identify *DW1* and thus clarify how it acts.

3.1.1 Finding the genetic basis of the mutant phenotype

To identify *DW1*, I will use whole genome sequencing (WGS) to identify a causative SNP. *U. gibba* has a 100 Mbp diploid genome which is smaller than *Arabidopsis*, making WGS a viable method for gene mapping. By sequencing DNA from different members of families segregating for wild type (*DW1*), intermediate (*dw1 EOD*) and extreme (*dw1 eod*) phenotypes, linkage to SNPs will help identify candidate loci.

As *dw1* and *eod* were generated by EMS, a signature can be searched for to identify causative mutations. EMS typically causes point mutations during replication through alkylation of guanine bases, creating a mismatch with thymine rather than cytosine (Leitão, 2012). Therefore, EMS mutants have signature mutations of G to A or C to T. A causative *dw1* SNP is hypothesised to cosegregate both classes of mutant phenotype (intermediate and extreme) and be private to the mutant family (i.e., absent in the parent line used for mutagenesis). Thus, the causative SNP should be homozygous in all mutants, be present in 2/3 wild types, and be absent in the progenitor line used for mutagenesis. The causative mutation would also likely be in a coding region that disrupts protein function. Using these signatures, I will generate a list of candidate SNPs.

Aim of this chapter:

- Identify the causative mutation of *dw1,* a potential tissue tension-compression mutant, to help understand the mechanism of gene action

3.2 Results

3.2.1 Identifying a candidate mutation through whole genome sequencing

To generate data to analyse for candidate SNP identification, 7 mutants and 13 wild type individuals from family D90-2 were selected for WGS. Samples were sent to collaborators at Chinese Academy of Science, Beijing for short-read sequencing using Illumina technology. Sequence data of the mutagenesis progenitor had already been acquired by pooled individual sequences from 72 clonally propagated wild type plants into a single sequence file. Sequence depth was very high (~174x) but this pool captured all sequence variation across individuals. These sequences were concatenated into a single file and included in the analysis. A causal SNP should cosegregate with *dw1* and be absent from the progenitor pool.

Initial analysis of the raw sequence data using fastqc revealed that all individuals were sequenced to at least 37x, with some reliably sequenced to > 50x depth (Table 3.1). Overall, the GC content and predicated duplications were as expected, with anomalies showing higher GC content highlighted in bold. Anomalies included sample D90-2 at the bottom of the table, which I used as the parent to generate the segregating mutant family, and therefore was a known *DW1/dw1* heterozygote. The sequencing anomalies could be attributed to noise or sequencing error. I continued with the analysis with all individuals in the knowledge that data from some samples may be omitted if there were discrepancies further on in the pipeline. The reads were mapped to a Chromium 10x reference assembly created from the progenitor sequence. Mapped SAM files were processed and filtered to removed overlaps and PCR duplicates, and to realign indels using GATK (McKenna *et al.*, 2010). With this pre-processing complete, the data had been checked for quality and could be analysed for candidate SNPs.

Table 3.1 Initial sequence quality screening shows all individuals are sequenced to an average depth of 49x

Performing fastqc analysis on raw sequence data revealed that samples generally had good quality data, with some anomalies with a higher than expected GC content (in bold)

	Plant ID	read	total sequence length	sequence depth	%GC	predicted duplication %
mutant	G1-003	R1	13331405	39.994	39	60.50
		R2	13331405	39.994	39	60.76
	G1-011	R1	13811018	41.433	39	54.08
		R2	13811018	41.433	39	55.15
	G1-012	R1	16095516	48.287	39	51.63
		R2	16095516	48.287	39	52.93
	G1-013	R1	15768964	47.307	40	56.67
		R2	15768964	47.307	40	58.01
	G1-014	R1	15053625	45.161	39	57.72
		R2	15053625	45.161	39	58.97
	G1-016	R1	17907307	53.722	39	58.83
		R2	17907307	53.722	39	60.06
	G1-019	R1	16486653	49.460	39	60.01
		R2	16486653	49.460	39	60.80
wild type	F5-013	R1	15711580	47.135	39	45.46
		R2	15711580	47.135	39	47.02
	F5-014	R1	13060125	39.180	39	52.63
		R2	13060125	39.180	39	53.78
	F5-027	R1	17305976	51.918	39	50.83
		R2	17305976	51.918	39	51.96
	F9-005	R1	15934208	47.803	39	55.41
		R2	15934208	47.803	39	56.71
	G1-004	R1	14220515	42.662	39	57.99
		R2	14220515	42.662	39	59.29
	G1-010	R1	15435027	46.305	39	53.12
		R2	15435027	46.305	39	54.41
	G1-015	R1	16702495	50.107	39	47.66
		R2	16702495	50.107	39	49.09
	G1-017	R1	21365332	64.096	39	53.19
		R2	21365332	64.096	39	54.65
	G1-020	R1	16054810	48.164	39	58.21
		R2	16054810	48.164	39	59.37
	G1-022	R1	14623777	43.871	**42**	66.60
		R2	14623777	43.871	**42**	67.40
	G1-023	R1	18465886	55.398	**42**	57.87
		R2	18465886	55.398	**42**	58.58
	G1-029	R1	14384314	43.153	**41**	58.85
		R2	14384314	43.153	**41**	59.80
	D90-2	R1	22477313	67.432	**51**	60.31
		R2	22477313	67.432	**51**	61.43

3.2.2 Three candidate SNPs were identified

To find candidate SNPs, I ran Haplotype Caller (Poplin *et al.*, 2018) on the processed .BAM files. Haplotype Caller identifies regions in the input sequences which show difference from the reference genome (ActiveRegions), assembles all plausible haplotypes depending on the reads and uses a pairwise alignment of haplotypes to obtain statistical likelihoods to assign a genotype to the locus. Sites can be mutant SNPs which are fixed or segregate across reads, indels, background heterozygosity or noise due to sequencing error. I identified 1,720,947 variable sites and performed initial filtering to remove indels and remove any polyallelic sites. Whilst it is possible that the causative SNP could have been filtered out here, I did this to remove noise. If no candidates were produced, I would then repeat the analysis without filtering.

I identified private SNPs by filtering for sites where the progenitor was homozygous for the reference allele, but which were segregating in the mutant family (at least one homozygote for the mutant allele in wild types, at least one homozygote for the mutant allele in mutants) and for sites that had an EMS signature (C to T or G to A). I generated a list of 831 sites, which in a 100 Mbp genome equates to a mutation rate of around 1 EMS SNP in 100 kbp. This rate is similar to that found in other systems (Till *et al.*, 2003; Stephenson *et al.*, 2010; Yan *et al.*, 2021). The diploid genome of *U. gibba* is around 100 Mbp with 14 chromosomes, therefore each chromosome is roughly 7Mbp long. If we assume 1 chiasma per chromosome, 100 kbp would correspond to about 1/70 cM, or a recombination distance of 1.5% between private SNPs.

A candidate *dw1* SNP should be absent from the progenitor sequence, homozygous in all mutant phenotypes and heterozygous or absent from phenotypically wild type individuals. I filtered the data for these terms and found only 3 candidates (table 3.2) which fulfilled these criteria. All 3 of the SNPs could be causative as they all segregated with the phenotype and each base change had a recognisable EMS signature. Whilst Haplotype Caller typically generated correct genotypes for each variable site, the algorithm sometimes made errors, so I manually checked the reads to genotype each candidate.

On further inspection, one candidate was not private to the mutant family as the progenitor was heterozygous for the mutation. Further mapping of 3 more mutant individuals revealed that one candidate was heterozygous in one of the mutants. These two discrepancies in genotyping suggest that whilst Haplotype Caller correctly identified a site of variation to the genome, it did not successfully genotype the loci for all individuals.

The remaining candidate, 28587:117186, was a C to T mutation that was fixed across 10 mutants, present in 4 out of 13 wild types. A candidate SNP would be expected to segregate across two-thirds of individuals with a wild-type phenotype, which would have been around 8 or 9 out of the 13 individuals sequenced. A pool of 13 wild type individuals may not have been large enough to reveal the expected segregation pattern. The candidate was also not present in the progenitor sequence and was heterozygous in D90-2, the parental heterozygote. Thus, 28587:117186 was a strong candidate for the *dw1* mutation.

Table 3.2 Three candidate SNPs emerged after filtering for privacy and cosegregation.

Applying filtering to a complete list of variable sites revealed that only three SNPs followed the rules of being fixed across mutant individuals, heterozygous or absent in wild type individuals and not found in the progenitor. Genotypes are highlighted in red (homozygous for the reference allele), orange (homozygous for the mutant allele) and light brown (heterozygous).

contig	position	wild type allele	mutant allele	mut01	mut03	mut04	mut05	mut06	mut07	mut08	mut09	mut10	mut11	mut12	wt01	wt02	wt03	wt04	wt05	wt06	wt07	wt08	wt09	wt10	wt11	wt12	wt13	progenitor
				G1-3	G1-11	G1-12	G1-13	G1-14	G1-16	G1-19	D675-5	F5-28	G1-27	G1-42	F5-013	F5-014	F5-027	F9-5	G1-4	G1-10	G1-15	G1-17	G1-20	G1-22	G1-23	G1-29	D90-2	U59-12
26119	2269	G	A	m/m	m/m	m/m	m/m	m/m	m/m	m/m	m/m	m/m	m/m	m/m	+	+	+	+	+	het	het	het	het	het	+	+	het	+
26358	477	C	T	m/m	m/m	m/m	m/m	m/m	m/m	m/m	m/m	m/m	m/m	m/m	het	het	het	+	+	+	het	het	het	het	+	+	+	+
28587	117186	C	T	m/m	m/m	m/m	m/m	m/m	m/m	m/m	m/m	m/m	m/m	m/m	+	+	+	+	+	+	+	het	het	+	het	+	het	+

3.2.3 The candidate SNP causes an early stop codon in the coding region of a brassinosteroid biosynthesis gene

To find out if the candidate SNP, 28587:117186, altered gene function, I looked at its location. Whilst the Chromium 10x assembly was a useful reference, as it was made from the progenitor to the mutagenesis, the assembly was not annotated. I therefore used the published genome to search for sequence around the candidate SNP using BLAST (Lan *et al.*, 2017). This gave me the precise coordinates of the SNP to search in the gene annotation of the published genome. Thus, the SNP at 28587:117186 in the Chromium assembly matched unitig_736:1056726 in the published genome. The SNP located to exon 8 of a predicted gene (figure 3.1A). The gene coordinates gave me the orientation and codon information that allowed me to manually build an annotated gene and transcript. The C to T mutation in the SNP produced an early stop codon in place of a tryptophan at position 416 of the transcript (figure 3.1B and C). This provided further evidence that SNP, 28587:117186, caused the *dw1* mutation.

To identify the function of the altered gene, I performed a BLASTn search with the open reading frame against the *Arabidopsis thaliana* genome. The best hit was against *AtDWARF4*, a gene which encodes a cytochrome P450 90B1 enzyme which catalyses the C22-alpha-hydroxylation step in the brassinosteroid biosynthesis pathway. Brassinosteroid (BR) is a growth promoting hormone and BR biosynthesis mutants in other systems are dwarf plants that show reduced cell elongation (Azpiroz *et al.*, 1998; Choe *et al.*, 1998; Clouse & Sasse, 1998). These phenotypes were consistent with the mutant phenotype in *U. gibba*, providing further evidence that the candidate SNP caused *dw1*.

A Scf00452.g17901

seqname	source	feature	start	end	score	strand	frame	attribute
unitig_736	AUGUSTUS	gene	1054537	1056987	0.25	+	.	ID=unitig_736.g22542
unitig_736	AUGUSTUS	transcript	1054537	1056987	0.25	+	.	ID=unitig_736.g22542.t1;Parent=unitig_736.g22542
unitig_736	AUGUSTUS	start_codon	1054537	1054539	.	+	0	Parent=unitig_736.g22542.t1
unitig_736	AUGUSTUS	intron	1054731	1054837	0.25	+	.	Parent=unitig_736.g22542.t1
unitig_736	AUGUSTUS	intron	1055163	1055239	1	+	.	Parent=unitig_736.g22542.t1
unitig_736	AUGUSTUS	intron	1055393	1055458	1	+	.	Parent=unitig_736.g22542.t1
unitig_736	AUGUSTUS	intron	1055708	1055791	1	+	.	Parent=unitig_736.g22542.t1
unitig_736	AUGUSTUS	intron	1055876	1055963	1	+	.	Parent=unitig_736.g22542.t1
unitig_736	AUGUSTUS	intron	1056043	1056117	1	+	.	Parent=unitig_736.g22542.t1
unitig_736	AUGUSTUS	intron	1056225	1056669	1	+	.	Parent=unitig_736.g22542.t1
unitig_736	AUGUSTUS	CDS	1054537	1054730	0.26	+	0	ID=unitig_736.g22542.t1.cds;Parent=unitig_736.g22542.t1
unitig_736	AUGUSTUS	CDS	1054838	1055162	0.96	+	1	ID=unitig_736.g22542.t1.cds;Parent=unitig_736.g22542.t1
unitig_736	AUGUSTUS	CDS	1055240	1055392	1	+	0	ID=unitig_736.g22542.t1.cds;Parent=unitig_736.g22542.t1
unitig_736	AUGUSTUS	CDS	1055459	1055707	1	+	0	ID=unitig_736.g22542.t1.cds;Parent=unitig_736.g22542.t1
unitig_736	AUGUSTUS	CDS	1055792	1055875	1	+	0	ID=unitig_736.g22542.t1.cds;Parent=unitig_736.g22542.t1
unitig_736	AUGUSTUS	CDS	1055964	1056042	1	+	0	ID=unitig_736.g22542.t1.cds;Parent=unitig_736.g22542.t1
unitig_736	AUGUSTUS	CDS	1056118	1056224	1	+	2	ID=unitig_736.g22542.t1.cds;Parent=unitig_736.g22542.t1
unitig_736	**AUGUSTUS**	**CDS**	**1056670**	**1056987**	**1**	**+**	**0**	**ID=unitig_736.g22542.t1.cds;Parent=unitig_736.g22542.t1**
unitig_736	AUGUSTUS	stop_codon	1056985	1056987	.	+	0	Parent=unitig_736.g22542.t1

B

C

Figure 3.1 Predicted gene annotation in published genome reveals candidate SNP causes an early stop codon in a coding region of *DW1*

A) BLAST using sequence around the candidate SNP to the published genome enabled locating it in a coding region (in bold)

B) Extracted sequence data was annotated to pinpoint the candidate SNP to exon8 of the gene of interest. The mutation replaced a cytosine with a thymine (yellow point)

C) Translating the sequence with the mutation revealed the base change caused an early stop codon to be introduced

3.2.4 Further genotyping with KASPAR confirms the candidate SNP is linked to mutant phenotype

I had identified a strong candidate SNP, 28587:117186, based on a family comprising 10 mutants and 13 phenotypically wild-type individuals. To provide more evidence that this SNP was causative, I used the KASPAR method (Smith & Maughan, 2015) to genotype 4 more mutants and 20 more wild types. Here, genotype-specific primers with fluorophore-labelled oligos were designed to bind to either allele. The sample DNA underwent a competitive allele-specific PCR run using these primers. The signal was then read by a FRET-capable reader by exciting at one wavelength and reading the omitted one (see methods). When excited, the sample emitted signal at one wavelength for wild type homozygous samples, the other wavelength for mutant homozygous samples or both wavelengths for heterozygotes. These signals are process by the reader and quantifies into relative fluorescence units (RFU). I also genotyped the previously sequenced individuals as a control. I found that all individuals with the mutant phenotype were homozygous for the mutation, and that the wild types were either heterozygous or lacked the mutant allele (figure 3.2). This analysis supports the sequence analysis and gives greater genetic confidence that the SNP is causal.

I was also able to narrow down the genetic region around the candidate SNP. The concordance between SNP genotype and phenotype across at total of 48 individuals, of which 15 were *dw1* mutant, showed the SNP was within a few cM of *dw1*. Genotyping more mutants would further narrow down the genetic region linked to the phenotype. The next identifiable private SNP (28587:617107) linked to the candidate SNP was around 500 kbp away and was heterozygous in 2 of the 15 *dw1* mutants, consistent with a map distance of about 10 cM.

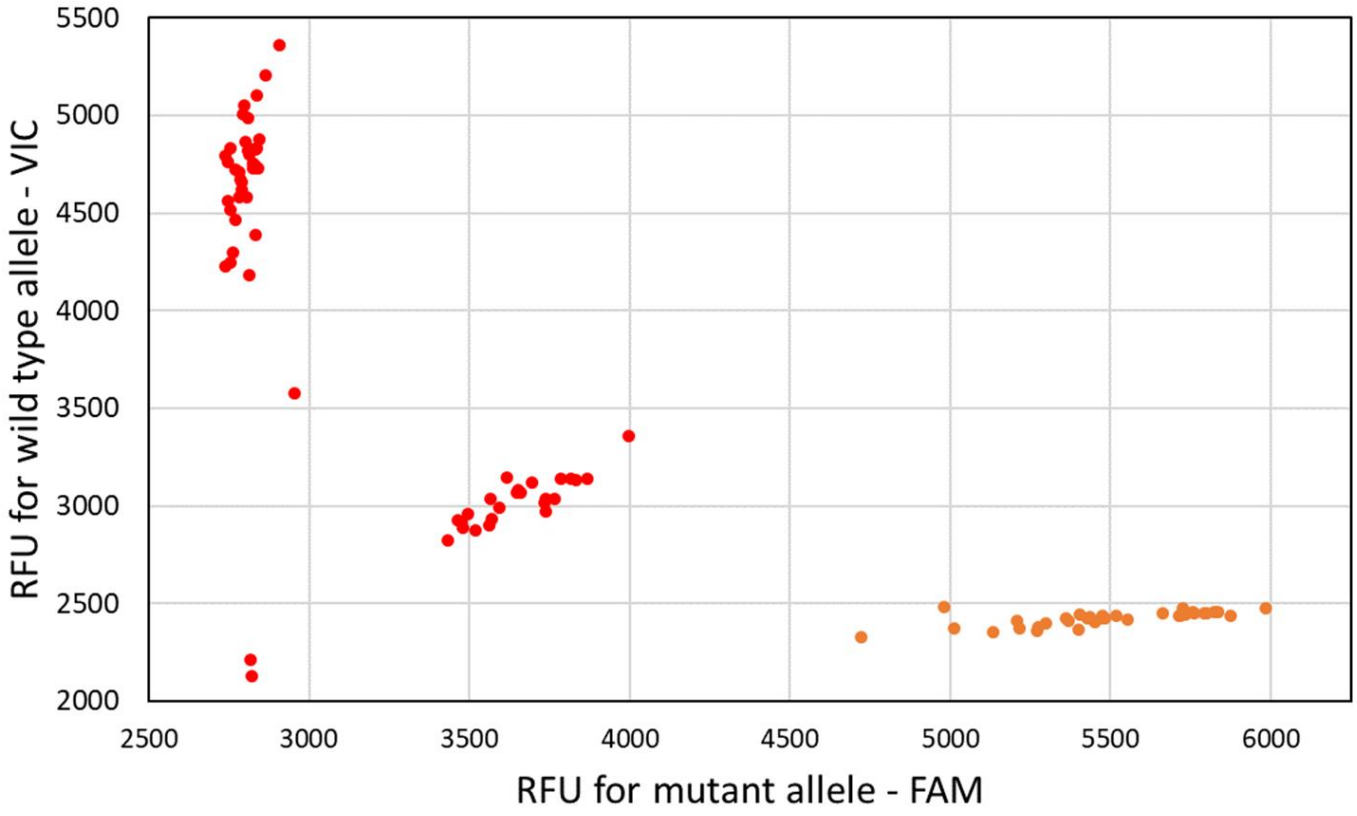

Figure 3.2 KASPAR genotyping shows all mutant individuals are homozygous for the candidate mutation

Sequenced and unsequenced individuals were genotyped for either the wild type (C – VIC probe) or mutant (T – FAM probe) allele. Red points indicated a wild-type phenotype and orange points are mutant phenotypes. Clustering of samples close to the y-axis indicate individuals are homozygous for the wild type allele, clustering close to the x-axis indicate individuals are homozygous for the mutant allele and in between are heterozygotes

3.2.5 Mass Spectrometry reveals BR precursors downstream of C22-alpha-hydroxylation in the brassinosteroid pathway are absent in mutants

Thus far I have provided evidence that SNP 28587:117186 causes the *dw1* mutation and introduces an early stop codon in the coding region of a candidate gene likely encoding an enzyme involved in BR biosynthesis. To provide evidence that *dw1* is a BR mutant, I analysed the metabolite profile of compounds in the BR biosynthesis pathway using Mass Spectrometry (MS). This work was done in collaboration with Paul Brett and Baldeep Kular at JIC, along with members of the phytohormone platform at CAS, Beijing. The enzyme encoded by the *DW1* candidate, a C22-alpha-hydroxylase, converts campestanol to 6-deoxocathasterone and 6-oxocampestanol to cathasterone (figure 3.3A). To test if *dw1* caused a block of BR biosynthesis after this point in the pathway, we assayed one compound upstream and 5 compounds downstream of *DW1*. Campesterol is upstream of C22-alpha-hydroxylase action and was present in both wild type and *dw1* mutants. Two of the compounds, 6-deoxocastasterone and castasterone, which are downstream of C22-alpha-hydroxylase action were present in wild type and not in *dw1* mutants (figure 3.3B). Two of the downstream compounds, teasterone and brassinolide (the most bioactive form of BR) were challenging to detect using GC/MS and none was found in wild type or *dw1*. Small amounts of the downstream compound typhasterol were detected in both wild type and *dw1* mutants but it is unclear whether these low quantities represent noise or low levels of metabolite. Taken together, these findings support the hypothesis that *DW1* encodes a C22-alpha-hydroxylase, known as *DWARF4* in *Arabidopsis.*

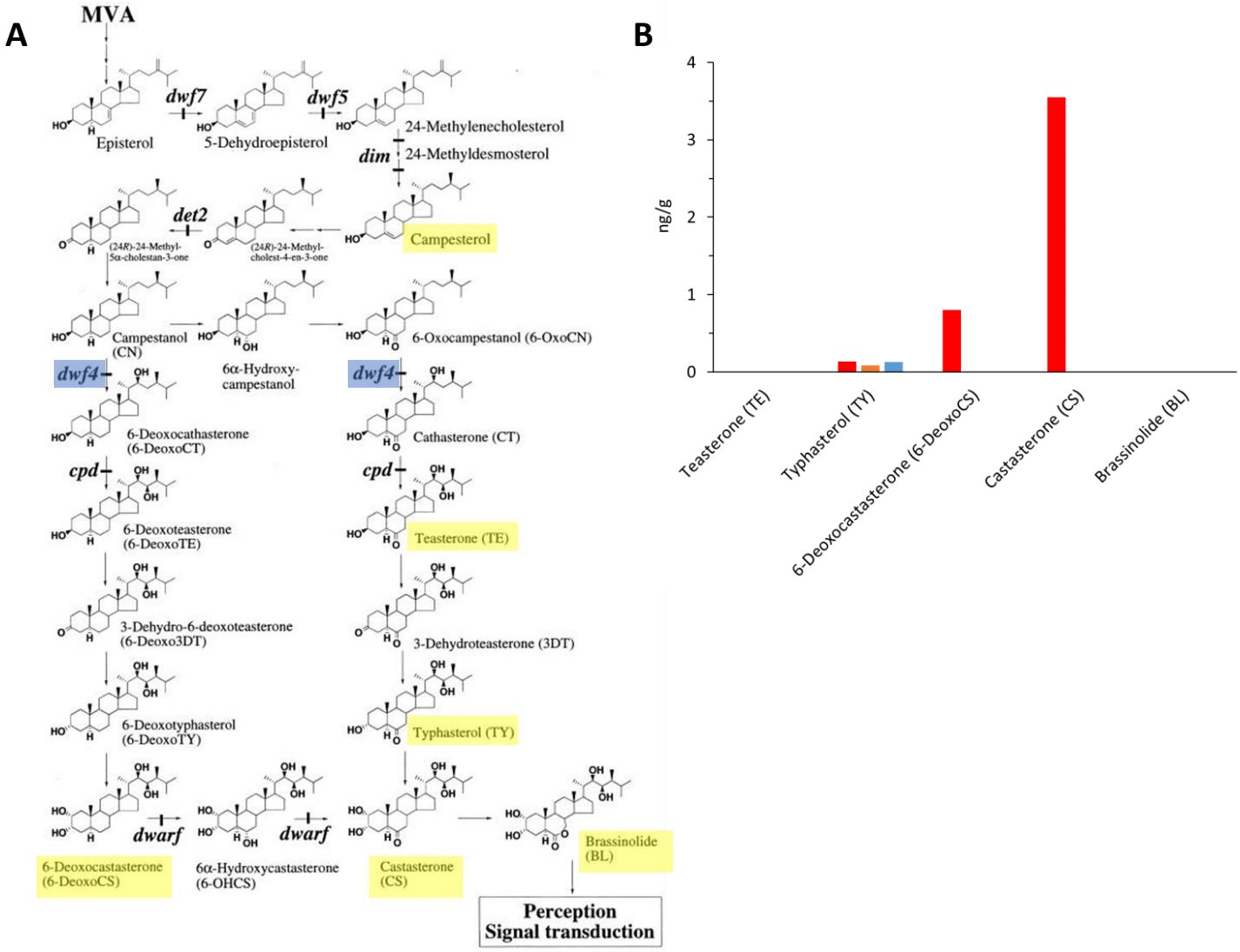

Figure 3.3 Mass Spectrometry reveals that compounds in the BR biosynthesis pathway downstream of *DW1* are not present in the mutants

A) An overview of the *Arabidopsis* brassinosteroid biosynthesis pathway (taken from Shimada *et al.*, 2001). Highlighted in blue are the points of catalysation of *AtDWF4*. In yellow are the compounds identifiable with mass spectrometry.

B) Quantification of yellow highlighted compounds in A. Red bars are wild type, orange are *dw1 EOD* and blue are *dw1 eod*. The biosynthesis pathway acts on compounds from left to right on the x-axis.

3.2.6 Candidates for *EOD*

As a candidate for *DW1* had been found, it would have been interesting to identify candidates for *EOD.* The hypothesis is that *EOD* is a recessive enhancer that was introduced by EMS and thus not found in the progenitor sequence. It may be possible that *EOD* is a dominant suppressor, so that the intermediate phenotype was a result of a double mutation, and the extreme mutant phenotype was due to a single mutation. However, the segregation of around 3:1 wild types to dwarf mutants, of which around a quarter are extreme suggests that *EOD* could be a recessive enhancer that exacerbates the phenotype of *dw1.* Therefore, I filtered SNPs with the following criteria: SNPs which were homozygous for the mutant allele in extreme phenotypes, SNPs which were not homozygous in *dw1 EOD* mutants or progenitor sequence, segregated in wild type and had an EMS signature, i.e., a C to T or a G to A. Using these filtering rules, I generated a list of 6 candidate SNPs. Of these, two SNPs were not found in coding regions of genes annotated in the published reference genome. Whilst these were not fully discarded, I selected the 4 other candidates to BLAST against the Viridiplantae to identify potential genes (table 3.3). SNP 78:10266 was in a *PUP3*-like gene, involved in cytokinin transport in the phloem and cytokinin retrieval in hydathodes in *Arabidopsis* (Gillissen *et al.*, 2000; Bürkle *et al.*, 2003). SNP 28603:684091 was in *DRP1E,* a gene associated with microtubules during cytokinesis (Hong, Bednarek*, et al.*, 2003; Kang *et al.*, 2003). SNP 28566:47991 was in an unidentified mRNA transcript and SNP 28615:2102460 was in a zinc-finger protein. As these last two genes did not have clearly defined roles, they were not able to be ruled out as candidates for *EOD*. Further work will involve generating more mutants and identifying the effect that these SNPs might on the ammino acid sequence of the transcript.

Table 3.3 Potential candidates for *EOD*

4 candidate SNPs were found to be fixed for the mutant allele in extreme mutants, not homozygous for the mutant allele in intermediate mutants or the progenitor, segregated across wild types and had an EMS signature

Coordinates in Chromium genome	Coordinates in PacBio genome	In CDS?	BLAST results
28566:47991	unitig_46:2492174	Yes	Unidentified mRNA
28615:2102460	unitig_0:3069816	Yes	Cysteine-tryptophan domain-containing zinc finger protein 3 (CWZF3)
78:10266	unitig_8:2737781	Yes	purine permase 3-like (PUP3-like - cytokinin transport)
28603:684091	unitig_5:2804	Yes	Dynamin-related protein 1E (DRP1E – microtubule related)

3.2.7 BR treatments rescues the *dw1* mutant phenotype

To further confirm that *dw1* is caused by loss of BR, I grew mutants in the presence of epibrassinolide (epiBL) which is a type of brassinosteroid used in plant tissue culture. I passaged treated material every week to ensure that the epiBL had not degraded in the media. All analysed tissue had been passaged in this way for more than 4 weeks, ensuring that it had been exposed to epiBL from meristem initiation to maturity.

I treated *dw1* with a range of concentrations of epiBL and imaged them after 3 and 7 days to perform a preliminary visual analysis (figure 3.4). I found that low concentrations of epiBL (0.005 µM, figure 3.4 B) had an effect on internode and leaf length and high concentrations (0.1 µM, figure 3.4 F) did not rescue the phenotype but causes aberrant growth in developing tissue. Based on this analysis, I selected a concentration of 0.01 µM epiBL (figure 3.4 C) to use to rescue the dwarf phenotype in *dw1*

(figure 3.4). This concentration is Treating with 0.01 µM epiBL partially rescued the *dw1 eod* (figure 3.5). The lack of complete rescue suggests that *eod* can have a phenotype effect even when brassinosteroid is exogenously restored.

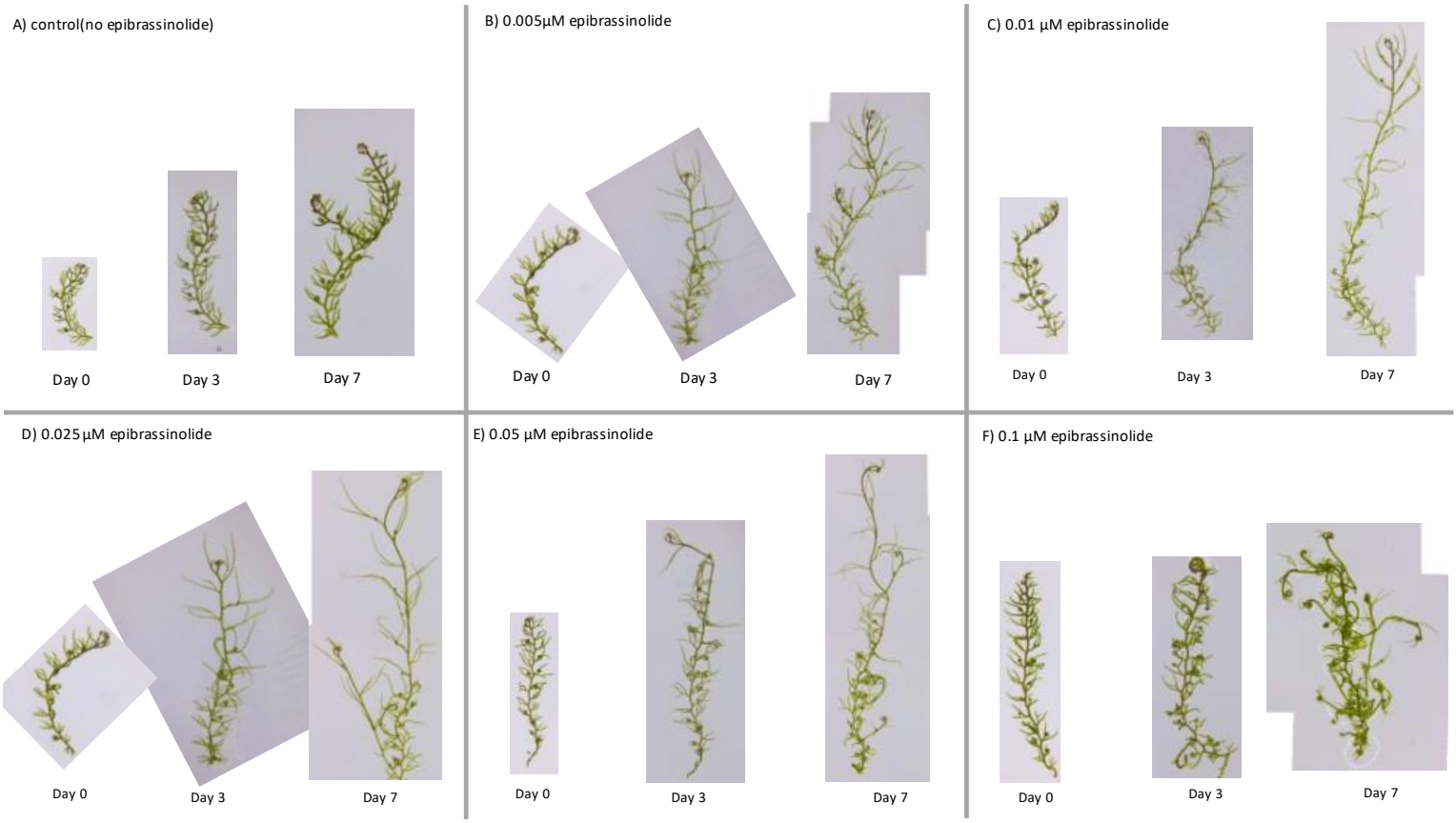

Figure 3.4 Effect of different concentrations of epibrassinolide on *dw1 EOD*

Stolon sections of *dw1* were treated with a range of concentrations of epiBL for 7 days then imaged. Images are not to scale.

To quantify the effect of epiBL on the mutants, I measured organ lengths and widths and compared them to wild types in figure 2.13. For *dw1 EOD*, treatment with epiBL increased leaf length around 3 times that of untreated *dw1 EOD* ($\bar{x}$ = 5.61 mm, *SD* = 0.04, *SEM* = 0.18 for *dw1 EOD* + 0.01 µM epiBL, compared to $\bar{x}$ = 1.99 mm, *SD* = 0.38 , *SEM* = 0.06 for the untreated *dw1 EOD*) and increased internode length around 3 times that of untreated *dw1 EOD* as well ($\bar{x}$ = 3.11 mm, *SD* = 0.59, *SEM* = 0.30, compared to $\bar{x}$ = 0.91 mm *SD* = 0.28 , *SEM* = 0.04 for the untreated *dw1 EOD*). These values of treated *dw1 EOD* were not significantly different ($p < 0.05$) from wild type leaf length ($\bar{x}$ = 7.96 mm, *SD* = 1.96, *SEM* = 0.20) and internode length ($\bar{x}$ = 2.59 mm, *SD* = 0.71, *SEM* = 0.56) (figure 3.6A), suggesting a rescue of the *dw1 EOD* phenotype.

For *dw1 eod*, treatment with epiBL increased leaf length to around 3 times the length of untreated *dw1 eod* ($\bar{x}$ = 1.71, *SD* = 0.30 , *SEM* = 0.07 for *dw1 eod* + 0.01 µM epiBL, compared to $\bar{x}$ = 0.54 mm, *SD* = 0.14 , *SEM* = 0.03 for untreated *dw1 eod*) and increased internode length to around 4 times the length of untreated *dw1 eod* ($\bar{x}$ = 1.57, *SD* = 0.54, *SEM* = 0.13 for *dw1 eod* + 0.01 µM epiBL, compared to $\bar{x}$ = 0.42 mm, *SD* = 0.12, *SEM* = 0.04). These values were significantly above the untreated control but significantly below wild type.

Internode width for *dw1 EOD* was increased by epiBL ($\bar{x}$ = 0.14, *SD* = 0.03, *SEM* = 0.01, compared to $\bar{x}$ = 0.18 mm *SD* = 0.04, *SEM* = 0.004 for untreated *dw1 EOD*), whereas leaf width was reduced ($\bar{x}$ = 0.08, *SD* = 0.01, *SEM* = 0.005, compared to $\bar{x}$ = 0.19, *SD* = 0.03, *SEM* = 0.01 for untreated *dw1 EOD*). Similarly, internode width of *dw1 eod* was increased by epiBL ($\bar{x}$ = 0.29, *SD* = 0.04, *SEM* = 0.01, compared to $\bar{x}$ = 0.20 mm, *SD* = 0.05, *SEM* = 0.02 for untreated *dw1 eod*) and leaf width reduced ($\bar{x}$ = 0.19, *SD* = 0.03, *SEM* = 0.07, compared to $\bar{x}$ = 0.17 mm *SD* = 0.07, *SEM* = 0.01 for untreated *dw1 eod*), although the latter was not statistically significant (figure 3.6B). Treating either mutant with epiBL significantly increases width compared to wild type internodes than wild type ($\bar{x}$ = 0.16 mm, *SD* = 0.03, *SEM* = 0.01) and leaves ($\bar{x}$ = 0.17 mm *SD* = 0.07, *SEM* = 0.01). The ratio of length to width increased in the treated

mutants (figure 3.6C). This data shows that treating *dw1 EOD* with epiBL rescues organ length but causes a slight decrease in leaf width and an increase in internode width.

Figure 3.5 Growing mutants in 0.01 µm epiBL rescues *dw1 EOD*

Light microscope images of A) wild type, B) *dw1 EOD*, C) *dw1 EOD* + 0.01 µM epibrassinolide, D) *dw1 eod* and E) *dw1 eod* + 0.01 µM epibrassinolide. Scale bar is 1 mm

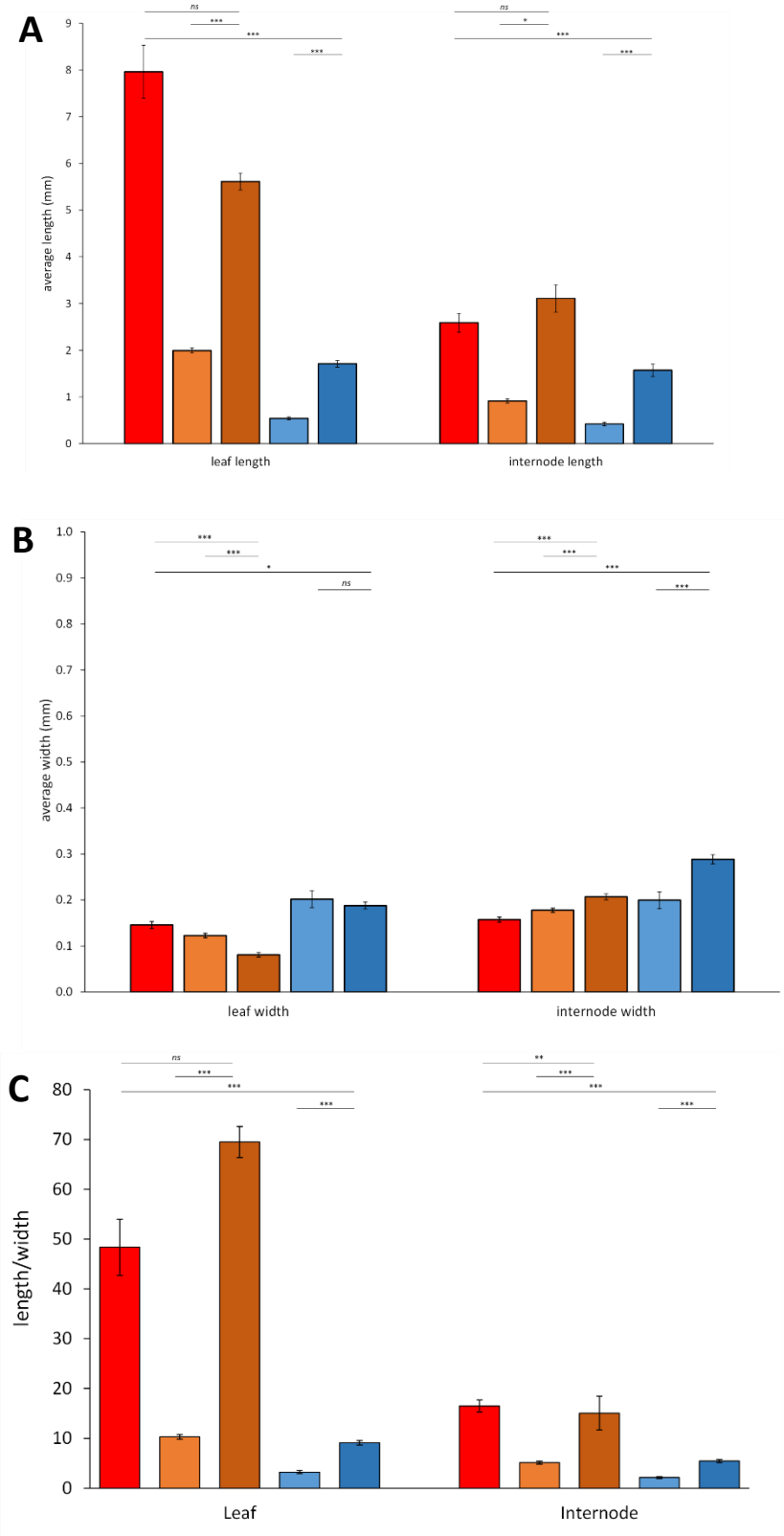

Figure 3.6 Treating with BR increases mutant leaf and internode elongation

A) Average leaf and internode length measurements of wild type (red), *dw1 EOD* (orange), *dw1 EOD* + 0.01 µM epibrassinolide (dark orange), *dw1 eod* (blue) and *dw1 eod* + 0.01 µM epibrassinolide (dark blue) mutants. Leaf length *t* tests: *dw1 EOD* + epiBL to *dw1 EOD* *p* = 8.472E-05 (***), *dw1 EOD* + epiBL to wild type *p* = 0.192436852 (ns), *dw1 eod* + epiBL to *dw1 eod* *p* = 1.66077E-12 (***), *dw1 eod* + epiBL to wild type 1.18409E-07 (***). Internode length *t* tests: *dw1 EOD* + epiBL to *dw1 EOD* *p* = 0.00115442 (*), *dw1 EOD* + epiBL to wild type *p* = 0.060072209 (*ns*), *dw1 eod* + epiBL to *dw1 eod* *p* = 2.38054E-07 (***), *dw1 eod* + epiBL to wild type *p* = 0.000474402 (***)

B) Average leaf and internode width measurements. Leaf width *t* tests: *dw1 EOD* + epiBL to *dw1 EOD* *p* = 2.56492E-05 (***), *dw1 EOD* + epiBL to wild type *p* = 4.15874E-06 (***), *dw1 eod* + epiBL to *dw1 eod* *p* = 0.102237167 (ns), extreme + epiBL to wild type *p* = 0.025869145 (*). Internode width *t* tests: *dw1 EOD* + epiBL to *dw1 EOD* *p* = 4.36896E-11 (***), *dw1 EOD* + epiBL to wild type *p* = 1.92372E-18 (***), *dw1 eod* + epiBL to *dw1 eod* *p* = 3.85346E-09 (***), *dw1 eod* + epiBL to wild type *p* = 1.05869E-22 (***)

C) Ratios of average leaf length to width and average internode length to width measurements. Leaf ratio *t* tests: *dw1 EOD* + epiBL to *dw1 EOD* *p* = 1.33747E-07 (***), *dw1 EOD* + epiBL to wild type *p* = 0.101543637 (ns), extreme + epiBL to *dw1 eod* *p* = 0.000180796 (***), *dw1 eod* + epiBL to wild type *p* = 1.75739E-06 (***). Internode ratio *t* tests: *dw1 EOD* + epiBL to *dw1 EOD* *p* = 0.000338759 (***), *dw1 EOD* + epiBL to wild type *p* = 0.001748004 (**), *dw1 eod* + epiBL to *dw1 eod* *p* = 2.79978E-06 (***), *dw1 eod* + epiBL to wild type *p* = 0.000147598 (***)

Error bars show SEM. Wild type: 3 individuals, stolons n= 12. *dw1 EOD*: 10 individuals, stolons n = 40. *dw1 EOD* + epiBL: 4 individuals, stolons n = 33. *dw1 eod*: 4 individuals, stolons n = 16. *dw1 eod* + epiBL: 5 individuals, stolons n = 15

To quantify the effect of epiBL on the epidermal cells, 2.5 D surface segmentation of the epidermis was performed in collaboration with Karen Lee. Heat maps of epidermal cell size showed that the treated mutants had larger cells than untreated (figure 3.7). Quantification of these changes showed that average cell area (figure 3.8A) were around three times larger in treated *dw1 EOD* compared to untreated ($\bar{x}$ = 869.00 µm^2, *SEM* = 26.57 for *dw1 EOD* + 0.01 µM epiBL, compared to $\bar{x}$ = 292.86 µm^2, *SEM* = 4.78 for untreated *dw1 EOD*); and around 2.5 times larger in the treated *dw1 eod* compared to untreated ($\bar{x}$ = 996.97 µm^2, *SEM* = 29.86 for *dw1 eod* + 0.01 µM epiBL, compared to $\bar{x}$ = 416.37µm^2, *SEM* = 9.46 for untreated *dw1 eod*). These increases in cell area are similar to wild type average cell area ($\bar{x}$ = 845.74 µm^2, *SEM* = 24.07), but there is a statistically significant difference.

Cell length parallel to the stolon (figure 3.8B) was significantly increased ($p < 0.001$), around 3 times in treated *dw1 EOD* compared to untreated ($\bar{x}$ = 32.26 µm, *SEM* = 0.92 for *dw1 EOD* + 0.01 µM epiBL, compared to $\bar{x}$ = 13.17 µm, *SEM* = 0.15 for untreated *dw1 EOD*); and around 3 times in treated *dw1 eod* compared to untreated ($\bar{x}$ = 43.45 µm, *SEM* = 1.21 for *dw1 eod* + 0.01 µM epiBL, compared to $\bar{x}$ = 16.11 µm, *SEM* = 0.30 for untreated *dw1 eod*). These increases in cell area are similar to wild type average cell length parallel to the stolon ($\bar{x}$ = 41.69 µm, *SEM* = 0.98), but there is a statistically significant difference.

Cell length perpendicular to the stolon (figure 3.8B) was slightly increased by treated with epiBL for *dw1 EOD* compared to untreated ($\bar{x}$ = 17.34 µm, *SEM* = 0.412 for *dw1 EOD* + 0.01 µM epiBL, compared to $\bar{x}$ = 17.08 µm, *SEM* = 0.23 for untreated *dw1 EOD*); and for *dw1 eod* compared to untreated ($\bar{x}$ = 19.78 µm, *SEM* = 0.40 for *dw1 EOD* + 0.01 µM epiBL, compared to $\bar{x}$ = 16.8 µm, *SEM* = 0.34 for untreated *dw1 EOD*). These values are similar to wild type ($\bar{x}$ = 18.66 µm, *SEM* = 0.33), but there is a statistically significant difference. Thus, treating with epiBL partially rescues mutant epidermal cell size of *dw1* by increasing cell length preferentially in the direction of the stolon, but the effect of *eod* further increases cell area and size past wild type.

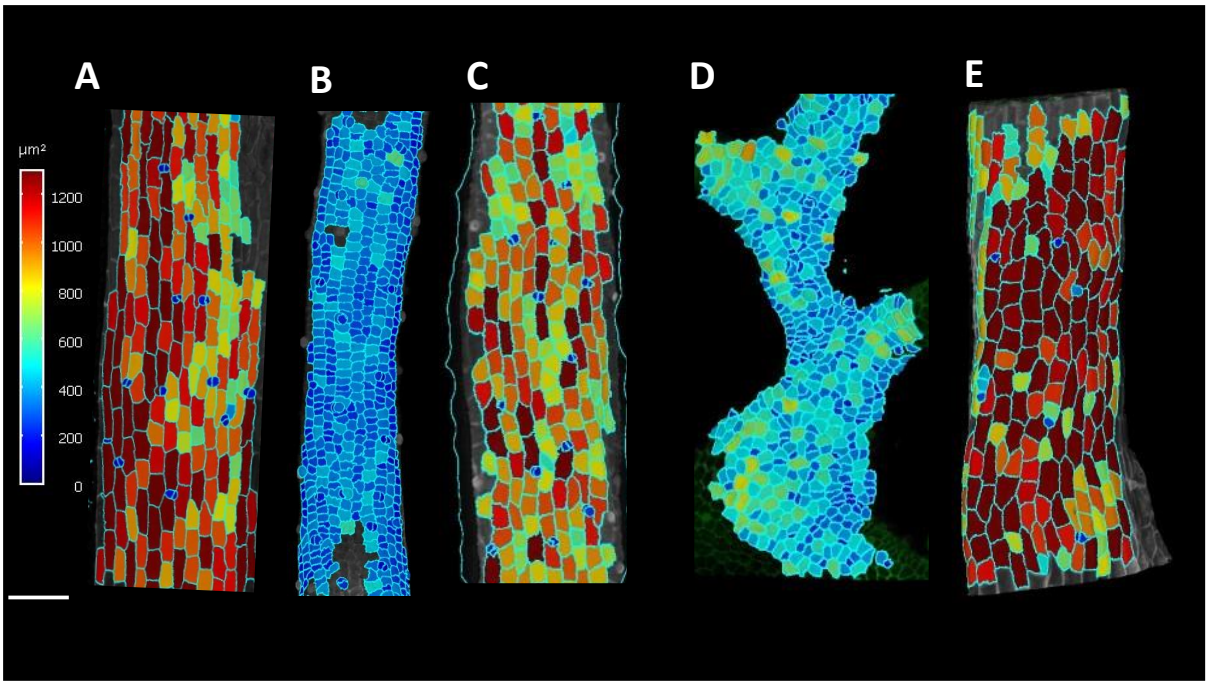

Figure 3.7 Epidermal cells are larger in the presence of BR

A heat map of cell area produced by MorphoGraphX reveals that for both the *dw1 EOD* and *dw1 eod* mutants treated with BR, cell area in the epidermis is greater than mutants without treatment.

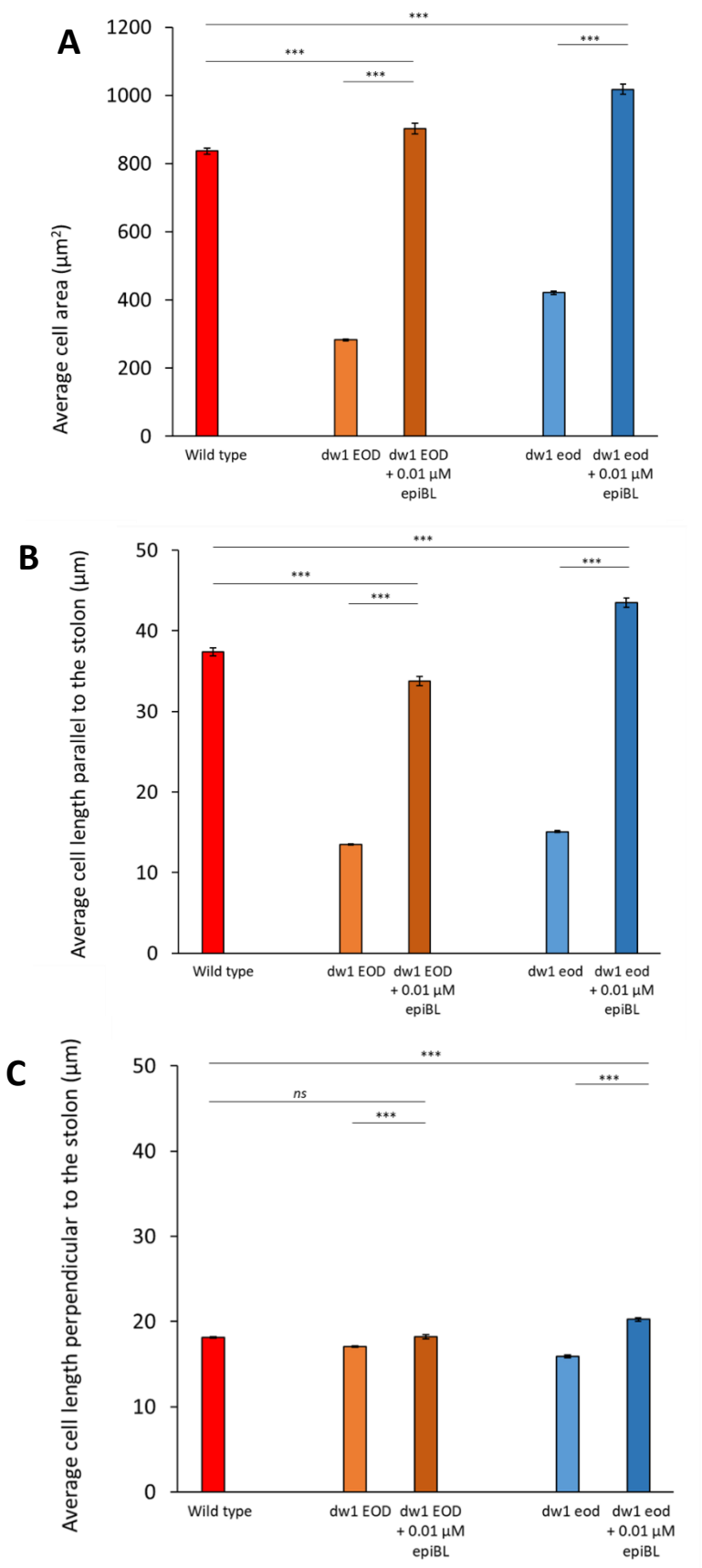

Figure 3.8 2.5D segmentation reveals treatment with BR increases cell area and length parallel to the stolon

A) Average cell area of epidermal cells from mature internodes. *t* tests: *dw1 EOD* to *dw1 EOD* + 0.01 µM epiBL *p* = 1.0644E-184 (***), wild type to *dw1 EOD* + 0.01 µM epiBL *p* = 0.000243997 (***), *dw1 eod* to *dw1 eod* + 0.01 µM epiBL *p* = 2.63E-172 (***), wild type to *dw1 eod* + 0.01 µM epiBL *p* = 1.00714E-23 (***).

B) Average cell length parallel to the stolon. Orientation is determined by a manually placed Bezier line. *t* tests: *dw1 EOD* to *dw1 EOD* + 0.01 µM epiBL *p* = 1.6998E-163 (***), wild type to *dw1 EOD* + 0.01 µM epiBL *p* = 7.34986E-07 (***), *dw1 eod* to *dw1 eod* + 0.01 µM epiBL *p* = 1.9259E-213 (***), wild type to *dw1 eod* + 0.01 µM epiBL *p* = 1.95908E-15 (***).

C) Average cell length perpendicular to the stolon. Orientation is determined by a manually placed Bezier line. *t* tests: *dw1 EOD* to *dw1 EOD* + 0.01 µM epiBL *p* = 2.25188E-05 (***), wild type to *dw1 EOD* + 0.01 µM epiBL *p* = 0.840412962 (ns), *dw1 eod* to *dw1 eod* + 0.01 µM epiBL *p* = 3.6901E-53 (***), wild type to *dw1 eod* + 0.01 µM epiBL *p* = 2.33335E-17 (***)

Wild type stolons n = 8, cells n = 1817 *dw1 EOD* stolons n = 5, cells n = 2289. *dw1 EOD* + 0.01 µM epiBL stolons n = 3, cells n = 721. *dw1 eod* stolons n = 4, cells n = 1494. *dw1 eod* + 0.01 µM epiBL stolons n = 4, cells n = 618. *dw1 EOD*

To characterise the effect of BR on the vasculature of the mutants, I imaged the internal tissue using confocal microscopy. After epiBL treatment, the wiggly vasculature of *dw1 EOD* was restored to a straight vasculature found in wild type (figure 3.9A). This restoration of vasculature phenotype was reflected in the ratio of vasculature length to epidermal length (figure 3.9B) in the treated *dw1 EOD* ($\bar{x}$ = 0.999, *SEM* = 0.001), which was not significantly different ($p > 0.05$) from wild type ($\bar{x}$ = 0.981, *SEM* = 0.012). By contrast there was a significant difference ($p < 0.05$) between the treated and the untreated *dw1 EOD* mutant ($\bar{x}$ = 1.127, *SEM* = 0.045). The ratio of vascular to epidermal length in the untreated ($\bar{x}$ = 1.020, *SEM* = 0.014) and treated *dw1 eod* ($\bar{x}$ = 0.998, *SEM* = 0.005) were not statistically different. These results suggest that epiBL restores straight vasculature to *dw1 EOD*.

A

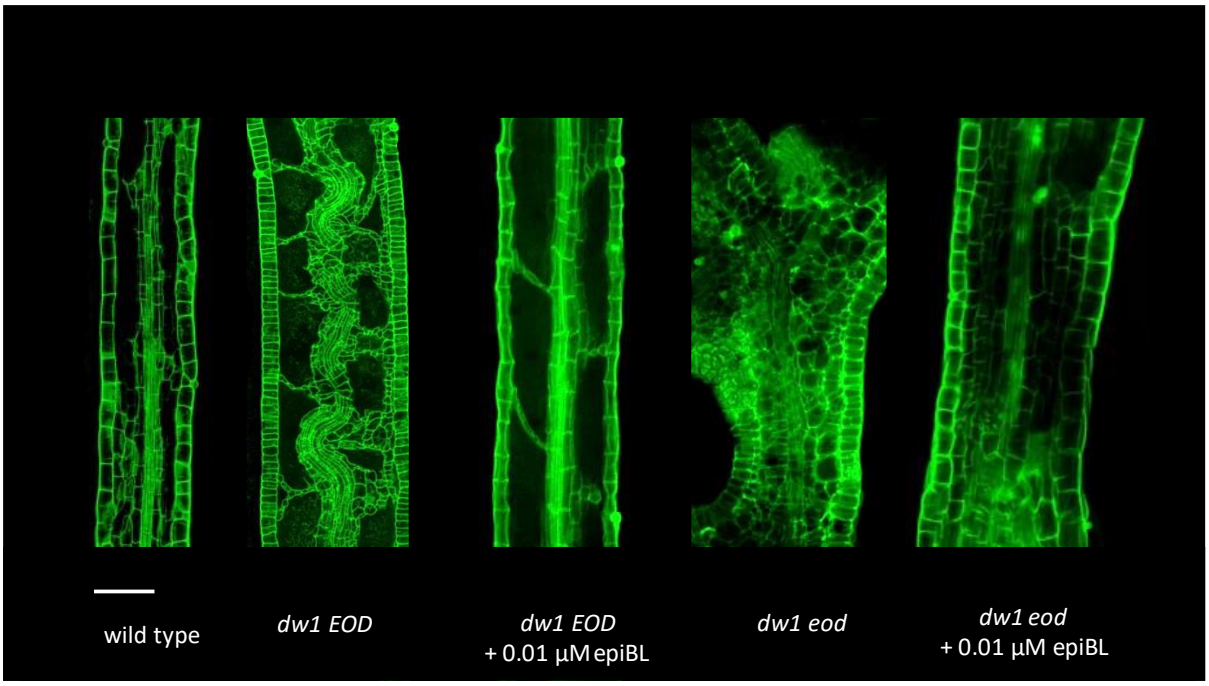

B

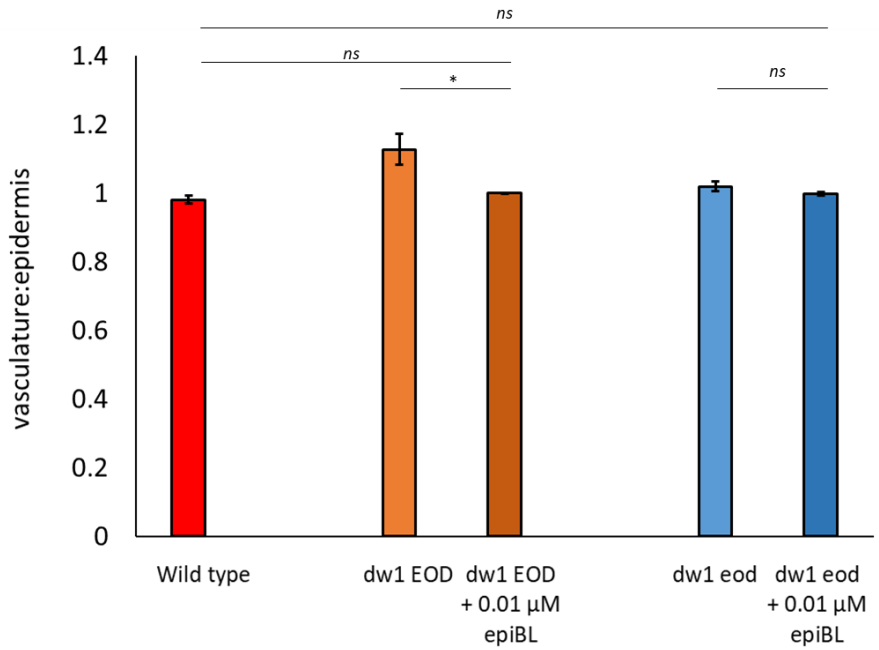

Figure 3.9 Mutant internal tissue phenotypes are rescued with BR

A) Mature stolons of *dw1 EOD* treated with epibrassinolide have straight vasculature, as does *dw1 eod*. Scale bar is 100 µm

B) Wild type n = 6, *dw1 EOD* mutant n = 5, *dw1 EOD* + 0.01 µM epiBL n = 6, *dw1 eod* n = 7, *dw1 eod* + 0.01 µM epiBL n = 3. *t* tests: *dw1 EOD* to *dw1 EOD* + 0.01 µM epiBL 0.04824372 ($p < 0.05$, *), wild type to *dw1 EOD* + 0.01 µM epiBL - 0.17647526 ($p > 0.05$, *ns*), *dw1 eod* to *dw1 eod* + 0.01 µM epiBL - 0.182594489 ($p > 0.05$, *ns*), wild type to *dw1 eod* + 0.01 µM epiBL - 0.241702508 ($p > 0.05$, *ns*)

3.2.8 RNA *in situ* hybridisation suggests that *DW1* localises to the epidermal layer

To determine the site of action of *DW1* in wild type *U. gibba*, I performed RNA *in situ* hybridisation. I performed this in collaboration with Beatriz Goncalves who had optimised the protocol in *U. gibba* (see Materials and Methods in (Whitewoods *et al.*, 2020)). As this method had been optimised for analysis of traps, it required tissue be in a ball when embedded in wax. Therefore, it was not easy to identify the precise origin of tissue from each section but could be clearly inferred from looking at a series of sections. We imaged section which had clear signal (figure 3.10). In these sections of leaves and stolons, signal is weak but appears to be localised more to the epidermal layer than inner tissues. This suggests that *DW1* is expressed in the epidermal layer. To confirm the localisation of this weak signal, a control staining either without the *DW1* antibody or a sense control could be perform to ensure that the signal shown in figure 3.10 is related to the gene and not an artifact of the experiment.

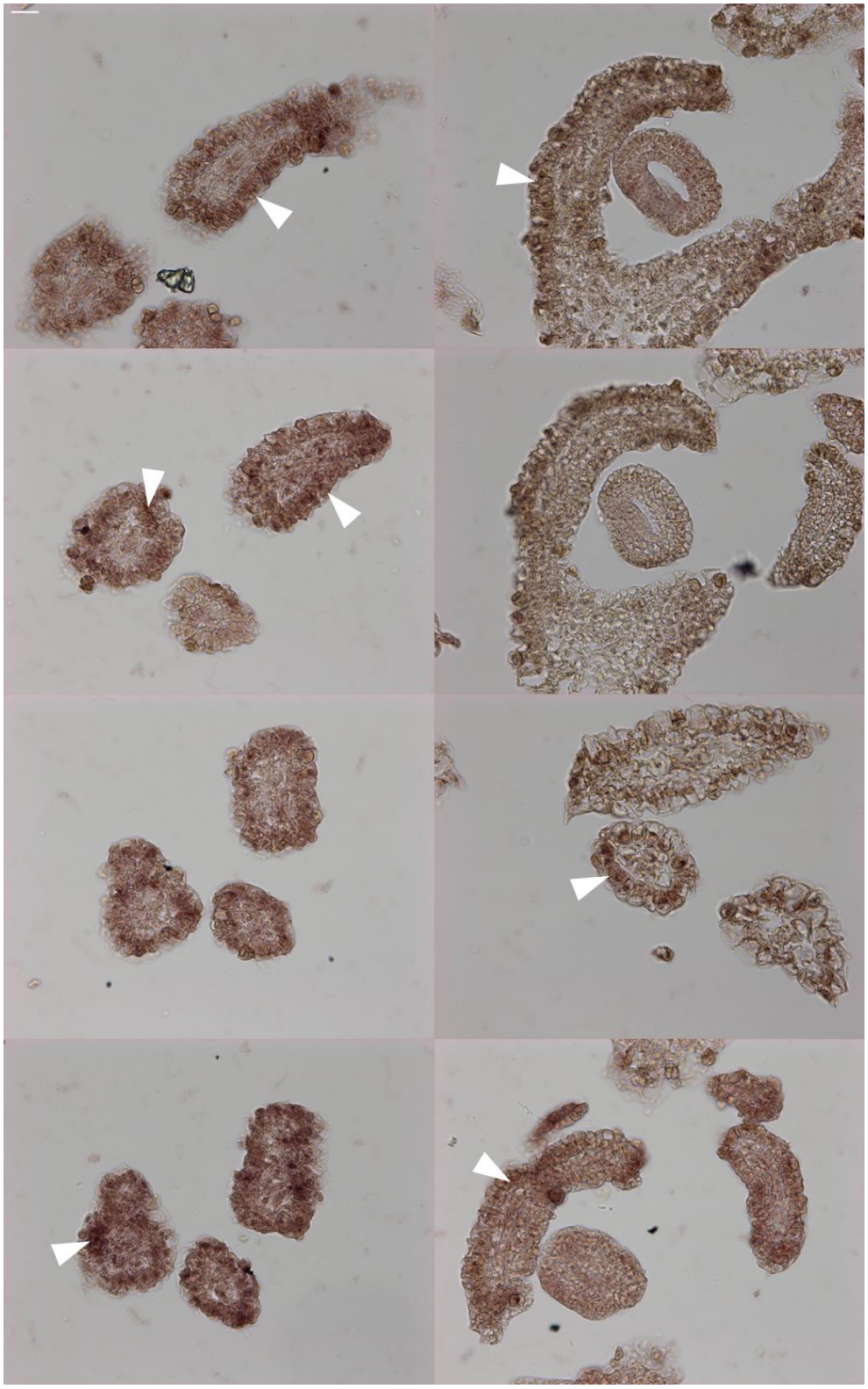

Figure 3.10 *DW1* may localise to epidermal layer

Sections of leaf, stolon and trap tissues suggest that *DW1* signal is localised to the epidermis. Arrows highlight areas of stronger signal. Scale bar is 20 µm

3.2.9 Attempts to genetically complement *dw1 EOD*

Whilst promising results have been obtained from sequence analysis, mass spectrometry and phenotyping the effect of adding epiBL to *dw1 EOD*, high confidence in successfully mapping *DW1* would have come from complementing *dw1 EOD* with *DW1* from wild type. In collaboration with Min-long Cui and Chulan Piao from Zhejiang Agricultural and Forestry University, China, we had developed a successful solid media tissue culture method to maintain and prepare *U. gibba* tissue for transformation using *Agrobacterium tumefaciens* as a vector. Min-long Cui has had success in developing successful and efficient transformation methods for challenging species, such as *Antirrhinum* (Cui et al., 2003) , Cotton (Cui *et al.*, 2020), *Digitalis purpurea* (Li et al., 2014) and *Chelone glabra* (Gao *et al.*, 2015) and had successfully transformed wild type *U. gibba* to produce a 35S::GFP line and a number of lines inducible by heat-shock using the Cre-lox system (Sieburth *et al.*, 1998). Thus, the transformation protocol could have been used to complement *dw1 EOD*.

The *DW1* gene and native promotor were synthesised, and constructs were made both with and without a GFP tag using Golden Gate, as was a heat-shock inducible *DW1* construct to explore the cell-autonomy of *DW1*. *dw1 EOD* tissue was grown on solid media containing epiBL so tissue grew similar to wild type. Several transformation attempts were undertaken, and some tissue clusters grow readily on selection, but no change in phenotype or background fluorescence could be observed, suggesting that the transformation may have been successful, but the construct may not have been functional. Whilst attempting to transform *dw1 EOD* as described, a protocol for transforming *U. gibba* was released using an alternate method (Oropeza-Aburto *et al.*, 2020). I attempted to complement *dw1 EOD,* using this method but did not succeed in generating successful transformants. An alternative method would have been to use CRISPR to generate a range of mutations in *DW1* to have a range of independent alleles and possibly a range of phenotype to increase confidence in mapping the gene.

Thus, whilst the genetic complementation of *dw1 EOD* would have given high confidence in mapping *DW1*, transforming a mutant in *U. gibba* was not successful.

3.3 Discussion

3.3.1 *DW1* likely encodes an enzyme needed for brassinosteroid biosynthesis

I have presented evidence that *U. gibba DW1* is a homologue of *AtDWARF4*. Only one SNP is homozygous in all mutants, heterozygous or absent in wild-type sibs, private to the mutant family and has a signature of EMS mutagenesis. This SNP causes an early stop codon in the coding sequence of a predicted gene in *U. gibba,* which is homologue of *DWARF4* in *Arabidopsis* (Choe *et al.*, 1998). Mutants are deficient in BR pathway compounds after the predicted enzymatic block and can be rescued by exogenous BR treatment. This rescue includes both the vasculature phenotype and epidermal cells, as shown by (Szekeres *et al.*, 1996). Collectively, this is strong evidence of mapping the *DW1* gene as a BR biosynthesis gene in *U. gibba*.

The phenotype of the mutants in *U. gibba* can be compared to the phenotypes of BR mutants in other systems. In Arabidopsis, *dwarf4* mutants display reduced overall height, shorter infertile siliques and smaller and rounder leaves compared to wild type (Azpiroz *et al.*, 1998). This phenotype has been quantified by Reinhardt *et al.* (2007), who demonstrated a preferential reduction in planar leaf length, associating BR with shape formation in 2D. These findings are similar to those for the *dw1 EOD* and *dw1 eod* mutants in *U. gibba* suggesting that lack of endogenous BR gives a common cellular phenotype across systems. BR mutants were initially discovered as light-response mutants: mutant hypocotyls did not etiolate when grown in the dark (Chory *et al.*, 1991). This phenotype was subsequently linked to reduced cell elongation (Azpiroz *et al.*, 1998). It has also been observed that BR action is linked to reorientation of microtubules into a transverse array and promoting cell elongation perpendicular to the microtubule alignment (Wang *et al.*, 2012), thus suggesting a link between BR and cell elongation. A preferential reduction in cell elongation parallel to the main growth

axis is observed in the epidermis of *U. gibba dw1*. Thus, *dw1* in *U. gibba* has both the genetic and phenotypic characteristics of a BR mutant.

3.3.2 BR reduces tissue tension-compression

Growing *dw1 EOD* in the presence of BR largely rescues the phenotype. Internode and leaf length are increased to the same as wild type, epidermal cell size and geometry is restored, and the vasculature is straight. Therefore, the process that causes the wiggly vasculature is restored by BR. It has been suggested that BR acts in the epidermis alone to control growth (Savaldi-Goldstein *et al.*, 2007). In *U. gibba*, application of BR to the mutant promotes growth in the epidermis, but it is not clear if the restoration of the vasculature phenotype is due to the increased epidermal length and/or BR action on the vasculature. *In situ* hybridisation of *DW1* suggests that it is localised to the epidermis. This is consistent with *DWF4* in *Arabidopsis* roots (Vukašinović *et al.*, 2021). However, as *DW1* is a biosynthesis enzyme, all that can be inferred is that this step in the biosynthesis pathway is in the epidermis, not that the acting site of BR is specifically in the epidermis. Length of the vasculature was affected by *dw1* (figure 2.18B), indicating that BR does not only act in the epidermis but in all tissues. In terms of tissue tension-compression, it is feasible that adding BR to the *dw1* mutant reduces the growth differential between tissue layers by preferentially promoting epidermal growth. It would therefore reduce tissue tension in the epidermis and tissue compression in the vasculature, leading to a straight vasculature.

3.3.3 Conclusion

DW1 from a mutant screen in *U. gibba* likely encodes a BR biosynthesis gene. BR could reduce tissue tension-compression in *U. gibba,* and the target site for BR action is likely in all tissues but the growth effect more pronounced in the epidermis.

4 Understanding the BR mode of action in *U. gibba*

4.1 Introduction

I have mapped *dw1* to a BR biosynthesis gene from a forward screen in *U. gibba* and have linked the *dw1* phenotype to BR deficiency. From phenotypic characterisation, it can be inferred that BR is involved in controlling anisotropic growth, as found in *Arabidopsis* (Fridman *et al.*, 2021; Xiong *et al.*, 2021). Characterising epidermal cells in the stolon of wild type, *dw1* and *dw1* + epiBL suggests that BR is involved in cell size through increasing cell length parallel to the direction of the stolon. Similar effects of BR on cell length have also been described in *Arabidopsis* (Yamagami *et al.*, 2017). Therefore, the dwarf phenotype of the *dw1* mutant is due to an absence of BR, leading to a reduction in cell size and length. In this chapter I analyse the effect of BR on the stolon to understand how BR controls anisotropic growth at the cellular and tissue levels.

4.1.1 Effect of BR on Cell Wall Thickness

BR has previously been shown to act on microtubules: addition of BR leads to a more transverse alignment (Catterou, 2001; Wang *et al.*, 2012; Liu *et al.*, 2018). However, as microtubule alignment is affected by cell geometry (Lagomarsino *et al.*, 2007; Durand-Smet *et al.*, 2020), it remains unclear whether microtubule realignment is a cause, or consequence, of change in cell shape. BR may act on wall extensibility (Wolf *et al.*, 2012), where the wall is loosened, allowing the cell to yield to turgor more easily. Or BR may act on cell wall synthesis, where a reduction or realignment in the biosynthesis of cell wall material leads to a weaker wall that also allows the cell to yield to turgor more easily (Rao & Dixon, 2017; Sánchez-Rodríguez *et al.*, 2017). These possibilities are not mutually exclusive.

In terms of tissue tension-compression, the cell wall is the load-bearing structure in the tissue and cell wall thickness is an indicator for tissue tension-compression as thicker epidermal walls will likely yield less to turgor because wall stress is reduced (stress depends on force divided by cross-sectional wall area)(Cosgrove, 1997). The outer epidermal cell walls are typically thicker than inner ones (Kutschera, 1992; Refrégier *et al.*, 2004; Derbyshire *et al.*, 2007), therefore changes in wall thickness of cells in the outer epidermal wall indicate changes in tissue tension. Therefore, measuring cell wall thickness in wild type, *dw1* and *dw1* + BR may provide an indication for how BR affects tissue tension-compression.

4.1.2 Timing of BR action

Narrowing down the timing of BR action may help to understand in how BR controls growth. In situ hybridisation of *AtDWARF4* has shown that the gene is expressed in actively growing regions of *Arabidopsis* (Kim *et al.*, 2006). However, the downstream action of BR does not necessarily directly relate to BR biosynthesis. BR is initially detected by the extracellular LRR-receptor *BRI1* before activating a signalling cascade which leads to downstream upregulation in transcription factors (Noguchi *et al.*, 1999; van Esse *et al.*, 2012). Therefore, only cells which have active *BRI1* will be sensitive to BR. The window of BR action therefore reflects both the presence of BR and perception by *BRI1*. In a BR biosynthesis mutant such as *dw1*, it can be assumed that the mechanisms of perception are fully working, evidenced by rescue of *dw1* by exogenous treatment with epiBL (Wang *et al.*, 2001). Here, the system is flooded with epiBL in the media. We can therefore assume that the presence of BR is not limiting, and the reaction of *dw1* solely reflects the endogenous perception mechanisms and downstream effects. This may give a clearer picture of when BR acts.

4.1.3 Timing of BR on different cell layers

Mature stolons in wild type have straight vasculature and mature stolons in *dw1* have a wiggly vasculature that is rescued by treatment with epiBL. In *dw1,* there is the question of when the vasculature wiggles form. They may form early in development as a result of aberrant orientations of growth, meaning that the wiggly vasculature phenotype will be visible at the early stages of stolon development. Alternately, they may form later in development due to increased tissue tension-compression. If BR acts on cell length preferentially in the epidermis and cell length is reduced in the mutant (Azpiroz *et al.*, 1998), the decrease in length would cause and increase in compression on the internal tissues (Fruleux & Boudaoud, 2019). The internal tissues may be under a certain level of compression in wild type, but an increase in tension in the epidermis may increase compression on the inner tissues such that it buckles. This would imply that the wiggly vasculature may form later on in development. Imaging a number of internodes will help resolve when the vasculature phenotype forms.

Aims of this chapter:

- Determine the effect of *dw1* on epidermal wall thickness
- Determine the timing of *dw1* sensitivity to rescue by epiBL
- Determine when the wiggly vasculature forms

4.2 Results

4.2.1 Internodes of *dw1* stop increasing in length from internode 0 onwards

To understand the difference in development of wild type and *dw1* stolons, I first identified when the internodal length reaches maturity. I assigned each node a number, with node 1 being defined as the node where a fully measurable leaf had emerged. Internodes were labelled according to their distal node number. From the light microscope images, it was unclear how many nodes had formed between the apical meristem and the first measurable leaf. It was also unclear how development of the internode differed between wild type and *dw1* in the apex. Whilst figure 4.1 indicates that internode 1 is roughly the same length in wild type as it is in *dw1*, it is not clear that wild type and *dw1* internode 1 are at the same developmental stage. Therefore, node assignments of a genotype could only be understood in relation to other nodes of the same genotype and could not be used to compare developmental stages between genotypes.

I measured average length of each internode of 12 wild type and 10 *dw1* plants up to around internode 9 (figure 4.1) and found that early wild type internodes elongated fivefold, from 0.54 mm at internode 1 to a mature length of 2.59 mm at around internode 4. *dw1* mutant internodes did not show a significant difference ($p > 0.05$) in length from average mature internode length from internode 1 onwards. Wild type internode length showed a lot of variation, especially at internodes 17 and 19. This could be explained by a small sample size for these more mature internodes ($n = 4$). All internode measurements have $n \geq 4$, but internodes 1 to 9 have $n \geq 9$. Therefore, wild type internodes reaches mature length at around internode 4, and *dw1* at or before internode 1.

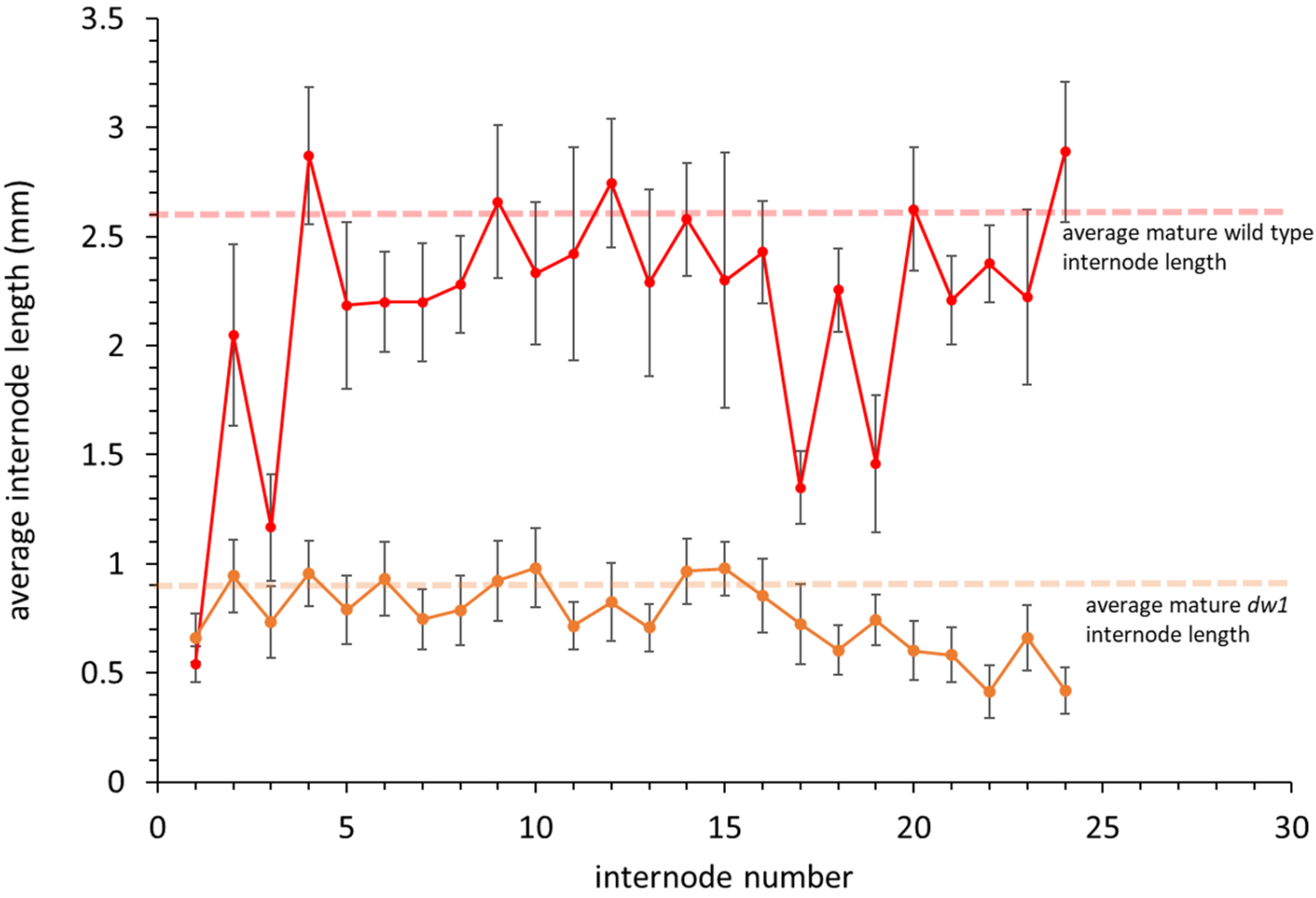

Figure 4.1 Wild type internodes show greater elongation before reaching maturity than *dw1*

Average length of individual internodes of wild type (red) and *dw1* (orange). Average internode lengths are shown in dashed lines. Error bars show SEM. n internodes ≥ 4 for wild type and *dw1*

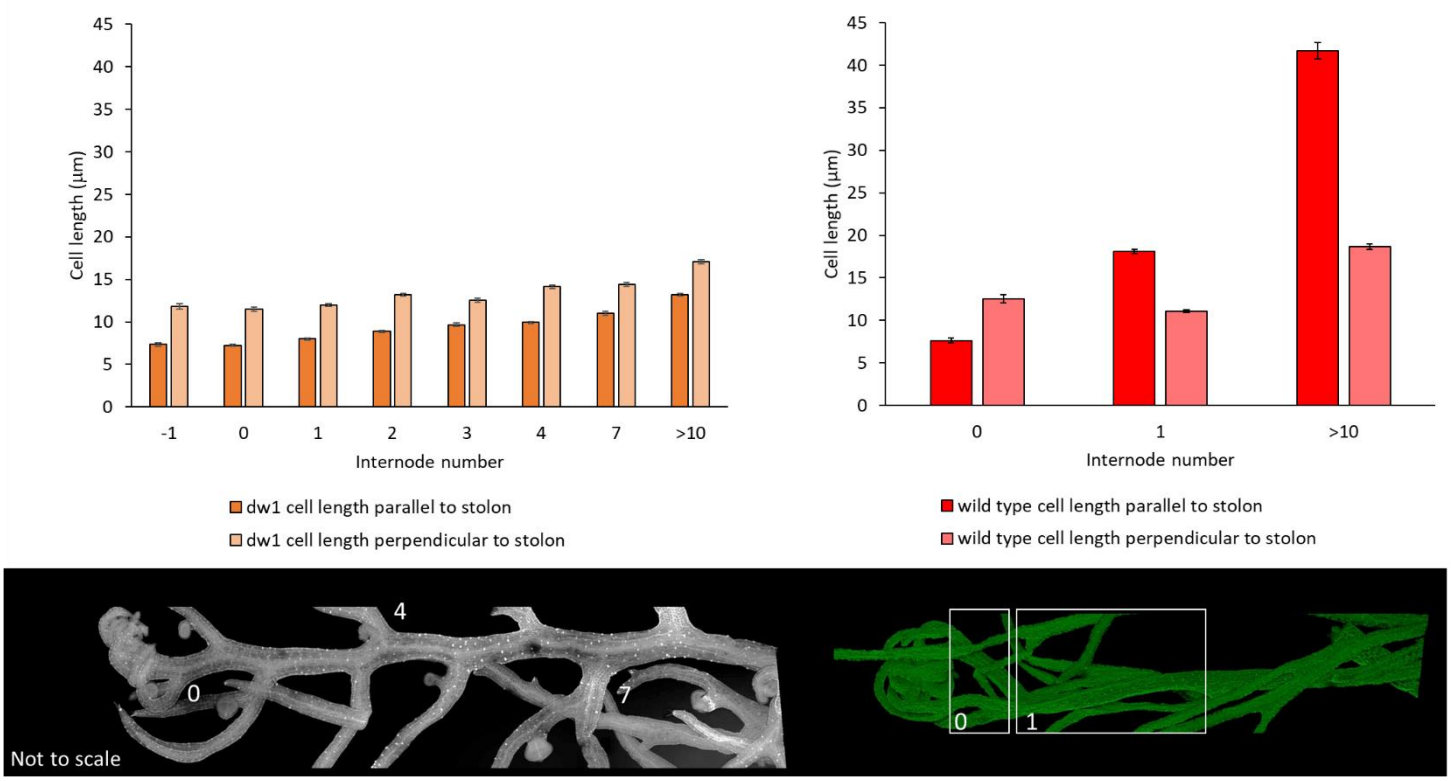

Figure 4.2 Orientation of maximal cell length does not change in *dw1*

2.5D cellular segmentation provided data for average cell length parallel and perpendicular to the of successive stolons in A) *dw1* and B) wild type

To determine how cell shape changes during development, 2.5D segmentation was performed on successive internodes proximal to the apex of wild type and *dw1* (figure 4.2). This was done in collaboration with Karen Lee who performed the segmentation and data acquisition. Internodes -1 to 7 were segmented for *dw1*, data for mature internodes (internode >10) were taken from figure 2.17B & C. For cells in all internodes measured in *dw1*, cell length perpendicular is always greater than cell length parallel to the stolon (figure 4.2B). In wild type, cell shape data could only be acquired for internode 0 and 1. In internode 0, cell length perpendicular to the stolon is greater than cell length parallel, as found in *dw1.* In internode 1 however, a change in the major axis of the cell has occurred, such that cell length parallel to the stolon is greater than cell length perpendicular, suggesting that cells have elongated axially. The difference in cell length parallel to cell length perpendicular is greater in cells of mature internodes (internodes >10, figure 2.12B & C), suggesting that cells at maturity have elongated even further. The switch in major orientation between internodes 0 and 1 could suggest that cell division has ceased at around internode 0 and cells at around internode 1 have begun elongation.

4.2.2 *dw1* internode length can be fully rescued by BR treatment at internode 0

To understand the timing of BR action on internode development, I tracked *dw1* over 14 days once treated with 0.01 µM epiBL. I isolated apical explants from a culture *dw1* and imaged them immediately (day 0). Explants were then placed in liquid media containing 0.01 µM epibrassinolide (figure 4.3A), or normal growing media without BR as a control (figure 4.3B). I imaged stolons at day 7 and day 14 and assigned node numbers based on day 0. Nodes which were not visible at day 0 but had developed and were measurable at day 14 were assigned a negative number.

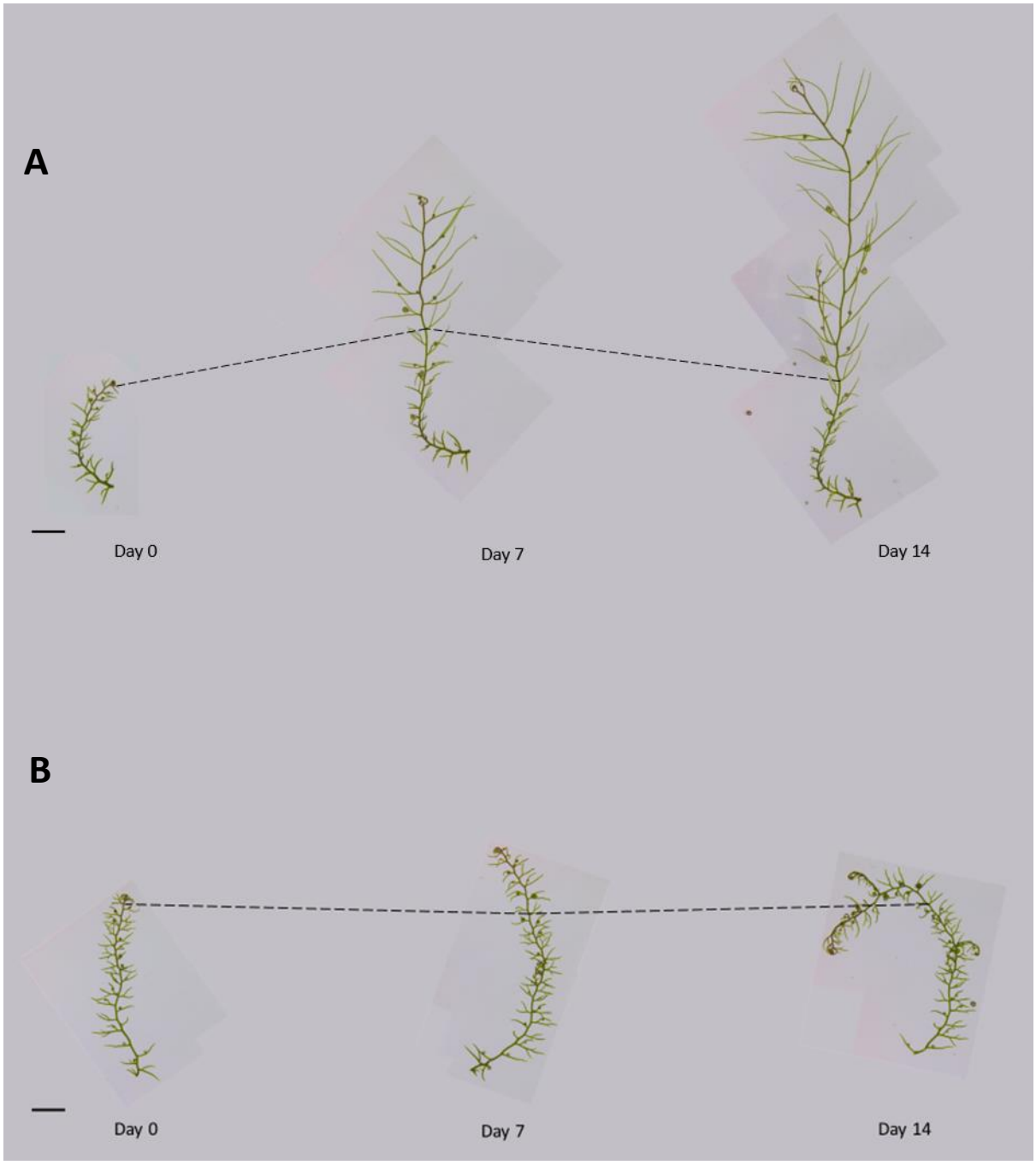

Figure 4.3 Tracking growth of *dw1* over 14 days reveals how treatment with BR affects development

A) Treating *dw1* with 0.01 µM epibrassinolide rescues the phenotype of newly developing tissue.

B) Tracking untreated *dw1* over the same time period shows how the mutant develops without treatment

Scale bars are 5 cm

To identify which internodes were sensitive to BR treatment, I measured the internode length at day 14 of treated *dw1* plants (figure 4.4). Control plants that were not treated with BR showed no increase in average mature internode length after 14 days (figure 4.4B), suggesting that the process of isolating single explants did not affect internode length. Average internode length of treated stolons (figure4.4A) showed a significant increase in length ($p < 0.05$) compared to control lengths at internodes 1 to 5. Internodes more mature than internode 5 were not significantly affected by BR. Treated plants showed no significant difference from mature wild type in internode lengths from internodes -10 to 0. Therefore, internode length is fully restored to wild type when treated with BR from internode 0 onwards, and internodes more mature than internode 5 were no longer sensitive to BR.

To measure *dw1* internode lengths at day 0 that could not be measured through light microscopy (i.e., negative internodes), I took fine confocal scans (z-step = 0.1 µm) and used the clipping plane function in VolViewer to find internodes in *dw1* (figure 4.5A). The circinate apex comprised many overlapping young leaves, making identifying the meristem and newly formed internodes challenging. I measured two apices in this way. Internode 1 was 0.37 mm long on average (figure 4.5B). This was less than the mean value of 0.66 mm in figure 4.1, but not significantly different given the sample size of only 2. Internodes 0 and -1 were 0.22 mm long on average and more negative internodes were successively smaller, though they could only be measured on a single sample. Given that BR treatment fully rescued internode 0 (figure. 4.3A), these results show that the length of *dw1* internodes of around 0.2 mm and less can be fully rescued by BR treatment.

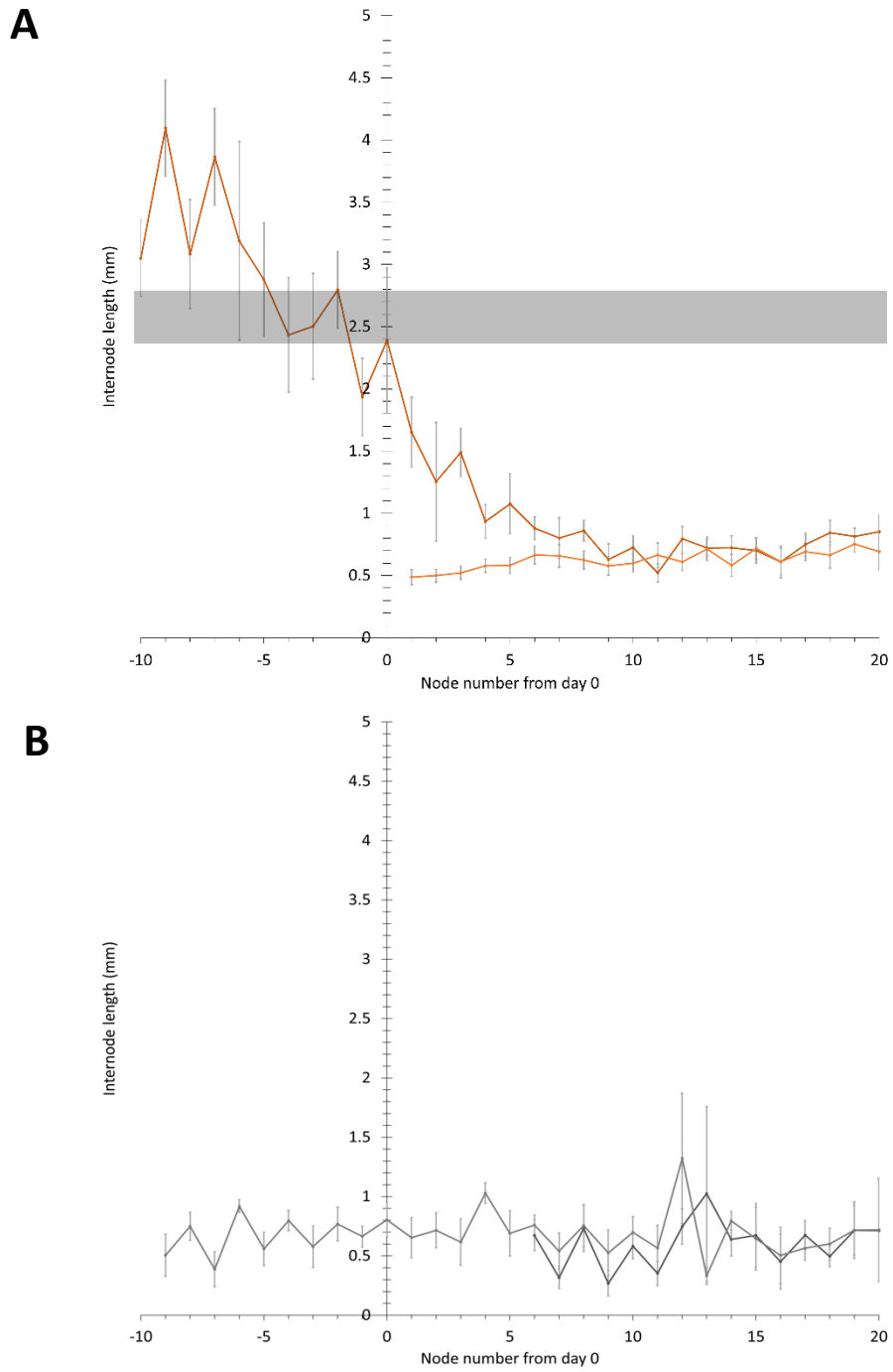

Figure 4.4 Tracking the effect of epiBL on *dw1* reveals a range of sensitive nodes

) Average length of *dw1* internodes at day 0 (orange) and at day 14 after treatment with 0.01 µM epiBL (dark orange). The first 5 nodes from each measured stolon were not included as to present mature internode length for each node. The grey band shows average wild type mature internode length ± SEM.

B) Average length of *dw1* internodes at day 0 (dark grey line) and at day 14 without treatment (grey line). The first 5 nodes from each measured stolon were not included as to present mature internode length for each node.

Error bars show SEM. n ≥ 10 for wild type and *dw1*.

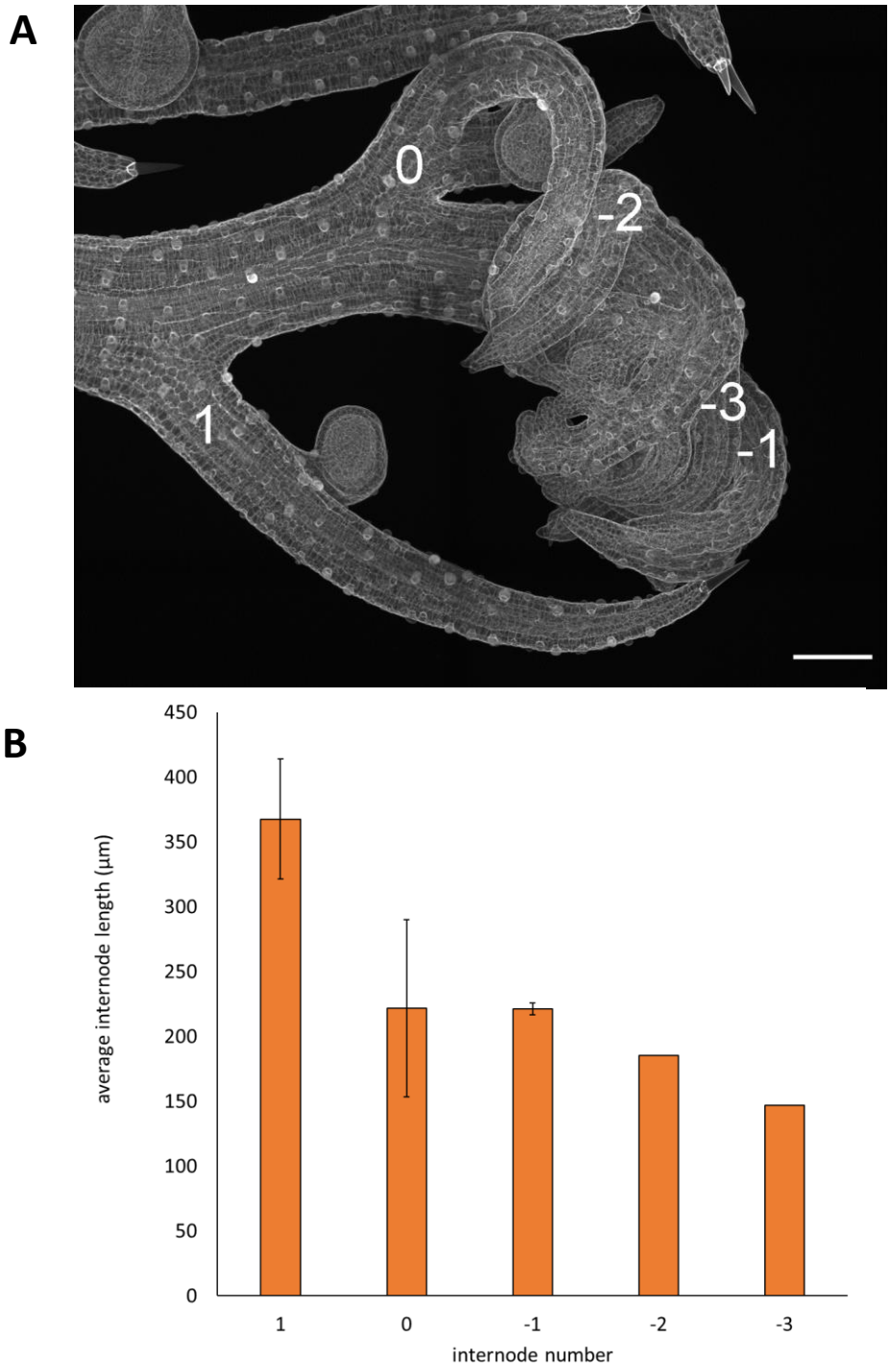

Figure 4.5 Internodes increase in length inside the circinate apex in *dw1*

A) Confocal scan of *dw1* apex. Distinguishable and measurable internodes are labelled at the leaf axil. Scale bar is 100 µm.

B) Length measurements of internode labelled in A). Error bars show SEM. Nodes 1,0 and -1: n = 2. Nodes -2 and -3: n = 1

4.2.3 Wiggly vasculature in *dw1* is identifiable at node 4 and consistent from node 9

To identify when in development the wiggly vasculature phenotype of *dw1* arose, I obtained confocal images of a single *dw1* stolon. Using large, tiled z-stack scans, I numbered each internode and characterised the vasculature along the length of the stolon (figure 4.6A). From node 4, the vasculature was not as straight as less mature nodes. A clear wiggly vasculature phenotype was consistently identifiable from internode 9 onwards. The wiggly vasculature could be observed up to node 16 (figure 4.6Biii and Biv) but was variable as there were some lengths of stolon which have straight vasculature (figure 4.6Biv and Bv). Therefore, based on this individual, wiggly vasculature arose from around node 4 of *dw1,* contrasting with internode length which did not change significantly from internode 0 onwards (figure 4.1 and 4.4).

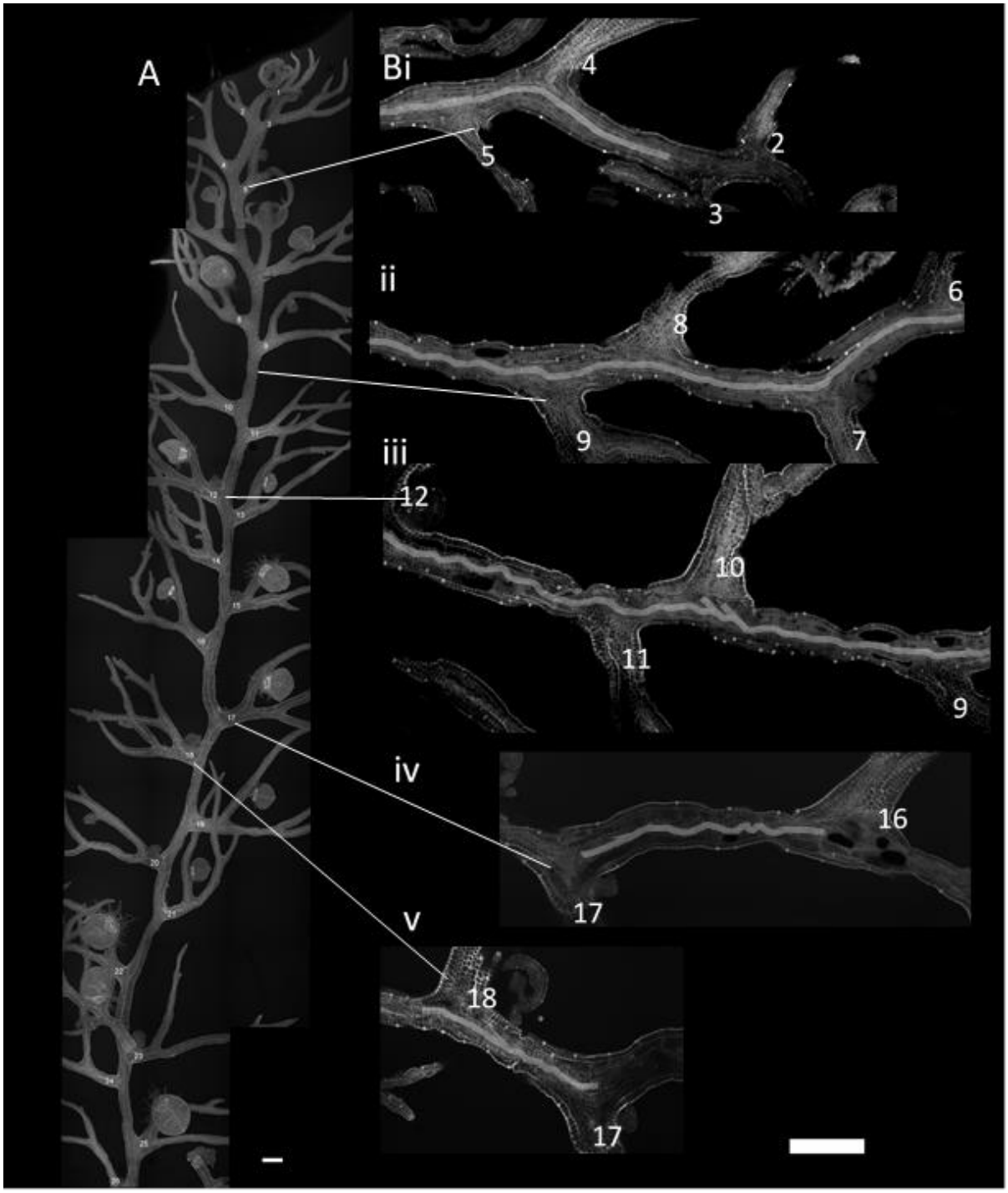

Figure 4.6 The wiggly vasculature phenotype in *dw1* is found from node 4

A) Confocal scan of a mounted *dw1* stolon stained with PI.

B) Capturing z-stacks along the *dw1* stolon shows that the vein is straight in between nodes 3 and 5 (i), begins to noticeably wiggle at node 9 (ii) and is consistently wiggly in more mature nodes (iii) with some variation (iv and v). Label internodes

Scale bars are 1cm

4.2.4 Outer epidermal walls are thicker in *dw1* compared to wild type

I measured OEW thickness of mature internodes (internode number > 10) in collaboration with Elaine Barclay in the JIC Bioimaging Team, who sectioned and acquired TEM images of the samples. I provided fixed material, performed image analysis and made measurements. I measured OEW thickness for transverse sections of mature stolons of wild type (figure 4.7Ai), *dw1* (figure 4.7Aii) and *dw1* + 0.01 µM epibrassinolide (figure 4.7Aiii). Average OEW thickness of *dw1* ($\bar{x}$ = 0.90 µm, *SEM* = 0.03) was significantly greater ($p > 0.01$) than wild type ($\bar{x}$ = 0.78 µm, *SEM* = 0.02) and *dw1* + epiBL ($\bar{x}$ = 0.78 µm, *SEM* = 0.02). There was no significant difference ($p > 0.05$) between the average outer epidermal cell wall thickness of wild type and *dw1* + epiBL. Therefore, OEWs of mature *dw1* internodes are about 15% thicker than those wild type and wall thickness can be rescued with application of epiBL.

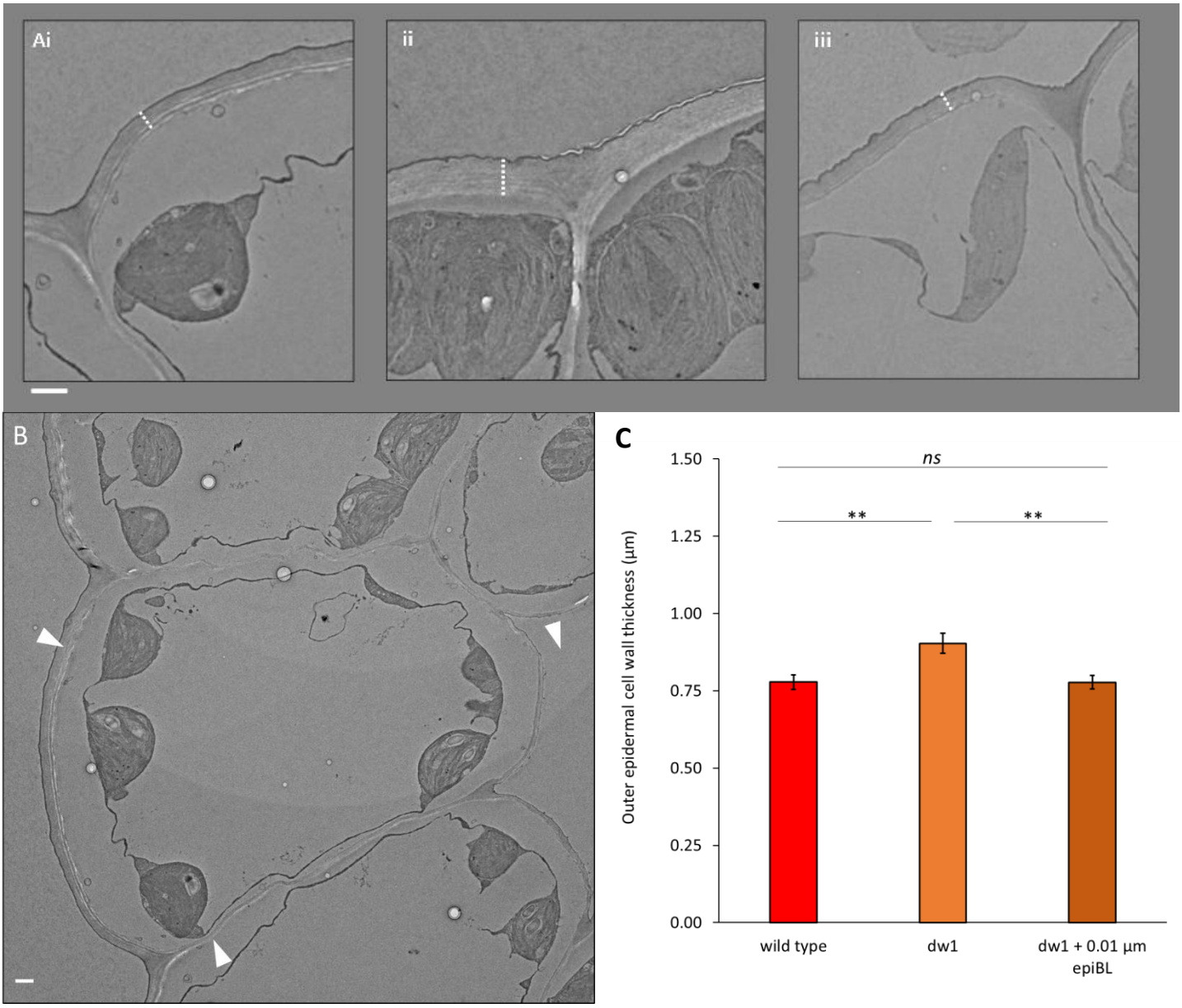

Figure 4.7 Outer epidermal cells walls are thicker in the absence of BR

A) Transmission electron micrographs of transverse sections of outer epidermal cell walls in i) wild type ii) *dw1* and iii) *dw1* + 0.01 µM epiBL. Wall thickness measurement examples are show as white dotted lines. Scale bar is 1 µm.

B) Overview of typical wild type epidermal cell. Arrows highlight thicker outer epidermal wall, thinner internal wall of the same cell and internal air space. Scale bar is 1 µm.

C) Average outer epidermal cell wall thickness measurement. OEW thickness *t* tests: wild type to *dw1* p = 0.003568 (**), wild type to *dw1* + 0.01 µM epiBL p = 0.974404 (*ns*), *dw1* to *dw1* + 0.01 µM epiBL p = 0.002494 (**). Wild type n cells = 21, *dw1* n cells = 19, *dw1* + 0.01 µM epiBL n cells = 19

4.3 Discussion

4.3.1 Summary

I have explored the effect of BR on the tissues and cells of *U. gibba*, summarised in figure 4.8. In *dw1*, the mean long axis of epidermal internode cells is circumferential to the stolon. Internode length increases from around 0.20 mm at internode -1 to around 0.94 mm at internode 2. Internode length at node 0 is 0.22 mm. *dw1* internodes can be fully rescued by continuous exposure to epiBL during the interval spanning internodes 0 to 5. Exposure in the later part of this interval to epiBL leads to partial rescue. The wiggly vasculature phenotype is observed at node 4 and consistent from node 9. In wild type, internode length increases from around 0.54 mm at internode 1 to around 2.87 mm at internode 4, an increase of by a factor of roughly 5. Between internode 0 and internode 1 the orientation of the longest cell axis switches from circumferential to parallel to the stolon (figure 4.2). Cells at internode 0 in wild type have a similar size and shape to cells at internode 0 to 2 of *dw1*. OEW thickness of mature epidermal cells of wild type, or *dw1* rescued with epiBL, is reduced by 15 % compared to *dw1*. In the following discussion I consider the implications of these findings for the mechanism of BR action.

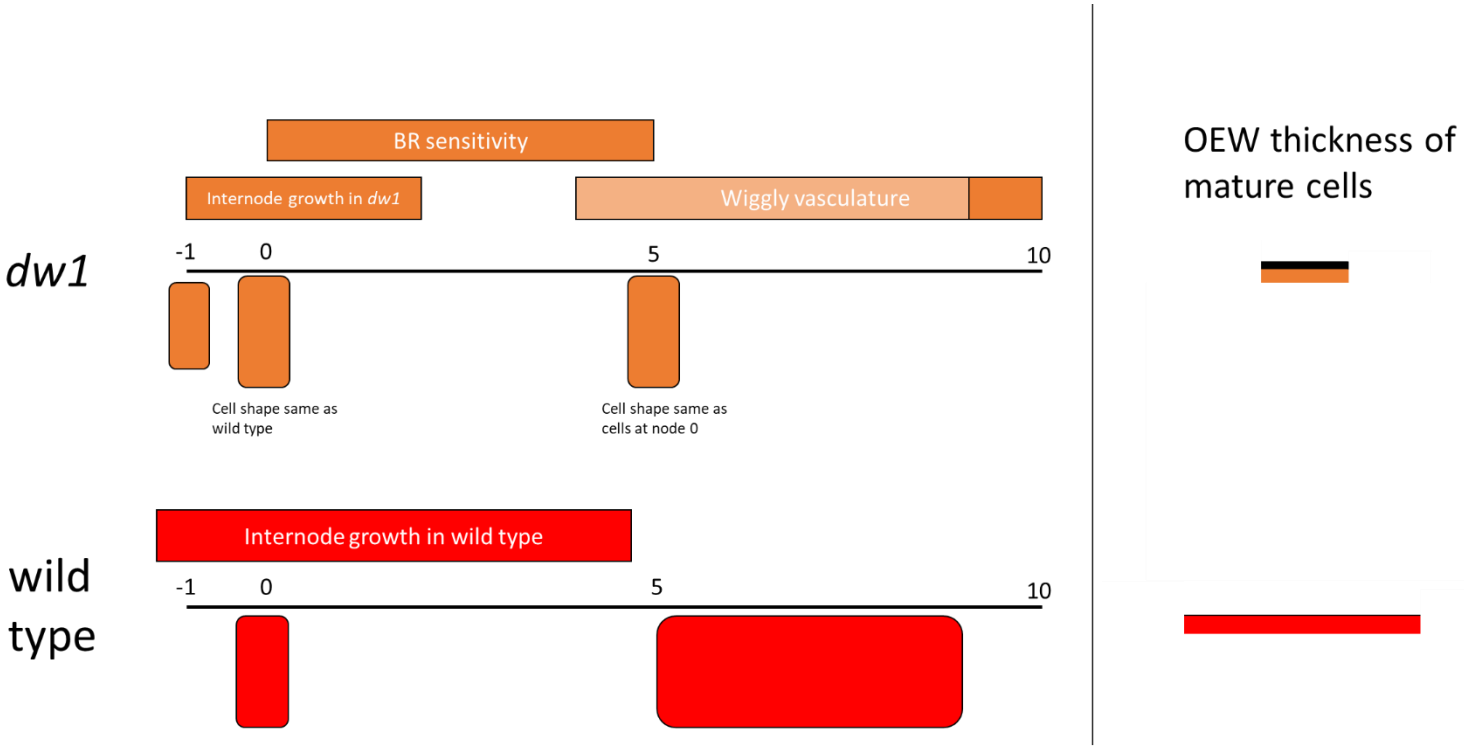

Figure 4.8 Summary of data comparing wild type to *dw1*

Black lines represent stolon, numbers represent internodes, boxes represent epidermal cell shape for wild type (red) and *dw1* (orange). Note that internode numbers refer to the respective genotype and cannot be assumed to correspond between genotypes.

4.3.2 Explaining why BR reduces OEW thickness

Epidermal cells of *dw1* are smaller and have thicker OEW than those of wild type or *dw1* + BR. BR is likely to have a role in increasing cell growth rate, an effect which may be more pronounced in areas of high cell anisotropy. The ventral midline of wild type traps has a higher growth rate than other parts of the trap. *dw1* traps are smaller and have a less isotropic and somewhat thicker ventral midline. As the trap is comprised of epidermal cells and OEW are thicker in *dw1* stolons, ventral midline thickness may be explained by and increase in cell wall thickness in *dw1* traps which may have a knock-on effect of growth rate in this region and thus on trap shape. Growth rate can increase through an increase in extensibility which is the ease of which cellulose microfibrils slide past each other, or through reduced wall thickness where the wall stress is increased as the cross-sectional area of the wall is reduced. In an anisotropic cell, the density of microfibrils running in each direction may be different. Thus, a more relevant measure than wall stress (force divided by cross-sectional wall area) would be fibre stress (force divided by cross-sectional fibre area), but this is difficult to measure without knowing the details of wall composition (i.e., proportion of fibres running in each direction).

BR might control cell growth by promoting cell wall extensibility (Wolf *et al.*, 2012). If the cell wall is more extensible in wild type and *dw1* + BR, synthesis of wall material may not be able to keep up with elongation, leading to a thinner wall. Such an interaction would lead to positive feedback mechanism, whereby increased extensibility causes the wall to become thinner through faster elongation, which increases stress on the wall (wall stress being inversely proportional to wall thickness) leading to even faster growth. The same feedback mechanism could lead to arrest of cell growth in *dw1*: as walls become thicker, they slow down growth, leading to less thinning and thus less stress, further slowing down growth. Whether such a feedback mechanism operates would depend on how wall synthesis is controlled in relation to growth rate. If wall synthesis is regulated such that it increases in proportion to growth rate, it would not work because wall thickness would be maintained by homeostatic control.

Alternately, BR might control cell growth through affecting cell wall synthesis (Rao & Dixon, 2017; Sánchez-Rodríguez *et al.*, 2017). If synthesis is reduced in the presence of BR, there is less wall thickness to resist turgor, increasing wall stress, so the cell would stretch more quickly. In *dw1*, if synthesis is not reduced then the cell wall will be thicker, thus reducing wall stress. Wall synthesis may differentially affect deposition of microfibrils according to orientation. If BR causes microfibrils to be preferentially reduced parallel to the stolon axis, this would increase microfibril stress in this orientation, leading to faster growth and would also cause reduced wall thickness.

4.3.3 Explaining how BR causes cell shape changes

In wild type, the orientation of cell long axis changes from circumferential at the early stages to axial. The principal orientation of growth cannot be inferred from the orientation of cell shape alone. If cell division walls are preferentially circumferential, the long axis of cells might also be biased in this orientation at early stages, even if growth is principally oriented axially. A further indication of growth orientation could come from the internode shape. Finding the length:width ratio of early internodes in *dw1* would help track changes in internode shape. For a cylinder in which circumference is equal to length, $L=2\pi r$, so the length:width ratio is $L/2r = \pi$. Early internodes may have a more or less isotropic shape, indicative of near isotropic growth (although without knowing the starting shape of the internode, the growth pattern cannot be rigorously inferred).

Assuming that early growth of *dw1* (prior to node 0) is isotropic, and assuming that BR promotes overall wall extensibility, adding BR to *dw1* would lead to larger isotropic cells and an increase in both girth and length of the internode. However, mature cell shape in *dw1* + BR is considerably longer parallel to the stolon than perpendicular, implying that BR has promoted growth in a directional manner. Similar findings have been found in *Arabidopsis* (Xiong *et al.*, 2021). It is possible that BR promotes wall extensibility in some orientations more than others. Alternatively, BR may affect wall

synthesis by modifying microtubule alignment (Catterou, 2001; Wang *et al.*, 2012; Liu *et al.*, 2018). If BR causes preferential reduction in microtubules aligned with the long axis of the stolon, then greater cell growth and elongation would be promoted in this orientation.

4.3.4 Explaining the timing of BR action

Only cells before a certain developmental stage are sensitive to BR, as has been shown by Lozano-Elena *et al.* (2018). Internodes of *dw1* more mature than internode 5 are not significantly increased in length after addition of epiBL and do not appear to be affected at all after internode 9 (figure 4.4A). If BR influences wall extensibility (e.g., by loosening microfibril-microfibril interactions), it is unclear why BR treatment is ineffective on *dw1* after internode 5. It could be that extensibility is only influenced by BR earlier than internode 5, or that the cell walls are so thick by internode 5 that reducing extensibility has no effect.

By contrast, if BR acts by reducing synthesis of axially oriented microfibrils, application of BR to *dw1* would be expected to be ineffective after internode growth ceases. This is because by this time there would be sufficient axial microfibrils in the wall to resist turgor, so reducing their synthesis rate after this point would have no effect. Such explanations have been reviewed by Höfte and Voxeur (2017).

dw1 internode length is fully rescued by continuous exposure to BR from internode 0 onwards. Rescue of internode length can be fully accounted for by increase in cell length. Treatment with epiBL increases cell length parallel to the stolon around 3 times from 13.17 µm for untreated *dw1* to 32.26 µm for *dw1* + 0.01 µM epiBL and increases internode length around 3 times from 1.99 mm for untreated *dw1* to 5.61 mm for *dw1* + 0.01 µM epiBL. Without BR treatment, internode length of *dw1* shows no significant increase after internode 0, implying both epidermal cell division and elongation have stopped. Thus, exposure to BR during progression from internode 0 to 5 of *dw1* likely acts after

cell division has stopped by changing wall properties and resistance to turgor in the axial orientation, leading to axial cell elongation.

In wild type, internode lengths significantly increase compared to those in *dw1* after wild-type internode 2. This increase is accounted for by increase in cell length. The switch in the orientation of the major axis in wild type cells between internode 0 and 1 suggests division has stopped (figure 4.2). BR may therefore start acting in wild type at around the time where cell division stops and promote wall elongation afterwards. BR biosynthesis may start in cells at wild-type internode 0 or may start earlier but is not perceived in wild type until internode 5. A delay in sensitivity has been described in Clouse (2011).

Wild-type internodes show no significant increase in length after internode 4, suggesting BR no longer affects elongation after this point. Thus, as in *dw1,* BR may act in wild type during a window comprising 4-5 internodes (internodes 0-5 of *dw1* + epiBL*,* internodes 0-4 of wild type).

4.3.5 Explaining the timing of vascular curvature

Wiggly vasculature *of dw1* is not observed until internode 4 (figure 4.6B), which is around when internode elongation stops. Wiggly vasculature is consistently observed from node 9 onwards. These results suggests that wiggle-formation may also depend on vascular growth continuing after epidermal growth has ceased. Thus, by the time the walls of epidermal cells have reached sufficient strength to resist turgor (stop growing), walls of vascular cells are still insufficiently strong to resist further stretching and growth. The resulting tissue tension-compression could lead to buckling, accounting for the wiggly vasculature.

Such buckling would only occur, however, if there is sufficient air space to accommodate the deformation. Wiggliness is greatly reduced in *dw1 eod* (figure 2.18) presumably because there are few air spaces. Air spaces in *dw1* could be assumed to become progressively larger in internodes

forming in the apex and may not increase further after internode 0. This may suggest that the timing of wiggle-formation is not set by the timing of air-space formation but would support the notion that they are formed by the continued growth of the vasculature relative to the epidermis.

The extent of vascular wiggliness in *dw1* is variable along the stolon from internode 4 onwards. There are some internodes more mature than node 9 which have a straight vasculature. The variability may reflect variability in growth rates of internodes and whether vasculature tissue compression reaches a threshold needed for buckling.

The straight vasculature of wild type may be explained by BR preferentially weakening epidermal cells walls so that they continue to grow for longer than *dw1* (until internode 4), thus relieving tissue tension in the epidermis and reducing the tissue compression in the vasculature. Tissue compression may still operate on vasculature of wild type, if the epidermal cell walls are thicker than the internal walls then they will carry more load and transfer compression on the vasculature but may not reach the threshold needed for buckling to occur. A key part of tissue tension-compression is the transmission of forces between cells layers through tissue connectivity. In systems such as A*rabidopsis,* there is continuous connectivity of adjacent cells across a tissue. In *U. gibba* the epidermis and vasculature are only join through the connective tissues which divide air spaces. If tissue tension-compression is to occur, where the epidermis is assumed to be under tension, then a compressive force will be transferred on the vasculature through the cells in the connective tissue.

An alternative to the tissue tension-compression hypothesis is that wiggly vasculature arises through orientations of vascular growth becoming more disorganised at later stages. One way of distinguishing these hypotheses is to analyse orthologues of *dw1* in other species. If BR acts by reducing tissue tension-compression, comparable effects should be observed.

4.4 Conclusion

I have explored the action of BR in *U. gibba* with the aim of identifying the window of sensitivity where *dw1* can be rescued by treating with epiBL. In the absence of BR, *dw1* internodes cease to elongate at around node 1, earlier than wild type and develops a wiggly vasculature phenotype at around node 4. I put forward the notion that BR mediates mechanical layer interactions through changing tissue tension-compression. This can be inferred from OEW being thicker in the absence of BR. Therefore, I have identified a role for BR in controlling tissue tension in *U. gibba* and identified that BR is involved in promoting cell length in actively growing regions. It remains unclear if this mode of action of BR is specific to *U. gibba* or found more generally in other plants.

5 Exclusivity of BR controlling tissue tension-compression in *U. gibba*

5.1 Introduction

5.1.1 Testing the effect of BR on tissue tension in other species

I have shown that BR may reduce tissue tension-compression in *U. gibba*, evidenced by wiggly vasculature in the *dw1* mutant. To further test this hypothesis, it would be good to look at the effect of BR on tissue tension-compression in other model species such as *Arabidopsis*. However, as *Arabidopsis* stems do not have internally patterned air spaces, it may be difficult to visualise the effects of increased tissue tension because closely packed cells would prevent buckling. BR has been shown to act on the vasculature by modulating bundle number through promoting early procambial divisions (Ibañes *et al.*, 2009), but it is unclear if this relates to changes in tissue tension-compression.

As described in the Introduction, early evidence for tissue tension-compression came from organ dissection (Sachs, 1865; Kraus, 1867). Genetic methods for tissue dissection through growth may now be possible. *quasimodo* mutants have weaker cell adhesion through a mutation in either a glycosyltransferase involved in homogalacturonan biosynthesis (*quasimodo1* (Bouton *et al.*, 2002)) or a mutation in a pectin methyltransferase (*quasimodo2* (Mouille *et al.*, 2007)). Both types of mutant exhibit epidermal cracks where cells have separated, typically at their proximodistal edges. The formation of these cracks is thought to depend on tissue tension-compression which provides a force that pulls cells apart (Verger *et al.*, 2018). If BR reduces tissue tension-compression, then inhibiting BR should enhance the crack phenotype, while adding BR should diminish the crack phenotype.

5.1.2 Testing the effect of other growth hormones on tissue tension-compression

Mutants in many other growth hormones, such as auxin (Mirza & Maher, 1987), cytokinin (Werner *et al.*, 2003), gibberellic acid (Koornneef & van der Veen, 1980) and ethylene (Alonso Jose *et al.*, 2003), give dwarf phenotypes. It is possible that these hormones reduce tissue tension-compression, as proposed for BR. If so, inhibiting these hormones in *U. gibba* might give a wiggly vasculature phenotype. Whilst testing this prediction for all hormones is outside the scope of this project, I investigated the role of gibberellic acid (GA) as it is a de-repressor of growth (Dill & Sun, 2001), similar to BR (He *et al.*, 2005). For these experiments I inhibit GA biosynthesis using paclobutrazol (PAC).

5.1.3 Aims

- Add or inhibit BR in the *A. thaliana quasimodo* mutant to further test the role of BR in regulating tissue tension-compression
- Test if other hormonal regulators of growth also reduce tissue tension-compression by inhibiting GA in *U. gibba*

5.2 Results

5.2.1 Treating *qua2-1* with epiBL rescues crack phenotype

To determine if epiBL could reduce the crack phenotype in *Arabidopsis qua 2-1*, I grew *qua 2-1* hypocotyls in the dark on medium containing 1 µM epiBL (treated) or without (untreated). A concentration of 1 µM had been used to rescue *Arabidopsis dwf4* to wild type (Azpiroz *et al.*, 1998). To visualise cell walls, I stained plants with propidium iodine 4 days after stratification (DAS) and imaged the whole hypocotyl using confocal microscopy. Consistent with previous findings (Verger *et al.*, 2018), untreated hypocotyls had long epidermal cells and cracks that typically spanned 1 or 2 cell files ($\bar{x}$ = 1.543, *SD* = 1.347, *SEM* = 0.106) (figure 5.1Ai and ii). Treatment with epiBL significantly reduced crack width ($p < 0.05$) (figure 5.1D), with most cracks spanning a single cell file ($\bar{x}$ = 1.087, *SD* = 0.417, *SEM* = 0.087) (figure 5.1Bi and ii). Also, the number of cracks per hypocotyl was higher (n cracks = 23) compared to the untreated control (n cracks = 162). Therefore, epiBL partially rescued the crack phenotype of *qua 2-1*.

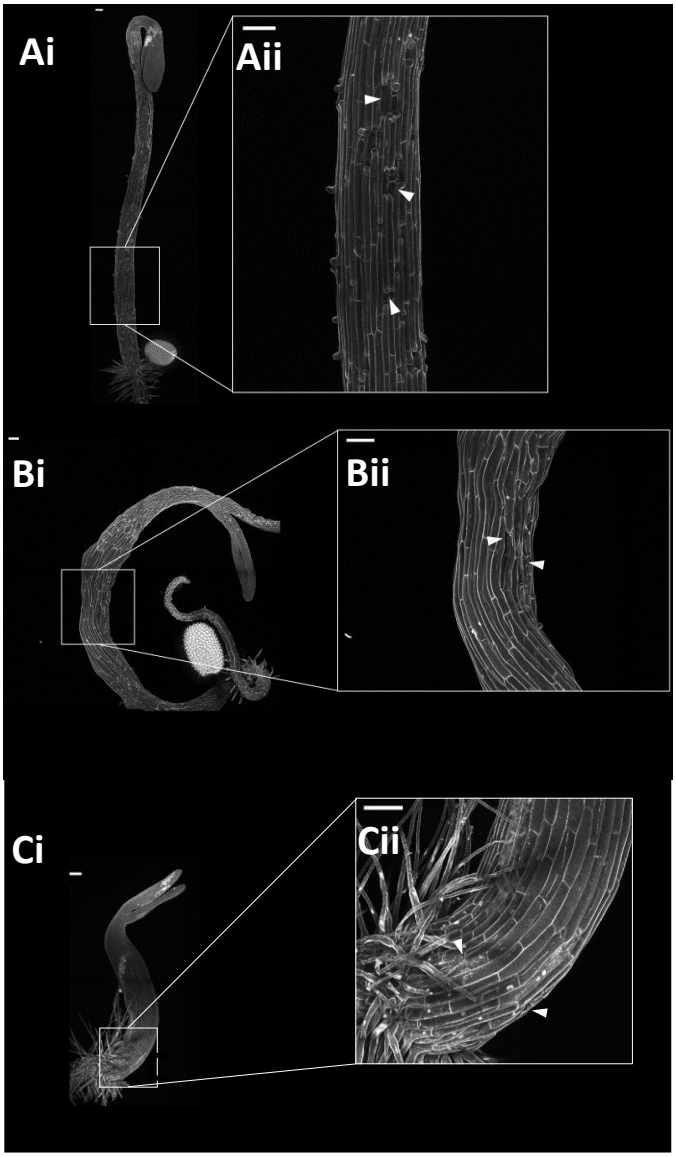

Figure 5.1 Treating *qua 2-1* with epibrassinolide rescues the crack phenotype

Ai) Dark grown *qua2-1* hypocotyl 4 days after stratification, ii) cracks highlighted with white arrows.

Bi) Dark grown *qua2-1* + 1 µM epiBL hypocotyl 4 days after stratification, ii) most cracks rescued but small cracks highlighted with white arrows.

Ci) Dark grown *qua2-1* + 2 µM BRZ hypocotyl 4 days after stratification, ii) possible cracks highlighted with white arrows.

Scale bars are 100 µm.

D) Average number of cell files a crack spans. Average crack width stats: *qua2-1* untreated to *qua2-1* + 1 µM epiBL 0.001198894 (*). *qua2-1* untreated n hypocotyls = 5, n cracks = 162. *qua2-1* + 1 µM epiBL n hypocotyls = 6, n cracks = 23

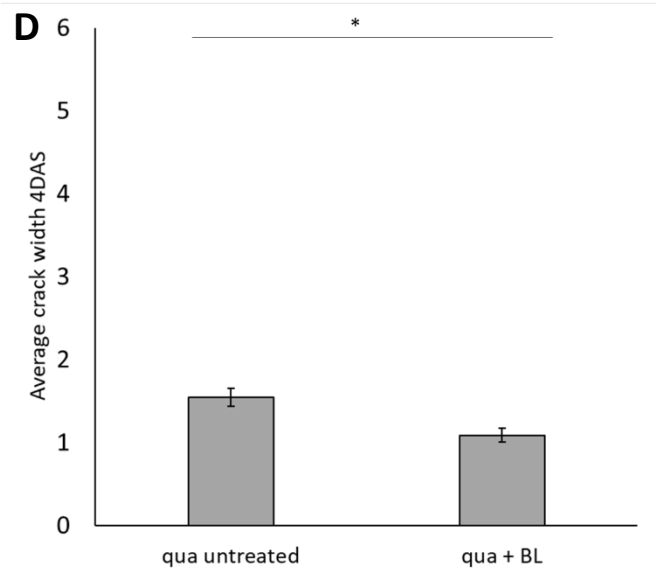

5.2.2 Crack phenotype is exacerbated by inhibiting BR

To determine whether the crack phenotype was exacerbated by inhibiting BR, I treated *qua 2-1* mutants with an inhibitor of BR biosynthesis brassinazole (BRZ). A concentration of 2 µM BRZ had been used to severely dwarf wild type *Arabidopsis* plants in (Nagata *et al.*, 2000). At 4DAS, hypocotyls treated with 2 µM BRZ had a crack number and phenotype similar to the untreated control (figure 5.1Ci and ii). At 9DAS there was no further increase in average crack width for untreated controls ($\bar{x}$ = 1.636, *SD* = 1.319, *SEM* = 0.230) (figure 5.2Ai and ii). By contrast, BRZ-treated hypocotyls displayed significantly larger cracks ($p < 0.001$) ($\bar{x}$ = 1.087, *SD* = 0.417, *SEM* = 0.087) (figure 5.2Bi and ii) at 9DAS (figure 5.2D). Therefore, inhibiting BR biosynthesis exacerbates the crack phenotype of *qua 2-1* at 9DAS.

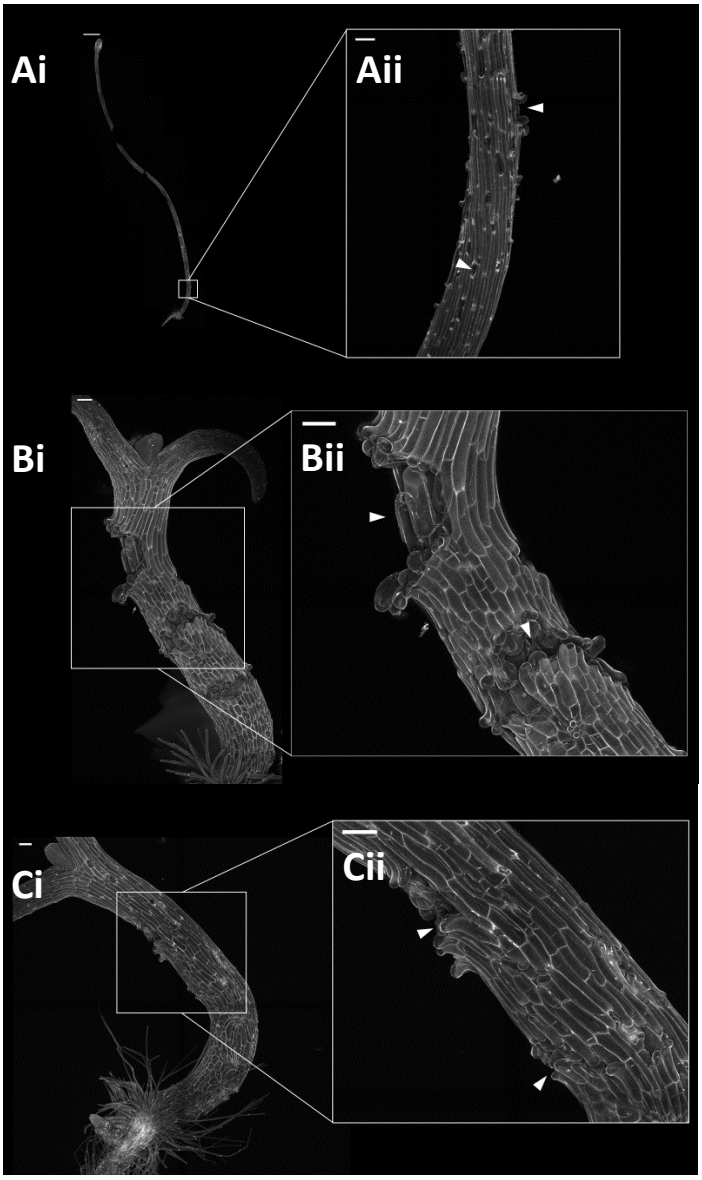

Figure 5.2 Treating *qua2-1* with BRZ, but not PAC, exacerbates the crack phenotype

Ai) Dark grown *qua2-1* hypocotyl 9 days after stratification, ii) cracks highlighted with white arrows

Bi) Dark grown *qua2-1* + 2 µM BRZ hypocotyl 9 days after stratification, ii) large cracks highlighted with white arrows

Ci) Dark grown *qua2-1* + 1 µM PAC hypocotyl 9 days after stratification, ii) cracks highlighted with white arrows

Scale bars are 100 µm except Ai which is 1 mm

D) Average number of cell files a crack spans. Average crack width stats: *qua2-1* untreated to *qua2-1* + 2 µM BRZ 7.10078E-05 (***). *qua2-1* untreated to *qua2-1* + 1 µM PAC 0.172728994 (ns). *qua2-1* + 2 µm BRZ to *qua2-1* + 1 µM PAC 0.001550632 (**).

qua2-1 untreated n hypocotyls = 1, n cracks = 33. *qua2-1* + 1 µM BRZ n hypocotyls = 4, n cracks = 43. *qua2-1* + 1 µM PAC n hypocotyls = 2, n cracks = 53

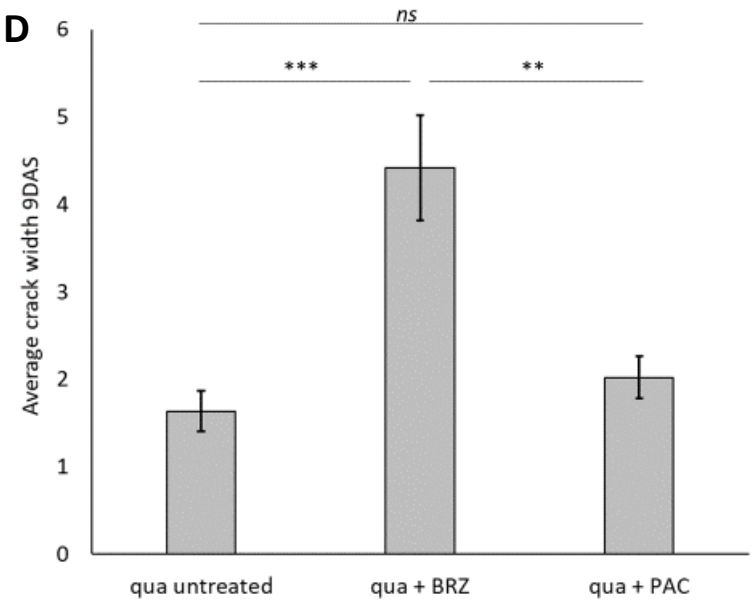

5.2.3 Inhibiting GA reduces internode length

To determine if this exacerbation of phenotype is specific to BR inhibition, I treated mutant hypocotyls with the GA biosynthesis inhibitor paclobutrazol (PAC) and characterised the crack phenotype at 9DAS (figure 5.2Ci and ii). I found that crack width ($\bar{x}$ = 2.022, *SD* = 1.640, *SEM* = 0.241) was not significantly increased compared to untreated mutants (figure 5.2D), suggesting that the exacerbation of the crack phenotype is not replicated by inhibiting GA.

To explore the effects of growth inhibitors on *U. gibba*, I passaged wild type tissue in either BRZ or PAC. I used a range of concentrations (0.05 – 1.0 µM BRZ and 0.5 – 100 nM PAC) and selected concentrations of 0.5 µM BRZ and 50 nM PAC as they produced an internode length roughly similar to the *dw1* mutant (figure 5.3A-D).

Figure 5.3 Treating wild type with growth inhibitors reduces the size of the plant

A) Untreated wild type, B) *dw1*, C) wild type treated with 0.5 µM BRZ and D) wild type treated with 50 nM PAC. Scale bar is 10 mm

Whilst the internode length of the wild type + BRZ ($\bar{x}$ = 0.561, *SD* = 0.130, *SEM* = 0.046) roughly phenocopied the *dw1* mutant (figure 5.3B and C), internode length was significantly shorter ($p < 0.001$). Wild type + PAC ($\bar{x}$ = 0.467, *SD* = 0.073, *SEM* = 0.021) was also significantly shorter than *dw1*. Leaf length in wild type + BRZ ($\bar{x}$ = 1.25, *SD* = 0.350, *SEM* = 0.124) was significantly shorter ($p < 0.001$) than wild type. Wild type + PAC leaf length ($\bar{x}$ = 0.367, *SD* = 0.056, *SEM* = 0.016) was also significantly shorter than wild type, and shorter than both *dw1* and wild type + BRZ ($p < 0001$) (figure 5.4A). Therefore, inhibiting BR and GA reduces vegetative organ length.

I also measured leaf and internode width (figure 5.4B). Leaf width for wild type + BRZ ($\bar{x}$ = 0.142, *SD* = 0.023, *SEM* = 0.008) was not significantly different ($p > 0.05$) from either untreated wild type or *dw1*, whereas wild type + PAC ($\bar{x}$ = 0.053, *SD* = 0.011, *SEM* = 0.003) was significantly narrower ($p < 0.001$) than both wild type and *dw1*. Internode width of wild type + BRZ ($\bar{x}$ = 0.188, *SD* = 0.005, *SEM* = 0.002) was significantly greater than untreated wild type ($p < 0.001$) and similar to *dw1* ($\bar{x}$ = 0.143). Wild type + PAC internode width ($\bar{x}$ = 0.097, *SD* = 0.015, *SEM* = 0.004) was significantly less than *dw1* or wild type ($p < 0.001$). This suggests that inhibiting BR leads to vegetative organs which are shorter in length but greater in width; whereas inhibiting GA leads to and reduction in both length and width of vegetative organs.

To further clarify the relationship between organ length and width, I plotted the ratio of length/width. The length/width for wild type + BRZ leaves ($\bar{x}$ = 8.75, *SEM* = 0.64) was around 50 % of *dw1* leaves ($\bar{x}$ = 16.94, *SEM* = 0.43) was around 20 % of wild type ($\bar{x}$ = 48.37, *SEM* = 5.64). Wild type + PAC leaves ($\bar{x}$ = 3.21, *SEM* = 0.30) was around 20 % of *dw1* and 7 % of wild type. Length/width for wild type + BRZ internodes ($\bar{x}$ = 2.99, *SEM* = 0.23) was also around 50 % of *dw1* internodes ($\bar{x}$ = 5.14, *SEM* = 0.30) and around 20 % of wild type ($\bar{x}$ = 16.49, *SEM* = 1.22). Wild type + PAC internodes ($\bar{x}$ = 4.96, *SEM* = 0.34) was comparable to *dw1* internodes and around 30 % of wild type. These results indicate that BRZ has a similar but stronger effect on length/width that *dw1,* and that PAC has a stronger effect on the leaf than the internode.

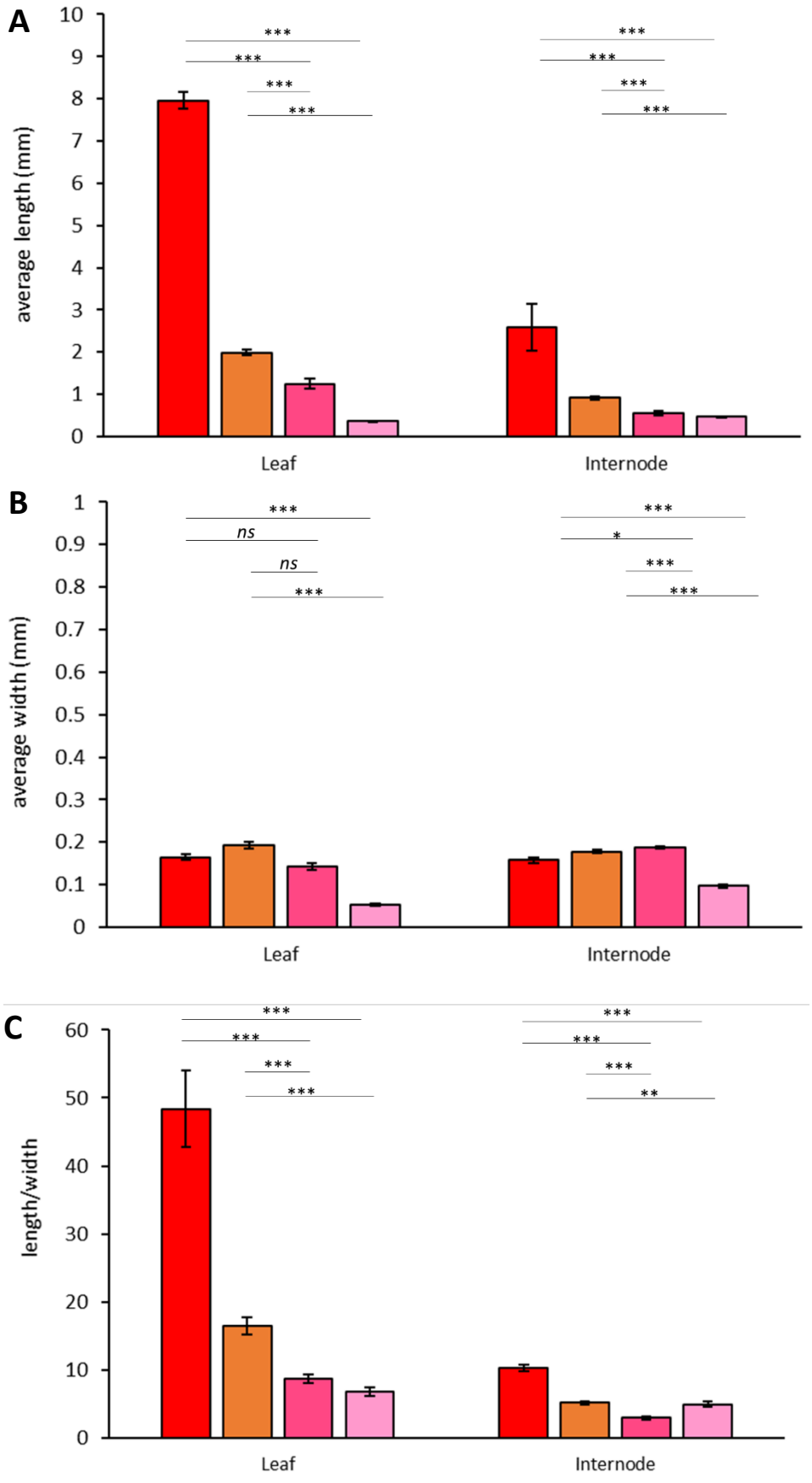

Figure 5.4 Both BRZ and PAC reduce vegetative organ size in U. gibba

A) Average leaf and internode length measurements of wild type (red*), dw1* (orange), wild type + 0.5 µM BRZ (dark pink) and wild type + 50 nM PAC (light pink). Leaf length stats: wild type to wild type + BRZ 3.79257E-08 (***), wild type to wild type + PAC 2.17751E-08 (***), *dw1* to wild type + BRZ 0.000302198 (***), *dw1* to wild type + PAC 4.33621E-23 (***). Internode length stats: wild type to wild type + BRZ 4.6803E-07 (***), wild type to wild type + PAC 4.68553E-07 (***), *dw1* to wild type + BRZ 3.67815E-05 (***), *dw1* to wild type + PAC 2.02854E-08 (***).

B) Average leaf and internode width measurements. Leaf width stats: wild type to wild type + BRZ 0.732410711 (*ns),* wild type to wild type + PAC 8.40175E-09 (***), *dw1* to wild type + BRZ 0.069407374 (*ns*), *dw1* to wild type + PAC 9.09049E-15 (***). Internode width stats: wild type to wild type + BRZ 0.030811323 (*), wild type to wild type + PAC 1.49182E-08 (***), *dw1* to wild type + BRZ 1.42191E-09 (***), *dw1* to wild type + PAC 6.62382E-08 (***).

C) Ratios of average leaf length to width and average internode length to width measurements. Leaf ratio stats: wild type to wild type + BRZ 1.83662E-06 (***), wild type to wild type + PAC 1.44862E-06 (***), *dw1* to wild type + BRZ 6.1253E-09 (***), *dw1* to wild type + PAC 1.10155E-13 (***). Internode ratio stats: wild type to wild type + BRZ 6.93906E-06 (***), wild type to wild type + PAC 5.68144E-05 (***), *dw1* to wild type + BRZ 2.66737E-08 (***), *dw1* to wild type + PAC 0.004555529 (**).

Error bars show SEM. wild type: 3 individuals, stolons n= 12. *dw1*: 10 individuals, stolons n = 40. wild type + BRZ: 2 individuals, stolons n= 8. wild type: + PAC 3 individuals, stolons n= 12

5.2.4 Inhibiting GA does not produce the same cellular phenotype as *dw1*

To determine the effect of inhibitors on epidermal cells, 2.5D cell segmentation was performed in collaboration with Karen Lee where I prepared samples and performed confocal microscopy and Karen performed the segmentation and produced cellular data. Heat maps revealed that cell area for wild type was around 3 times the size of *dw1* (figure 2.16 and 2.17A). Cell area for wild type + BRZ was roughly similar to that of *dw1*; whereas cell area for wild type + PAC was greater than *dw1* and slightly less than wild type (figure 5.5). There was no statistically significant difference ($p > 0.05$) between average cell area (figure 5.6A) for wild type + BRZ ($\bar{x}$ = 281.97 µm^2, *SEM* = 2.47) and *dw1* ($\bar{x}$ = 292.82 µm^2, *SEM* = 4.78). Average cell area for wild type + PAC ($\bar{x}$ = 786.39 µm^2, *SEM* = 11.73) was larger than *dw1* or wild type + BRZ, and slightly less than wild type ($\bar{x}$ = 845.74 µm^2, *SEM* = 24.07) ($p < 0.001$), indicating that PAC has a small effect in reducing cell area. Average cell length parallel to the stolon (figure 5.6B) was around four times longer in wild type ($\bar{x}$ = 41.69 µm, *SEM* = 0.98) than *dw1* ($\bar{x}$ = 13.17 µm, *SEM* = 0.15). Cell length parallel to the stolon was comparable for *dw1* ($\bar{x}$ = 13.17 µm, *SEM* = 0.15) and wild type + BRZ ($\bar{x}$ = 15.07 µm, *SEM* = 0.122) whilst cells were longer in wild type + PAC ($\bar{x}$ = 30.44 µm, *SEM* = 0.41), but still slightly shorter than wild type. Average cell length perpendicular to the stolon (figure 5.6C) was similar in wild type ($\bar{x}$ = 18.66 µm, *SEM* = 0.33) and *dw1* ($\bar{x}$ = 17.08 µm, *SEM* = 0.23). Cell length perpendicular to the stolon was less for wild type + BRZ ($\bar{x}$ = 15.82 µm, *SEM* = 0.11) than *dw1* ($\bar{x}$ = 17.08 µm, *SEM* = 0.30) or wild type; whereas wild type + PAC ($\bar{x}$ = 22.40 µm, *SEM* = 0.26) was greater than wild type. Thus, treating wild type with 0.5 µM BRZ has a similar effect on epidermal cell size and shape as the *dw1* mutation; whereas treating wild type with PAC has a small effect in reducing cell length parallel and increasing cell length perpendicular to the stolon, with no strong effect on cell area. Therefore, inhibiting GA does not have the same effect on epidermis cell shape and size as inhibiting BR.

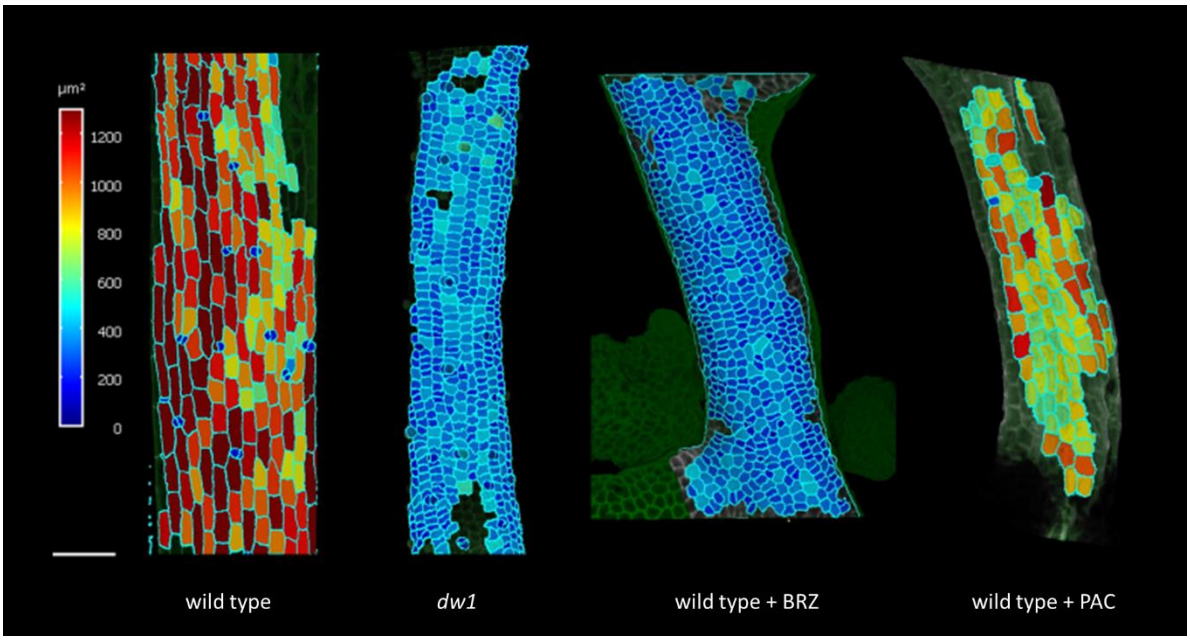

Figure 5.5 Inhibiting BR, but not GA, in wild type reduces epidermal cell size

Heat maps from 2.5D surface segmentation reveals that epidermal cell size is reduced in wild type + BRZ compared to untreated wild type, similar to *dw1*. In wild type + GA, cell size is not reduced compared to wild type. Scale bar is 100 µm.

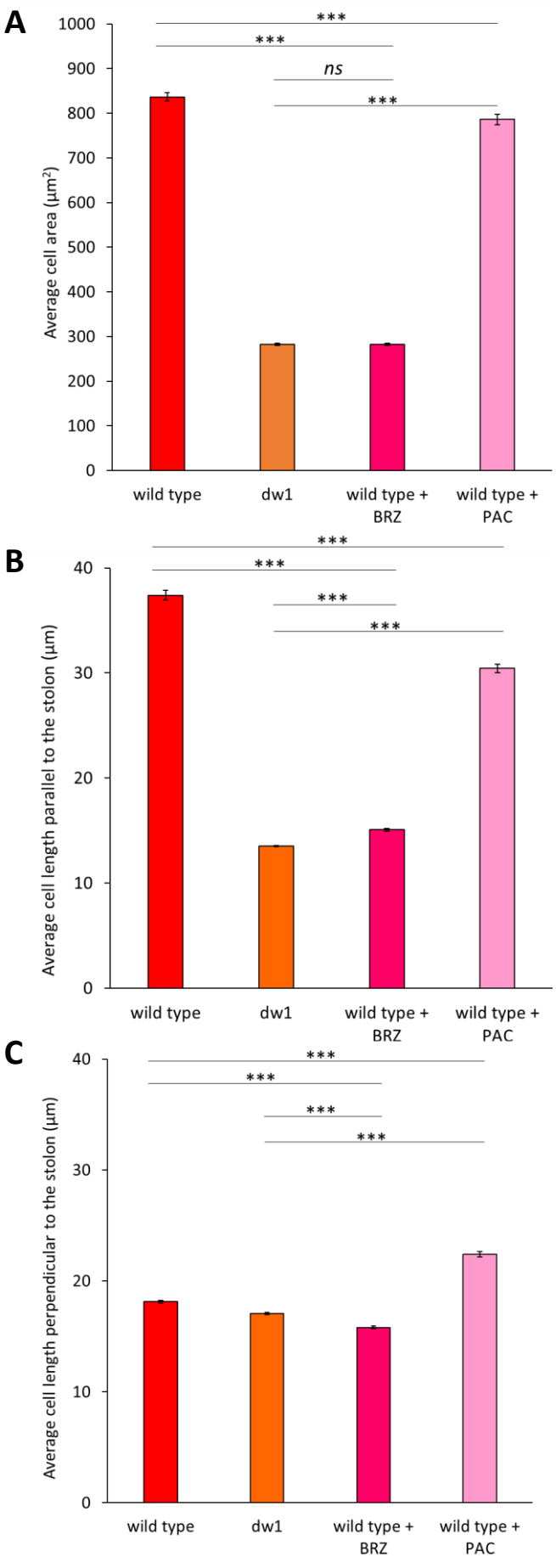

Figure 5.6 Data from cell segmentation analysis indicates that BRZ, but not PAC, has a similar effect on cell size and shape as dw1

A) Average cell area. Cell area *t* tests: wild type to wild type + BRZ *p*=0 (***), wild type to wild type + PAC *p*=0.000624708 (***), *dw1* to wild type + BRZ *p*=0.896104737 (ns), *dw1* to wild type + PAC *p*=4.2907E-182 (***).

B) Average cell length parallel to the stolon. Cell length parallel *t* tests: wild type to wild type + BRZ *p*=0 (***), wild type to wild type + PAC *p*=6.68048E-28 (***), *dw1* to wild type + BRZ *p*=6.69774E-27 (***), *dw1* to wild type + PAC *p*=2.3636E-176 (***).

C) Average cell length perpendicular to the stolon. Cell length perpendicular *t* tests: wild type to wild type + BRZ *p*=3.54517E-45 (***), wild type to wild type + PAC *p*=1.75774E-43 (***), *dw1* to wild type + BRZ *p*=3.42488E-17 (***), *dw1* to wild type + PAC *p*=1.88754E-56 (***).

wild type n stolons = 8, n cells = 1817, *dw1* n stolons = 5, n cells = 2289, wild type + BRZ n stolons = 2, n cells = 1104, wild type + PAC n stolons = 3, n cells = 581

To find out how the inhibitors had affected the inner tissues compared to the epidermis, I used confocal microscopy to identify if the wiggly vasculature phenotype had been replicated through reducing the length of the internode (figure 5.7). I found examples of the wiggly vasculature phenotype in wild type + BRZ, although it was not as common as in *dw1.* In wild type + PAC I did not find any examples of the wiggly vasculature phenotype. Therefore, the straight vasculature and larger epidermal cell size suggests that inhibiting GA has a different effect on tissue layers than inhibiting BR.

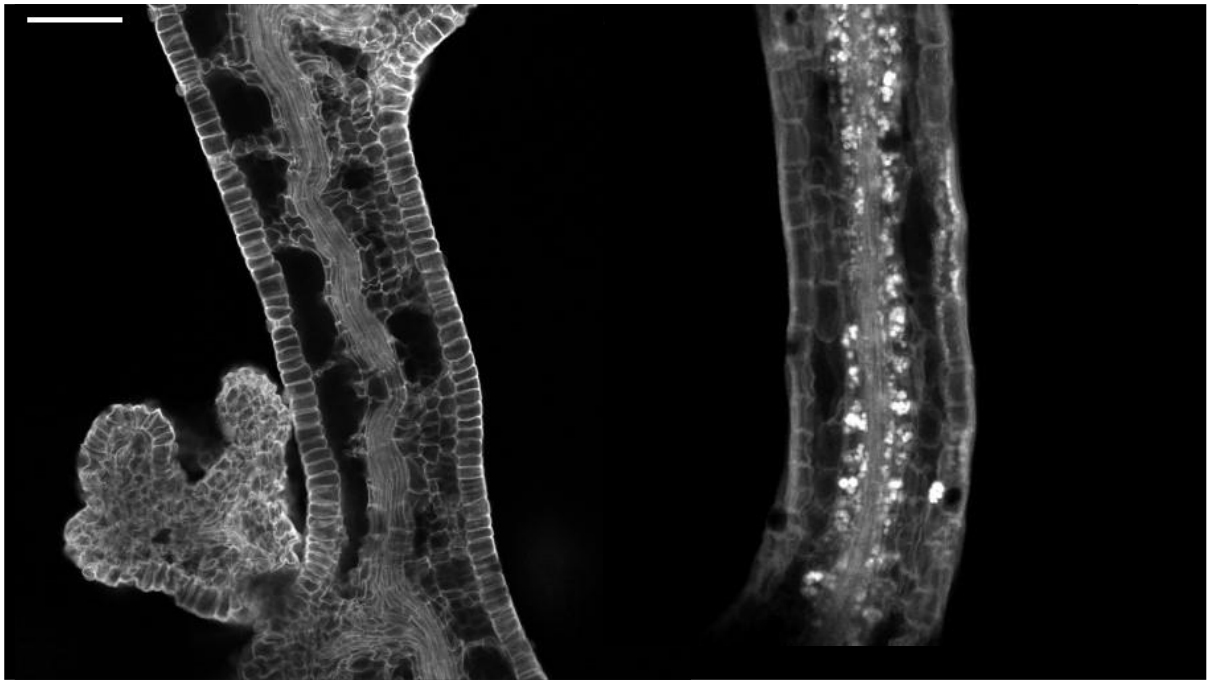

Figure 5.7 Wiggly vasculature phenotype can be replicated in *U. gibba* with BRZ, but not PAC

Confocal scans of inner tissues of mature stolons of A) wild type + 0.5 µM BRZ showing a wiggly vasculature and B) wild type + 50 nM PAC showing a straight vasculature. Scale bar is 100 µm

5.3 Discussion

5.3.1 Inhibiting BR likely increases tissue tension-compression in *Arabidopsis*

Inhibiting BR by BRZ results in larger, wider cracks in the epidermis of *qua2-1* at 9DAS. This suggests an increase in tissue tension-compression, caused by increased specified growth differential between the epidermis and inner tissues. In *qua2-1*, the reduction of cell-to-cell adhesion causes a weaker epidermis that cannot support the increase in tension and therefore larger cracks appear. This hypothesis predicts that the OEW of *qua2-1* + BRZ, or even Col-0 + BRZ, would likely be thicker than untreated OEW. Further TEM imaging may confirm this. Treating *qua2-1* with epiBL leads to fewer cracks in the epidermis. This can be explained by a reduced growth differential between tissue layers and a therefore a reduction in tissue tension-compression.

Alternatively, epiBL and BRZ could act on cell adhesion and not on tissue tension-compression. In this scenario, treating with BRZ may further inhibit cell adhesion which leads to larger cracks, with the inverse being true for treating with epiBL. Whilst this explanation cannot be discounted, an indication of tissue tension-compression being involved can be seen in figure 5.2Bii. Here, cells of *qua2-1* treated with BRZ have split at the epidermis. Epidermal cells at the edge of the crack are highly curved and the ends rounded due to turgor (Ivakov & Persson, 2013). This may be because the outer wall, which was under tissue tension, has shrunk and the inner wall, which was under compression, has expanded. Whilst the curved tips of cells can be observed in the untreated *qua2-1* mutant, they are not as prominent as in *qua2-1* + BRZ. Measuring the curvature of these cells may provide another measure of tissue tension-compression.

Cracks are only in the epidermal cell layer and not the inner tissues which are visible under the cracks. Here, where the cells have split apart, they have not bent away from each other, but remain parallel to the direction of growth. This confirms that the forces acting on the inner tissues are not the same

as in the epidermis and that the enhanced cracks following BRZ treatment likely arise through increased tissue tension-compression.

5.3.2 Tissue tension-compression phenotypes are not replicated by inhibiting GA

Treating wild type *U. gibba* with BRZ reduces internode length and cell size, and can also lead to a wiggly vasculature phenotype. This raised the question whether these phenotypes could be reproduced by treating with other growth hormone inhibitors or whether they were BR specific. To test if inhibiting GA replicated the phenotypes created through inhibiting BR, I treated *qua2-1* with the GA synthesis inhibitor PAC. Treating *Arabidopsis qua2-1* with PAC does not significantly increase crack width. This suggests that treating with PAC does not increase tissue tension-compression. Furthermore, a wiggly vasculature phenotype does not form when treating wild type *U. gibba* with PAC, further indicating that tissue tension-compression is not increased. Whereas internode length decreases in wild type + PAC, epidermal cell size does not decrease as much as treating wild type with BRZ or in *dw1*. This indicates cell number might be reduced through treatment with PAC. Alternately, PAC could act earlier than BRZ and inhibits growth while cells are still dividing. Given that the wiggly vasculature arises later in development (after internode 4) when cell divisions have stopped, it may be that the differential effects on the epidermis would have little effect at this stage or that PAC affects all layers equally. To confirm that these results are generated by the absence of GA and not a biochemical side-effect of PAC, future experiments would treat with both PAC and GA. Taken together, my results suggest that the mechanism of modulating tissue tension-compression that I have explored here is BR specific.

5.4 Conclusion

BR can reduce tissue tension-compression in a system without internal air spaces. Inhibiting BR in both *U. gibba* and the *Arabidopsis qua2-1* mutant results in two distinct phenotypes which arise from the same mechanical process. These phenotypes are not replicated when treating with or inhibiting GA, suggesting that reduced tissue tension-compression is a specific effect of BR.

6 General Discussion

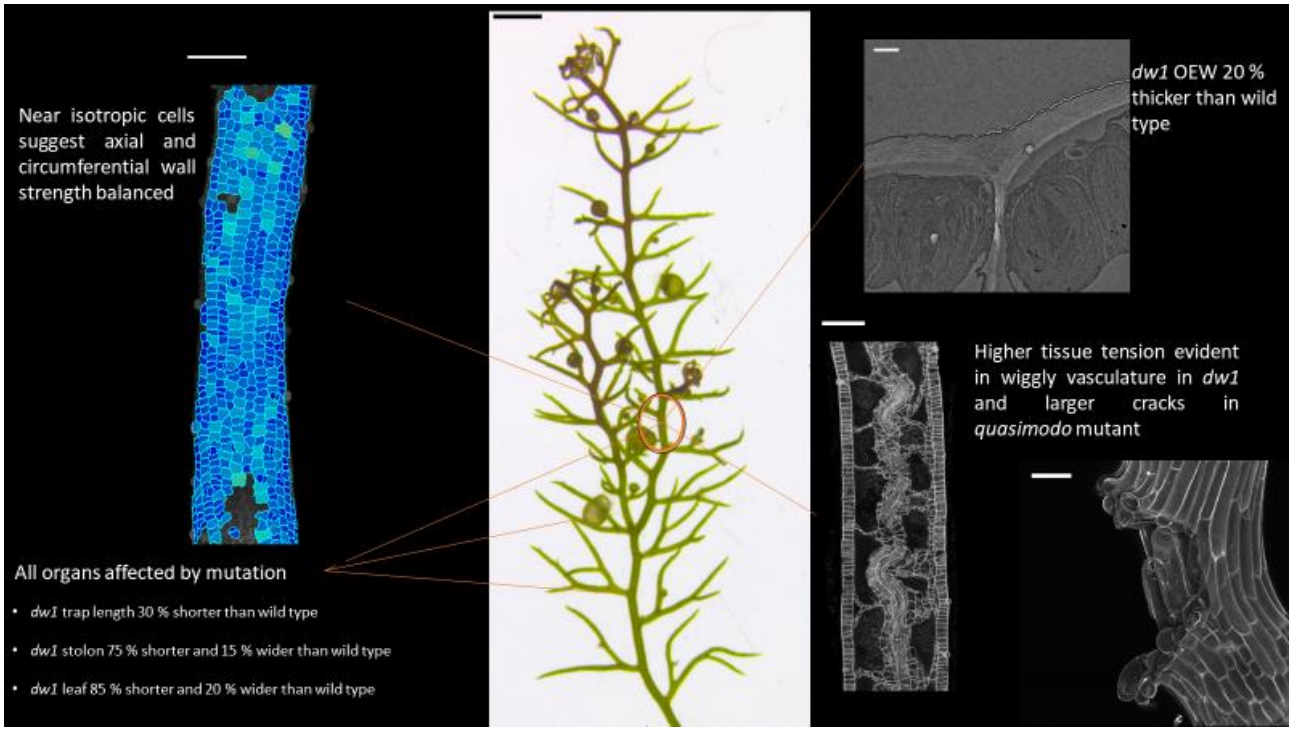

Figure 6.5.1 Summary of results in the absence of BR

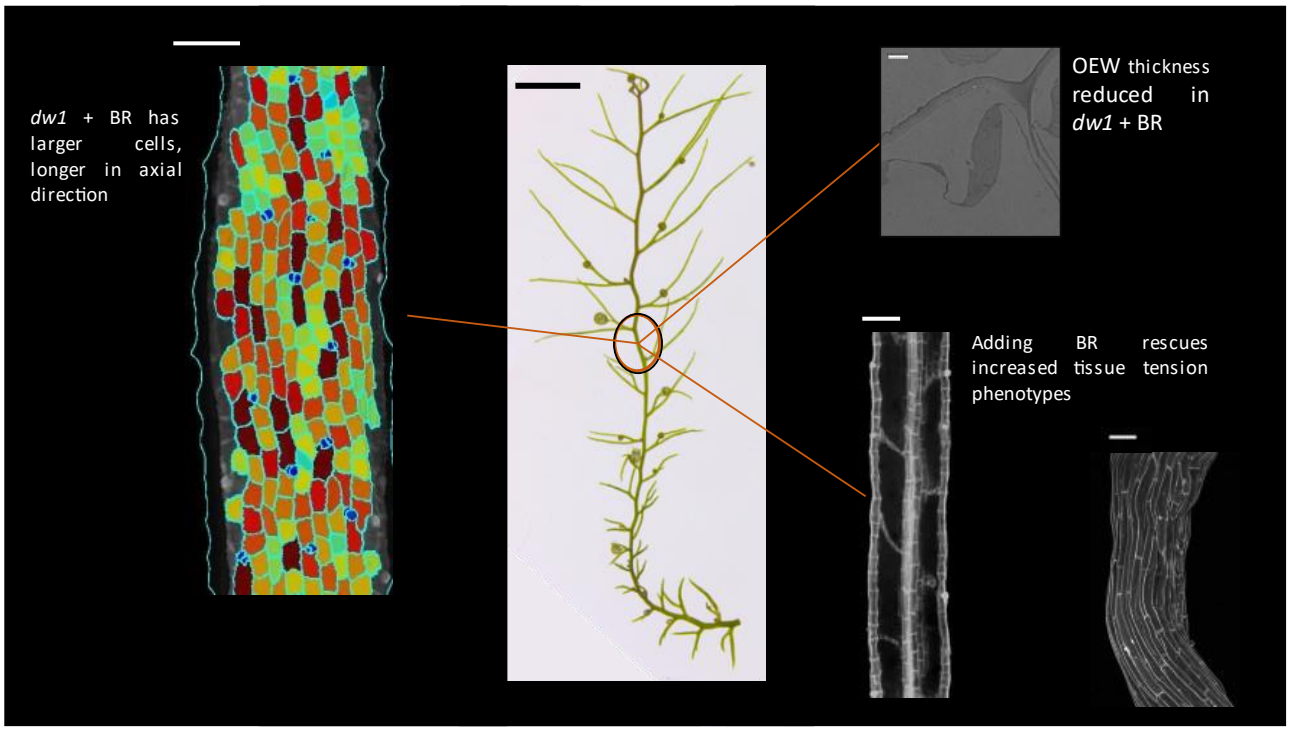

Figure 6.2 Summary of results in the presence of BR

6.1 *DW1* encodes a BR biosynthetic enzyme

A dwarf mutant was recovered from an EMS mutagenesis screen in *U. gibba* (figure 2.4, chapter 2). The mutant had two classes of phenotype, where internode and leaf length were reduced to either an intermediate or extreme extent compared to wild type (figure 2.5, chapter 2). Segregation analysis suggested that two mutations were segregating in the mutant family: recessive *dw1*, which caused a dwarfing phenotype and a recessive modifier of *dw1* (*eod*) which enhances the dwarfing phenotype. Sequence analysis from WGS produced only one candidate SNP was identified in the CDS of a BR biosynthesis gene, where an early stop codon was introduced (figure 3.1, chapter 3). Analysis of wild type and *dw1* using mass spectrometry revealed that no BR precursors after the candidate enzyme were detected in wild type. Furthermore, exposing *dw1* to epiBL fully rescued the mutant phenotype. Thus, together this data provides strong evidence that *DW1* is a BR biosynthesis gene.

6.2 DW1 is involved in organ anisotropy

The mutation in *dw1* affects all vegetative parts of the plant. More isotropically-shaped organs, such as the trap, are less affected in *dw1* (30 % shorter than wild type, figure 2.3, chapter 1) than the more anisotropic organs (figure 2.7, chapter 1) such as the stolon (75 % shorter and 15 % wider) and the leaf (85 % shorter and 20 % wider). Therefore, the *dw1* mutation makes the vegetative plant organs more isotropic in shape. These results suggest that BR increases growth anisotropy and therefore its removal has greatest effect on those organs which normally have greatest anisotropy. Unfortunately, I could not get *dw1* to flower, as it would have been interesting to compare the complex floral organs to wild type. The stunted growth, inability to flower, as well as the dysfunctional trap (figure 2.6, chapter 1), indicate that *DW1* contributes to fitness in natural populations.

6.3 BR reduces tissue tension-compression in stolons and stems

I present evidence for elevated tissue tension-compression in *dw1* compared to wild type (figure 6.1). The evidence is based on the wiggly vasculature phenotype of *dw1* (figure 2.8, chapter 1) and differential thickness of OEW (figure 4.6, chapter 3). As described in the Introduction, if specified growth rates differ between layers, a mechanical conflict arises (Coen & Rebocho, 2016). Failure to resolve the conflict leads to elevated tissue tension-compression. In wild type, the epidermis may have lower specified growth rate than inner tissue, as suggested by the thicker outer epidermal cell walls in other species (Kutschera, 1992). If unresolved, the conflict would generate tissue tension in epidermis and tissue compression in the internal tissue, which is resolved by growth. The tissue compression on internal tissue, however, is insufficient to cause buckling of the vasculature. In *dw1*, specified growth is globally reduced compared to wild type, but in the epidermis may be reduced by more in than the inner tissues, evidenced by epidermal walls of greater thickness, thus increasing tissue tension-compression. The degree of tissue tension-compression can be reduced by curvature of the vasculature, which allows it to grow in length more than the epidermis, thus explaining the wiggly phenotype. Adding BR to *dw1* restores vegetative organ length, but not width, to wild type (figure 3.5, chapter 2) and the wiggly vasculature phenotype in *dw1* is rescued when treating with BR. This suggests that BR has increased the specified growth rate in the epidermis of *dw1* to match the specified growth rate of the inner tissues, similar to wild type. This leads to a reduction of excessive tensile force on the epidermis and therefore, a reduction in the excess compressive forces on the internal tissues. Adding BR to a system with unresolved conflicts, resolves the conflicts without the vasculature needing to yield to the extra compressive forces (figure 6.2). Key to these tissue layer dynamics is the differential specified growth rate between layers. *In situ* hybridisation of *DW1* provides some indication that *DW1* is localised to the epidermis. Vukašinović *et al.* (2021) used a

DWF4-GFP reporter line to identify the expression of *DWF4* in *Arabidopsis* roots. They found that *DWF4* expression was maximal in the epidermis and somewhat absent in the inner tissues. Whilst this can inform our knowledge on the production sites of BR biosynthesis enzymes, it does not infer that action of BR is localised to the epidermis.

Adding epiBL to *qua2-1* rescues the crack phenotype, it can be assumed that untreated *qua2-1* still has the same levels of endogenous BR found in wild type *Arabidopsis*. Therefore, treating *qua2-1* with epiBL provides excess BR, suggesting that an epidermal specified growth rate higher than found in untreated *qua2-1* is required to rescue the crack phenotype. That untreated *qua2-1* still forms cracks suggests that tissue tension-compression is still present and may be necessary for growth in wild type. Furthermore, whilst OEW thickness is reduced in *dw1* + epiBL to wild type, observations in TEM images suggest that OEW are still thicker than internal walls in both wild type and *dw1* + epiBL. Whilst this is not yet quantified, thicker OEW compared in inner walls are found in wild types of other systems (Kutschera & Niklas, 2007), suggesting that endogenous BR plays a role in maintaining tissue tension-compression at a level that is advantageous to the plant. That adding BR releases tissue tension-compression is supported in treatments of *qua2-1* with epiBL where the crack phenotype of untreated *qua2-1* is almost completely rescued. Observations in both systems can be accounted for by BR releasing tissue tension-compression.

An alternative hypothesis to tissue tension-compression is that wiggly vasculature is due to changes in the specified orientation of vascular growth (Buschmann *et al.*, 2004). The observation that vasculature tissue forms in a straight line and becomes wiggly later development (figure 4.5, chapter 3), suggests that if specified orientation of vascular is modified *in dw1*, this modification occurs late in development.

The two hypotheses (elevated tissue tension-compression vs modified growth orientation) make different predictions for the effect of BR inhibition in *Arabidopsis*. If BR inhibition increases tissue tension-compression, wiggly vasculature is not expected in *Arabidopsis* because the vasculature is

surrounded by closely packed cells which prevent buckling. However in *qua 2-1*, if BR inhibition changes orientation of inner tissue growth, vascular alignment might be expected to be disrupted by BR inhibition in *Arabidopsis* and there would be no expectation of elevated crack formation in the epidermis.

My observations support the predictions of the tissue tension-compression hypothesis. Inhibiting BR in the *qua2-1* mutant of *Arabidopsis* produces larger cracks (figure 5.2B, chapter 4). As there is reduced adhesion between epidermal cells, the mechanical conflict is reduced through epidermal cells separating. Therefore, observations in both *U. gibba* and *Arabidopsis* support the hypothesis that a loss of BR increases tissue tension-compression.

6.4 BR increases growth anisotropy by modifying cell wall properties

Mature *dw1* epidermal cells are smaller than wild type and almost isotropic in shape (figure 2.11, chapter 1). The cell shape phenotype in *dw1* is comparable to other BR mutants (Azpiroz *et al.*, 1998). Cell shape depends on the patterns of cell division and cell growth. Plant cell division typically follows the shortest-wall algorithm, whereby the new division wall takes the shortest path passing through the cell centre, reviewed in (Prusinkiewicz & Runions, 2012). Cell division also likely depends on cells reaching a threshold size, though this size may be under genetic control (Kuchen *et al.*, 2012). According to these rules, repeated rounds of division will produce cells with near-isotropic shapes and similar cells sizes. Length:width cell ratios would a maximum of 2:1 if growth is anisotropic, with the longest walls being aligned with the orientation of maximal growth and cell areas would vary by a factor of two.

In wild type stolons, epidermal cell divisions likely stop around wild-type node 0. At this stage cell shape is longer nearly twice as longer perpendicular to the stolon compared to parallel, suggesting

growth rate is greater circumferentially (figure 4.2, chapter 3). After cell division stops, cells elongate preferentially parallel to the stolon axis, reaching a length:width ratio of around 2 (figure 2.12, chapter 1) In *dw1* however, cell shapes remain the same as those produced during the expected cell division phase, and elongation parallel to the stolon does not occur (figure 4.2, chapter 3). Epidermal cell walls are also thicker than those of wild type (figure 4.6, chapter 3). These findings suggest that BR normally reduces the resistance of epidermal cell walls to expansion in the axial orientation.

As discussed in chapter 3, reduced cell size and shape in *dw1* could be attributed to increased synthesis of microfibrils parallel to the stolon axis compared to wild type. This explanation matches that of Xie *et al.*, (2011) who show that BR mutants contain less cellulose than wild type. Contrary to this idea, (Sánchez-Rodríguez *et al*., 2017) identify that *BIN2,* a negative regulator of BR signalling, has been linked with downregulation of the microfibril synthesis enzyme *CESA1*. In the absence of BR, *BIN2* inhibits *CESA1* and reduces cellulose synthesis. Why then might *dw1* epidermal cells have thicker walls than wild type?

Treating *dw1* with epiBL causes epidermal cell area to increase by around a factor of 3 (figure 3.7A, chapter 2), but wall thickness only reduces by around 15% (figure 4.6B, chapter 3). Similar results are obtained by comparing *dw1* with wild type (figure 4.6B, chapter 3). These findings suggest that BR affects the balance between increase in wall thickness through synthesis and reduction in wall thickness by stretching through growth. BR could reduce the proportion of microfibrils oriented parallel to the stolon, leading to greater growth (wall stretching) in that orientation. BR could also cause an overall increase in wall synthesis, but not quite enough to keep up with the wall thinning caused by wall extension. Thus, at any given time there would be fewer microfibrils in the wall aligned with the stolon axis.

Another possibility is that BR could promote wall extensibility (microfibril slippage) (Somssich *et al.*, 2021) rather than influencing the pattern of wall synthesis. To explain the enhanced anisotropy in the presence of BR, extensibility would have to be reduced preferentially perpendicular to the stolon axis.

BR would still have to elevate wall synthesis to counteract the thinning caused by cell expansion, but not quite enough, accounting for slightly reduced epidermal wall thickness.

Treatment of *dw1* stolons with epiBL rescues the mutant phenotype if treatment is given from internode 0 onwards. Treatment from internode 1 onwards gives partial rescue. The level of rescue decreases if treatment starts at progressively later internodes until internode 5, after which there is no rescue. *dw1* internodes stop growing at about internode 0. Thus, BR can act on *dw1* from about the time growth arrests. This may be that *BRI1* and other parts of the signalling pathway are not active once cell growth has stopped (Oh *et al.*, 2012). Alternately, *dw1* cell walls may have been modified at the point of maturity to such an extent that they resist the effect of BR, whether it be increasing extensibility or reducing wall synthesis. Therefore, the effect of treating with BR is not perceived in node 5 tissue that that is more mature. Full rescue of *dw1* internode length to wild type is found at node 0 and in less mature nodes, implying that it is around this stage that BR is acting on cell elongation in wild type. This may be due to an increase in cell wall thickness that can partially resist the effects of BR. In this divergence point between wild type and *dw1*, tissue tension-compression may build from a progressive thickening of the OEW at each developing internode. Whilst internal cell walls may thicken as well, an increase in OEW thickness will feed back to reduce the specified growth rate and increase tension in the epidermis and thus compression in the inner tissues. The inner tissues may have sufficient integrity to withstand the low degree of conflict placed upon it, but as compression increases with further OEW thickening, the degree of conflict may be such that the vasculature needs to buckle to resolve it. As node 0 is fully rescued, it could be assumed that OEW thickness in *dw1* is roughly the same as wild type. In node -1 and less mature, exposure to epiBL appears to rescue internode length to longer than wild type. Towards the end of the cell cycle, the treatment may provide BR at a level that is higher than wild type, leading to thinner walls at an earlier stage that allows for a greater resultant growth period during the cell elongation stage, suggesting that BR does not act this early in wild type. Therefore, the stage of development that *U. gibba* is sensitive to BR is between node 0 and node 5.

It possible that BR acts on both wall extensibility and synthesis (i.e., the two modes are not mutually exclusive). In both cases, a positive feedback can arise if the balance between cell wall thickening via synthesis and thinning through growth is upset. If synthesis does not keep up with growth, the wall becomes thinner and weaker, further increasing specified growth rate. Conversely, if synthesis outpaces growth, the wall becomes thicker and stronger, which further reduces specified growth. In wild type, the balance may be different for the epidermal and inner tissues. For the outer epidermal wall, synthesis may outpace growth, leading to thicker walls and thus increasing tissue tension. In *dw1* this balance is further shifted towards synthesis in the epidermal walls, leading to even thicker walls, increased tissue tension, and resulting in epidermal growth arrest early on. If cells division depends on cells reaching a threshold area (Prusinkiewicz & Runions, 2012) , early arrest of growth would also lead to arrest of cells division. Resolving the brassinosteroid-mediated cellular growth dynamics cannot be resolved without data on the cytoskeleton, future work would aim to uncover this in *Arabidopsis* and if possible, in *Utricularia* as well. Furthermore, the results from *qua2-1* could be used to generate hypotheses that could be tested using computer modelling.

6.5 Action from inhibition of GA is not the same as inhibiting BR

In the absence of BR, epidermal cells are smaller and have reduced elongation in the direction of growth through reducing the specified growth rate in the epidermis. In *dw1,* the effect on the epidermis is stronger than the vasculature. The results are not repeated when using the GA biosynthesis inhibitor PAC. Treating wild type *U. gibba* with PAC leads to shorter internodes but does not have the same strength of effect on reducing epidermal cell size as BRZ does, nor does treating with PAC replicate the wiggly vasculature. This suggests that vasculature straightness is maintained by the absence of a strong growth differential between tissue layers. Epidermal cells are larger and longer parallel to the stolon that *dw1* or wild type + BRZ, suggesting that PAC does not provide the mechanism

required to form the wiggly vasculature. This is supported in *qua2-1*, where treating with PAC does not have the same effect on crack width as BRZ, suggesting that tissue tension-compression has not been affected through epidermal constraint. As wild type + PAC epidermal cell size is larger than *dw1* or wild type + BRZ, yet stolon length is shorter than wild type, it could be inferred that the dwarfing effects of GA occur during cell division. This is consistent with findings in *Arabidopsis gai* mutant where fewer mitoses were found in the developing internode, without a strong effect on cell size (Serrano-Mislata *et al.*, 2017). Thus, the absence of GA does not have the same tissue layer effects as the absence of BR does, suggesting that the method of mechanic tissue layer interaction is BR specific.

6.6 Potential causal chain of events

Here I present a potential causal chain of events based on the above observations. In wild type, upregulation of BR towards the end of cell division reduces microtubules, and thus microfibrils, in the longitudinal orientation, preferentially weakening the wall in that orientation. BR also increases wall extensibility (microfibril slippage), promoting cell growth. The wall thinning due to growth is partially balanced by BR also increasing wall synthesis to maintain wall thickness. Eventually wall strength and inextensibility exceed turgor, leading to growth arrest of wild type.

In *dw1,* cell growth arrests early in the epidermis because wall strength and low extensibility fully resist turgor, giving a thick OEW. Division also stops because cells no longer reach their threshold size for division. The effects of BR are greater in the epidermis than the inner tissues, leading to epidermal specified growth arrest preceding that of internal tissue and tissue tension-compression. In *Utricularia*, air spaces allow the internal tissue can continue to grow despite the constraint from the epidermis, leading to buckling of vasculature. In *Arabidopsis* BR mutants, the internal tissue is constrained by the lack of intercellular spaces, leading to accumulation of tissue tension-compression

rather than tissue buckling. By promoting specified growth preferentially in the epidermis, BR treatment reduces tissue tension-compression in both cases. Thus, in addition to possible signalling mechanisms, BR influences cell layer interactions directly via tissue mechanics.

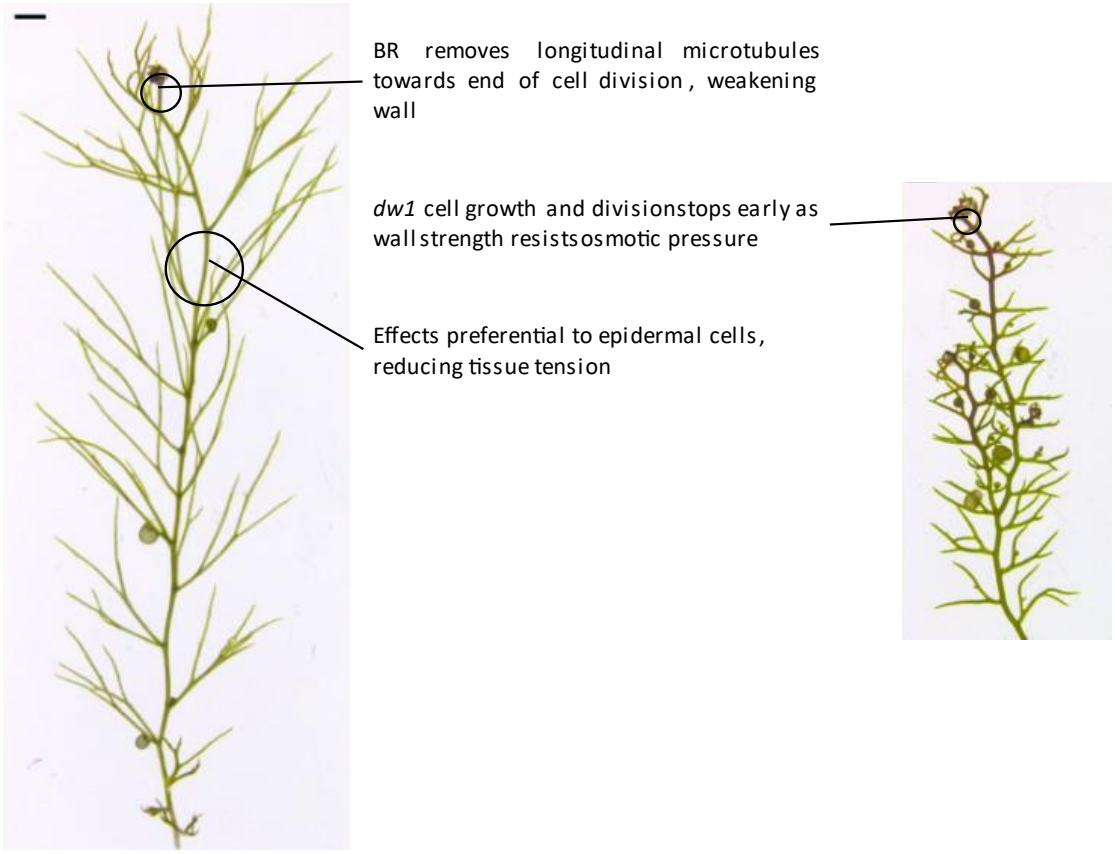

Figure 6.3 Potential causal chain of BR-mediated events in *U. gibba*

One question that arises is whether tissue tension-compression is adaptive. When the term was coined in the 19th century, plant physiologists thought of it as a resultant property of growth dynamics in plants (Sachs, 1875). Goriely (2019) has proposed that tissue tension-compression in cylinders promotes flextural rigidity – how much the stem resists bending. As the epidermal wall material is stretched, stiffness may increase in a non-linear fashion. Goriely hypotheses that as the OEW are stretched through tissue tension-compression, they become stiffer, increasing flextural rigidity. As BR reduces tissue tension-compression, this would be at the expense of some flextural rigidity. A prediction is that stems of BR mutants should be more resistant to bending than wild type. However, epidermal cell walls are also thicker in BR mutants which would also increase flextural rigidity. Separating these two effects may be difficult.

6.7 Future work

Previous experiments in sunflower have demonstrated tissue tension-compression through peeling of hypocotyl, where the excised outer tissues contracted, and the inner tissues expanded (Kutschera & Niklas, 2007). If a similar experiment is possible in a system with internal air spaces, a prediction could be made that the difference in shrinking/expansion of outer/inner tissues respectively would be greater in *dw1* than wild type and would be rescued in *dw1* + BR. Other classic tissue tension-compression experiments are longitudinal cutting experiments, also in sunflower hypocotyls. Here, the outward bending of the cut tissue indicates tissue tension-compression. It could be predicted that in the absence of BR, the amount of bending in the cut tissue would be increased due to increased tissue tension-compression. Perhaps such experiments could also be performed in other BR mutant such as *d2* in rice (Hong, Ueguchi-Tanaka*, et al.*, 2003) or *lil1* in maize (Castorina *et al.*, 2018). These systems could be advantageous over sunflower as genetic mutants of BR would be used instead of chemical inhibitors. On this topic, the use of BRZ in *qua2-1* does not necessarily give strong evidence

of the genetic control of tissue tension-compression through BR. If the same large crack phenotype could be replicated by crossing *dwf4* to *qua2-1*, then a stronger argument for BR genes acting on tissue tension-compression can be made. At the point of writing, crosses between heterozygotes of *dwf4* and *qua2-1* have been made and seed that requires screening has been collected. Through adding BR to *dw1* and *qua2-1,* I have shown that BR is involved in reducing tissue tension-compression. One effect that BR has is reducing OEW thickness is *dw1*. OEW have been specifically measured as they carry the greatest tensile load in the tissue (Kutschera & Niklas, 2007). A prediction could also be made on other cell walls across the tissue. It could be expected that the walls of epidermal cells other than the outer wall would also be thicker in *dw1* compared to wild type and *dw1* + BR. If wall thickness of cells in the inner tissues is not affected in *dw1,* this may provide further evidence that BR is acting preferentially in the epidermis.

6.8 Concluding remarks

I present examples of how tissue layers interact through a purely mechanical mechanism. This does not rule out signal-based methods of tissue layer interaction, whether they be based on chemical or mechanical (mechanosensing). But I have shown that the purely mechanical mechanism plays a part and is enhanced in mutants deficient in the growth-promoting hormone brassinosteroid. This thesis thus provides novel insights into growth mechanisms by integrating tissue layer interactions, tissue mechanics, the cellular basis of growth and hormone activity.

7 Methodology

7.1 *U. gibba* plant material and growth conditions

7.1.1 Tissue culture

Utricularia gibba seeds of wild-type plants were purchased from The FlyTrap Plants (Bergh Apton, UK). Plant material was grown in liquid MS plant tissue culture media (0.22 % Murashige and Skoog Medium (Duchefa Biochemie M0233), 2.5 % sucrose, pH 5.8) and maintained in a controlled environment room at 23 ±1 °C light at an intensity of 180 µmol/m^2/s with a 16-h light/8-h dark photoperiod.

7.1.2 Glasshouse conditions

Plant material was grown in the glasshouse to induce flowering for seed collection. Plants were grown in containers containing a 2 cm layer of peat and sand mix, topped up with reverse osmosis water.

7.1.3 Seed sterilisation

Seeds were washed for 5 minutes in 70 % ethanol, 0.1 % SDS, followed by a wash in sterile water. Seeds were then transferred to 4% parazone bleach, 0.2 % triton 100 for 10 minutes and then washed 3 times with sterile water.

7.1.4 Seed germination

Seeds were sown in sterilin jars containing a layer of solid culture medium (0.22 % Murashige and Skoog Medium (Duchefa Biochemie M0233), 2.5 % sucrose, 0.3 % agar, pH 5.8) topped up with liquid MS culture medium containing 0.1 mM ethephon (Sigma C0143). To make ethephon containing media, a concentrated 2.5 M ethephon solution was first made in a pH 3 buffer (41 mM disodium hydrogen phosphate, 79 mM citric acid) and then diluted in liquid media to a final concentration of 0.1 mM ethephon. Seedlings were germinated at 23 °C long day conditions (16 hours light/8 hours dark cycles). Once seeds had germinated, seedlings were removed from ethephon containing media and grown in MS liquid media as described above.

7.2 *A. thaliana* plant material and growth

7.2.1 Tissue culture

A. thaliana quasimodo 2-1 plants were grown on plates containing MS media (0.441% Murashidge & skoog including vitamins, 1% (w/v) glucose, 0.05% (w/v) MES, 1% Difco agar, pH to 5.7). Sterilised seeds were stratified in the dark at 4°C for 2 days, then exposed for light for 4 hours at 20°C in controlled environment before being wrapped in three layers of tin foil to ensure etiolation.

7.2.2 Seed sterilisation

Seeds were sterilised used 70% ethanol with 0.05% SDS for 5 minutes, followed by at least three washes in 100% ethanol. Seeds were then air-dried on sterile filter paper before being plated. If seeds

were receiving hormonal treatment, then this was added to the media that the seeds would germinate on.

7.3 General methods

7.3.1 Treating plant tissue with EMS

U. gibba plants were grown up in sterile culture for EMS treatment. Plant material was treated with; 0.01 %, 0.05 %, 0.01 %, 0.15 %, 0.2 %, or 0.25 % EMS (ethyl methanesulphonate) diluted in 0.02 % tween 20 (Sigma-Aldrich, P9416). Treatment was carried out on propagated *U. gibba* tissue which was divided into pieces that were just small enough to fill approximately half of a 50 ml falcon tube. Tissue was incubated with the EMS solution overnight in 50 ml falcon tubes which were continually agitated for 18 hours. Treated tissue was then passed through a series of 10 x 20-minute washes in 40 ml 0.02 % tween. Finally, tissue was washed twice in water. Plants were initially placed in the growth room under standard growth conditions and incubated overnight in water. Tissue was then divided further into separate M1 plants in the glasshouse (each division consisted of approximately 5 cm of stolon).

7.3.2 Propidium iodide staining for optical projection tomography

The propidium iodide staining protocol for whole-mount imaging (Truernit *et al.*, 2008) was followed to stain *U. gibba* traps for Optical Projection Tomography (OPT). Tissue was fixed in pre-cooled 50 % methanol, 10 % acetic acid and stored at 4 ^{o}C for up to 1 month. Samples were then washed with water twice before being dehydrated to 80% ethanol through 40 %, 60 %, 80 % Ethanol (x 2 each). Tissue was then incubated in an 80 °C water bath for 10 minutes, followed by rehydration through 60

%, 40 %, 20 % ethanol, water (x2 each). Samples were incubated for 12 hours in alpha-amylase solution (20mM sodium phosphate buffer, (pH7), 2mM NaCl, 0.25mM $CaCl_2$, 0.3mg/ml alpha-amylase from *Bacillus licheniformis* (Sigma Aldrich A4551)) at 37°C. Samples were washed with water (x 3) and incubated with 1 % periodic acid (Sigma Aldrich, 3951) for 1 hour at room temperature in the fume hood. Tissue was washed again with water (x 2) and then incubated with Shiff reagent with propidium iodide (100mM sodium metabisulphite and 0.15M HCl; propidium iodide to a final concentration of 100 mg/mL) for 2 hours. Samples were washed with water (x2) and then kept in water at 4 °C overnight.

7.3.3 Propidium iodide staining for confocal imaging

Samples were treated as above for OPT with the following extra steps. After the final water wash, tissue was mounted onto glass slides with added Frame-Seal Incubation Chambers (BIO-RAD, SLF0601). A drop of ½ chloral hydrate solution was added to cover the tissue and samples were incubated over night at room temperature. Excess chloral hydrate was removed, and samples were correctly spaced on the cover slip. Samples were mounted in Hoyer's solution and a slide was placed on top to ensure samples were close to the coverslip for imaging.

For *qua2-1,* hypocotyls were placed in 0.25 mg/ml propidium iodide for 10 minutes, washed in water then placed on a glass slide with added Frame-Seal Incubation Chambers (BIO-RAD, SLF0601) plus water before imaging.

7.3.4 Optical projection tomography

OPT was performed by Karen Lee using the protocol published in (Lee *et al.*, 2006). Visualisation of OPT scans was achieved using a freely available software package VolViewer which enables interaction of volumes in 3D and is available at:

http://cmpdartsvr3.cmp.uea.ac.uk/wiki/BanghamLab/index.php/VolViewer#Description.

7.3.5 Confocal imaging

Tissue samples were PI stained and mounted as described above. Imaging was performed using a x10 or x20 dry lens on a Zeiss 780 or 880. 561 nm excitation was used, collected at 625-690 nm.

7.3.6 Light microscopy imaging

Live plant tissues were imaged in water using a Leica M205C stereomicroscope with Leica DFC495 camera. Plant phenotype measurements were taken using ImageJ software (http://imagej.nih.gov/ij/).

7.3.7 KASPar genotyping

Genotypic confirmation of individuals was performed via PCR using the KASP genotyping platform (Kompetitive Allele Specific PCR, LGC Group (https://www.biosearchtech.com/products/pcr-kits-and-reagents/genotyping-assays/kasp-genotyping-chemistry).). This method attaches fluorescent tags to the end of primers specific to the SNP of interest (optimised by Des Bradley and Hugo Tavares). Two different primers with two different coloured tags are used to bind to extracted DNA of the sample. When excited the probe fluoresces, and the wavelength is read by the reading machine. Excitation in

one wavelength indicates homozygosity of one allele or the other depending on wavelength. Excitation of both wavelengths indicate a heterozygote.

Primers designed for the forward strand of DNA did not give clear results so the following primers for the reverse strand were made:

- VIC (wild type) 5'-GAAGGTCGGAGTCAACGGATTAGGGGAGGAGCGGGCCTCGTGG-3'
- FAM (mutant) 5'-GAAGGTGACCAAGTTCATGCTAGGGGAGGAGCGGGCCTCGTGA-3'
- Common reverse primer 5'- GTAGCTGCTTCTCGACGGCTCC-3'

A minimum of 24 samples were analysed at any one time to get a range of homozygotes and heterozygotes for the programme to anchor enough values, replicates were made if not enough samples. A primer mix was made first then added to the reaction mix.

Reaction Mix:

- x2 KASPAR mix 5 µl
- H_20 4 µl
- Primer mix 0.14 µl

Primer Mix:

- FAM oligo 6 µl
- VIC oligo 6 µl
- Common reverse 15 µl
- H_20 23 µl

Opaque, low profile, non-skirted 96-well plates were used (ThermoFisher Scientific, AB0700). Wells were filled on ice with 9 µl of reaction mix plus 1 µl sample gDNA for genotyping, foil sealed and spun down. Sites of interest with probes were amplified via PCR.

1. 94 °C for 15 minutes
2. 94 °C for 20 seconds
3. 64 °C for 1 minute
4. Go to step 2 to for 10 cycles, decreasing by 1°C each time
5. 94 °C for 20 seconds
6. 57 °C for 1 minute
7. Go to step 5 to for 40 cycles
8. Finish at 16 °C

Plates were analysed using BioRad CFX96 Q-PCR reader and data was analysed using BioRad CFX Manager 3.1. The output of allelic discrimination is a graph with the signal for the two probes on each axis, quantified as relative fluorescence units (RFU), the stronger the signal the higher the value. Samples are given an RFU value for each probe wavelength.

7.3.8 Passaging *U. gibba* hormone treatments

Wild type and *dw1* plant material were treated in liquid culture using either epibrassinolide (Sigma Aldrich, E1641) to provide exogenous brassinosteroid, or brassinazole (Sigma Aldrich, SML 1406) to inhibit brassinosteroid biosynthesis. Newly grown plant material was sub-cultured into fresh media

containing fresh treatment every week to ensure exposure level. Treated plant cultures were maintained in a CER in conditions described above.

7.3.9 Tracking hormone treated stolons

To track the effect that epiBL had on growth of *dw1*, ~2 cm length of *dw1* of stolon with an apex were isolated in sterilin jars for one week, imaged at day 0 on a plate containing water then again isolated in sterilin jars of liquid media containing the appropriate treatment and returned to a CER in conditions described above. Individual stolons were imaged at day 7 then returned to fresh media containing the appropriate treatment for a week before being imaged at day 14. Individual images were stitched together in Photoshop and nodes labelled to identify node 0 at day 0 and nodes which had subsequently grown in treatment at day 14, labelled with negative numbers. Length measurements were made in ImageJ.

7.3.10 Transmission electron microscopy

The leaves and stolons were cut into small pieces and immediately placed in a solution of 2.5% (v/v) glutaraldehyde in 0.05M sodium cacodylate, pH 7.3 for fixation, and left overnight at room temperature. The samples were then found to be too thin for the smallest Leica EM TP baskets, so they were then embedded in 2% (v/v) low gelling temperature agarose in water and plunged into ice. Once the agarose had set, blocks of approximately $1mm^3$ containing the leaves and stolons were cut out and these were placed in a solution of 2.5% (v/v) glutaraldehyde in 0.05M sodium cacodylate, pH 7.3 and left overnight to fix. The samples were then loaded into the Leica EM TP embedding machine (Leica, Milton Keynes, UK) using the following protocol. The fixative was washed out by three

successive 15-minute washes in 0.05M sodium cacodylate and post-fixed in 1% (w/v) OsO_4 in 0.05 M sodium cacodylate for one hour at room temperature. The osmium fixation was followed by three, 15-minute washes in distilled water before beginning the ethanol dehydration series (30%, 50%, 70%, 95% and two changes of 100% ethanol, each for an hour). Once dehydrated, the samples were gradually infiltrated with LR White resin (London Resin Company, Reading, Berkshire) by successive changes of resin:ethanol mixes at room temperature (1:1 for 1hr, 2:1 for 1hr, 3:1 for 1hr, 100% resin for 1 hr then 100% resin for 16 hrs and a fresh change again for a further 8 hrs) then the samples were transferred into gelatin capsules full of fresh LR White and placed at 60^{o}C for 16 hrs to polymerize. The material was sectioned with a diamond knife using a Leica UC7 ultramicrotome (Leica, Milton Keynes, UK) and ultrathin sections of approximately 90nm were picked up on 200 mesh copper grids which had been formvar and carbon coated (EM resolutions, Sheffield, UK). The sections were stained with 2% (w/v) uranyl acetate for 1hr and 1% (w/v) lead citrate for 1 minute, washed in distilled water and air dried. The grids were viewed in a FEI Talos 200C transmission electron microscope (FEI UK Ltd, Cambridge, UK) at 200kV and imaged using a Gatan OneView 4K x 4K digital camera (Gatan, Cambridge, UK) to record DM4 files.

7.3.11 Statistical methods

Data was analysed using *t*-tests in Microsoft Excel with heteroscedastic variance and two-tailed distribution. Significance values were set at $p < 0.05$ (*), $p < 0.01$ (**) and $p < 0.001$ (***). $\bar{x}$ shows average, *SD* shows standard deviation and *SEM* shows standard error of the mean. Segregation analysis was performed using a chi-squared test.

7.4 Mass spec

7.4.1 GC/MS

GC/MS was used to detect cathasterone at JIC, UK.

- Add 300 µl of ethyl acetate to freeze dried plant tissue powder
- Extract for 1 hour at 60 °C with shaking in an eppendorf shaker or use sonication assisted extraction
- centrifuge to pellet the leaf material
- transfer 50 µl of the supernatant to a vial insert
- inject 1µl of that into the GC for direct analysis
- or evaporate the 50 µl of ethyl acetate and carry out the trimethylsilylation first, buy adding 50 µl of derivatising reagent and heating at 70 °C for 30 mins before GC/MS analysis.
- GC/MS was performed as described in (Suzuki *et al.*, 1995)

7.4.2 LC/MS

Teasterone, typhasterol, 6-deoxocastasterone, castasterone and brassinolide were detected using deuterium-labelled standards at IDGB, China, as described in (Xin *et al.*, 2016)

As brassinolide levels were not detectable in *U. gibba* with our collaborators in China, the metabolite platform at JIC developed a method for detection.

7.4.2.1 Extraction

1. Dry the fresh sample on filter paper
2. Weigh 0.3g into metal ball mill grinding containers
3. Add 3 ml of ice-cold 80% MeOH and metal ball into each tube
4. Homogenize the sample in the Tissue Lyser, 30Hz for 4mins, do this in short bursts
5. Transfer the sample into a clean universal bottle
6. Rinse the metal tube with 1 ml of ice cold 80% MeOH three times
7. Combine extracts and sonicate for 10mins
8. Centrifuge 10mins at 4000rpm
9. Transfer the supernatant to a clean universal bottle
10. To the residue, add 3 ml ice cold MeOH and repeat steps 8 to 10 twice
11. Combine the MeOH extracts and concentrate to the aqueous phase using N_2 and hot water to the universal bottle rack to speed up the evaporation step

7.4.2.2 Purification with Dichloromethane (DCM)

1. Can add 1ml milliq water to each sample so that we get better separation of the 2 layers
2. Add 3 ml of DCM. Mix gently couple of times. Centrifuge at 4000rpm for 2 minutes
3. Remove the DCM layer (bottom layer) into a clean glass universal bottle
4. To the aqueous layer (top layer) add 3 ml of DCM, mix gently and centrifuge as before
5. Repeat steps 3 and 4
6. The combined DCM layers were evaporated to dryness using hot water and N_2. Can leave overnight in the fume hood to evaporate
7. Resuspend in 1 ml of 100% MeOH. Can leave in freezer

7.4.2.3 Solid Phase Extraction (SPE)

Clean up the sample using SPE columns (Phenomenex, 8B-S100-TBJ)

1. Condition column with 5 ml of 100% MeOH
2. Equilibrate with 5 ml water and 5 ml 40 mM Ammonium acetate, pH 6.5

   (0.308g in 100 ml of water, pH with acetic acid if high or with ammonium hydroxide if low)
3. Load 1 ml of sample in 80% MeOH (or S12 standard) (fraction A)
4. Elute with 3 ml of 100% MeOH (fraction B)
5. Pool both fractions A and B in 10ml universal bottles
6. Dry under N_2 and use hot water to the universal bottle rack to speed up the evaporation step
7. Resuspend the sample in 100 µl of 80% MeOH.
8. Resuspend the standard in 1 ml of 80% MeOH

7.4.2.4 Determination of brassinolide

Analysis was performed on Waters Xevo TQ-S triple quad according to method described in (Huo *et al.*, 2012).

7.5 Sequence analysis

7.5.1 Sequencing

Genomic DNA were sent for sequencing at the Chinese Academy of Science, Beijing. Libraries were prepared using a TruSeq Nano DNA kit and sequencing was performed on an Illumina Hiseq X Ten to produce 150bp paired-end reads.

7.5.2 Bioinformatic pipeline

Data was reived as compressed fastq.gz files. Symbolic links were made for each data file:

```
ln -s ./(link path).fastq.gz (file path).fastq.gz
```

and initial quality control was performed using fastqc (0.11.3) to check for estimated depth of coverage and abnormalities such as a high GC content:

```
fastqc (file path).fastq.gz
```

7.5.2.1 Processing sequence data

All processing of sequence data was performed on the JIC High Performance Computing (HPC) cluster. The cluster was accessed using the PuTTY client, bash scripts were written for each task and submitted to the cluster using the SLURM job scheduler. Each script was headed in a standardised format to give the correct parameters to each task:

```
SBATCH -p          Which partition to send to (short, medium or long)
SBATCH -N          Number of nodes to assign
SBATCH -c          Number of cores to assign
SBATCH –mem        Amount of memory to assign
SBATCH -t          Amount of time to assign
SBATCH -D          Which directory to direct task to
SBATCH -o          Which directory to send output report to
SBATCH -e          Which directory to send error report to
```

Appropriate tools were sourced for the task or a path defined for a required piece of software, eg:

```
source samtools-1.7

GATK_path=/nbi/software/testing/GATK/3.5.0/x86_64/jars/
```

7.5.2.2 Mapping reads to reference

The sequence data for each individual is a collection of short (~150 bp) reads which require aligning and mapping to a reference genome. Reads were mapped using the Burrows-Wheeler Aligner algorithm (bwa) and used a Chromium 10x reference genome which was assembled from the progenitor of the mutagenesis. The published reference genome was created using PacBio technology from a collection of Mexican individuals. Even though the genomes are from the same species, local variation may be present between the two geographically distinct population. Mapping individuals

from the mutagenesis to the sequence of the progenitor aligns a greater number of reads, giving a greater chance of finding novel mutations:

```
source bwa-0.7.17

srun bwa mem -M -t 6 -R "@RG\tID:mut01\tSM:mut01\tLB:mut01
\tPL:ILLUMINA\tPU:NNNNN" $ref $out_dir/$outfile.R1.fastq.gz
$out_dir/$outfile.R2.fastq.gz > $alignments/$outfile.10x.bwa.sam
```

BWA-MEM (Maximum Exact Matches) is the preference algorithm for reads 70 bp or longer across a range of sequencing platforms, including Illumina. -M allows for compatibility with Picard software, -t defines the number of threads (6), -R allows for the read group header line to be defined. Defining ID and SM identifiers was important for keeping alignment files unique for SNP calling. The output file format is a Sequence Alignment Map (.sam) file which stores all aligned read information in a headed file.

7.5.2.3 Processing SAM files

The resulting .SAM files contain large amounts of data and therefore occupy a lot of storage. It is therefore preferable to sort and process the .SAM files into a compressed binary format called Binary Alignment Map (.bam). These files sort the same positional information on the aligned reads as .sam files but in a binary format. A typical .sam file for this sequence data was around 15 Gb whereas the .bam file was 1-2 Gb. Files were processed using samtools (1.7) and specifying 8 cores:

```
source samtools-1.7
```

```
srun samtools sort -@ 8 -o $outfile.10x.bwa.sorted.bam
$outfile.10x.bwa.sam
```

Sequencing platforms often use PCR methods to amplify fragments of DNA for hybridisation to sequencer flowcells. Sometime multiple PCR fragments from a single template molecule are sequenced multiple times giving a bias to that sequence. A worst-case scenario is that the PCR fragment is amplified with an error in potentially leading to false positive variant calls. PCR duplicates are therefore identified and removed using picard MarkDuplicates (1.134) and an index file created using samtools:

```
source jre-7.21
source samtools-1.7
pic_path=/nbi/software/testing/picard/1.134/x86_64/jars/

srun java -Xmx16g -jar $pic_path/picard.jar MarkDuplicates
REMOVE_DUPLICATES=true ASSUME_SORTED=true
VALIDATION_STRINGENCY=SILENT MAX_FILE_HANDLES_FOR_READ_ENDS_MAP=900
TMP_DIR=/jic/scratch/groups/Enrico-Coen/Rob/Temp/
INPUT=$outfile.10x.bwa.sorted.bam
OUTPUT=$outfile.10x.bwa.sorted.rmdup.bam
METRICS_FILE=$outfile.10x.bwa.sorted.rmdup.metrics

srun samtools index $outfile.10x.bwa.sorted.rmdup.bam
```

To run this program, Java (jre-7.21) and picard (1.134) were invoked. The program requires a temporary directory to store intermediate steps in the process (TMP_DIR) and the maximum number of temporary files can be limited to reduce storage consumption (MAX_FILE_HANDLES_FOR_READ_ENDS_MAP=900).

It was identified that the insert size was quite small (<180 bp), implying that read1 and read2 would overlap in some places. The points where reads overlap will falsely inflate sequence coverage due to redundancy in the data. Overlaps were removed using bamutil (1.0.14) and an index file created:

```
source samtools-1.7
source bamutil-1.0.14

bam clipOverlap --in mut01.10x.bwa.sorted.rmdup.bam --out
mut01.10x.bwa.sorted.rmdup.nooverlap.bam --stats --params

samtools index mut01.10x.bwa.sorted.rmdup.nooverlap.bam
```

At this point all required processing had been performed prior to variant calling, therefore the processed .bam files were analysed (table 2) using DepthOfCoverage from Genome Analysis ToolKit (GATK 3.5.0):

```
source jre-7.21
GATK_path=/nbi/software/testing/GATK/3.5.0/x86_64/jars/
```

```
java -jar $GATK_path/GenomeAnalysisTK.jar -T DepthOfCoverage -R
/jic/scratch/groups/Enrico-
Coen/Rob/assemblies/Chromium_assembly/U_gibba_v2_assembly_ph1.fasta
-o output_coverage_stats_2  --omitDepthOutputAtEachBase -I
bamlist.list -ct 1 -ct 5 -ct 10 -ct 15 -ct 20
```

Java (jre-7.21) and GATK were invoked and the path to the reference genome .fasta file defined. The input .bam files were collated into a .list file to analyse all files in one job. The -ct flags are depth thresholds and work out the percentage of bases which have coverage to that depth (e.g. 94.9% of bases in mut01 have a coverage above 10x).

7.5.2.4 Identifying variable sites

The processed .bam files had been filtered for overlaps and PCR duplicates and were ready to be analysed. Initial analysis aimed to find all variation across the population in the form of SNPs. Variable sites were identified across the processed .bam files using HaplotypeCaller (GATK-4.0.9.0). This program compares aligned sequences with the reference genome and identifies all sites with variation (active regions), collates which different nucleotides feature at that site, quantifies them and assigns a genotype:

```
source jre-1.8.0_45

/hpc-home/bellowr/group_cluster/software/gatk-4.0.9.0/gatk
HaplotypeCaller -R $ref -I bamlist.list -O output.vcf --java-options
"-Xmx16G"
```

Java is invoked and HaplotypeCaller is called from the gatk4 software. -R inputs the reference .fasta file, -I is the input .bam files (in this case a .list file) and -O is the output file. This output is a Variant Call Format (.vcf) file which is specifically used to store large datasets of gene sequence variations in a single file. It is a headed file with position information given by the CHROM (chromosome or contig) and POS (coordinate of the variation in the contig) headings. Variation is recorded under two headings, REF (reference or wild type allele) and ALT (the alternate or mutant allele). Therefore, mutations are often referred to as alt to the ref allele.

As well as SNPs, HaplotypeCaller also identifies indels and polyallelic sites as variation. These variable sites are not of interest as they may be natural variation between individuals or sequencing errors. Sequencing errors can also account for variation where there is only a singleton alt allele on a read. As the mutation I was looking for was an EMS-introduced SNP that is fixed across multiple individuals, these sites were filtered out using the view command in BCFtools (1.8) to extract only biallelic sites with a minimum allelic count of 1:

```
bcftools view -m 2 -M 2 -O v -c 1:minor
```

Whilst the .vcf file format can be edited and analysed, it can also be converted into a .txt file for manipulation with a range of programs, including GUI accessible ones such a Microsoft Excel. Data was tabulated using VariantsToTable (GATK-4.0.9.0):

```
source jre-7.21
GATK_path=/nbi/software/testing/GATK/3.5.0/x86_64/jars/
```

```
srun  java -Xmx8g -jar  $GATK_path/GenomeAnalysisTK.jar -T
VariantsToTable  -R $ref -V output.vcf -o output.txt -F CHROM -F POS
-F REF -F ALT -GF GT
```

As with HaplotypeCaller which is also from GATK, Java was invoked and the VariantsToTable located in the software filepath. -R is the reference genome, -V in the input .vcf file and -o is the output text file. -F are the header names from standardised .vcf fields to include in the .txt file. -GF GT notates that the genotype field outputs base information for each individual at each variable site for both reference and alternate alleles.

7.5.2.5 Segregation

Genotypic information is called by HaplotypeCaller as bases that have the majority of reads the same or different form the reference (homozygosity) or a mixture of reads differing (heterozygosity). Individual data for REF and ALT alleles for each individual was therefore concatenated in Excel so that each site had a single genotype per individual (AA = homozygous for reference allele, AB = heterozygous, BB = homozygous for mutant allele, N = null sites) using a presence or absence IF statement:

```
=IF(output.txt!E2=$C2,A",IF(output.txt!E2=$D2,"B",IF(output.txt!E2=".","N")))
```

Columns were added at the end of the dataset summing up the number of counts of AA, AB and BB to identify segregation patterns of the SNP across the population as well as a total count of all SNPs to

confirm that there are no null sites. Finally, columns were added for total counts of BB (homozygous for the mutation) across either all wild type or all mutant individuals to confirm the SNP is fixed. Therefore, these initial filtering steps were applied:

1) Genotype information for all individuals (total_count = 21)
2) Fixed across mutants (mut_total_BB = 7)
3) Not present in progenitor pool (pro = AA)

For this initial filtering only seven mutant individuals were used for analysis, this further explored in the troubleshooting section of this chapter. With this filtering applied, only three candidate sites arose (table 4). Further analysis found that one candidate was not private to the mutation as the site is heterozygous in the progenitor, and another candidate site was heterozygous in a mutant sequence, leaving only one candidate. The mutation is a transition and was not found in the progenitor sequence which is consistent with an EMS mutation.

Table 7.1 Genotypic information for candidate SNP

Position 28587:117186 on Chromium 10x reference. C is reference allele and T is alternate allele.

Allele	C	T
mut01	0	26
mut03	0	31
mut04	0	19
mut05	0	23
mut06	0	29
mut07	0	37
mut08	0	16
mut09	0	18
mut10	0	23
mut11	0	24
wt01	19	0
wt02	9	0
wt03	22	0
wt04	28	0
wt05	27	0
wt06	26	0
wt07	24	0
wt08	18	15
wt09	11	15
wt10	20	0
wt11	10	9
wt12	20	0
wt13	9	9
progenitor	107	0

7.5.2.6 Alignment to DWF4

The following sequence surrounding the candidate SNP was extracted and BLASTed against the published PacBio reference genome which contain gene annotation information (Lan *et al.*, 2017) (highlighted in yellow is the candidate SNP).

GAAGGCTATATGACTGCAAGAATGAATTGCATAATCTTCTCAAGGAAGAGGCATGCTTTATCATTCAACTCTGTGATCTTT
CTTTGTGACTATGCATTCTCCTTCCTCTGCTTAGCCTTGAAAATGCATTTACTTTGGTCCTAGTGTGCACCAGATACGCAAAT
GATGCATCTTTTCTAGTTTCTCGTATGCTCAACAAAGATACCTTACTTCTTTGACAGAGGTTGTCAGGGTCGTCCCTATTGA
TCTTTGCAAATAAGCAGGACATACAAGGTTCTCTTTCACCTGATGATATTGCAAAGGTGCGATATGTCCTCAGCTGCTACC
TCTTTGCTTCATTTCACTTTCGTTATAATCACAGAAGCAGAAGTTCTGTAGCTACGTTTATGTTGCTGATGTCAACCCACAG
GTGCTAGAGTTAGATGCCATGGACAAAAGCCGACACTGGAGGATTGTGGGATGCAGTGCTTACACAGGGCAAGGGCTTC
TCGAGGGCTTCGACTGGCTTGTTCAGGATATAGCCTCAAGAATTTACATGCTTGATTAACCCTGTTGTCACTGTATCAGTTG
CAAAAACATGTACCCCTTGCTTCGGATACCGCCACGTGTCCGTGTCCGGTTGCAAAGCCATGTTGGGCTGGCCCATGTTTC
AGAGTCTCATTATCTGTTAAGTAAAGCTAGCTGCCTACTACGACCCAAGTCCCAAATGGAATCCAACAAAGCCGGTCCATG
TGTGAGCATCATTACACTAAGAAACCATGAATCGGCTTTGCCTTTTTATTGGTCAAGCTGCCCTCTTCAGAAACAATTATCT
ACTGCTTACTCTCACTAAAGCACCCCTTTTTTGTTACTACAACTCCCCATCGGTTCTTTGGACATGGATGCGCAACCCCTGG
GGGAAGTCGACGAAGGGGAATGCGAAGGGGTGATCATCGGACCCATCAAGCCTCCACCTGAAGTTGAGCACCAGGTGG
TGAAGAAACACCGCCATCTCAAGCTTCGCCAGCTCCGATCCGGCGCACAGCCGCGGCCCTCCCCCGAAGGCCATGAAGTA
GCTGCTTCTCGACGGCTCCGA**C**CACGAGGCCCGCTCCTCCCCTCTGCCCTGAAATGATTTCCGAAGAGGGGAGTCACACTT
GCGCAGTCCAAGGAAAGGCATCGTAAATTCAAAACTGTAAGCTAAGGAGGATGGATGATGTCTCATGGATTGAGGGAGG
GAGATTGGGCCTAGGGGGACCGAGATGGAAACGGGGGCACACGTGCGAACGCACACCCCACGTGTGATCCACATGGGG
GTTGGCGTTGTCAGAACAATTAATCATGAGGGGTGGGCCCCTACACACCCACGTGTGCCCTGCCTTGCAGTCTGGCTCTG
GTTTTTTGTTTGCTTCTCTTAACTCCTCCTCCTCCTCCCCTCTGTTTCTCTCTCTCGCCCACACGGCTTCTTTAAATTTACT
GCACCTTCACTTCCTGTGCCCGGTCCCCTTCCCATGGAAAATACTATTTTTTTCTTCTTTTTTTTTTTTTGGAACCTTTTCTTCTA
TTCCTTTATGGAACGAAAGTGCGTAATTTGCTTTTAACAAACCTGCCATCTCCATGGATCAAAGCGGCAGGGATGGTCGAA
AAGGGATTCGTCCAAATGAACGGCTGAGATCACCGGCAACACCTTCCACCCGCAAGGAATTTCATACTCTGGGGGAGCAA
GAAAACAGACTCACTAATACGATGAGAAAGATAAAAGATAGGTGTGAGATAGTGGGGTGCTTACCTCCATACCTGACGT
CCTTGAGAGCTTTTCTATGGAGAAATCTGACAACATTTCCCAGTCTGAGAGTCTCGTGAACAACCTGCAACGACGAGTGCC
AAGGATGACTCTCTTACATCGGGAGAAGAGAGAATGAATTTGATTGGTGGGTTTTTTTGCGCTCACGCATTGTGTGAAGG
CCATTTTCTTGTAATCCTCCCACGTCA

The mutation was found in exon 8 of a gene at unitig_736:1056726 (figure 2). The sequence of the gene of interest was extracted and annotated in Geneious (11.0.5). The mutation was found to cause an early stop codon in place of a Tryptophan at position 416 of the transcript. To identify the function of the gene of interest, the sequence was BLASTed across the Viridiplantae in the BLASTn database and revealed a 78% homology to cytochrome P450 90B1, also known as *DWARF4* in Arabidopsis.

7.6 Transformation of *U. gibba*

7.6.1 Synthesising *DW1 and pDW1*

The sequence of *DW1* was obtained from the published genome using the coordinates found in figure 3.1A and 1000 bp upstream of the *DW1* start codon was used for *pDW1*. For synthesised gene sequences to be used in Golden Gate, they needed to be domesticated to remove BsaI, BpiI and DraIII restriction sites for use as Level 0 modules.

7.6.2 Golden Gate

The Golden Gate cloning platform allows for generation of single binary transformation vectors through progressive stages of cloning using standardised parts. Initially synthesised level 0 (L0) components are combined to make level 1 (L1) transcriptional units, which can be combined to make level 2 (L2) multigene units that can be transformed into plants (Weber *et al.*, 2011). This cloning method is based on the ability of bacterial type IIS endonuclease restriction enzymes (BsaI, BpiI and ESp3I) to cut downstream of a specific recognition site. By using specific 3' and 5' overhangs (fusion sites), fragments cut by the same type IIS endonuclease can then be linearly ligated by T4 ligase in a given order (Weber *et al.*, 2011).

For generating L1 modules, 100 ng of L1 vector backbone was combined with 100 ng of each L0 part, 1.5 µl of 10x BSA (New England Biolabs, NEB), 1.5 µl of 10 x T4 Buffer (NEB), 1 µl of BsaI enzyme (NEB), 1 µl of T4 ligase (NEB) and H_2O to a total volume of 15µl. For L1 constructs containing a *lox* component, the 1 µl of BsaI was replaced with a mixture of 0.5 µl of BsaI and 0.5 µl of ESp3I (NEB). The reaction was then incubated in a G-STORM® Thermocycler (GT40361) with the following program:

1. 37 °C for 3 minutes
2. 16 °C for 4 minutes
3. Go to step 1 to for 40 cycles
4. 50 °C for 5 minutes
5. 80 °C for 5 minutes
6. Finish at 10 °C

The completed reaction was transformed into *E. Coli* and grown on selective media. For level 2 module cloning, 100 ng of L2 vector backbone was combined with 100 ng of each relevant L1 transcriptional unit and 1.5 µl of 10x BSA (NEB), 1.5 µl of 10 x T4 Buffer (NEB), 1 µl of BpiI enzyme (NEB), 1 µl of T4 ligase (NEB) and H_2O to a total volume of 15µl. The reaction was then incubated in a G-STORM® Thermocycler with the same program described above.

7.6.3 Transformation of *E. coli*

Transformation of *E. coli* was carried out by heat-shock using Library efficiency DH5α chemically competent *E. coli* (Invitrogen Life Technologies) or Maximum Efficiency One Shot® OmniMAX™ 2 T1 Phage-Resistant Chemically competent *E. coli* (Invitrogen Life Technologies). Competent cells were thawed on ice for 10 minutes and 1-5 µl of ligation produce or plasmid DNA was added to cells and mixed gently. Cells were incubated on ice for 30 minutes and then heat shocked at 42 °C for 30 seconds, followed by 2 minutes on ice. 250 µl of SOC medium (Invitrogen Life Technologies, 2% Tryptone, 0.5% Yeast Extract, 10 mM NaCl, 2.5 mM KCl, 10 mM $MgCl_2$, 10 mM $MgSO_4$, 20 mM glucose) was then added and cells were incubated at 37 °C with shaking for 1 hour for recovery. Cells were plated onto LB (lysogeny broth) plates with relevant antibiotic selection and incubated at 37 °C overnight.

7.6.4 Transformation of *A. tumefaciens*

A. tumefaciens strain GV3101 was used for transformation. 40 µl of electro-competent cells were defrosted on ice for 10 minutes. ~100 ng of plasmid DNA was added to the cells and mixed gently before being transferred to pre-chilled cuvettes. For electroporation, cells were pulsed using the BioRad GenePulser ® II (Voltage: 1800 V, Capacitance: 25 µF, Resistance: 400 Ω). 250 µl fresh, chilled SOC media was added to the cuvette and transferred to 1.5ml Eppendorf tubes. The cells were incubated for 1 hour at 28 °C before being plated on LB media with kanamycin (100 mg/ml) and rifampicin (100 mg/ml). Plates were incubated for 3 days at 28 °C. Single colonies were picked from plates and incubated in 5 ml of liquid LB at 28 °C, shaken at 200 rpm for 16–24 hours with the same concentration of antibiotics as the plates. For long-term storage equal quantities of *A. tumefaciens* culture and 30% sterile glycerol were mixed and stored at -80 °C.

7.6.5 Chemicals

- MS salts including vitamins (Duchefa Biochemie, M0222.0050)
- Sucrose (Fisher Chemical, S/8600/60)
- MES hydrate (Sigma-Aldrich, M2933)
- 6-Benzylaminopurine (6-BA, Sigma-Aldrich, B3274)
- Naphthaleneacetic acid (NAA, Sigma-Aldrich, N1641)
- Ceftriaxone sodium (Cef, Melford Laboratories Ltd, C51000)
- G418 (Melford Laboratories Ltd, G64000)
- Gelzan (Sigma-Aldrich, G1910)

7.6.6 Materials

- 100 x 20 mm petri dishes (734-0006, R&L Slaughter Ltd)
- Forceps
- Sterilin jars- (185AM, R&L Slaughter Ltd)
- Pasteur pipettes – plastic sterile
- Falcon tubes
- Scissors
- Micropore tape

7.6.7 Media

- MS media, liquid media: 4.4 g/l MS salts, 25 g/l sucrose, pH 5.8, autoclaved

- Ug 0, stock culture medium for seed germination: 4.4 g/l MS salts, 25 g/l sucrose, 0.5 g/l MES hydrate, 2.8 g/l Gelzan, pH 5.8, autoclaved

- Ug 1, pre-culturing tissue in preparation for transformation: 4.4 g/l MS salts, 25 g/l sucrose, 0.5 g/l MES hydrate, 1 mg/ml 6-BA, 0.5 mg/ml NAA, 2.8 g/l Gelzan, pH 5.8, autoclaved

- Ug 2, liquid media for vacuum infiltration: 4.4 g/l MS salts, 25 g/l sucrose, 0.5 g/l MES hydrate, 1 mg/ml 6-BA, 0.5 mg/ml NAA, 20 mg/ml AC, pH 5.8, autoclaved

- Ug 2-1, co-cultivation of plant tissue and *Agrobacterium tumefaciens*: 4.4 g/l MS salts, 25 g/l sucrose, 0.5 g/l MES hydrate, 1 mg/ml 6-BA, 0.5 mg/ml NAA, 20 mg/ml AC, 2.8 g/l Gelzan, pH 5.8, autoclaved

- Ug 3, elimination of *Agrobacterium* and regenerating tissue after antibiotic selection: 4.4 g/l MS salts, 25 g/l sucrose, 0.5 g/l MES hydrate, 1 mg/ml 6-BA, 0.5 mg/ml NAA, 250 mg/ml Cef, 2.8 g/l Gelzan, pH 5.8, autoclaved

- Ug 4, antibiotic selection of transformed plant tissue: 4.4 g/l MS salts, 25 g/l sucrose, 0.5 g/l MES hydrate, 1 mg/ml 6-BA, 0.5 mg/ml NAA, 250 mg/ml Cef, 150 mg/ml G418, 2.8 g/l Gelzan, pH 5.8, autoclaved

7.7 *U. gibba* transformation protocol

7.7.1 Preculture

1. After 4 weeks of establishment in liquid culture, preculture mature stolons for transformation in petri dishes with Ug1 media.
2. Arrange tissue into clusters 1 cm across, lightly pressed into the surface of the media, arranged as in figure 2a.
3. Keep plates in a controlled environment chamber at 25 ±1 °C under fluorescent light at an intensity of 180 μmol/m^2/s with a 16-h light/8-h dark photoperiod.
4. Clusters of tissue are ready for transformation when individual healthy, green stolons have elongated by 1 – 2 cm (figure 3b).

5. After several weeks of growth, some clusters of *U. gibba* can develop callus-like tissue in the centre. This tissue does not easily regenerate shoot growth and is therefore discarded at each stage.

7.7.2 Preparation of *Agrobacterium* culture for inoculation

1. 5 ml of liquid LB solution containing kanamycin (100 mg/ml) and rifampicin (100 mg/ml) was transferred to a sterile 50 ml Falcon tube.
2. Add a single colony or 100 µl of stock *Agrobacterium* harbouring required construct. Keep culture at 28 °C for 18 hours with 200 rpm agitation.
3. Take 2 ml of culture and centrifuge at 3000 rpm for 5 minutes. Discard the supernatant and resuspend pellet in 1000 µl of Ug 2 liquid medium.
4. Adjust optical density to between OD_{600} = 0.1 – 0.2 using Ug2 liquid medium. Transfer to new sterile 50 ml Falcon tube and fill to 40 ml with Ug 2 liquid medium.

7.7.3 Vacuum infiltration

1. Thoroughly sterilise desiccator with 70% EtOH. Prepare 90 mm petri dish, 50 mm filter paper and tissue (all autoclaved) for drying tissue. Layer base of petri dish with tissue paper and place 5 – 8 sheets of filter paper on top.
2. Cut approximately half a plate of mature, healthy plant material (figure 2b) into 1- 1.5 cm lengths using sterile scissors and place in Falcon tube with *Agrobacterium* inoculum.
3. Slightly loosen lid of Falcon tube and seal with micropore tape

4. Draw vacuum for approximately 1 minute and 30 seconds. Times for infiltration may vary between vacuum pumps and may need to be adjusted. Adequate infiltration is indicated when larger bubbles begin to form in the Falcon tube, at which point the pump should be immediately turned off and pressure valve gently released.
5. Transfer tissue from falcon tube onto filter paper using sterilized forceps. Dry tissue by distributing across filter paper. Dry for 5 minutes or when filter paper is saturated, and tissue begins absorbing liquid.

7.7.4 Co-culture and elimination of *Agrobacterium*

1. Transfer tissue to plates with Ug 2-1 (figure 2c). Around 3 plates are needed per full Falcon tube of tissue.
2. Co-culture plates in dark conditions at 23 °C for 2 days.
3. Transfer tissue to 20 mm deeps plates containing Ug 3 media for 2 weeks to eliminate excess *Agrobacterium* (figure 2d). Keep plates in a controlled environment chamber at 25 ±1 °C under fluorescent light at an intensity of 180 µmol/m^2/s with a 16-h light/8-h dark photoperiod.
4. If a visible excess *Agrobacterium* grows in this time, select only clusters without excess *Agrobacterium* and transfer to new plates containing Ug 3 media.

7.7.5 Selection and regeneration (figure 7.1)

1. Transfer tissue to 20 mm deep plates containing Ug 4 media. Transfer to fresh Ug 4 media every 2 weeks.

2. After 4 weeks, some tissue in each cluster became necrotic. This tissue is discarded, and only healthy tissue is transferred to new plates.
3. After 8-12 weeks of regular media changes, untransformed tissue will have been selected against and only transformed clusters remain.
4. Check for fluorescence in these clusters to confirm successful transformation.
5. Isolate transformed tissue on individual Ug 3 plates to establish independent transformed lines. Transfer tissue to liquid media when required.

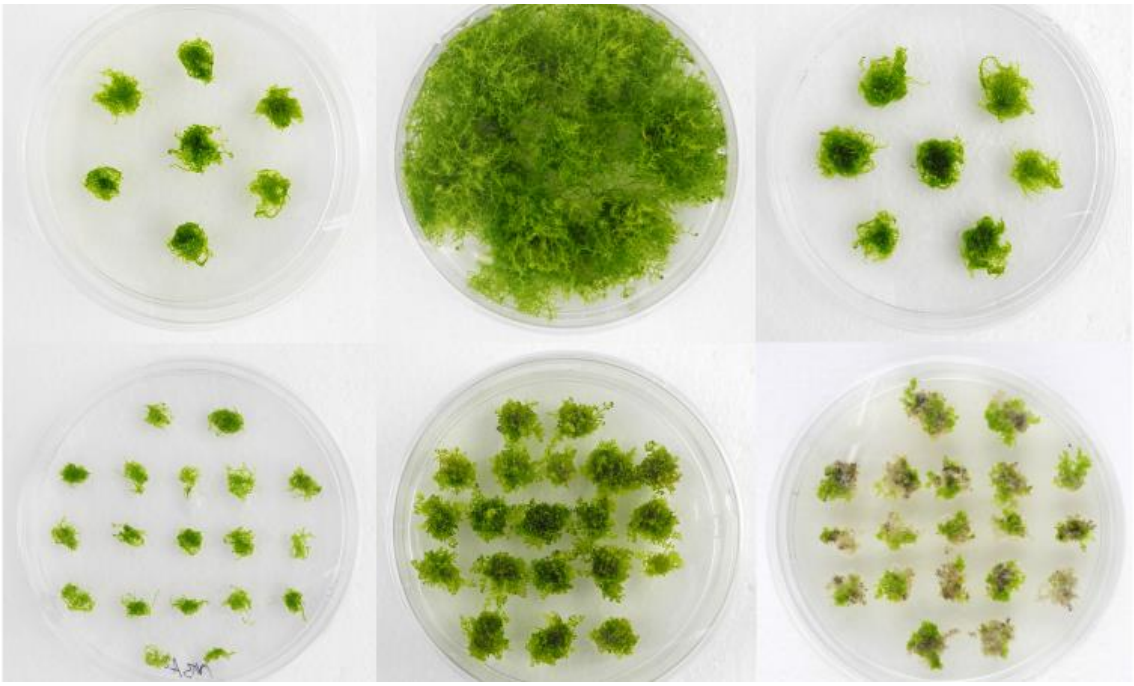

Figure 7.1 *U. gibba* tissue maintenance, regeneration and selection on solid media

a) Freshly subbed tissue

b) Mature plate ready to transform

c) Inoculated tissue ready for co-culture (large clusters)

d) Co-cultured tissue on Cef (small clusters)

e) After two weeks on Cef

f) After 1 month on selection

7.8 *In situ* hybridisations

7.8.1 Tissue fixation and preparation for *in situ* hybridisation

U. gibba circinnate apexes were collected into either 4 % paraformaldehyde (PBS pH 7, Water, 16 % paraformaldehyde solution (Electron Microscopy Sciences, 15710) with 4 % DMSO and 0.1 % Triton X) or FAA (50 % ethanol, 5 % acetic acid, 3.7 % formaldehyde (sigma Aldrich, F8775), water, 1 % DMSO and 0.1 % Triton X), for *in situ* hybridisation. Tissue in solution was placed under vacuum pressure for three rounds of 10 minutes, or until the samples dropped to the bottom of the solution. Samples were incubated at 4 ° C overnight.

Samples were removed from the paraformaldehyde and washed with cold 0.85 % saline for 30 minutes at 4 °C, followed by a cold 50 % ethanol/0.85 % saline solution for 3 hours at 4 °C. Samples were then transferred to 70 % ethanol/0.85 % saline for a further 3 hours. The solution was then replaced with fresh 70 % ethanol/0.85 % saline and samples were stored at 4 °C. The FAA solution was removed and replaced with cold 50 % ethanol for 3 hours at 4 °C, followed by cold 70 % ethanol for 3 hours at 4 °C. The solution was then exchanged for fresh 70 % ethanol and samples were stored at 4 °C.

All samples were transferred to mesh biopsy cassettes (Sakura) in 70 % ethanol. These were placed in a Tissue-Tek® vacuum infiltration processor (VIP) machine (Sakura) with the following programme:

Table 7.2 Tissue- Tek® VIP machine program for paraffin embedded samples

Step	Solution	Time (hours)	Temperature (°C)	Pressure/Vacuum cycle (P/V)	Agitation
1	70 % EtOH	4	35	on	on
2	80 % EtOH	4	35	on	on
3	90 % EtOH	4	35	on	on
4	100 % EtOH	4	35	on	on
5	100 % EtOH	4	35	on	on
6	100 % EtOH	4	35	on	on
7	Xylene	4	35	on	on
8	Xylene	4	35	on	on
9	Xylene	4	35	on	on
10	Paraffin Wax	4	60	on	on
11	Paraffin Wax	4	60	on	on
12	Paraffin Wax	4	60	on	on
13	Paraffin Wax	4	60	on	on

Samples were then embedded in blocks of paraffin wax using the Tissue-Tek® TEC (Sakura) embedding machine and kept at 4 °C until sectioning.

Samples embedded in wax blocks were sliced in 8 µm thick ribbons using a microtome (Reichet-Jung 2030). Tissue slices were mounted on Polysine™ microscope slides (VWR, 631-0107) with water. Slides were left to dry on a 37 °C hotplate for 48 hours to ensure the slices were dry and flat on the slide. Once dried, slides were stored covered at 4 °C.

7.8.2 Probe design

Primers were designed to amplify approximately 500 bp unique fragments of the target gene in varying positions, amplified from DNA of the progenitor:

UgDW1_F1: GGTCCGCTGGAAAACTACAC

UgDW1_F2: TTCCTCCAGAGCTGTCCATC

The fragment was then cloned into the pCR®4-TOPO® vector using the Invitrogen Life Technologies TOPO®TA Cloning® kit according to the manufacturer's guidelines. The ligation product was transformed into One Shot® TOP10 chemically competent *E. coli* (Invitrogen, C4040) using heat-shock as described in the manufacturer's protocol. Cells were plated on selective LB media containing 50 µg/ml kanamycin. Colonies were analysed using colony PCR. Chosen colonies were streaked onto new LB plates containing 50 µg/ml kanamycin. Single colonies were then selected and grown overnight in LB/ kanamycin broth, shaking at 30 ^{O}C. Plasmids were extracted from 6 ml of culture using the QIAprep Spin Miniprep kit (Qiagen, 27106) as per the manufacturer's instructions. Clones were validated via sequencing. RNA probes were produced using the protocol published in (Coen *et al.*, 1990) with the following modifications. The T7 or T3 transcription start site and the probe coding sequence were amplified using PCR. The PCR product was then purified using the QIAGEN QIAquick PCR purification kit (QIAGEN, 28106) as per the manufacturer's instructions. Approximately 1 µg of purified PCR product was digoxigenin-UTP labelled using T7 or T3 RNA polymerase. Probes were washed in 70 % EtOH and resuspended in 50 µl RNAse free H_2O and then stored at -20 ^{O}C.

7.8.3 *In situ* hybridisation protocol

The protocol used was based on that published in (Coen *et al.*, 1990) and is as follows. Slides were placed in metal racks and rehydrated in the following solutions in order:

Solution	**Time**
Histoclear	10 min
Histoclear	10 min
100 % EtOH	1 min
100 % EtOH	1 min
95 % EtOH	1 min
85 % EtOH, 0.85 % saline	1 min
50 % EtOH, 0.85 % saline	1 min
30 % EtOH, 0.85 % saline	1 min
0.85 % saline	2 min
PBS	2 min

Sections were then treated with pronase or proteinase K to digest the cell wall proteins. The enzymatic reaction was stopped using glycine and sections were then dehydrated through an ethanol series as follows:

Solution	**Time**
Pronase (0.125 mg/ml in pronase buffer: 50 mM Tris-HCl pH 7.5, 5mM EDTA)	12 min
Or	
Proteinase K (10 µg/ml in pronase buffer)	15 min
Glycine (0.2 % in PBS)	3 min
PBS	2 min
4 % Paraformaldehyde in PBS	10 min
PBS	2 min
PBS	2 min
Acetic anhydride (5 µl/ ml in 0.1 M triethanolamine, pH 8)	10 min
PBS	2 min
0.85 % saline	2 min
30 % EtOH, 0.85 % saline	1 min
50 % EtOH, 0.85 % saline	1 min
85 % EtOH, 0.85 % saline	1 min
95 % EtOH	1 min
100 % EtOH	1 min
100 % EtOH	Kept at 4 ^{o}C for up to 2 hours

Probes were prepared for hybridisation of each slide with a mix of 2 µl probe, 2 µl RNAse free H_2O, and 4 µl deionised formamide per slide. Probes were denatured at 80 ^{O}C for 2 minutes and then kept on ice. The probe solution was then made up to 100 µl/ slide by adding the appropriate volume of hybridisation buffer (hybridisation salts with a final concentration of 300 mM NaCl, 10 mM Tris-HCl pH 6.8, 10 mM $NaPO_4$, 5 mM EDTA added to 50 % deionised formamide, 25 % dextran sulphate, 1.25 % tRNA, 2.5 % Denhardt's salts (Thermo Scientific, 1 % BSA, 1 % Ficoll, 1 % polyvinylpyrrolidone in water), 8.75 % H_2O).

Ethanol was allowed to evaporate from the slides and 100 µl hybridisation buffer/probe solution was added to each slide. Slides were then covered with a plastic coverslip (Sigma, Hybri-slips H0 784-1006A) avoiding bubbles. Slides were placed in a humid chamber lined with paper soaked in 2X SSC, 50 % formamide, the chamber was sealed and incubated at 50 ^{O}C overnight for hybridisation.

Slides were soaked in 2x SSC until the coverslips could be removed easily. Slides were washed in 0.2x SSC at 55 ^{o}C for 35 minutes. Slides were then washed twice more in pre heated 0.2x SSC at 55 ^{o}C for 25 minutes. Incubation in the following solutions was then carried out to digest any excess probe that was not hybridised:

Solution	**Time**	**Temperature**
NTE buffer (500 mM NaCl, 10 mM Tris-HCl pH 7.5, 1 mM EDTA)	5 min	37 ^{o}C
NTE buffer	5 min	37 ^{o}C
NTE buffer with 20 µg/ ml RNase A	30 min	37 ^{o}C
NTE buffer	5 min	RT
NTE buffer	5 min	RT

Antibody staining was carried out through the following solutions at room temperature:

Solution	**Time**
Buffer 1 (100 mM Tris-HCl pH 7.5, 150 M NaCl)	5 min
Buffer 2 (0.5 % blocking reagent (Roche) in buffer 1)	1 hour
Buffer 3 (1 % BSA, 0.3 % Triton X-100 in buffer 1)	30 min
Buffer 4 (Anti-digoxigenin-AP (Sigma, A7906) 1:3000 in buffer 3)	90 min
Buffer 1 with 0.3 % Triton X-100	4 x 25 min
Buffer 1	5 min
Buffer 5 (buffer 5a (100 mM Tris-HCl pH 9.5, 100 M MaCl) + buffer 5b (0.5 M $MgCl_2$)	5 min
Buffer 6 (buffer 5 + 2 µl/ ml NBT and 1.5 µl/ ml BCIP)	Overnight in dark or until signal develops

To stop development of the signal further, slides were washed with water and then kept in water at 4 ^{o}C. Slides were imaged using a Leica DM6000 microscope.

8 Bibliography

Alonso Jose, M., Stepanova Anna, N., Solano, R., Wisman, E., Ferrari, S., Ausubel Frederick, M., & Ecker Joseph, R. (2003). Five components of the ethylene-response pathway identified in a screen for weak ethylene-insensitive mutants in Arabidopsis. *Proceedings of the National Academy of Sciences, 100*(5), 2992-2997. doi:10.1073/pnas.0438070100

Arioli, T., Peng, L., Betzner, A. S., Burn, J., Wittke, W., Herth, W., Camilleri, C., Hofte, H., Plazinski, J., & Birch, R. (1998). Molecular analysis of cellulose biosynthesis in Arabidopsis. *Science, 279*(5351), 717-720.

Atmodjo, M. A., Hao, Z., & Mohnen, D. (2013). Evolving views of pectin biosynthesis. *Annual review of plant biology, 64*, 747-779.

Azpiroz, R., Wu, Y., LoCascio, J. C., & Feldmann, K. A. (1998). An Arabidopsis Brassinosteroid-Dependent Mutant Is Blocked in Cell Elongation. *The Plant cell, 10*(2), 219-230. doi:10.1105/tpc.10.2.219

Bichet, A., Desnos, T., Turner, S., Grandjean, O., & Höfte, H. (2001). BOTERO1 is required for normal orientation of cortical microtubules and anisotropic cell expansion in Arabidopsis. *Plant J, 25*(2), 137-48. doi:10.1046/j.1365-313x.2001.00946.x

Blumenstiel, J. P., Noll, A. C., Griffiths, J. A., Perera, A. G., Walton, K. N., Gilliland, W. D., Hawley, R. S., & Staehling-Hampton, K. (2009). Identification of EMS-Induced Mutations in Drosophila melanogaster by Whole-Genome Sequencing. *Genetics, 182*(1), 25-32. doi:10.1534/genetics.109.101998

Bouton, S., Leboeuf, E., Mouille, G., Leydecker, M.-T. r. s., Talbotec, J. l., Granier, F., Lahaye, M., Höfte, H., & Truong, H.-N. (2002). QUASIMODO1 Encodes a Putative Membrane-Bound Glycosyltransferase Required for Normal Pectin Synthesis and Cell Adhesion in Arabidopsis. *The Plant cell, 14*(10), 2577-2590. doi:10.1105/tpc.004259

Bradley, D., Carpenter, R., Copsey, L., Vincent, C., Rothstein, S., & Coen, E. (1996). Control of inflorescence architecture in Antirrhinum. *Nature, 379*(6568), 791-797.

Brown, C. L., Sommer, H. E., & Pienaar, L. V. (1995). The Predominant Role of the Pith in the Growth and Development of Internodes in Liquidambar styraciflua (Hamamelidaceae). II. Pattern of Tissue Stress and Response of Different Tissues to Specific Surgical Procedures. *American Journal of Botany, 82*(6), 777-781. doi:10.2307/2445618

Bürkle, L., Cedzich, A., Döpke, C., Stransky, H., Okumoto, S., Gillissen, B., Kühn, C., & Frommer, W. B. (2003). Transport of cytokinins mediated by purine transporters of the PUP family expressed in phloem, hydathodes, and pollen of Arabidopsis. *Plant J, 34*(1), 13-26. doi:10.1046/j.1365-313x.2003.01700.x

Buschmann, H., Fabri, C. O., Hauptmann, M., Hutzler, P., Laux, T., Lloyd, C. W., & Schäffner, A. R. (2004). Helical Growth of the Arabidopsis Mutant tortifolia1 Reveals a Plant-Specific Microtubule-Associated Protein. *Current Biology, 14*(16), 1515-1521. doi:10.1016/j.cub.2004.08.033

Castorina, G., Persico, M., Zilio, M., Sangiorgio, S., Carabelli, L., & Consonni, G. (2018). The maize lilliputian1 (lil1) gene, encoding a brassinosteroid cytochrome P450 C-6 oxidase, is involved in plant growth and drought response. *Annals of botany, 122*(2), 227-238. doi:10.1093/aob/mcy047

Catterou, M. D., F; Schaller, H; Aubanelle, L; Vilcot, B; Sangwan-Norreel, BS; Sangwan, RS. (2001). Brassinosteroids, microtubules and cell elongation inArabidopsis thaliana. II. Effects of brassinosteroids on microtubulesand cell elongation in the bul1 mutant. *Planta, 212*, 673-683.

Choe, S., Dilkes, B. P., Fujioka, S., Takatsuto, S., Sakurai, A., & Feldmann, K. A. (1998). The DWF4 gene of Arabidopsis encodes a cytochrome P450 that mediates multiple 22alpha-hydroxylation steps in brassinosteroid biosynthesis. *The Plant cell, 10*(2), 231-243.

Chory, J., Nagpal, P., & Peto, C. A. (1991). Phenotypic and Genetic Analysis of det2, a New Mutant That Affects Light-Regulated Seedling Development in Arabidopsis. *The Plant cell, 3*(5), 445-459. doi:10.1105/tpc.3.5.445

Clouse, S. D. (2011). Brassinosteroid signal transduction: from receptor kinase activation to transcriptional networks regulating plant development. *The Plant cell, 23*(4), 1219-1230. doi:10.1105/tpc.111.084475

Clouse, S. D., & Sasse, J. M. (1998). BRASSINOSTEROIDS: Essential Regulators of Plant Growth and Development. *Annu Rev Plant Physiol Plant Mol Biol, 49*, 427-451. doi:10.1146/annurev.arplant.49.1.427

Coen, E., & Rebocho, A. B. (2016). Resolving Conflicts: Modeling Genetic Control of Plant Morphogenesis. *Dev Cell, 38*(6), 579-83. doi:10.1016/j.devcel.2016.09.006

Cosgrove, D. J. (1993). Wall extensibility: its nature, measurement and relationship to plant cell growth. *New Phytologist, 124*(1), 1-23. doi:https://doi.org/10.1111/j.1469-8137.1993.tb03795.x

Cosgrove, D. J. (1997). ASSEMBLY AND ENLARGEMENT OF THE PRIMARY CELL WALL IN PLANTS. *Annual Review of Cell and Developmental Biology, 13*(1), 171-201. doi:10.1146/annurev.cellbio.13.1.171

Cosgrove, D. J. (2005). Growth of the plant cell wall. *Nature Reviews Molecular Cell Biology, 6*(11), 850-861. doi:10.1038/nrm1746

Cui, M.-L., Handa, T., & Ezura, H. (2003). An improved protocol for Agrobacterium-mediated transformation of Antirrhinum majus L. *Molecular Genetics and Genomics, 270*(4), 296-302. doi:10.1007/s00438-003-0923-2

Cui, M.-L., Liu, C., Piao, C.-L., & Liu, C.-L. (2020). A Stable Agrobacterium rhizogenes-Mediated Transformation of Cotton (Gossypium hirsutum L.) and Plant Regeneration From Transformed Hairy Root via Embryogenesis. *Frontiers in Plant Science, 11*.

Derbyshire, P., Findlay, K., McCann, M. C., & Roberts, K. (2007). Cell elongation in Arabidopsis hypocotyls involves dynamic changes in cell wall thickness. *Journal of Experimental Botany, 58*(8), 2079-2089. doi:10.1093/jxb/erm074

Dill, A., & Sun, T.-p. (2001). Synergistic Derepression of Gibberellin Signaling by Removing RGA and GAI Function in Arabidopsis thaliana. *Genetics, 159*(2), 777-785. doi:10.1093/genetics/159.2.777

Durand-Smet, P., Spelman Tamsin, A., Meyerowitz Elliot, M., & Jönsson, H. (2020). Cytoskeletal organization in isolated plant cells under geometry control. *Proceedings of the National Academy of Sciences, 117*(29), 17399-17408. doi:10.1073/pnas.2003184117

Ellison, A. M., & Gotelli, N. J. (2009). Energetics and the evolution of carnivorous plants—Darwin's 'most wonderful plants in the world'. *Journal of Experimental Botany, 60*(1), 19-42. doi:10.1093/jxb/ern179

Fridman, Y., Strauss, S., Horev, G., Ackerman-Lavert, M., Reiner-Benaim, A., Lane, B., Smith, R. S., & Savaldi-Goldstein, S. (2021). The root meristem is shaped by brassinosteroid control of cell geometry. *Nature Plants, 7*(11), 1475-1484. doi:10.1038/s41477-021-01014-9

Fruleux, A., & Boudaoud, A. (2019). Modulation of tissue growth heterogeneity by responses to mechanical stress. *Proceedings of the National Academy of Sciences, 116*(6), 1940-1945. doi:10.1073/pnas.1815342116

Fuchs, M., & Lohmann, J. U. (2020). Aiming for the top: non-cell autonomous control of shoot stem cells in Arabidopsis. *Journal of Plant Research, 133*(3), 297-309. doi:10.1007/s10265-020-01174-3

Gao, Z., Li, Y., Chen, J., Chen, Z., & Cui, M.-L. (2015). A Rapid and Stable Agrobacterium-Mediated Transformation Method of a Medicinal Plant Chelone glabra L. *Applied Biochemistry and Biotechnology, 175*(5), 2390-2398. doi:10.1007/s12010-014-1414-0

Gilbert, S. F. (2000). *Comparative Embryology in Developmental Biology*. Sunderland, Mass.; Bethesda, MD: Sinauer Associates

Gillissen, B., Bürkle, L., André, B., Kühn, C., Rentsch, D., Brandl, B., & Frommer, W. B. (2000). A new family of high-affinity transporters for adenine, cytosine, and purine derivatives in Arabidopsis. *The Plant cell, 12*(2), 291-300. doi:10.1105/tpc.12.2.291

Goriely, A. (2019). *Mathematics and mechanics of biological growth*. [Place of publication not identified]: SPRINGER.

Graeff, M., Rana, S., Marhava, P., Moret, B., & Hardtke, C. S. (2020). Local and Systemic Effects of Brassinosteroid Perception in Developing Phloem. *Curr Biol, 30*(9), 1626-1638.e3. doi:10.1016/j.cub.2020.02.029

Hales, S. (1727). *Vegetable staticks*.

Hall, B. K. (1998). Germ Layers and the Germ-Layer Theory Revisited. In M. K. Hecht, R. J. Macintyre, & M. T. Clegg (Eds.), *Evolutionary Biology* (pp. 121-186). Boston, MA: Springer US.

Hamant, O., & Haswell, E. (2017). Life behind the wall: sensing mechanical cues in plants. *BMC Biology, 15*(1), 59. doi:10.1186/s12915-017-0403-5

Hamant, O., & Traas, J. (2010). The mechanics behind plant development. *New Phytol, 185*(2), 369-85. doi:10.1111/j.1469-8137.2009.03100.x

Hantke, S. S., Carpenter, R., & Coen, E. S. (1995). Expression of floricaula in single cell layers of periclinal chimeras activates downstream homeotic genes in all layers of floral meristems. *Development, 121*(1), 27-35. doi:10.1242/dev.121.1.27

He, J.-X., Gendron Joshua, M., Sun, Y., Gampala Srinivas, S. L., Gendron, N., Sun Catherine, Q., & Wang, Z.-Y. (2005). BZR1 Is a Transcriptional Repressor with Dual Roles in Brassinosteroid Homeostasis and Growth Responses. *Science, 307*(5715), 1634-1638. doi:10.1126/science.1107580

Hofmeister, W. (1859). Ueber die Beugungen saftreicher Pflanzentheile nach Erschutterung. *Jahrbucher fur wissenschaftliche Botanik, 2*, 237-266.

Höfte, H., & Voxeur, A. (2017). Plant cell walls. *Current Biology, 27*(17), R865-R870. doi:https://doi.org/10.1016/j.cub.2017.05.025

Hong, Z., Bednarek, S., Blumwald, E., Hwang, I., Jurgens, G., Menzel, D., Osteryoung, K., Raikhel, N., Shinozaki, K., & Tsutsumi, N. (2003). A unified nomenclature for Arabidopsis dynamin-related large GTPases based on homology and possible functions. *Plant molecular biology, 53*(3), 261-265.

Hong, Z., Ueguchi-Tanaka, M., Umemura, K., Uozu, S., Fujioka, S., Takatsuto, S., Yoshida, S., Ashikari, M., Kitano, H., & Matsuoka, M. (2003). A Rice Brassinosteroid-Deficient Mutant, ebisu dwarf (d2), Is Caused by a Loss of Function of a New Member of Cytochrome P450. *The Plant cell, 15*(12), 2900-2910. doi:10.1105/tpc.014712

Huo, F., Wang, X., Han, Y., Bai, Y., Zhang, W., Yuan, H., & Liu, H. (2012). A new derivatization approach for the rapid and sensitive analysis of brassinosteroids by using ultra high performance liquid chromatography-electrospray ionization triple quadrupole mass spectrometry. *Talanta, 99*, 420-5. doi:10.1016/j.talanta.2012.05.073

Ibañes, M., Fàbregas, N., Chory, J., & Caño-Delgado, A. I. (2009). Brassinosteroid signaling and auxin transport are required to establish the periodic pattern of Arabidopsis shoot vascular bundles. *Proceedings of the National Academy of Sciences of the United States of America, 106*(32), 13630-13635. doi:10.1073/pnas.0906416106

Ibarra-Laclette, E., Lyons, E., Hernández-Guzmán, G., Pérez-Torres, C. A., Carretero-Paulet, L., Chang, T.-H., Lan, T., Welch, A. J., Juárez, M. J. A., Simpson, J., Fernández-Cortés, A., Arteaga-Vázquez, M., Góngora-Castillo, E., Acevedo-Hernández, G., Schuster, S. C., Himmelbauer, H., Minoche, A. E., Xu, S., Lynch, M., Oropeza-Aburto, A., Cervantes-Pérez, S. A., de Jesús Ortega-Estrada, M., Cervantes-Luevano, J. I., Michael, T. P., Mockler, T., Bryant, D., Herrera-Estrella, A., Albert, V. A., & Herrera-Estrella, L. (2013). Architecture and evolution of a minute plant genome. *Nature, 498*, 94. doi:10.1038/nature12132

https://www.nature.com/articles/nature12132#supplementary-information

Ivakov, A., & Persson, S. (2013). Plant cell shape: modulators and measurements. *Frontiers in Plant Science, 4*. doi:10.3389/fpls.2013.00439

Jackson, D., Veit, B., & Hake, S. (1994). Expression of maize KNOTTED1 related homeobox genes in the shoot apical meristem predicts patterns of morphogenesis in the vegetative shoot. *Development, 120*(2), 405-413.

Jankowicz-Cieslak, J., & Till, B. J. (2016). Chemical Mutagenesis of Seed and Vegetatively Propagated Plants Using EMS. *Current Protocols in Plant Biology, 1*(4), 617-635. doi:https://doi.org/10.1002/cppb.20040

Kang, B.-H., Busse, J. S., & Bednarek, S. Y. (2003). Members of the Arabidopsis dynamin-like gene family, ADL1, are essential for plant cytokinesis and polarized cell growth. *The Plant cell, 15*(4), 899-913. doi:10.1105/tpc.009670

Kathryn Barton, M. (1998). Cell type specification and self renewal in the vegetative shoot apical meristem. *Current opinion in plant biology, 1*(1), 37-42. doi:https://doi.org/10.1016/S1369-5266(98)80125-8

Kelly, A. J., & Meeks-Wagner, D. R. (1995). Characterization of a gene transcribed in the L2 and L3 layers of the tobacco shoot apical meristem. *The Plant Journal, 8*(1), 147-153.

Kempin, S. A., Mandel, M. A., & Yanofsky, M. F. (1993). Conversion of Perianth into Reproductive Organs by Ectopic Expression of the Tobacco Floral Homeotic Gene NAG1. *Plant Physiology, 103*(4), 1041-1046. doi:10.1104/pp.103.4.1041

Kim, H. B., Kwon, M., Ryu, H., Fujioka, S., Takatsuto, S., Yoshida, S., An, C. S., Lee, I., Hwang, I., & Choe, S. (2006). The Regulation of DWARF4 Expression Is Likely a Critical Mechanism in Maintaining the Homeostasis of Bioactive Brassinosteroids in Arabidopsis. *Plant Physiology, 140*(2), 548-557. doi:10.1104/pp.105.067918

Kim, Y., Schumaker, K. S., & Zhu, J.-K. (2006). EMS Mutagenesis of Arabidopsis. In J. Salinas & J. J. Sanchez-Serrano (Eds.), *Arabidopsis Protocols* (pp. 101-103). Totowa, NJ: Humana Press.

Kohorn, B. D., Zorensky, F. D. H., Dexter-Meldrum, J., Chabout, S., Mouille, G., & Kohorn, S. (2021). Mutation of an Arabidopsis Golgi membrane protein ELMO1 reduces cell adhesion. *Development, 148*(10), dev199420. doi:10.1242/dev.199420

Koornneef, M., & van der Veen, J. H. (1980). Induction and analysis of gibberellin sensitive mutants in Arabidopsis thaliana (L.) heynh. *Theoretical and Applied Genetics, 58*(6), 257-263. doi:10.1007/BF00265176

Kraus, G. (1867). Die Gewebespannung des Stammes und ihre Folgen. *Botanische Zeitung, 25*, 105-142.

Kuchen, E. E., Fox, S., Barbier de Reuille, P., Kennaway, R., Bensmihen, S., Avondo, J., Calder, G. M., Southam, P., Robinson, S., Bangham, A., & Coen, E. (2012). Generation of Leaf Shape Through Early Patterns of Growth and Tissue Polarity. *Science, 335*(6072), 1092-1096. doi:10.1126/science.1214678

Kutschera, U. (1992). The Role of the Epidermis in the Control of Elongation Growth in Stems and Coleoptiles. *Botanica Acta, 105*(4), 246-252. doi:https://doi.org/10.1111/j.1438-8677.1992.tb00294.x

Kutschera, U. (2008). The Growing Outer Epidermal Wall: Design and Physiological Role of a Composite Structure. *Annals of botany, 101*(5), 615-621. doi:10.1093/aob/mcn015

Kutschera, U., & Niklas, K. J. (2007). The epidermal-growth-control theory of stem elongation: An old and a new perspective. *Journal of Plant Physiology, 164*(11), 1395-1409. doi:https://doi.org/10.1016/j.jplph.2007.08.002

Lagomarsino, M. C., Tanase, C., Vos, J. W., Emons, A. M. C., Mulder, B. M., & Dogterom, M. (2007). Microtubule Organization in Three-Dimensional Confined Geometries: Evaluating the Role of Elasticity Through a Combined In Vitro and Modeling Approach. *Biophysical Journal, 92*(3), 1046-1057. doi:https://doi.org/10.1529/biophysj.105.076893

Lan, T., Renner, T., Ibarra-Laclette, E., Farr, K. M., Chang, T.-H., Cervantes-Pérez, S. A., Zheng, C., Sankoff, D., Tang, H., Purbojati, R. W., Putra, A., Drautz-Moses, D. I., Schuster, S. C., Herrera-Estrella, L., & Albert, V. A. (2017). Long-read sequencing uncovers the adaptive topography of a carnivorous plant genome. *Proceedings of the National Academy of Sciences, 114*(22), E4435-E4441. doi:10.1073/pnas.1702072114

Lee, K., Avondo, J., Morrison, H., Blot, L., Stark, M., Sharpe, J., Bangham, A., & Coen, E. (2006). Visualizing plant development and gene expression in three dimensions using optical projection tomography. *The Plant cell, 18*(9), 2145-2156. doi:10.1105/tpc.106.043042

Lee, K. J. I., Bushell, C., Koide, Y., Fozard, J. A., Piao, C., Yu, M., Newman, J., Whitewoods, C., Avondo, J., Kennaway, R., Marée, A. F. M., Cui, M., & Coen, E. (2019). Shaping of a three-dimensional carnivorous trap through modulation of a planar growth mechanism. *PLOS Biology, 17*(10), e3000427-e3000427. doi:10.1371/journal.pbio.3000427

Leitão, J. (2012). Chemical mutagenesis. *Plant mutation breeding and biotechnology*, 135-158.

Lenhard, M., & Laux, T. (1999). Shoot meristem formation and maintenance. *Current opinion in plant biology, 2*(1), 44-50. doi:https://doi.org/10.1016/S1369-5266(99)80009-0

Leyser, O. (1999). Plant hormones: Ins and outs of auxin transport. *Current Biology, 9*(1), R8-R10. doi:10.1016/S0960-9822(99)80033-5

Li, Y., Gao, Z., Piao, C., Lu, K., Wang, Z., & Cui, M.-L. (2014). A Stable and Efficient Agrobacterium tumefaciens-Mediated Genetic Transformation of the Medicinal Plant Digitalis purpurea L. *Applied Biochemistry and Biotechnology, 172*(4), 1807-1817. doi:10.1007/s12010-013-0648-6

Liu, X., Yang, Q., Wang, Y., Wang, L., Fu, Y., & Wang, X. (2018). Brassinosteroids regulate pavement cell growth by mediating BIN2-induced microtubule stabilization. *Journal of Experimental Botany, 69*(5), 1037-1049. doi:10.1093/jxb/erx467

Lloyd, C. (2007). The expanding cell. *Annals of botany, 100*(1), 153-154. doi:10.1093/aob/mcm101

Lloyd, C., & Chan, J. (2008). The parallel lives of microtubules and cellulose microfibrils. *Current opinion in plant biology, 11*(6), 641-6. doi:10.1016/j.pbi.2008.10.007

Lloyd, F. E. (1942). *The Carnivorous Plants*.

Lockhart, J. A. (1965). An analysis of irreversible plant cell elongation. *J Theor Biol, 8*(2), 264-75. doi:10.1016/0022-5193(65)90077-9

Lozano-Elena, F., Planas-Riverola, A., Vilarrasa-Blasi, J., Schwab, R., & Caño-Delgado, A. I. (2018). Paracrine brassinosteroid signaling at the stem cell niche controls cellular regeneration. *Journal of Cell Science, 131*(2), jcs204065. doi:10.1242/jcs.204065

Lu, P., Porat, R., Nadeau, J. A., & O'Neill, S. D. (1996). Identification of a meristem L1 layer-specific gene in Arabidopsis that is expressed during embryonic pattern formation and defines a new class of homeobox genes. *The Plant cell, 8*(12), 2155-2168.

Marks, M. D., & Feldmann, K. A. (1989). Trichome Development in Arabidopsis thaliana. I. T-DNA Tagging of the GLABROUS1 Gene. *The Plant cell, 1*(11), 1043-1050. doi:10.1105/tpc.1.11.1043

Martin David, N., Proebsting William, M., & Hedden, P. (1997). Mendel's dwarfing gene: cDNAs from the Le alleles and function of the expressed proteins. *Proceedings of the National Academy of Sciences, 94*(16), 8907-8911. doi:10.1073/pnas.94.16.8907

McKenna, A., Hanna, M., Banks, E., Sivachenko, A., Cibulskis, K., Kernytsky, A., Garimella, K., Altshuler, D., Gabriel, S., Daly, M., & DePristo, M. A. (2010). The Genome Analysis Toolkit: A MapReduce framework for analyzing next-generation DNA sequencing data. *Genome Research, 20*(9), 1297-1303.

McQueen-Mason, S., Durachko, D. M., & Cosgrove, D. J. (1992). Two endogenous proteins that induce cell wall extension in plants. *The Plant cell, 4*(11), 1425-33. doi:10.1105/tpc.4.11.1425

Mirza, J. I., & Maher, E. P. (1987). Physiological characteristics of two auxin-resistant mutants of Arabidopsis thaliana, aux-2 and Dwf. *Plant Growth Regulation, 5*(1), 41-49. doi:10.1007/BF00035018

Monna, L., Kitazawa, N., Yoshino, R., Suzuki, J., Masuda, H., Maehara, Y., Tanji, M., Sato, M., Nasu, S., & Minobe, Y. (2002). Positional cloning of rice semidwarfing gene, sd-1: rice "green revolution gene" encodes a mutant enzyme involved in gibberellin synthesis. *DNA research, 9*(1), 11-17.

Mouille, G., Ralet, M.-C., Cavelier, C., Eland, C., Effroy, D., Hématy, K., McCartney, L., Truong, H. N., Gaudon, V., Thibault, J.-F., Marchant, A., & Höfte, H. (2007). Homogalacturonan synthesis in Arabidopsis thaliana requires a Golgi-localized protein with a putative methyltransferase

domain. *The Plant Journal, 50*(4), 605-614. doi:https://doi.org/10.1111/j.1365-313X.2007.03086.x

Noguchi, T., Fujioka, S., Choe, S., Takatsuto, S., Yoshida, S., Yuan, H., Feldmann, K. A., & Tax, F. E. (1999). Brassinosteroid-Insensitive Dwarf Mutants of Arabidopsis Accumulate Brassinosteroids. *Plant Physiology, 121*(3), 743-752. doi:10.1104/pp.121.3.743

Oh, M.-H., Wang, X., Clouse Steven, D., & Huber Steven, C. (2012). Deactivation of the Arabidopsis BRASSINOSTEROID INSENSITIVE 1 (BRI1) receptor kinase by autophosphorylation within the glycine-rich loop. *Proceedings of the National Academy of Sciences, 109*(1), 327-332. doi:10.1073/pnas.1108321109

Oropeza-Aburto, A., Cervantes-Pérez, S. A., Albert, V. A., & Herrera-Estrella, L. (2020). Agrobacterium tumefaciens mediated transformation of the aquatic carnivorous plant Utricularia gibba. *Plant Methods, 16*(1), 50. doi:10.1186/s13007-020-00592-7

Peng, J., Richards, D. E., Hartley, N. M., Murphy, G. P., Devos, K. M., Flintham, J. E., Beales, J., Fish, L. J., Worland, A. J., Pelica, F., Sudhakar, D., Christou, P., Snape, J. W., Gale, M. D., & Harberd, N. P. (1999). 'Green revolution' genes encode mutant gibberellin response modulators. *Nature, 400*(6741), 256-261. doi:10.1038/22307

Peters, W. S., Richter, U., & Felle, H. H. (1992). Auxin-induced H(+)-pump stimulation does not depend on the presence of epidermal cells in corn coleoptiles. *Planta, 186*(2), 313-6. doi:10.1007/bf00196261

Peters, W. S., & Tomos, D. (1996). The Epidermis Still in Control? *Botanica Acta, 109*(4), 264-267. doi:https://doi.org/10.1111/j.1438-8677.1996.tb00572.x

Petrášek, J., & Friml, J. i. (2009). Auxin transport routes in plant development. *Development, 136*(16), 2675-2688. doi:10.1242/dev.030353

Poethig, S. (1989). Genetic mosaics and cell lineage analysis in plants. *Trends in Genetics, 5*, 273-277. doi:https://doi.org/10.1016/0168-9525(89)90101-7

Poplin, R., Ruano-Rubio, V., DePristo, M. A., Fennell, T. J., Carneiro, M. O., Van der Auwera, G. A., Kling, D. E., Gauthier, L. D., Levy-Moonshine, A., Roazen, D., Shakir, K., Thibault, J., Chandran, S., Whelan, C., Lek, M., Gabriel, S., Daly, M. J., Neale, B., MacArthur, D. G., & Banks, E. (2018). Scaling accurate genetic variant discovery to tens of thousands of samples. *bioRxiv*, 201178. doi:10.1101/201178

Poppinga, S., Weisskopf, C., Westermeier, A. S., Masselter, T., & Speck, T. (2015). Fastest predators in the plant kingdom: functional morphology and biomechanics of suction traps found in the largest genus of carnivorous plants. *AoB PLANTS, 8*, plv140. doi:10.1093/aobpla/plv140

Prusinkiewicz, P., & Runions, A. (2012). Computational models of plant development and form. *New Phytol, 193*(3), 549-569. doi:10.1111/j.1469-8137.2011.04009.x

Purushotham, P., Cho, S. H., Díaz-Moreno, S. M., Kumar, M., Nixon, B. T., Bulone, V., & Zimmer, J. (2016). A single heterologously expressed plant cellulose synthase isoform is sufficient for cellulose microfibril formation in vitro. *Proceedings of the National Academy of Sciences, 113*(40), 11360-11365.

Rao, X., & Dixon, R. A. (2017). Brassinosteroid Mediated Cell Wall Remodeling in Grasses under Abiotic Stress. *Frontiers in Plant Science, 8*. doi:10.3389/fpls.2017.00806

Ray, P. M., Green, P. B., & Cleland, R. (1972). Role of Turgor in Plant Cell Growth. *Nature, 239*(5368), 163-164. doi:10.1038/239163a0

Rayle, D. L., & Cleland, R. E. (1992). The Acid Growth Theory of auxin-induced cell elongation is alive and well. *Plant Physiology, 99*(4), 1271-1274. doi:10.1104/pp.99.4.1271

Refrégier, G., Pelletier, S., Jaillard, D., & Höfte, H. (2004). Interaction between wall deposition and cell elongation in dark-grown hypocotyl cells in Arabidopsis. *Plant Physiology, 135*(2), 959-968. doi:10.1104/pp.104.038711

Reinhardt, B., Hänggi, E., Müller, S., Bauch, M., Wyrzykowska, J., Kerstetter, R., Poethig, S., & Fleming, A. J. (2007). Restoration of DWF4 expression to the leaf margin of a dwf4 mutant is sufficient

to restore leaf shape but not size: the role of the margin in leaf development. *The Plant Journal, 52*(6), 1094-1104. doi:doi:10.1111/j.1365-313X.2007.03304.x

Reut, M. S., & Płachno, B. J. (2020). Unusual developmental morphology and anatomy of vegetative organs in Utricularia dichotoma—leaf, shoot and root dynamics. *Protoplasma, 257*(2), 371-390. doi:10.1007/s00709-019-01443-6

Sachs, J. (1865). *Handbuch der physiologischen Botanik*. Leipzig: Engelmann.

Sachs, J. (1875). *Text-book of botany, morphological and physiological*. Oxford: Clarendon Press.

Sánchez-Rodríguez, C., Ketelaar, K., Schneider, R., Villalobos Jose, A., Somerville Chris, R., Persson, S., & Wallace Ian, S. (2017). BRASSINOSTEROID INSENSITIVE2 negatively regulates cellulose synthesis in Arabidopsis by phosphorylating cellulose synthase 1. *Proceedings of the National Academy of Sciences, 114*(13), 3533-3538. doi:10.1073/pnas.1615005114

Satina, S., Blakeslee, A. F., & Avery, A. G. (1940). Demonstration of the Three Germ Layers in the Shoot Apex of Datura by Means of Induced Polyploidy in Periclinal Chimeras. *American Journal of Botany, 27*(10), 895-905. doi:10.2307/2436558

Savaldi-Goldstein, S., Peto, C., & Chory, J. (2007). The epidermis both drives and restricts plant shoot growth. *Nature, 446*, 199. doi:10.1038/nature05618

https://www.nature.com/articles/nature05618#supplementary-information

Scheller, H. V., & Ulvskov, P. (2010). Hemicelluloses. *Annual review of plant biology, 61*, 263-289.

Schneeberger, K. (2014). Using next-generation sequencing to isolate mutant genes from forward genetic screens. *Nat Rev Genet, 15*(10), 662-76. doi:10.1038/nrg3745

Serrano-Mislata, A., Bencivenga, S., Bush, M., Schiessl, K., Boden, S., & Sablowski, R. (2017). DELLA genes restrict inflorescence meristem function independently of plant height. *Nat Plants, 3*(9), 749-754. doi:10.1038/s41477-017-0003-y

Sessions, A., Weigel, D., & Yanofsky, M. F. (1999). The Arabidopsis thaliana MERISTEM LAYER 1 promoter specifies epidermal expression in meristems and young primordia. *Plant J, 20*(2), 259-63. doi:10.1046/j.1365-313x.1999.00594.x

Sieburth, L. E., Drews, G. N., & Meyerowitz, E. M. (1998). Non-autonomy of AGAMOUS function in flower development: use of a Cre/loxP method for mosaic analysis in Arabidopsis. *Development, 125*(21), 4303-4312. doi:10.1242/dev.125.21.4303

Sinha, N., & Hake, S. (1990). Mutant characters of Knotted maize leaves are determined in the innermost tissue layers. *Developmental Biology, 141*(1), 203-210. doi:https://doi.org/10.1016/0012-1606(90)90115-Y

Smith, S. M., & Maughan, P. J. (2015). SNP genotyping using KASPar assays. *Methods Mol Biol, 1245*, 243-56. doi:10.1007/978-1-4939-1966-6_18

Somerville, C. (2006). Cellulose Synthesis in Higher Plants. *Annual Review of Cell and Developmental Biology, 22*(1), 53-78. doi:10.1146/annurev.cellbio.22.022206.160206

Somssich, M., Vandenbussche, F., Ivakov, A., Funke, N., Ruprecht, C., Vissenberg, K., VanDer Straeten, D., Persson, S., & Suslov, D. (2021). Brassinosteroids Influence Arabidopsis Hypocotyl Graviresponses through Changes in Mannans and Cellulose. *Plant Cell Physiol, 62*(4), 678-692. doi:10.1093/pcp/pcab024

Steeves, T. A., & Sussex, I. M. (1989). *Patterns in plant development*: Cambridge University Press.

Stephenson, P., Baker, D., Girin, T., Perez, A., Amoah, S., King, G. J., & Østergaard, L. (2010). A rich TILLING resource for studying gene function in Brassica rapa. *BMC Plant Biology, 10*(1), 62. doi:10.1186/1471-2229-10-62

Suzuki, H., Inoue, T., Fujioka, S., Saito, T., Takatsuto, S., Yokota, T., Murofushi, N., Yanagisawa, T., & Sakurai, A. (1995). Conversion of 24-methylcholesterol to 6-oxo-24-methylcholestanol, a putative intermediate of the biosynthesis of brassinosteroids, in cultured cells of Catharanthus roseus. *Phytochemistry, 40*(5), 1391-1397. doi:https://doi.org/10.1016/0031-9422(95)00579-V

Szekeres, M., Németh, K., Koncz-Kálmán, Z., Mathur, J., Kauschmann, A., Altmann, T., Rédei, G. P., Nagy, F., Schell, J., & Koncz, C. (1996). Brassinosteroids Rescue the Deficiency of CYP90, a

Cytochrome P450, Controlling Cell Elongation and De-etiolation in Arabidopsis. *Cell, 85*(2), 171-182. doi:https://doi.org/10.1016/S0092-8674(00)81094-6

Theresa, A. C., & Jennifer, H. R. (2012). An architectural model for the bladderwort Utricularia gibba (Lentibulariaceae). *The Journal of the Torrey Botanical Society, 139*(2), 137-148. doi:10.3159/TORREY-D-11-00088.1

Thoma, S., Hecht, U., Kippers, A., Botella, J., De Vries, S., & Somerville, C. (1994). Tissue-specific expression of a gene encoding a cell wall-localized lipid transfer protein from Arabidopsis. *Plant Physiology, 105*(1), 35-45.

Till, B. J., Reynolds, S. H., Greene, E. A., Codomo, C. A., Enns, L. C., Johnson, J. E., Burtner, C., Odden, A. R., Young, K., Taylor, N. E., Henikoff, J. G., Comai, L., & Henikoff, S. (2003). Large-Scale Discovery of Induced Point Mutations With High-Throughput TILLING. *Genome Research, 13*(3), 524-530.

Traas, J., & Vernoux, T. (2002). The shoot apical meristem: the dynamics of a stable structure. *Philosophical Transactions of the Royal Society of London. Series B: Biological Sciences, 357*(1422), 737-747. doi:10.1098/rstb.2002.1091

Truernit, E., Bauby, H., Dubreucq, B., Grandjean, O., Runions, J., Barthélémy, J., & Palauqui, J. C. (2008). High-resolution whole-mount imaging of three-dimensional tissue organization and gene expression enables the study of Phloem development and structure in Arabidopsis. *The Plant cell, 20*(6), 1494-503. doi:10.1105/tpc.107.056069

van Esse, G. W., van Mourik, S., Stigter, H., ten Hove, C. A., Molenaar, J., & de Vries, S. C. (2012). A Mathematical Model for BRASSINOSTEROID INSENSITIVE1-Mediated Signaling in Root Growth and Hypocotyl Elongation. *Plant Physiology, 160*(1), 523-532. doi:10.1104/pp.112.200105

Vanholme, R., De Meester, B., Ralph, J., & Boerjan, W. (2019). Lignin biosynthesis and its integration into metabolism. *Current Opinion in Biotechnology, 56*, 230-239.

Verger, S., Long, Y., Boudaoud, A., & Hamant, O. (2018). A tension-adhesion feedback loop in plant epidermis. *eLife, 7*, e34460. doi:10.7554/eLife.34460

Vincent, O., Weißkopf, C., Poppinga, S., Masselter, T., Speck, T., Joyeux, M., Quilliet, C., & Marmottant, P. (2011). Ultra-fast underwater suction traps. *Proceedings of the Royal Society B: Biological Sciences, 278*(1720), 2909-2914. doi:10.1098/rspb.2010.2292

Volkov, A. G., Adesina, T., & Jovanov, E. (2007). Closing of venus flytrap by electrical stimulation of motor cells. *Plant Signal Behav, 2*(3), 139-45. doi:10.4161/psb.2.3.4217

von Hanstein, J. L. E. R. (1868). *Die Scheitelzellgruppe im Vegetationspunkt der Phanerogamen*.

Vukašinović, N., Wang, Y., Vanhoutte, I., Fendrych, M., Guo, B., Kvasnica, M., Jiroutová, P., Oklestkova, J., Strnad, M., & Russinova, E. (2021). Local brassinosteroid biosynthesis enables optimal root growth. *Nature Plants, 7*(5), 619-632. doi:10.1038/s41477-021-00917-x

Wang, X., Zhang, J., Yuan, M., Ehrhardt, D. W., Wang, Z., & Mao, T. (2012). Arabidopsis MICROTUBULE DESTABILIZING PROTEIN40 Is Involved in Brassinosteroid Regulation of Hypocotyl Elongation. *The Plant cell, 24*(10), 4012-4025. doi:10.1105/tpc.112.103838

Wang, Z.-Y., Seto, H., Fujioka, S., Yoshida, S., & Chory, J. (2001). BRI1 is a critical component of a plasma-membrane receptor for plant steroids. *Nature, 410*(6826), 380-383. doi:10.1038/35066597

Weber, E., Engler, C., Gruetzner, R., Werner, S., & Marillonnet, S. (2011). A Modular Cloning System for Standardized Assembly of Multigene Constructs. *PLOS ONE, 6*(2), e16765. doi:10.1371/journal.pone.0016765

Werner, T., Motyka, V., Laucou, V., Smets, R., Van Onckelen, H., & Schmülling, T. (2003). Cytokinin-deficient transgenic Arabidopsis plants show multiple developmental alterations indicating opposite functions of cytokinins in the regulation of shoot and root meristem activity. *The Plant cell, 15*(11), 2532-50. doi:10.1105/tpc.014928

Whitewoods, C. D. (2021). Riddled with holes: Understanding air space formation in plant leaves. *PLOS Biology, 19*(12), e3001475. doi:10.1371/journal.pbio.3001475

Whitewoods, C. D., Gonçalves, B., Cheng, J., Cui, M., Kennaway, R., Lee, K., Bushell, C., Yu, M., Piao, C., & Coen, E. (2020). Evolution of carnivorous traps from planar leaves through simple shifts in gene expression. *Science, 367*(6473), 91-96. doi:10.1126/science.aay5433

Wolf, S., Mravec, J., Greiner, S., Mouille, G., & Höfte, H. (2012). Plant Cell Wall Homeostasis Is Mediated by Brassinosteroid Feedback Signaling. *Current Biology, 22*(18), 1732-1737. doi:https://doi.org/10.1016/j.cub.2012.07.036

Xie, L., Yang, C., & Wang, X. (2011). Brassinosteroids can regulate cellulose biosynthesis by controlling the expression of CESA genes in Arabidopsis. *Journal of Experimental Botany, 62*(13), 4495-4506. doi:10.1093/jxb/err164

Xin, P., Yan, J., Li, B., Fang, S., Fan, J., Tian, H., Shi, Y., Tian, W., Yan, C., & Chu, J. (2016). A Comprehensive and Effective Mass Spectrometry-Based Screening Strategy for Discovery and Identification of New Brassinosteroids from Rice Tissues. *Frontiers in Plant Science, 7*.

Xiong, Y., Wu, B., Du, F., Guo, X., Tian, C., Hu, J., Lü, S., Long, M., Zhang, L., Wang, Y., & Jiao, Y. (2021). A crosstalk between auxin and brassinosteroid regulates leaf shape by modulating growth anisotropy. *Mol Plant, 14*(6), 949-962. doi:10.1016/j.molp.2021.03.011

Yamagami, A., Saito, C., Nakazawa, M., Fujioka, S., Uemura, T., Matsui, M., Sakuta, M., Shinozaki, K., Osada, H., Nakano, A., Asami, T., & Nakano, T. (2017). Evolutionarily conserved BIL4 suppresses the degradation of brassinosteroid receptor BRI1 and regulates cell elongation. *Scientific Reports, 7*(1), 5739. doi:10.1038/s41598-017-06016-2

Yan, W., Deng, X. W., Yang, C., & Tang, X. (2021). The Genome-Wide EMS Mutagenesis Bias Correlates With Sequence Context and Chromatin Structure in Rice. *Frontiers in Plant Science, 12*.

Zhao, F., Du, F., Oliveri, H., Zhou, L., Ali, O., Chen, W., Feng, S., Wang, Q., Lü, S., Long, M., Schneider, R., Sampathkumar, A., Godin, C., Traas, J., & Jiao, Y. (2020). Microtubule-Mediated Wall Anisotropy Contributes to Leaf Blade Flattening. *Current Biology, 30*(20), 3972-3985.e6. doi:https://doi.org/10.1016/j.cub.2020.07.076

Zhong, R., & Ye, Z.-H. (2015). Secondary Cell Walls: Biosynthesis, Patterned Deposition and Transcriptional Regulation. *Plant and Cell Physiology, 56*(2), 195-214. doi:10.1093/pcp/pcu140